UNIVERSITI TEKNOLOGI MARA

REDUCED GRAPHENE OXIDE LOADED SILVER NANOSTARS EMBEDDED HYDROGELS FOR OPTICAL FIBRE BIOSENSORS

AZIB HAIMAN BIN ROSLAN

MSc

August 2026

UNIVERSITI TEKNOLOGI MARA

REDUCED GRAPHENE OXIDE LOADED SILVER NANOSTARS EMBEDDED HYDROGELS FOR OPTICAL FIBRE BIOSENSORS

AZIB HAIMAN BIN ROSLAN

Thesis submitted in fulfilment
of the requirements for the degree of
Master of Science
(Mechanical Engineering)

Faculty of Mechanical Engineering

August 2026

CONFIRMATION BY PANEL OF EXAMINERS

I certify that a Panel of Examiners has met on 11 Jun 2026 to conduct the final examination of Azib Haiman Bin Roslan on his Master of Science thesis entitled "Reduced Graphene Oxide Loaded Silver Nanostars Embedded Hydrogels for Optical Fibre Biosensors" in accordance with Universiti Teknologi MARA Act 1976 (Akta 173). The Panel of Examiners recommends that the student be awarded the relevant degree. The Panel of Examiners was as follows:

Mohamad Ali Ahmad, PhD
Associate Professor
Faculty of Mechanical Engineering
Universiti Teknologi MARA
(Chairman)

Irnie Azlin @ Nur Aqilah Zakaria, PhD
Associate Professor
College of Mechanical Engineering
Universiti Teknologi MARA
(Internal Examiner)

Wan Fahmin Faiz Wan Ali, PhD
Associate Professor
Faculty of Mechanical Engineering
University Teknologi Malaysia
(External Examiner)

PROF DR HJH ZURAEDA IBRAHIM
Dean
Institute of Postgraduate Studies
Universiti Teknologi MARA

Date: 14 August 2026

AUTHOR'S DECLARATION

I declare that the work in this thesis was carried out in accordance with the regulations of Universiti Teknologi MARA. It is original and is the results of my own work, unless otherwise indicated or acknowledged as referenced work. This thesis has not been submitted to any other academic institution or non-academic institution for any degree or qualification.

I, hereby, acknowledge that I have been supplied with the Academic Rules and Regulations for Postgraduate, Universiti Teknologi MARA, regulating the conduct of my study and research.

Name of Student	:	Azib Haiman Roslan
Student ID. No.	:	2022526417
Programme	:	Master of Science (Mechanical Engineering) – CEEM750
Faculty	:	Mechanical Engineering
Thesis Title	:	Reduced Graphene Oxide Loaded Silver Nanostars Embedded Hydrogels for Optical Fibre Biosensors
Signature of Student	:	
Date	:	August 2026

ABSTRACT

This study investigates the development of a fibre-optic biosensing platform integrating silver nanostars (AgNs), reduced graphene oxide (rGO), and hybrid hydrogels (HH) for protein detection. Despite the promising optical properties of AgNs and rGO, fibre-optic sensors coated with these materials alone often suffer from limited sensitivity, stability, and biomolecule immobilization capability. To address these limitations, an rGO–AgNs nanocomposite was developed and optimized for fibre-optic coating applications. The synthesis of AgNs was optimized by varying hydroxylamine concentration to produce highly optical AgNs. AgNs sample I exhibits a strong interaction with light, as confirmed in UV-Vis spectrometer analysis. The star-shaped AgNs sample I managed to display a consistent morphological structure with a spike length of 352.62 ± 59.72 nm under SEM and TEM imaging. To improve stability and optical performance, rGO was synthesized via the Tour method using ascorbic acid as a green reducing agent and then integrated with AgNs. Other parameters, such as the amount of graphene oxide precursor and the volume of hydrogen peroxide, were varied to obtain the optimal conditions for synthesising rGO. This can be confirmed by UV-Vis spectroscopy, with rGO I showing absorbance at 241 nm and 306 nm, surpassing other rGO samples, which can be attributed to stronger light interaction. At the same time, the crinkled graphitic structure was confirmed under the SEM imaging. rGO also exhibits the highest hydrophobicity at 111.0° with a zeta potential of –36.1 mV. The structural composition was also confirmed under EDX and FTIR analysis. The defect structure was confirmed via Raman spectra, with an I_D/I_G ratio of 1.102. The rGO–AgNs composite with a 1:5 mixing ratio demonstrated balanced signal enhancement and stability, making it a suitable candidate for fibre-optic cladding. A 24-hour dipping time for the rGO-AgNs coating yields stronger signal performance than 12- or 6-hour dips. The optimised rGO–AgNs composite was successfully coated onto bare optical fibres and further integrated into chitosan-agarose-based hybrid hydrogels via a layer-by-layer (LbL) approach with a 24-hour dipping time. The untreated fibre-coated rGO–AgNs–HH configuration exhibited the highest sensitivity (63132 intensity/RUI) and acceptable linearity (0.8012) for refractive index (RI) detection. The signal strength produced by the fibre-coated tri-composite material was 9194.89 a.u., which is 192.04% higher than fibre-coated AgNs alone, 160% higher than fibre-coated with rGO, and 26.16% higher than rGO-AgNs coating. Protein detection was evaluated using the streptavidin–biotin interaction; no signal shift was observed with biotin alone, confirming specificity. Upon introducing streptavidin, the signal shifted from 662.92 nm to 663.17 nm, indicating successful incorporation of streptavidin into the sensing medium. The peak began to shift again as biotin entered the system, with a shift in wavelength from 663.17 nm to 664.2 nm, indicating successful detection of protein interactions. Overall, this work demonstrates the feasibility of an rGO–AgNPs–HH fibre-optic biosensing system with enhanced optical performance, stability, and specificity, highlighting its potential for future biosensing applications.

ACKNOWLEDGEMENT

Praise be to Allah Subhanahwata'la for providing me the time, strength to work, and good health while completing this study.

My deepest gratitude and appreciation go to my supervisor, Dr Siti Rabizah Makhsin, for her absolute guidance, generous assistance, encouragement, patience, and unwavering support throughout this study.

My appreciation goes to my co-supervisors, Assoc. Prof. Ir. Ts. Dr. Rozina Abdul Rani and Prof. Dr. Khairunnisak Abdul Razak who provided me with support and encouragement in completing this research with the facility's equipment and assistance during sampling. Special thanks as well to my colleagues and friends for helping me with this project.

Acknowledgement on behalf of academics at the Faculty of Mechanical Engineering for providing me with the opportunity to continue my research studies to the next level. In addition to that, I'd like to express my gratitude to all technical staff and support from the College of Engineering and Faculty of Applied Science, UiTM, Shah Alam, for their patience, guidance, and provision of the necessary equipment for this study.

This work is financially supported by the GIP UiTM (600-RMCGIP5/3(106/2022)), grant, FRGS grant (FRGS/1/2019/TK03/UITM/02/8) by the Ministry of Higher Education Malaysia xx, and Global Research Reputation Grant, UiTM (600-RMC 5/3/GRR (008/2020)).

Also, many thanks to my family, friends, and those who were directly or indirectly involved in this study for believing in me, supporting me, and providing me with moral support while completing the project's objective.

Above all, I wish everyone success and happiness in their lives. May Allah bless our lives in this world and the next with loved ones.

TABLE OF CONTENTS

		Page
CONFIRMATION BY PANEL OF EXAMINERS		**ii**
AUTHOR'S DECLARATION		**iii**
ABSTRACT		**iv**
ACKNOWLEDGEMENT		**v**
TABLE OF CONTENTS		**vi**
LIST OF TABLES		**x**
LIST OF FIGURES		**xii**
LIST OF SYMBOLS		**xvii**
LIST OF ABBREVIATIONS		**xix**
LIST OF NOMENCLATURES		**xxii**
CHAPTER 1	**INTRODUCTION**	**1**
1.1	Research Background	1
1.2	Problem Statement	3
1.3	Research Objectives	4
1.4	Research Questions	5
1.5	Significance of the Study	5
1.6	Assumption	6
1.7	Ethical committee	7
1.8	Thesis Scope and Limitation	7
1.9	Thesis Outline	9
CHAPTER 2	**LITERATURE REVIEW**	**11**
2.1	Introduction	11
2.2	Fibre Optics	11
2.2.1	Introduction to Fibre Optics Technology	11
2.2.2	Type of Fibre Optics	12
2.2.3	Fabrication of Fibre Optic Sensor	15
2.2.4	Fibre Optics Sensor Mechanism	16
2.2.5	Fibre Optic Biosensing Application	18
2.3	Method to Enhance the Signal of an Optical Fibre Sensor	25

2.3.1 Redesign The Fibre Optic Structure 25
2.3.2 Sensing Material Deposition 26
2.4 Silver Nanoparticles (AgNPs) 27
2.4.1 Introduction to AgNPs 27
2.4.2 Synthesize of AgNs 27
2.4.3 Characterization of AgNPs 31
2.4.4 AgNPs-Based Fibre Optic Sensors 34
2.5 Reduced Graphene Oxide (rGO) 39
2.5.1 Introduction to Graphene-Based Materials 39
2.5.2 Synthesize of rGO 40
2.5.3 Characterization of rGO 45
2.6 Hybrid rGO-AgNPs-Based 47
2.6.1 Synthesis of rGO-AgNPs 47
2.6.2 Characteristics of rGO-AgNPs 50
2.7 Research Gap Analysis on Tri-hybrid Composites of AgNPs-Graphene Based-Hydrogel 52
2.7.1 Hydrogels 52
2.7.2 Tri-hybrid-Based Graphene/Ag/Hydrogel-Based Fibre Optic Biosensors 54
2.8 Summary 60

CHAPTER 3 RESEARCH METHODOLOGY 61

3.1 Introduction 61
3.2 Materials and Chemicals 63
3.3 Phase 1: Synthesis of AgNs and rGO 64
3.3.1 Synthesis of AgNs 64
3.3.2 Synthesis of rGO 65
3.4 Phase 2: Fabrications of AgNs Embedded rGO 68
3.4.1 Characterization of AgNs, rGO, and rGO-AgNs on Glass Slide 69
3.5 Phase 3: Embedding of rGO-AgNs on the Sensing Probe 70
3.5.1 Sensing Probe Preparations 70
3.5.2 Embedding the AgNs, rGO, and rGO-AgNs on the Sensing Probe 71
3.5.3 Surface Treatment of rGO-AgNs Embedding the Sensing Probe 71
3.6 Phase 4: Embedding the rGO-AgNs-HH on the Sensing Probe 71
3.6.1 Hybrid Hydrogels 71
3.6.2 Coating the Fibre Optics with rGO-AgNs-HH 72

3.6.3 Characterization of AgNs, rGO, rGO-AgNs, and rGO-AgNs-HH on Sensing Probe 73
3.7 Signal Sensing on Embedded Sensor Probe 74
3.7.1 Signal Performance on The Embedded Sensing Probe 74
3.7.2 RI Detection on The Embedded Sensing Probe 75
3.7.3 Recovery and Reusability Evaluation on The Fibre Sensor 75
3.8 Phase 5: Binding Kinetics and Porosity of Sensor Probe 76
3.8.1 Coating Sequence Configuration 76
3.8.2 Porosity of Sensor Probe 77
3.8.3 Detection of Protein Interaction on the Sensing Probe 78
3.8.4 Specificity of Protein Detection 79

CHAPTER 4 RESULTS AND DISCUSSION 80

4.1 Overview 80
4.2 Phase 1: Synthesis and Characterization of AgNs and rGO 81
4.2.1 AgNs 81
4.2.2 rGO 84
4.3 Phase 2: rGO-AgNs 112
4.3.1 Optical Properties of rGO-AgNs 112
4.3.2 Surface Morphology of rGO-AgNs with Different Ratios 113
4.3.3 Chemical and Structural Analysis of rGO–AgNs Nanocomposite 115
4.4 Phase 3: Characterization of Optical Fibre Coated with Sensing Materials (AgNs, rGO, and rGO-AgNs) 117
4.4.1 SEM and EDX Analysis 117
4.4.2 Signal Sensor on Fibre Optics Coated with The Sensing Materials 119
4.4.3 Effect of Surface Enhancer on Sensing Medium 123
4.5 Phase 4: Embedding rGO-AgNs-HH on the Sensing Probe 131
4.5.1 Signal Detection 131
4.5.2 SEM and EDX 133
4.6 Phase 4: Signal Sensing (RI Sensitivity and Stability) on Fibre-Coated rGO-AgNs-HH 135
4.6.1 RI sensitivity 135
4.6.2 Stability - Recovery Error on Fibre-Coated rGO-AgNs-HH After Washing Processes 136
4.7 Phase 5: Binding Kinetics and Porosity of Sensor Probe 138
4.7.1 Porosity of Sensor Probe 138

4.7.2 Detection of Protein (Streptavidin-Biotin) Interactions on The Sensing Probe 139
4.7.3 Specificity of Detection 141
4.8 Mechanism for Protein Detection in the rGO-AgNs-HH Based Fibre Optic Biosensor 142

CHAPTER 5 CONCLUSION AND RECOMMENDATIONS 144

5.1 Conclusions 144
5.2 Recommendations 146
REFERENCES 148
APPENDICES 169
AUTHOR'S PROFILE 179

LIST OF TABLES

Tables	Title	Page
Table 2.1	Type of Fibre Optics	13
Table 2.2	Compilation of Methods in Protein Detection	22
Table 2.3	Summary of Various Shapes of AgNPs and Their Applications	29
Table 2.4	Compilation of AgNPs in Biosensing Applications	35
Table 2.5	Compilation of Past rGO Methods	42
Table 2.6	Records on the Procedure in Synthesizing rGO-NMNPs	48
Table 2.7	Research Gap on Utilizing rGO, AgNPs, and HH in Biosensor Applications	55
Table 3.1	List of Chemicals and Materials Used in this Research	63
Table 3.2	Parameter Sets on Hydroxylamine Concentrations in Synthesizing AgNs	65
Table 3.3	Parameters Set on Synthesized rGO	67
Table 3.4	Parameters on rGO-AgNs with Different Ratios	68
Table 3.5	Compiled Procedure for Synthesizing Surface Treatment Solutions	71
Table 3.6	Fibre Optics Dipping Sequence Procedure and Coating Layers	73
Table 4.1	EDX Analysis Results on GO and rGO Samples A, B, C, and D	88
Table 4.2	EDX Analysis on GO, rGO E, rGO F, and rGO G	99
Table 4.3	EDX Analysis Result on rGO H, rGO I, and rGO J	107
Table 4.4	EDX Results of GO, rGO, AgNs, and rGO-AgNs at Various Mixing Ratios	115

Table 4.5	EDX Analysis and Thickness Measurement of Uncoated and Coated Fibre Optics Probes with AgNS, rGO, and rGO-AgNS at Various Mixing Ratios	118
Table 4.6	Signal of Light Intensity Reading Detected when the Sensing Platform of Fibre Optic Probe Coated with AgNs, rGO, and rGO-AgNs at Various Mixing Ratios	120
Table 4.7	Recovery Error (%) on Treated and Untreated Fibre Optics Coated rGO-AgNs	127
Table 4.8	Recovery Error on Untreated and Treated Fibre Coated rGO-AgNs (1:5)	130
Table 4.9	Element Composition on the Surface of the Cleaved Fibre Optics Coated rGO-AgNs-HH	135
Table 4.10	Recovery Error on Fibre Optics Coated rGO-AgNs-HH	137

LIST OF FIGURES

Figures	Title	Page
Figure 1.1	Conceptual Design of the Proposed Fibre Optic Sensing Platform Modified with the AgNs–rGO–HH Nanocomposite Layer	2
Figure 2.1	Standard Configuration of SOF Probe. (Roslan et al., 2025)	15
Figure 2.2	Fibre Optic Sensing Categories	16
Figure 2.3	(A) TIR Phenomenon and (B) Evanescence Field. (Millis, 2012)	17
Figure 2.4	Optical fibres with altered geometries. (Alam et al., 2017)	25
Figure 2.5	TEM image of Ag NPs with different shapes: (A) nanosphere, (B) nanowire, (C) nanorods, (D) nanocube, (E) nanotriangle, (F) nanoflower, (G) nanostar and (H) nanocrystal. Adapted from (Loiseau et al., 2019)	28
Figure 2.6	Range of Shapes and Sizes of AgNs. Adapted from (Garcia-Leis et al., 2013)	32
Figure 2.7	(a) Polydispersity and (b) Aggregation of AgNs. Adapted from (Garcia-Leis et al., 2017)	34
Figure 2.8	Morphological structure of (a) graphite, (b) graphite oxide, (c) GO, and (d) rGO. Adapted from (Chuah et al., 2020)	45
Figure 2.9	SEM Image on the Morphological Structure of rGO-AgNPs Under (A) In-Situ (Kasztelan et al., 2021) and (B) LbL Sandwich Method (Tran et al., 2015).	51
Figure 3.1	Flowchart of the Overall Research Methodology	62
Figure 3.2	Procedure in Synthesizing AgNs	64
Figure 3.3	Procedure in Synthesizing rGO	67

Figure 3.4 Physical Appearance of rGO-AgNs with Ratios of 1:5, 1:10, 1:15, and 1:20 68

Figure 3.5 Uncladding of Fibre Optics 70

Figure 3.6 Splicing of both fibre optic ends using a fusion splicer prior to signal measurement 74

Figure 3.7 Integration of Hybrid Hydrogels and rGO-AgNs on the Surface of Optical Fibre 77

Figure 3.8 Procedure of (A) Protein Detection and (B) Specificity of Protein Detection 78

Figure 4.1 UV-Vis on AgNs Samples Synthesized Using Various Concentrations of Hydroxylamine 81

Figure 4.2 TEM Images (a-d) and FESEM Images (e-f) of the Synthesized AgNs Samples with Sample L (a and e), Sample M (b and f), Sample N (c and g), and Sample O (d and h) 83

Figure 4.3 UV-vis Spectrum on rGO with Different Amounts of GO 85

Figure 4.4 SEM Images of (a) GO and (b-e) rGO Samples with (b) Sample A, (c) Sample B, (d) Sample C, and (e) Sample D 86

Figure 4.5 Morphological Structure of (a) Graphite (Sahudin et al., 2021), (b) GO, and (c) rGO B under FESEM Imaging 87

Figure 4.6 XRD Results on GO and rGO Samples A, B, C, and D 89

Figure 4.7 Zeta Potential and Contact Angle of GO and rGO A, rGO B, rGO C, and rGO D 90

Figure 4.8 Physical Observation of the rGO Samples A, B, C, and D After 24 Hours 91

Figure 4.9 FTIR Analysis on GO and rGO Samples A, B, C, and D 93

Figure 4.10 Raman Spectra of GO and rGO A, rGO B, rGO C, and rGO 94

Figure 4.11	UV Spectrum of the Synthesized rGO Sample E.1, E, F, and G	96
Figure 4.12	Zeta Potential and Contact Angle Analysis on rGO Sample E.1, E, F, and G	97
Figure 4.13	Physical Observation on rGO Samples E.1, E, F, and G After 24 Hours	98
Figure 4.14	SEM Images of rGO Samples (a) Sample E, (b) Sample F, and (c) Sample G	99
Figure 4.15	XRD Spectrum on rGO Samples E, F, and G	100
Figure 4.16	Result of FTIR Analysis on GO and rGO Samples E, F, and G	101
Figure 4.17	Raman Spectrum on rGO Samples E, F, and G	102
Figure 4.18	Absorbance Performance of GO, rGO H, rGO I, and rGO J	103
Figure 4.19	Zeta Potential and Contact Angle Analysis on rGO H, rGO I, and rGO J	104
Figure 4.20	Physical Observation on rGO Sample H, I, and J After 24 Hours	105
Figure 4.21	SEM Images of rGO Samples (a) rGO H, (b) rGO I, and (c) rGO J	106
Figure 4.22	Plane Peak Appearance on GO, rGO H, rGO I, and rGO J under XRD Analysis	107
Figure 4.23	FTIR Spectrum on GO and rGO Samples H, I, and J	109
Figure 4.24	Raman Spectra Analysis Result on GO, rGO H, rGO I, and rGO J	110
Figure 4.25	TEM Imaging on (a) Graphite, (b) GO, and (c) Synthesized rGO I. TEM images of graphite and GO were previously reported by (Sahudin et al., 2022)	111
Figure 4.26	Absorbance Peak Intensity Produced by rGO-AgNs with Different Ratios Using a UV-vis Spectrometer	113

Figure 4.27	SEM Images of rGO-AgNs with a Mixing Ratio of (1) 1:5, (2) 1:10, (3) 1:15, and (d) 1:20 at 5000 (a) and 10000 (b) Magnification under SEM Imaging	114
Figure 4.28	FTIR Spectrum on rGO, AgNs, and rGO-AgNs (1:5)	115
Figure 4.29	Raman Spectrum of GO, rGO, GO-AgNs (1:5), and rGO-AgNs (1:5)	116
Figure 4.30	SEM Images of the Sensing Platform Coated with (a) AgNs, (b) rGO, and rGO-AgNs with a Ratio of (c) 1:5, (d) 1:10, (e) 1:15, and (f) 1:20	117
Figure 4.31	Surface of Cross-Sectional Structure of the (a) Uncoated/Bare Fibre Optics (a) and Fibre Optics Coated with rGO-AgNs with a Ratio of (b) 1:5, (c) 1:10, (d) 1:15, and (e) 1:20	119
Figure 4.32	Signal Strength on the Fibre Optics Coated rGO-AgNs with Different Ratios for (a) 6 Hours, (b) 12 Hours, and (c) 24 Hours	122
Figure 4.33	Light Intensity on Treated Fibre Optics Coated with rGO-AgNs (1:5)	123
Figure 4.34	RI Detection on Treated Fibre Optics Coated with rGO-AgNs (1:5) with (a) Chromic Acid, (b) Ethanol, (c) NaOH, (d) Piranha Solution, (e) Silane, and (f) Untreated Probe	125
Figure 4.35	Full RI Detection Cycles of rGO–AgNs (1:5)-Coated Fibre-Optic Probes Under Different Surface Treatments: (a) Chromic Acid, (b) Ethanol, (c) NaOH, (d) Piranha Solution, (e) Silane, and (f) Untreated Fibre	129
Figure 4.36	Peak Intensity of Different Variations of rGO-AgNs-HH	132
Figure 4.37	SEM Images of rGO–AgNs–HH-Coated Fibre-Optic Probes Showing Side-View Morphology (a, b) and Cross-Sectional Structure (c, d) at Low (a, c) and High Magnifications (b, d)	134

Figure 4.38 EDX Spot and Area Analysis of the Cross-Sectional Area on the Surface of Cleaved Fibre Optics Coated rGO-AgNs-HH 135

Figure 4.39 RI Sensitivity and Linearity Performance of Fibre-Coated rGO-AgNs-HH 136

Figure 4.40 Full Test Cycle of the RI Detection Test on Fibre Optics Coated rGO-AgNs-HH 137

Figure 4.41 Porosity Test on Fibre Optics Coated rGO-AgNs-HH 139

Figure 4.42 Protein Detection of Fibre-Coated rGO-AgNs-HH 140

Figure 4.43 Specificity Test on Fibre Optics Coated rGO-AgNs-HH 142

Figure 4.44 Schematic Diagram of Fibre Optics Coated rGO-AgNs-HH in Biosensing Mechanism 142

LIST OF SYMBOLS

Symbols

M	Molar Concentration ($mol \cdot L^{-1}$)
μm	Micron, Micrometre (10^{-6} m)
cm	Centimetre (10^{-2} m)
nm	Nanometre (10^{-9} m)
g	Gram
mg	Milligram (10^{-3} g)
mL	Millilitre (10^{-3} L)
μL	Microlitre (10^{-6} L)
Θ	Angle
pH	Measure of Acidity or Alkalinity of a Solution
cm^{-1}	Inverse Centimetre
°C	Degree Celsius
a.u.	Arbitrary Units
mV	Millivolts
°	Degree
%	Percentage Concentrations
% (w/v)	Weight Per Volume Percentage
% (v/v)	Volume Per Volume Percentage
at. %	Atomic Weight Percentage
RIU	Refractive Index Unit

RIU^{-1}	Inverse Refractive Index Unit, Used in Sensitivity Calculations
intensity/RIU	Sensor Sensitivity Expressed as Signal Intensity Change Per Refractive Index Unit
R^2	Coefficient of Determination, Indicating Linearity of Response
mg/mL	Mass Concentration (milligram per millilitre)

LIST OF ABBREVIATIONS

Abbreviations

AgNFs	Silver Nanoflowers
AgNPs	Silver Nanoparticles
AgNs	Silver Nanostars
AuNPs	Gold Nanoparticles
BiFC	Bimolecular Fluorescence Complementation
BSA	Bovine Serum Albumin
CAH	Chitosan-Agarose Hydrogels
CROF	Cladding-Removed Optical Fibre
CVD	Chemical Vapour Deposition
DI	Deionized
DNA	Deoxyribonucleic Acid
EDX	Energy-Dispersive X-ray
ELISA	Enzyme-Linked Immunosorbent Assay
ERGO	Electrochemically Reduced Graphene Oxide
FC	Ferrule Connector
FCC	Face-Centered Cubic
FESEM	Field Emission Scanning Electron Microscopy
FREP	Förster Resonance Energy Transfer
FTIR	Fourier Transform Infrared
FTO	Fluorine-doped Tin Oxide

GO	Graphene Oxide
GQDs	Graphene Quantum Dots
HH	Hybrid Hydrogels
IgG	Immunoglobulin G
LbL	Layer-by-Layer
LSPR	Localized Surface Plasmonic Resonance
LSS	Liquid-Solid-Solution
MIC	Minimum Inhibitory Concentration
MIPs	Molecular Imprinted Polymers
MMF	Multi-Mode Fibre
NIR	Near-Infrared
NMNPs	Noble Metal Nanoparticles
NPs	Nanoparticles
ORR	Oxygen Reduction Reaction
PBG	Photonic-Band Gap
PBS	Phosphate-Buffered Saline
PCF	Photonic Crystal Fibre
PEG	Polyethylene Glycol
POF	Plastic-Optical Fibre
Ppy	Polypyrrole
PtNPs	Platinum Nanoparticles
PVP	Polyvinylpyrrolidone
rGO	Reduced Graphene Oxide

RI	Refractive Index
RNA	Ribonucleic Acid
SA-LbL	Spin-Assisted Layer-by-Layer
SEM	Scanning Electron Microscopy
SERS	Surface-Enhanced Raman Scattering
SiO	Silicon Monoxide
SMF	Single-Mode Fibre
SPR	Surface Plasmonic Resonance
TEM	Transmission Electron Microscopy
TiO	Titanium Monoxide
TIR	Total Internal Reflection
UV-Vis	Ultra-Violet Visible
XRD	X-Ray Diffraction

LIST OF NOMENCLATURES

Nomenclatures

π	Pi Electron Orbital (Or Pi Electron System) Involved in Conjugation
π–π	Non-Covalent Interaction Between Aromatic Rings (π–π Stacking)
π–π^*	Electronic Transition from Bonding π Orbital to Anti-Bonding π^* Orbital
d-spacing	Interplanar Spacing Between Crystallographic Planes
-OH	Hydroxyl Functional Group
-O	Oxygen-Containing Functional Group
-COOH	Carboxyl Functional Group
sp^2	Carbon Atoms in Graphene or rGO Exhibiting Planar Trigonal Geometry and π-Conjugation
C/O	Carbon-To-Oxygen Atomic Ratio, Indicating the Degree of Reduction of Graphene-Based Materials
O-H	Oxygen–Hydrogen Bond Vibration
C-O	Carbon–Oxygen Bond Vibration
C-C	Carbon–Carbon Bond Vibration
C=O	Carbonyl Functional Group
C=C	Carbon–Carbon Double Bond Associated With sp^2 Carbon Networks
C≡C	Carbon–Carbon Triple Bond
O=C=O	Linear Molecular Structure of Carbon Dioxide

(hkl)	Miller Indices Representing Crystallographic Planes in XRD Analysis
D-band	Defect-Induced Raman Band of Carbon Materials
G-band	Graphitic Raman Band Associated with sp^2 Carbon
I_D/I_G	Intensity Ratio of D-Band to G-Band in Raman Spectra
2D-band	Second-Order Raman Band Associated with Graphitic Stacking and Layer Number
D+G band	Combination Raman Band Arising from Simultaneous D- and G-Band Scattering
y	Dependent Variable in Linear Regression Analysis
m	Slope of the Linear Regression Line
c	Intercept of the Linear Regression Line
Θ_{Res}	Residual Value in Regression Analysis
x_1	Individual Data Point in Regression Analysis
x	Independent Variable in Linear Regression Analysis
2Θ	Diffraction Angle in X-ray Diffraction Analysis
Ag^+	Silver Ion
Ag^0	Metallic Silver (Neutral State)

CHAPTER 1
INTRODUCTION

1.1 Research Background

Fibre optics biosensors have found diverse applications across various fields, such as spanning microbiological testing, bioimaging, cancer diagnosis, and biomolecular detection (Rithesh Raj & Sudarsanakumar, 2017; Zibaii et al., 2014). In fibre optics biosensors, both physical and biological components are essential for their functionality. Fibre optics serves as the physical component due to its capability to transmit light through a strand of glass or plastic over long distances with minimal losses (Jachetta, 2007). When light is produced at a specific wavelength, total internal reflection (TIR) occurs as it hits the interface between two media at an angle greater than the critical angle, causing the light to reflect completely back into the medium from its surroundings (Tan et al., 2023). This phenomenon happens multiple times within the fibre optics, creating an evanescent field outside the medium interface.

Unlike conventional reflections, where light bounces off a surface, in TIR within an optical fibre, light penetrates slightly into the cladding region instead of stopping at the core-cladding boundary. This penetration generates an electromagnetic field, known as the evanescent field, which extends beyond the core of the fibre but decays exponentially with distance from the core/cladding interface (Pahurkar et al., 2015). This evanescent field is frequently utilized in sensing applications because it can interact with substances outside the fibre core, enabling the detection of biological and chemical analytes. However, the evanescent field produced by fibre optics alone isn't strong enough to detect protein interactions at the surface of the medium.

One promising strategy to enhance the optical performance of fibre-optic-based biosensors is the incorporation of noble metal nanoparticles (NMNPs) into the sensor platform. Noble metals such as gold nanoparticles (AuNPs), silver nanoparticles (AgNPs), and platinum nanoparticles (PtNPs) have been widely explored in biosensing applications due to their plasmonic characteristics (Doria et al., 2012). These nanoparticles exhibit localized surface plasmon resonance (LSPR), a phenomenon in which collective oscillations of conduction electrons are induced upon interaction with specific wavelengths of incident light (Sau et al., 2010). The resulting enhancement of

the local electromagnetic field significantly amplifies light–matter interactions at the sensing interface, thereby improving sensitivity and detection performance.

Nevertheless, because of the inherent instability of AgNPs, the graphene-based materials can be introduced as a matrix layer to the sensing configuration (C. Xu & Wang, 2012). The graphitic structure facilitates the inhibition of AgNPs' structure, thereby aiding in stabilizing them. Hydrogel materials such as chitosan and agar can be used to integrate into the fibre optic sensing platform to facilitate the bioconjugation process (Wu, Wu, et al., 2023) while aiding in amplifying the evanescent signal (Wu, Xu, et al., 2023). Consequently, this modification by integrating trihybrid materials consisting of AgNPs with graphene-based materials and hydrogel is an ideal combination that promises to elevate the performance of the fibre optic biosensor. Thus, the optimization in synthesizing higher quality of these sensing materials together with designing and fabricating the sensor's configuration is critically desired. Figure 1.1 illustrates the conceptual design of the proposed sensing platform, in which the modified fibre optic sensing region is functionalised with the AgNs–rGO–HH nanocomposite layer. The success of the integration of these sensing materials for biosensing activities is evaluated via the detection of streptavidin (Streptomyces avidinii) interacting with biotin as the target analyte.

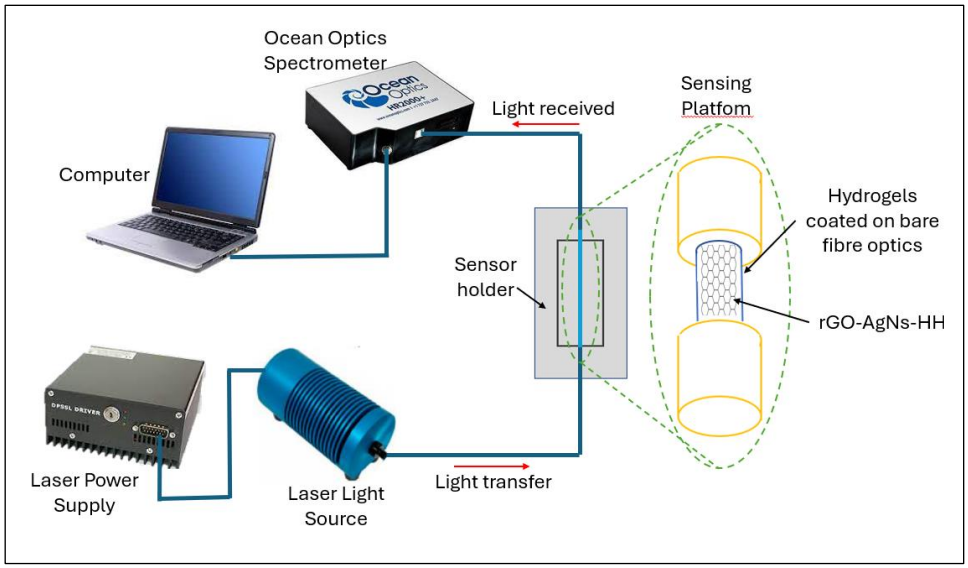

Figure 1.1 Conceptual Design of the Proposed Fibre Optic Sensing Platform Modified with the AgNs–rGO–HH Nanocomposite Layer

1.2 Problem Statement

The application of fibre optics in biomedical settings is attributed to its high sensitivity in detecting minute changes and robust optical properties, rendering it well-suited for integration into biological materials. To detect biomolecules effectively, fibre optics requires integration with biosensing materials capable of detecting their presence with high sensitivity (Mostufa et al., 2024). To achieve stronger biomolecule detection, enhancing the sensitivity of the fibre optics is critical. Incorporating noble-metal nanomaterials such as AgNPs into the fibre can further enhance its optical performance and sensitivity. One crucial criterion for AgNPs in augmenting the optical strength of fibre optics is their surface area. A larger surface area of AgNPs facilitates increased interaction with light, leading to further enhancement of LSPR.

Silver nanostars (AgNs) exhibit particularly robust LSPR responses compared to other shapes (Garcia-Leis et al., 2013) due to their sharp branches and multiple protruding tips in nanostar structures, which allow them to generate intense electromagnetic "hot spots," resulting in enhanced light–matter interactions. In addition to their optical advantages, AgNs can be synthesized via relatively simple chemical reduction methods. Garcia-Leis et al., (2017) introduced a single-step hydroxylamine-mediated reduction approach that is straightforward, cost-effective, and safer compared to conventional multi-step or high-temperature synthesis routes.

However, a notable issue with AgNs is their relatively lower stability compared to other NMNPs, resulting in their optical properties not lasting as long. This instability can lead to degradation of their plasmonic properties over time, resulting in poor optical properties of the samples (Zare, 2016). Thinh et al., (2022) reported that the lattice structure of graphene-based materials can be an effective solution to this agglomeration issue. Hence, a method in synthesizing rGO and embedding the AgNs into rGO will be studied to decide on which method is the most suitable for applying to this research.

In designing the biosensor configuration system, biomaterial detectors are necessary to detect the biomaterials in contact with the embedded fibre optics. Biosensors rely on both physical and biological platforms for the detection (D'Souza, 2001). Therefore, to enable interaction between physical and biological properties, hydrogels are needed to facilitate the immobilization of biological detectors into sensing platform, allowing fibre optics to detect these interactions. Hydrogels are widely used in biosensing applications due to their 3-dimensional polymeric network capacity to

facilitate the inhibition of biomaterial detectors (Sengar & Dubey, 2026). The hybrid hydrogel consisting of chitosan-agarose of hybrid hydrogels (HH) has demonstrated promising results in biosensing applications (Makhsin et al., 2020). The interaction between the target protein and the sensing layer resulted in a significant shift in peak intensity and wavelength, confirming effective biomolecular recognition. Furthermore, the coating of chitosan-agarose hydrogels onto single-mode fibre has been shown to enhance optical signal performance due to favourable light–material interactions at the sensing interface (Akashah et al., 2023).

While silver-based NPs combining with graphene-based materials have been demonstrated for fibre optic signal enhancement (Aziz et al., 2015; A. H. Roslan et al., 2024), and hybrid hydrogel-AuNPs coatings have shown improved fibre optic performance (Makhsin et al., 2023; Sadani et al., 2019), an integrated tri-hybrid coating combining AgNs, rGO, and HH for fibre optic biosensing has not been widely reported. Moreover, the optimal tri-hybrid sequence has yet to be confirmed due to its influence on sensor sensitivity, signal enhancement, stability, and protein detection performance. Therefore, the proposed AgNs–rGO–HH tri-hybrid configuration presents a promising strategy to address the aforementioned challenges in the development of supersensitive fibre-optic biosensors, especially for protein detection applications.

1.3 Research Objectives

The aim of this research is to:

1. To optimize the synthesis parameters of AgNs and rGO via the chemical reduction method.
2. To characterize the morphology, optical properties, and stability of AgNs and rGO using suitable elemental analysis instrumentation.
3. To develop an integrated structure of AgNs loaded rGO embedded HH as sensing materials for a fibre optic sensing configuration.
4. To analyze the sensing characteristics of rGO-AgNs-HH nanocomposites in terms of signal sensitivity and suitability for the protein detection.

The synthesis process of AgNs will successfully be formed to achieve desirable morphology and good plasmonic properties to afford a large fibre optic intensification by configuring the parameters. Subsequently, rGO-loaded AgNs embedded hydrogel

will be successfully fabricated and then conjugated with biomolecules (such as aptamers) to validate the biosensing ability. Lastly, the signal performance of the developed fibre optic biosensors will increase after encapsulation with fabricated nanocomposites (rGO-AgNs) embedded hydrogel.

1.4 Research Questions

This research aims to address the following questions:

1. How does the hydroxylamine concentration affect the optical properties and morphology of silver nanostars (AgNs)?
2. Can rGO synthesized via the Tour method using ascorbic acid exhibit optical properties suitable for fibre optic sensing applications?
3. What are the optical and structural characteristics of AgNs and rGO as determined using UV–Vis, SEM, EDX, XRD, FTIR, Raman, and zeta potential analyses?
4. How different are the AgNs-to-rGO mixing ratios, which will influence the optical performance and morphological integration of rGO–AgNs nanocomposites?
5. How does the incorporation and sequencing of HH affect the signal performance of fibre optic sensing systems?
6. Can the optimized rGO–AgNs–HH coated fibre selectively detect protein interactions via the streptavidin–biotin mechanism?

1.5 Significance of the Study

This research contributes to the advancement of nanotechnology, where enhanced optical biosensors are achieved through the development of a newly integrated trihybrid sensing platform, consisting of AgNs, rGO, and a HH matrix on a fibre optic system. By improving optical signal strength and stability, the study addresses key limitations in sensitivity and reliability commonly encountered in fibre optic biosensing technologies. The integration of plasmonic nanomaterials with graphene-based structures offers potential improvements in early biomolecular detection, particularly in monitoring protein interactions and refractive index changes. Enhanced sensitivity in such sensing systems may support future applications in rapid

disease diagnostics, pathogen detection, and biomedical monitoring, contributing to improved healthcare screening and public health surveillance.

Moreover, this study aligns with Malaysia's National Nanotechnology Policy and Strategy (NNPS) 2021–2030, led by NanoMalaysia Bhd (NMB) and MOSTI, with the plan aiming to integrate nanotechnology into sectors like energy, healthcare, and agriculture, targeting advancements in smart materials and Internet of Things (IoT) technologies. This plan emphasizes in strengthening nanotechnology research, innovation, and commercialization to position Malaysia as a high-technology nation. Thus, by contributing to advanced material development and optical sensing technologies, this work will be able to support national objectives in healthcare, agriculture, food safety, and environmental monitoring.

From a healthcare perspective, this research will also contribute to creating improved fibre optic biosensors that will offer potential applications in early disease detection and biomolecular monitoring. In the long term, such platforms may be extended for pathogen detection, supporting public health surveillance and biosafety management. Additionally, the development of sensitive and real-time optical sensing systems also aligns with Industry 4.0, that aim to focus on delivering real-time decision making via a product that is flexible and easier to adapt to multiple platforms. This will assist industries in building a cost-effective fibre-based sensing material that can support local hospitals by enabling faster and more accurate disease detection, reducing waiting time for laboratory testing, and improving patient treatment response. At the same time, it can also be applied in the food industry to monitor contamination, detect harmful microorganisms, and ensure food products are safe before reaching consumers.

1.6 Assumption

This study assumes that the chemical synthesis procedures for AgNs, GO, and rGO are produced under controlled laboratory conditions. It is assumed that the coating and drying process of the fibre optic-coated sensing medium was done under the same environmental conditions. It is also assumed that the fibre optic sensing systems used are properly calibrated and capable of recording multiple accurate readings at the same time. The fibre optics used in this research is assumed to have the same range of insertion loss (signal reduction) and return loss (back reduction), allowing a better understanding of reading the signal detection. Environmental conditions such as

temperature and ambient light are assumed to remain sufficiently stable during signal measurements so as not to significantly influence the recorded spectral responses.

1.7 Ethical committee

This research does not involve human participants, animal subjects, or clinical samples. Therefore, ethical committee approval was not required for this study.

1.8 Thesis Scope and Limitation

The general purpose of this study is to improve the signal performance of fibre optic biosensors utilizing the trihybrid nanostructures of AgNs-rGO-HH. In this study, AgNs, rGO, and HH were in-house synthesized with the optimum synthesis conditions were systematically studied. AgNs was synthesized using a single-step chemical reduction using hydroxylamine, while rGO was synthesized from further exfoliation of GO. The parameters involved in changing the hydroxylamine concentration during the synthesis of AgNs with concentrations set at 7.2 x 10^{-4} %, 3.8 x 10^{-4} %, 1.8 x 10^{-4} %, and 0.9 x 10^{-4} % to determine a suitable size of nanoparticles. Meanwhile, rGO synthesis parameters involved by changing the weight of GO powder (500 mg, 400 mg, 300 mg, and 200 mg) to find an appropriate amount needed to produce rGO. Moreover, the change in ascorbic acid powder (5 g, 4 g, and 3 g) and the change in volume of hydrogen peroxide (12 mL, 10 m, and 8 mL) will be set on the parameters study as well to identify the optimum quantity required to effectively reduce the GO and volume needed to assist in removing residual reducing agents, ensuring better stability and quality of the synthesized rGO. Prior to that, GO was prepared using the modified Hummers method. The success of synthesized AgNs, rGO, and HH was determined by characterization testing using ultraviolet-visible (UV-Vis) spectroscopy, scanning electron microscopy (SEM), energy dispersive x-ray (EDX), zeta analyzer, contact angle, x-ray diffraction (XRD), Fourier transform infrared (FTIR), and Raman spectroscopy.

For the fabrication of the sensors, a single-mode silica fibre (SOF) fibre optic with FC-FC type was used as a sensing platform. The different dipping times, which are 6, 12, and 24 hours, were set as parameters to study their optical performance at different layered rGO-AgNs. By different layered rGO-AgNs, the fibre coating was set with a mixture of 1:5 ratio (1 part of rGO and 5 parts of AgNs) firstly before repeating the procedure on new fibre with different mixture ratio of coating, such as 1:10, 1:15,

and 1:20. Once coated with rGO-AgNs, the tip end of fibre optic coated with rGO-AgNs is spliced to allow light to pass through when tested with optical spectrometer analysis. For each fabrication and sensor evaluation testing, individual materials, bare/AgNs/rGO/ were used as a control.

Before embedding the bare fibre optics with rGO-AgNs, surface treatment such as sodium hydroxide, silane, ethanol, chromic acid, and piranha solution was applied on the surface of the fibre to strengthen the binding coating. The suitable coating treatment can be confirmed by recording their signal performance, refractive index (RI) sensitivity, and linearity test. Upon confirming suitable surface treatment, the HH will be introduced to provide a platform for the biomolecule to be immobilized. The sequence of rGO-AgNs and HH will be studied to determine the most suitable coating order for improving the optical signal response of the fibre optic sensing platform. The selected coating sequence of the tri-compound sensing medium (rGO-AgNs-HH) was validated via Ri and porosity test before introducing the streptavidin-biotin interaction for the protein detection test. Specificity detection was recorded to confirm the detection of protein interactions.

However, there are limitations in realizing the production of the sensor and it requires many more steps to ensure that it can be realized before being translated into practical applications. The fabrication process involves multiple material synthesis and coating stages, including AgNs, rGO, and HH preparation, which may introduce variability in terms of consistency and precision when manufacturing in large quantities. While the sensor performed well in a controlled streptavidin–biotin model, it has not been applied against real-world samples like blood or food. Subsequently, the device has yet to be tested against complex matrices, such as blood, serum, or environmental samples, where background interference and non-specific binding could potentially compromise accuracy. Moreover, this study did not explore the detection of alternative targets, such as pathogens or nucleic acids, nor did it evaluate the sensor's long-term stability and field readiness. Therefore, further optimization and real-sample validation are necessary to establish its practical applicability.

1.9 Thesis Outline

This thesis is organized into five chapters, where Chapter 1 introduces the background of fibre optics biosensors and the purpose of integrating the AgNs, graphene-based materials, and hydrogel-based for optical sensor applications. This chapters consist of the problem statement, research objectives, research questions, assumptions, thesis scope, and the significance of the study, providing an overall framework for the research.

Chapter 2 reviews the relevant literature related to fibre optics and discusses how fibre optics can be applied to biosensors. It establishes the gap analysis in current research. This chapter highlights the purpose of introducing Ag nanostructures to the fibre biosensor system and how different shapes of nanoparticles can produce different results. Moreover, it also reviews the special characteristics of graphene-based materials and highlights the importance of their lattice structure in supporting the metallic nanoparticles. The synthesis method of rGO was compiled to study and understand the benefits and their applications. The methods for incorporating both rGO and AgNs from past researchers were also compiled to study and understand how both components can be integrated in biosensing applications. A study related to hydrogels was also conducted, and all methods used to integrate with AgNs and graphene-based materials were compiled to understand the characteristics of hydrogels and how to take advantage of them in adapting them into the fibre biosensor. A method for uncladding the protective layer of fibre and cladding it with a sensing medium was studied in this chapter as well. This study helps in understanding how to clad the bare silicon fibre that is slippery with the sensing medium and determine if there is a way to support the binding of the coating. Fibre. In addition, the method of introducing biomolecules onto the sensing platform was investigated to determine how the detection of biomolecules was conducted and to find out which method is suited for this biosensor system.

Chapter 3 describes the materials, synthesis procedures, and experimental methods employed in this research. This includes the synthesis and optimization of AgNs, preparation of rGO using the Tour method, fabrication of rGO–AgNs nanocomposites, and integration with hydrogels. The testing needed to characterize were listed in this chapter, including the list of equipment needed to characterize them. The step needed in preparing the fibre optic for the coating process was also included in this chapter, along with the method in treating the surface of the bare fibre to allow

stronger binding during the coating process. Method in testing the signal strength and RI detection were then used to test their signal performance and find a suitable sequence that can produce a better signal. Finally, this chapter will include the method for detecting the biomaterial and how to confirm the specificity of the detection.

Chapter 4 provides the results, data analysis and discussions obtained from the experimental work. The chapter begins with the optimization of AgNs and rGO synthesis parameters, highlighting the importance of hydroxylamine concentration and reduction conditions on nanoparticle morphology and their optical behavior. Thorough characterization of AgNs, rGO, and AgNs–rGO nanocomposites is then discussed via UV–VIS spectroscopy, SEM–EDX, FTIR, Raman spectroscopy, zeta potential, and contact angle analysis to evaluate their structural, elemental, and stability properties. Subsequently, the integration of rGO-AgNs embedded within the hydrogel matrix onto the fibre optic platform is studied, with emphasis on evaluating different coating sequences to determine the configuration that yields optimal optical performance. The selected sequences were then subjected to RI detection to evaluate the signal sensitivity and linearity responses. The suitable sensing platform was then introduced to streptavidin and biotin, and the signal it exhibited during the introduction was continuously recorded to study the real-time interaction behavior of the biomolecular binding process. Specificity tests were then conducted by removing the streptavidin to confirm successful detection.

Finally, Chapter 5 focus summarizing the key findings of the research following the objectives set. The overall performance of the developed fibre optic biosensing platform is evaluated, and recommendations for future work are provided to further enhance the system and extend its application to other biomolecular detection scenarios.

CHAPTER 2
LITERATURE REVIEW

2.1 Introduction

This chapter describes the properties, synthesis and characterisation methods, and the implementation of silver-based nanoparticles, graphene-based materials, and hydrogel for biosensing purposes. Previous works, advantages and limitations will be discussed in detail to define the gaps. The implementation of AgNPs, rGO, and hydrogel-based sensing layers will be described, focusing on improved sensitivity, stability, and specificity of the sensor, specifically in the context of fibre optic biosensors. Finally, all these sensing materials will be compared to develop a fibre optic biosensor for protein detection.

2.2 Fibre Optics

2.2.1 Introduction to Fibre Optics Technology

Fibre optics involves the transmission of information through thin, flexible, and transparent fibres crafted from glass or plastic (W. C. Wang et al., 2019). These optical fibres convert electrical signals into light, enabling the rapid, efficient transmission of data over long distances (Agrell et al., 2016). The advent of fibre-optic technology has revolutionised numerous industries, enabling faster, more reliable communication, data transfer, and signal transmission. Its applications span across various sectors, including internet telecommunications, broadcasting, mechanical sensing detection, food testing, and the biomedical industry (Culshaw, 2000; Dike & Ogbe, 2013; Pesapane et al., 2010).

In the medical field, fibre optics is widely used in advanced applications such as endoscopy, laparoscopy, laser surgery, optical coherence tomography, and biomedical sensing (G. Hong et al., 2017). Fibre optics plays a multifaceted role not only in imaging the morphological structure of particles but also in detecting biomolecular particles. This will thereby enable a precise identification of biomaterials. This capability empowers fibre optics to investigate symptoms, confirm diagnoses through biopsies,

and offer solutions for symptom alleviation or cure. Thus, fibre optic biosensors were developed to achieve these purposes.

2.2.2 Type of Fibre Optics

In general, fibre optics encompasses various types, including single-mode fibre (SMF), multi-mode fibre (MMF), plastic optical fibre (POF), step-index fibre, graded-index fibre, and photonic crystal fibre (PCF). These differences and the applications of each fibre type are summarized in Table 2.1. Each type of fibre is composed of different materials and has distinct cross-sectional dimensions, each serving a specific purpose.

Among various types of fibres, PCF optics show promising potential for integration into biosensing applications due to their sensitivity to RI changes in their surroundings. By tuning the hole count and hole diameter in PCF optics, more light can interact with the sensing medium, enabling easier detection of RI changes. However, the high cost of engineering and manufacturing each PCF fibre renders it impractical for the research. Using POF optics in these applications may be possible due to their flexibility and cost-effectiveness. However, the POF material is unsuitable for sensing applications due to its tendency to burn and melt easily when used for long-range transmission. Moreover, the core size of POF is larger than that of SMF, resulting in lower interaction with the surrounding medium. Using MMF optics instead of PCF optics is also possible. Because MMF typically has higher dispersion and lower bandwidth, it can still be suitable for certain sensing applications that do not require high precision or sensitivity. However, to detect interactions between biomaterials and the sensor medium, the fibre must be highly sensitive to detect the subtle interactions of bioparticles. Additionally, their limited suitability for long-distance transmission may render them less effective substitutes for PCF optics.

In biosensing applications where detecting subtle changes in the surrounding environment is crucial, the higher sensitivity of SMFs can be advantageous. The SMF optics may not offer the same unique properties as PCF; however, they are easily accessible and more cost-effective. Moreover, the SMF optics are suitable for high-speed data transmission or long-distance communication. Although they may not offer the same level of sensitivity or specialized capabilities as PCFs, they can still be used effectively in various sensing applications, especially when cost is a primary concern. Therefore, among the available fibre types, SMF optics are well-suited for this study.

Table 2.1
Type of Fibre Optics

Type of Fibre	Cross-section	Descriptions	Benefits	References
SMF	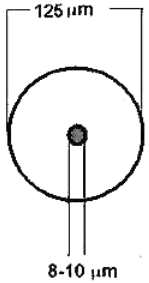	An ultra-thin fibre core, made of either glass or silicon, allows only a single ray of light to pass at a time. Has less dispersion and attenuation due to its small core size. The core size is ~ 9 µm	Suitable for long-distance data transmission wavelengths and has very little signal loss over distance. The wavelength flexibility from the visible to the IR region enables the use of a wide range of light sources and detection techniques, thereby enhancing the versatility of biosensing applications.	(Warier, 2024)
MMF	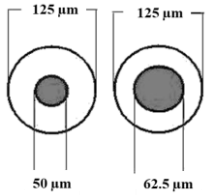	Made of glass or silicon fibre core where the light travels in the core in multiple rays. The core ranges from 50 to 100 µm (common sizes are 62.5 µm)	Suitable for short distances due to higher dispersion and attenuation compared to SMF	(Bourdine et al., 2023) (Warier, 2024)
POF	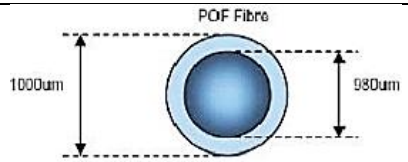	Similar to SMF but made of plastic. The core size ~1 mm	Suitable for short-range data transmission due to high attenuation. Cheaper compared to glass fibre	(Bartlett et al., 2000) (Sudas et al., 2023)
Step-index fibre		Made of silica glass, and its core has a uniform RI and a sharp step change in RI at the core-cladding interface. Core diameters range from 5 to 200 µm.	The path of light propagates in a zig-zag manner due to uniform RI. High attenuation in multi-mode (short range), but low attenuation in single-mode (long range).	(Gangopadhyay, 2019) (*Multimode Fibre and Multimode Fibre Optic Cable Tutorial – Fosco Connect*, 2024)

Graded-index fibre	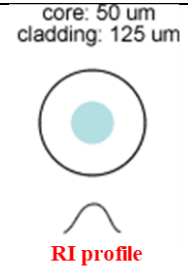	Made of silica, where the optical fibre is characterized by a core with a RI that steadily decreases as the radial distance from the optical axis of the fibre increases. Core diameter ~ 50 µm.	The light propagates in helical rays and remains at low attenuation. Has a higher bandwidth, allowing more data transfer over longer distances without degrading its signal.	(Arumugam, 2001) (*Multimode Fibre and Multimode Fibre Optic Cable Tutorial – Fosco Connect*, 2024)
PCF	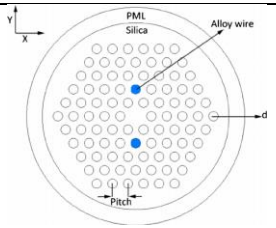	Made of silica or polymer and contains numerous air holes situated in the cladding region of the fibre. It can be distinguished by its utilization of either the effective index mechanism or light confinement through the photonic band gap (PBG) phenomenon	Capable of tunable core diameters to suit various applications. Can exhibit high RI contrast between the core and cladding, resulting in minimal signal loss.	(Singh et al., 2023)

2.2.3 Fabrication of Fibre Optic Sensor

To fabricate the fibre-optic sensing platform, the protective coating of the fibre-optic probe must be removed to expose the core region, as illustrated in Figure 2.1. The protective coating, which consists of sheathing, jacket, and a transparent coating (cladding layer), is removed manually using a stripper (Rickelt et al., 2015). This method allows the core region to be embedded with sensing materials. However, this method requires a fibre stripper to remove the protective fibre-optic coating manually.

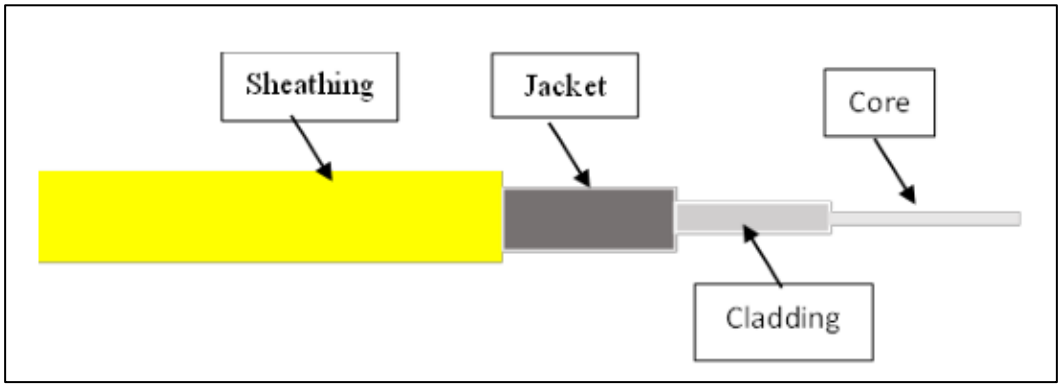

Figure 2.1 Standard Configuration of SOF Probe.
(Roslan et al., 2025)

Prior to depositing the sensing materials onto the exposed core area, the area was cleaned with acetone, ethanol, or alcohol to remove any residual from the removed layer (Oliva et al., 2009). One approach to depositing sensor materials in the fibre core is by dipping. The dipping method is the simplest method for integrating the sensing medium (J. R. Lee et al., 2011). However, this method relies on optimizing the dipping time and the hydrophilicity of the sensing medium to determine optimal conditions for even coating of the fibre optics. When integrating the sensing medium with hydrogel materials, the layer-by-layer (LbL) method via multiple dip-coating steps can provide better control over layer formation (Rivero et al., 2019). Hence, a few layers of coating materials can be applied to the fibre-optic probe during fabrication of the sensor platform, allowing flexibility to the sensor configuration.

2.2.4 Fibre Optics Sensor Mechanism

A fibre optics sensor operates on two types of absorption: intrinsic and extrinsic, as shown in Figure 2.2. These can be determined by how light is guided through the optical fibre and by its interactions with the surrounding environment. In intrinsic sensors, the fibre-optic cable itself serves as the sensor, whereas in extrinsic sensors, the fibre-optic cable is used solely to guide light to and from a conventional sensor (Morris & Langari, 2021). Intrinsic fibre is not only used in illumination applications, but also in imaging applications, where it is used to picture locations that are too small or too far to reach (Pendão & Silva, 2022). In a spectrometer, light transmitted from the spectrometer to a substance cannot be placed inside the spectrometer itself, enabling the analysis of its composition. A spectrometer analyzes substances by bouncing light off and through them. By employing fibres, a spectrometer can be used to study objects remotely. Meanwhile, in an extrinsic fibre, the fibre serves as a conduit for transporting light to and from an external optical device where sensing occurs (Nahid et al., 2025), meaning these fibres are only used to deliver light to the sensing region.

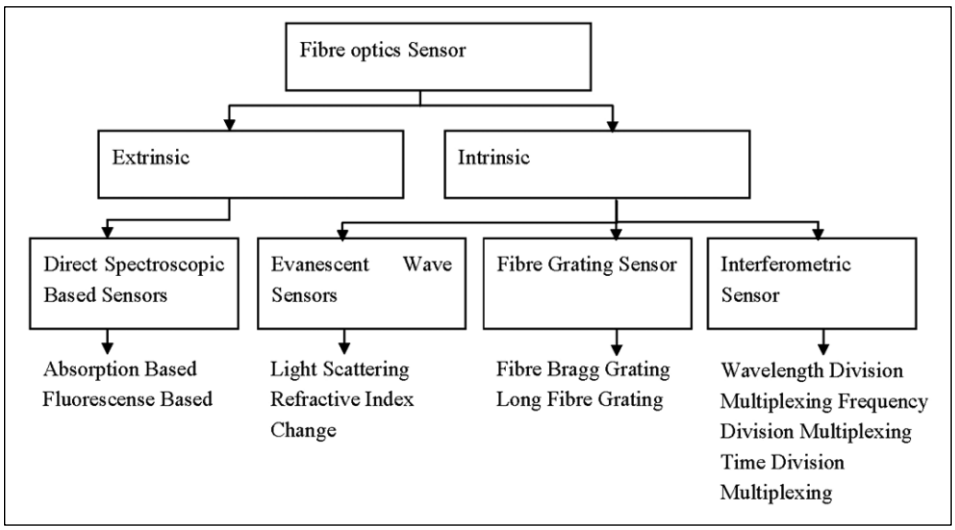

Figure 2.2 Fibre Optic Sensing Categories

Among these fibre types, the intrinsic method is a much more suitable approach for detecting biomaterials and their compositions. Intrinsic fibres can be divided into 3 types of sensor mechanisms: evanescent-wave, fibre-grating, and interferometric. Evanescent wave sensors utilise the phenomenon of the evanescent field, an electromagnetic field that extends beyond the core of an optical fibre into the

surrounding medium (Fabian et al., 2009). These sensors work by allowing the electromagnetic field of light to extend beyond the fibre's core into the surrounding medium. When the evanescent field interacts with molecules or particles in the surrounding medium, it can change intensity, phase, or wavelength.

The evanescent field occurs under certain conditions. First, the TIR will be created in the core fibre when light is travelling from a medium with a higher RI to a medium with a lower RI at an angle greater than the critical angle (Villar, 2020). Instead of refracting into the lower RI medium, the light is completely reflected into the higher RI medium, as illustrated in Figure 2.3(A). At the interface between the two media, where TIR occurs, the electromagnetic field associated with the light extends into the lower RI medium. This extended portion of the electromagnetic field is known as the evanescent field, as shown in Figure 2.3(B). The evanescent field is an oscillating electric field that does not propagate as an electromagnetic wave but instead has its energy concentrated in the vicinity of the source (Nellambakam et al., 2023).

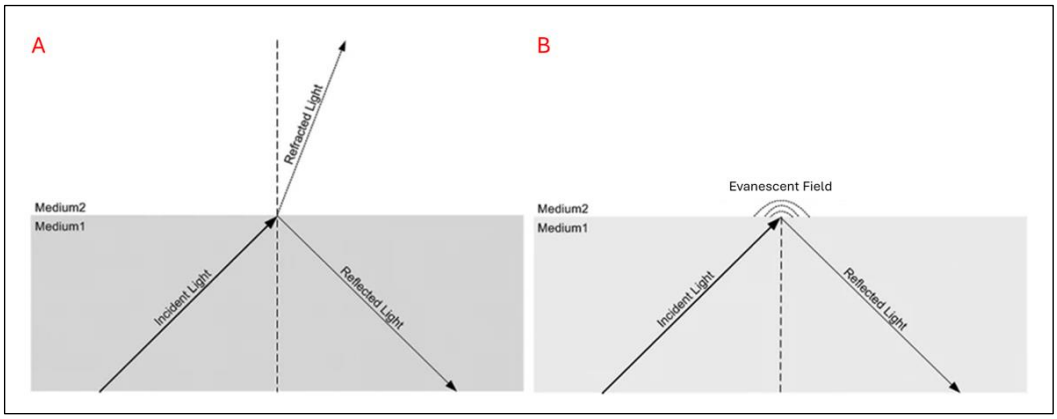

Figure 2.3 (A) TIR Phenomenon and (B) Evanescence Field.
(Millis, 2012)

When the evanescent field interacts with the external environment, it changes intensity, phase, or wavelength due to variations in RI caused by analytes (Adányi et al., 2017). These interactions will cause light scattering, altering the direction or intensity of light passing through the core (Samavati et al., 2019). Subsequently, by measuring changes in the intensity, phase, or wavelength of the scattered light, evanescent wave sensors can detect and quantify changes in the RI of the surrounding medium. These changes form the basis of evanescent wave sensors, which can be used for various sensing applications such as detecting the presence of specific molecules or

measuring changes in RI. Therefore, using fibre optics in evanescent-wave sensors is an ideal method for detecting biomolecular interactions.

Meanwhile, fibre grating sensors come in various forms, such as uniform, long, chirped, tilted, or phase-shifted, each featuring a periodic perturbation of the RI in the optical fibre's core (Sahota et al., 2020). The light was introduced into the core through an interference pattern that creates the periodic modulation of RI along the core's length. This modulation will form a Bragg grating structure (J. Chen et al., 2011). When changes in the external environment, such as strain, temperature, or the presence of an analyte, are detected, they alter the periodicity or the RI of the Bragg wavelength in the fibre core. These changes will cause a shift in reflected wavelength.

A fibre-optic interferometer relies on the interference between two beams that have travelled through different optical paths within a single fibre or through two separate fibres (B. H. Lee et al., 2012). These sensors typically use a Fabry-Perot interferometer or Mach-Zehnder interferometer configuration within the optical fibre. Changes in the RI of the surrounding medium will induce phase shifts or changes in the interference pattern of the light waves. The change in interference can be used to detect and quantify the presence analytes in the surrounding environment (B. H. Lee et al., 2012). Among these three types of sensor detection, evanescent wave sensors are suitable for biosensing applications due to their ability to detect changes in RI in the external environment upon biomaterial interaction.

2.2.5 Fibre Optic Biosensing Application

Upon applying the protein to the sensor embedded with the sensing material, the sensor's performance and detection reliability should also be evaluated. The methods available for detecting the biological component include light intensity, and a simple regression analysis is widely used to assess biosensor performance (Bellacicco et al., 2019). This analysis can be performed by collecting the data on the different RI values of the sensing materials and light intensity peaks.

2.2.5.1 Detection of RI

Prior to protein detection, RI detection is essential in fibre-optic biosensors to assess the ability of the sensing materials deposited on the probe to detect changes. The

RI detection system requires a reference or baseline to accurately understand changes in RI when proteins are added (Oliva et al., 2009). To evaluate the performance of fibre sensors across a broad RI range, an analyte such as glycerol solutions can be employed due to their stable, extra-fine particles and adjustable refractive indices (Apriyanto et al., 2018). Based on a previous study, RI measurement using glycerol as a test medium was conducted on multimode fibre sensors, and the sensor demonstrated effectiveness over a wide dynamic RI range, from 1.316 to over 1.608 at a wavelength of 1550 nm, achieving a resolution of 2.2447×10^{-5} RI units (RIU) in certain configurations (Apriyanto et al., 2018). Hence, it is possible to conduct RI detection using glycerol with varied RI values to ensure that the protein can be detected on the modified fibre optics.

The graph obtained by plotting both components will yield the slope of the regression line, which represents the sensitivity of light to changes in RI. A steeper slope indicates greater sensitivity, as small changes in RI result in larger changes in light intensity. From a slope regression line, an equation can be formed as in Equation (2.1), where m represents the value of sensitivity and c is the value of the y-intercept. To measure the variability of this slope, the standard deviation was calculated to estimate the slope of the regressed line following Equation (2.2), where the value of σ residual, x_i, and $(x)\bar{}$represent the standard deviation of residuals (differences between observed and predicted value), RI value, and the mean of RI value. The closer the variability value to 1, the stronger the correlation between the independent variable (RI value) and the dependent variable (light intensity), as represented by the coefficient of determination (R^2).

$$y = mx + c \tag{2.1}$$

$$Std.of\ slope = \frac{\sigma_{residual}}{\sqrt{\sum(x_i - \bar{x})^2}} \tag{2.2}$$

The study of porosity when different RI values were applied to the fibre optics is also recorded. The purpose of this testing is to determine how the sensing material absorbs the glycerol with different RI values and how the light behaves upon interacting with the absorbed glycerol. Previous research reported that the SPR-based fibre sensor was developed to measure the RI of solutions with different glycerol concentrations

(Pathak et al., 2016). Their work demonstrated that as glycerol concentration increased, the solution's RI increased, leading to measurable shifts in the SPR signal. The optical behaviour of the SPR fibre shows that as the RI of glycerol approaches that of water, the resonance dip occurs at a shorter wavelength. These changes produce different intensities of transmitted light due to variations in evanescent-wave penetration. Hence, this mechanism can be used in this research to study SPR fibre-optic interactions with proteins as they bind to the SPR sensor surface, altering the RI of the sensing medium and causing a similar wavelength shift.

2.2.5.2 Protein Detection

The possible methods for detecting protein interactions are summarized in Table 2.2, a compilation of methods in protein detection. To explain further, the antigen-antibody and enzyme-linked immunosorbent assay (ELISA) methods are widely used due to their high specificity and ability to amplify the signal (Paulie et al., 2023). However, antibodies are expensive to acquire and degrade quickly. There is an issue with the ELISA method, where the antibody can bind to unwanted proteins on the plate, leading to inaccurate detection and making it unsuited for fibre-optic detection of the protein.

In contrast, the molecular imprinted polymer (MIP) method offers high selectivity and specificity for the target, excellent stability under harsh conditions, and lower production costs. Nevertheless, it can only detect the large size of proteins, which can make it difficult to create binding sites that specifically recognize the protein's unique configuration (Akgönüllü et al., 2023).

The aptamer-based method shows good stability and high specificity in detecting proteins. The aptamer-based method is used to detect small proteins, such as tumour-associated proteins, due to its lower production cost (Y. Cao et al., 2025). This makes it highly suited for optical detection that requires precise detection and can only detect biomolecules. Yet, this interaction is effective only with small biomolecular proteins, requiring the researcher to create a new aptamer-based construct that can target a wider range of biomolecular sizes, a process that can be lengthy and complex.

The main strength of the fluorescent-based method is its ability to monitor protein interactions in living cells. This method involves fluorophores that bind to proteins and absorb light at specific excitation wavelengths. Upon excitation, the

fluorophores emit light at a longer wavelength, generating a visible fluorescent signal. By observing changes in fluorescent intensity, real-time interactions between proteins can be studied. Despite this, the method is subject to interference from autofluorescence in biological samples and from overlapping signals from other fluorescent molecules (Harms et al., 2001), making accurate detection more challenging. Additionally, this technique often requires expensive reagents, specialised imaging equipment, and computational analysis, thereby contributing to the high overall production costs.

The LSPR method relies on changes in the optical properties of NPs upon protein binding, allowing for real-time detection (Unser et al., 2015). The surface of the NPs can be functionalized to enhance specificity, with strategies such as streptavidin-biotin interactions or antibody-antigen binding improving sensitivity (Jain & Cheng, 2016).

To summarise, although antibody-antigen interactions are highly specific, they can be disrupted, whereas streptavidin-biotin systems are stable under a variety of experimental conditions. Furthermore, unlike the LSPR or fluorescence approaches, streptavidin-avidin does not require expensive equipment or considerable optimization. Subsequently, streptavidin-avidin interaction stands out due to its unparalleled binding strength, stability, and adaptability making it a highly reliable option for protein detection.

Table 2.2
Compilation of Methods in Protein Detection

Protein Detection	Main functions	Basic structure	Applications	References
LSPR	Identify specific proteins via the change in light absorption when a protein binds to the surface coated with metal NPs. Streptavidin-biotin interaction is used to detect protein interactions by monitoring the changes of light absorption.	Commonly used AuNPs or AgNPs that can resonate with the specific light wavelength. The nanoparticles were conjugated to recognition molecules, such as antibodies or aptamers, to enable specific binding to target proteins. Upon interaction, it will alter the light absorption or scattering by the nanoparticles. The changes that were detected indicate the presence of the targeted protein.	Protein detection	(X. Li et al., 2009)
Enzyme-linked	Use antibodies linked to enzymes to detect and measure protein. Commercially used for ELISA	The main step is to attach the target protein (antigen) to a surface (like a plate) so it can be detected. The method can be done in 2 ways: **Directly**: The protein sticks directly to the plate. **Indirectly**: An antibody (designed to grab the protein) is first attached to the plate. Then, the protein binds to this antibody.	Protein detection	(Sakamoto et al., 2017)
Aptamer-based	Use aptamers (short DNA or RNA molecules) that bind specifically to target proteins.	A transducer signal is used to detect the interaction between aptamers and protein. The detection signals from the sensor include colourimetry, fluorescent assays, SPR, SERS, and electrochemical detection. The signal processor enables qualitative analysis of viral protein levels. The	Virus detection	(Lou et al., 2022)

		integration of these components enables the aptasensor to detect viral proteins with high specificity and sensitivity, making it a promising tool for rapid, accurate virus detection.		
Fluorescent-based protein	To visualize and study proteins and their interactions in real-time within live cells. Tagging the proteins with fluorescent markers allows monitoring of localization, movement over time, and interactions.	Targeted proteins are genetically fused to fluorescent proteins (FPs) to create fluorescent tags. These tags emit light when excited, enabling visualisation under a microscope. Studies of interaction are: • Förster Resonance Energy Transfer (FRET): Interactions between two proteins by measuring energy transfer between two fluorophores in close proximity. • Bimolecular Fluorescence Complementation (BiFC): Splitting a fluorescent protein into two non-fluorescent fragments, each fused to different proteins. When these proteins interact, the fragments come together to reconstitute fluorescence. • Fluorescence microscopes equipped with sensitive detectors will capture the emitted light, enabling	Living cell observation	(Stoneman & Raicu, 2023)

		real-time monitoring of protein dynamics and interactions within live cells.		
MIP	The main function is to recognize and bind specific proteins. This selective binding enables the detection and quantification of target proteins in various samples.	Sensors begin with a template molecule, with the protein used as a target for detection. Functional monomers are arranged around the template and bind to the target protein, thereby forming a specific interaction. A cross-linker is then added to stabilize the entire structure, forming a rigid three-dimensional polymer matrix. The template is then removed once the polymer is fully formed, leaving behind tiny cavity. When a sample is introduced, the target protein will bind to these specific cavities, and the sensor detects this interaction, converting it into a measurable signal.	Protein detection	(Akgönüllü et al., 2023)

2.3 Method to Enhance the Signal of an Optical Fibre Sensor

Multiple methods have been used to enhance optical properties, including redesigning the optical fibre, modifying the surface, resonance coupling, and utilising plasmonic structures and other promising materials, such as graphene-based and hydrogel materials.

2.3.1 Redesign The Fibre Optic Structure

Tapering fibre optics is one method used to enhance optical properties by redesigning the optics as shown in Figure 2.4(a). This involves modifying the fibre's design, typically by reducing the core diameter and enlarging the output angle (Korposh et al., 2019). In some cases, Korposh et al. also state that the fibres are not only tapered but also restructured into U-shaped or S-shaped configurations. These modifications aim to increase the interaction of the evanescent wave with the surrounding medium, thereby enhancing sensitivity.

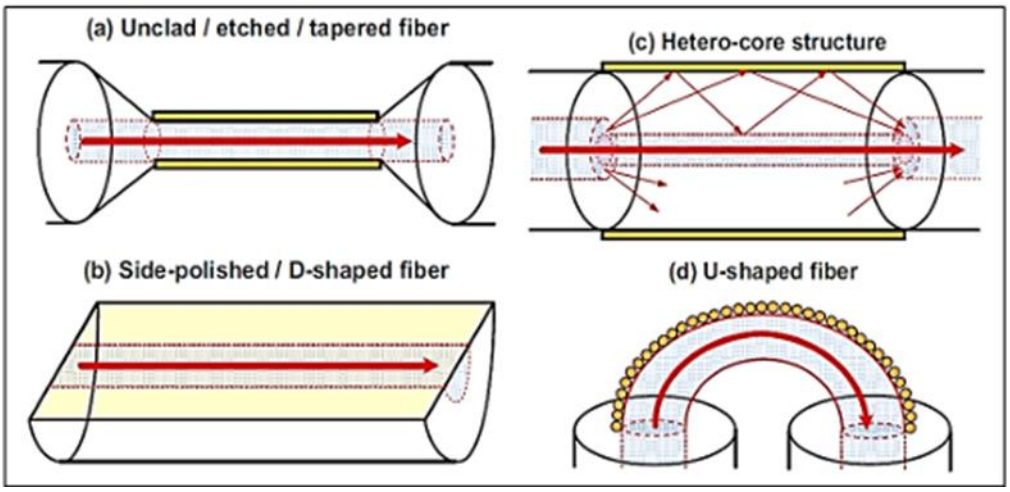

Figure 2.4 Optical fibres with altered geometries.
(Alam et al., 2017)

Some researchers have altered fibre optics using resonance coupling, in which light interacts more with the core surface in the bending region, thereby changing the RI (Londero et al., 2023). Bending the fibre redirects some of the light energy from the core to the outer cladding region via resonance, requiring precise wavelength matching. The energy transferred to the cladding is absorbed by the fibre's protective coating after

the bend, preventing unwanted light leakage. This absorption creates distinct "notches" in the spectrum of transmitted light at specific wavelengths.

In summary, applying the tapering method to the sensor is feasible. However, reducing the fibre diameter may make the tapered region more fragile, rendering it impractical for rugged environments. Additionally, shaping the fibre by applying strain requires careful handling to prevent breakage. Therefore, further investigation into bending radius and gradual bending is necessary to prevent fibre damage, such as fractures or microcracks.

2.3.2 Sensing Material Deposition

A more recent strategy involved modifying the fibre-optic sensor by applying a plasmonic structure to enhance its sensitivity. A nanoparticle is a particle in the nanoscale size that can be composed of various materials such as noble metals, metal oxides, polymers, ceramics, or carbon-based materials (Ealias & Saravanakumar, 2017). Due to their small size and large surface area-to-volume ratio, nanoparticles exhibit distinct characteristics and behaviours that can be used to improve the performance of fibre optics, such as surface plasmon resonance, enhanced surface reactivity, and size-dependent properties (Mujahid et al., 2022).

Among the nanoparticles, NMNPs such as AgNPs, AuNPs, and PtNPs show promising behavior in sensing applications (Doria et al., 2012). Despite AuNPs being commonly used in sensing applications due to their stability, AgNPs exhibit a strong LSPR (N. Ibrahim et al., 2021) and are cost-effective (Hosny et al., 2025) compared to other NMNPs, making them suitable for biosensing applications. Strong LSPR changes in AgNPs make them particularly sensitive to their local environment, resulting in wavelength shifts when fibre optics is in contact with certain chemicals or biological analytes (Loiseau et al., 2019). However, LSPR depends on the morphological surface structure, including size, shape, and surface features. Changes in the morphological surface structure of AgNPs can shift the LSPR peak wavelength and intensity. Later, the sensors were integrated with sensing materials, such as hydrogels, buffer solutions, and microfluidic systems. These configurations enable the attachment of bioreceptors to the sensor, facilitating specific interactions with specific biomaterials.

The modified fibre-optic surface, functionalized with receptor molecules such as antibodies or aptamers, was also recorded (Zhao et al., 2022). These modifications

not only enhance the sensitivity of the optics but also enable them to specifically bind to target analytes, improving specificity and selectivity in detection. Consequently, the sensor becomes more specific in detecting these biomaterials.

On the other hand, using plasmonic structures as sensing materials is a safer, easier method to enhance the sensor's optical properties, as it involves external applications. Subsequently, integrating it with a receptor holder enables specific biosensing. Hence, embedding plasmonic structures, such as AgNPs, is an ideal method for enhancing sensor sensitivity and enabling specific detection of biomaterials.

2.4 Silver Nanoparticles (AgNPs)

2.4.1 Introduction to AgNPs

AgNPs exhibit distinctive plasmonic characteristics that make them highly responsive to changes in the surrounding dielectric environment. Their LSPR originates from the collective oscillation of conduction band electrons when excited by incident light, producing strong absorption and scattering bands in the visible region. The sensing performance of AgNPs-based platforms is strongly governed by their plasmonic resonance behaviour, which is influenced by particle size, geometry, and surrounding medium. Variations in these parameters can result in measurable spectral shifts that form the basis of LSPR-based detection.

2.4.2 Synthesize of AgNs

Silver salt (e.g., silver nitrate; $AgNO_3$) can be reduced to nanoparticle form using various methods, including physical forces (crushing, grinding, and milling), electrical forces (electrical discharge), and thermal reduction of $AgNO_3$ via vapour-condensation. Physically synthesized nanoparticles not only possess high purity but are also more likely to appear uniform in particle size distribution (Capek, 2017). However, a key drawback is the lack of stabilisers or capping agents, which makes them prone to agglomeration. While chemical reduction methods can be effective, concerns over toxicity have limited their use in biological applications. Thus, green methods of chemical reduction have emerged to enable AgNPs to enter these applications, opening new avenues such as biosensing, diagnostic platforms, drug delivery, and medical device coating.

The chemical reduction method employs the use of a reduction agent and a capping agent. The standard procedure for this method is to dissolve the silver nitrate beforehand (commonly in water) to separate into two ions: the silver ion (Ag^+) and the nitrite ion (NO_3^-). As the reducing agent (a substance that donates electrons) was added to the solution, the Ag^+ gained an electron (e^-), forming metallic silver (Ag^0). The Ag^0 then underwent aggregation, with nucleation and growth of particles, which will determine the shape and size of AgNPs. Small clusters of Ag^0 atoms will form during nucleation, serving as the foundation for particle growth. Growth occurs as additional silver atoms deposit onto these nuclei, forming nanoparticles with defined sizes and morphologies. Finally, a stabilising or capping agent was added to the procedure to stop the growth and aggregation of NPs, ensuring the stability of AgNPs.

Various methods for synthesising AgNPs have been used and improved to meet the demand for these nanoparticles and to control their structure (Loiseau et al., 2019). Different shapes of AgNPs are synthesized and compiled in Table 2.3. Syntheses of anisotropic NPs have piqued the interest of researchers because their structural, optical, electronic, magnetic, and catalytic properties differ from, and are frequently superior to, those of spherical NPs of comparable size (Loiseau et al., 2019) Figure 2.5 shows images of AgNPs in various shapes, including nanospheres, nanowires, nanorods, nanocubes, nanotriangles, nanoflowers, nanostars, and nanocrystals.

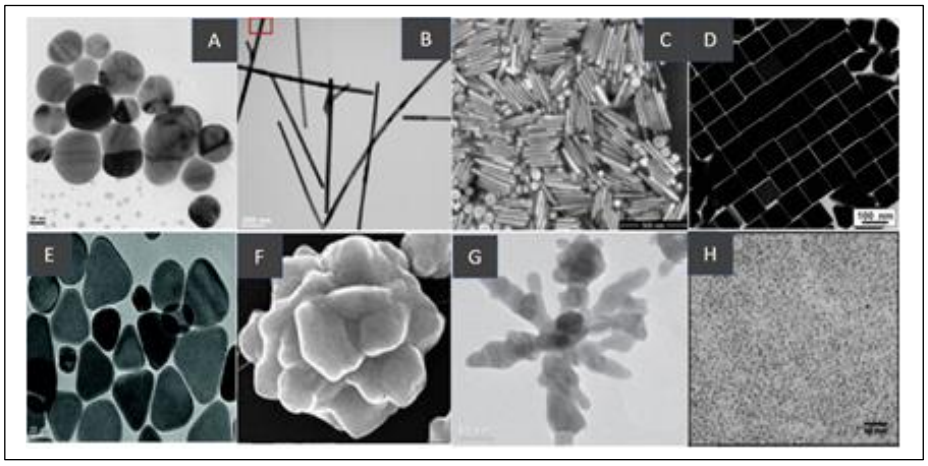

Figure 2.5 TEM image of Ag NPs with different shapes: (A) nanosphere, (B) nanowire, (C) nanorods, (D) nanocube, (E) nanotriangle, (F) nanoflower, (G) nanostar and (H) nanocrystal.
Adapted from (Loiseau et al., 2019)

Table 2.3
Summary of Various Shapes of AgNPs and Their Applications

Ag Shape	Methods	Size (nm)	Benefits	Applications	Ref
Nanosphere	Chemical reduction method with polyethylene glycol (PEG) is used both as a solvent and reducing reagent and the polymer polyvinylpyrrolidone (PVP) is used as a capping agent	54	Morphology and dimensions of the AgNPs can be easily modulated by controlling the synthesize temperature and the molar ratio of PVP to $AgNO_3$	Optical and chemical applications	(Xi & Wu, 2004)
Nanowire	Spin-Assisted Layer-by-Layer (SA-LbL) method	50	Similar growth mechanism compared to the polyol process	Nanoelectronics and nanodevices	(Kriaa et al., 2025)
Nanorod	Modified seed-mediated synthesize	633 – 527	The SERS enhancement varies with the excitation wavelength used and it is highest when the plasmon resonance of the metal matches the laser excitation wavelength.	Biosensing	(Rekha et al., 2018)
Nanocube	Polyol process	35–95	Serve as sacrificial templates to fabricate Au-based nanocages with tunable LSPR peaks in the near-IR region. Outstanding substrates for optical sensing and SERS detection and strong SERS activity due to the preserved sharp corners and edges	SERS performance	(Pawlik et al., 2023)

Nanotriangle	Seed-mediated growth method	60.07-77.28	Have significant catalytic properties in the shape-dependent electrocatalytic reduction of CO_2 to CO	Thermal sensing applications	(S. Liu et al., 2017)
Nanoflower	Electrodeposition-approach for the synthesize of silver nanoflowers (AgNFs) on nitrogen-doped carbon nanotubes (NCNTs) for the oxygen reduction reaction (ORR) in alkaline media has been developed.	455-513 nm	Excellence catalytic for oxygen reduction reaction (ORR)	Various fuel cells as a cathode catalyst.	(Yasmin et al., 2017)
Nanostar	Two-step chemical reduction method with hydroxylamine and sodium citrate as reducing agents.	400 –700	Superior sensing signal due to exhibiting a greater active surface area	Detection of amyloid fibrils related to Alzheimer's disease.	(Garcia-Leis et al., 2013)
Nanocrystal	Liquid-solid-solution (LSS) phase transfer and separation	4-15	Has great potential in the synthesize of a broad range of new-type nanocrystals and/or nanoparticles	Nanoscience & Nanotechnology	(X. Wang & Li, 2007)

Based on Table 2.3, the sphere-shaped method is the most common because AgNPs were originally spherical. However, by varying synthesis conditions, such as temperature, pH, and chemical concentrations, the growth and morphology of AgNPs can be altered. These changes lead to the production of different shapes, such as wire, rod, or platelet, depending on the desired application and the required properties. These methods have been largely applied to biosensor applications. However, fine-tuning the method can also yield shapes such as squares, triangles, crystals, stars, and flowers, further expanding its applications. Due to the method's complexity, only a few succeed in entering the biosensor field.

Subsequently, a method for synthesising AgNs by Garcia et al. shows interesting results in SERS performance, where AgNs can be synthesized with less complexity using hydroxylamine as a reducing agent (Garcia-Leis et al., 2013). Hydroxylamine is a mild reducing agent that is often used chemically because it reduces compounds without introducing additional cations or complexing capabilities (Sager, 1992). This method produces tunable AgNs with reduced toxicity yet excellent optical properties, making them more attractive for future biosensor applications.

2.4.3 Characterization of AgNPs

Based on previous research, nanoparticles synthesized by chemical reduction exhibit a star-shaped morphology under SEM. However, variations in hydroxylamine concentration and synthesis time after its addition can significantly influence the formation of these structures, as shown in Figure 2.6. An increase in hydroxylamine concentration has been observed to alter the star shape, transforming small, dull spikes into long, sharp ones (Garcia-Leis et al., 2013). These changes also affect the number of visible spikes in SEM images, indicating that hydroxylamine plays a crucial role in controlling the size and shape of nanoparticles. The research study also states that AgNs synthesized manage to produce 6 spikes with an average diameter of 300–400 nm.

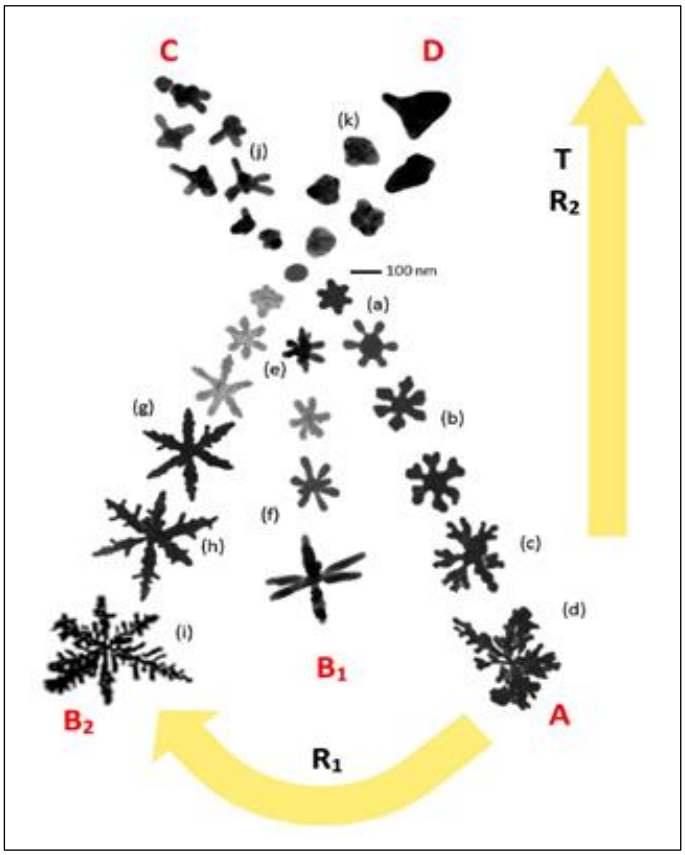

Figure 2.6 Range of Shapes and Sizes of AgNs.
Adapted from (Garcia-Leis et al., 2013)

However, there are some cases where the AgNs manage to produce 8 spikes with an average diameter of 130.13 ± 64 nm (Roslan et al., 2022). The mechanism behind this transformation is linked to hydroxylamine's role as a reducing agent and stabiliser, which influences the nucleation and growth of silver atoms. Higher concentrations may promote anisotropic growth, leading to distinct star-like formations with varying spike lengths and densities.

When assessing the purity and structural integrity of AgNPs, XRD can confirm their nanoscale nature. The characteristic diffraction peaks of AgNPs commonly correspond to 2Θ degrees of 38.19° (111), 48.18° (200), 67.44° (220), and 77.7° (311) (Castañeda-Aude et al., 2023). The (111) plane is usually the most intense, indicating that silver nanoparticles predominantly grow along this orientation. The presence of these peaks confirms the formation of crystalline AgNPs and helps assess their purity and structural integrity. The composition of AgNPs can be determined by FTIR, with characteristic absorption bands typically reported in the mid-infrared region between approximately 4000–500 cm^{-1} (Ramzan et al., 2024). However, there are some cases

where the characteristic peaks are observed at 2927 cm^{-1}, 1631 cm^{-1}, and 1383 cm^{-1} due to using the green-based reducing agent when synthesizing AgNPs (Devaraj et al., 2013). Peaks observed near ~2927 cm^{-1} are commonly associated with C–H stretching vibrations from organic capping or stabilizing agents, bands around ~1631 cm^{-1} correspond to C=O stretching indicative of carbonyl interactions, and features around ~1383 cm^{-1} may be attributed to C–N or C–O vibrations arising from amine or alcohol groups associated with biomolecules, such as peptides and proteins. Such assignments fall within the expected FTIR range, which will help in identifying the functional groups present on green-synthesized AgNPs surfaces.

UV-Vis spectroscopy is a crucial technique for studying the optical properties of AgNPs. A sharp peak at around 410 nm is characteristic of spherical AgNPs and is attributed to their LSPR (Hart et al., 2013). This resonance occurs when free electrons on the nanoparticle surface oscillate in response to incident light, leading to strong absorption at specific wavelengths. A narrow, well-defined peak suggests that the AgNPs are monodispersed, meaning they have a uniform shape and size, with a size distribution standard deviation of less than 5% (Hart et al., 2013). Meanwhile, the AgNs synthesized by Garcia-Leis et al. were detected at 100-600 nm, indicating their polydispersity (Garcia-Leis et al., 2017). Figure 2.7 (a) shows noticeable variations in core diameter, spike length, spike density, and degree of aggregation among the nanostars, confirming its polydispersity. This broader peak arises from the presence of different nanoparticle sizes and shapes, each interacting with light at a different wavelength. The multiple spikes or irregular features of AgNs give rise to different plasmonic resonance modes, broadening the absorption spectrum. Moreover, the overlapping particles or aggregation in Figure 2.7 (b) may also contribute to additional spectral broadening and red-shifting in the peak spectrum during the characterization process. Subsequently, tuning the AgNs allows the nanomaterials to be tailored for specific applications by adjusting their size, shape, and distribution. Therefore, applying these tuned materials to the fibre sensor could flexibly enhance the sensing performance, making it a subject worth studying.

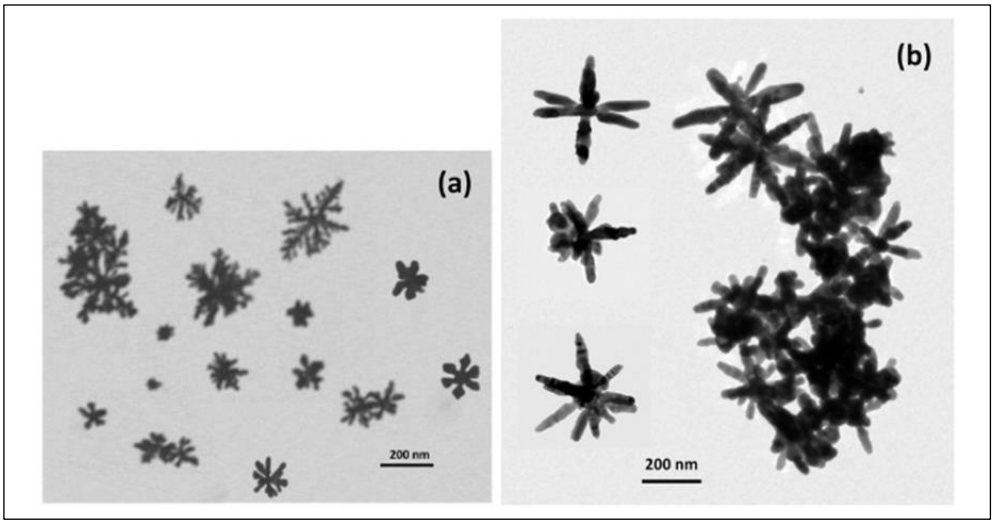

Figure 2.7 (a) Polydispersity and (b) Aggregation of AgNs.
Adapted from (Garcia-Leis et al., 2017)

2.4.4 AgNPs-Based Fibre Optic Sensors

Due to the LSPR effect, the AgNPs have been applied in biosensing applications to enhance the optical properties of the sensing mechanism and Table 2.4 consists of the latest compilation on these applications that are related to AgNPs. The latest study shows that green-based synthesized AgNPs manage to interact directly with L-cysteine due to the –SH (thiol) group in it (Matos et al., 2024). The spherical-shaped AgNPs manage to record a peak intensity at 400–450 nm of wavelength under UV–Vis spectra. As L-cysteine is introduced the AgNPs, the –SH (thiol) group of cysteine strongly binds to silver, causing the AgNPs to agglomerate. The agglomeration causes the peak of the UV-vis spectrum to broaden, with a minimum of 0.1 nM concentration of cysteine needed to cause this effect. This interaction shows that AgNPs alone can detect biomaterials, specifically those with an -SH (thiol) group. However, the effect shows that detection can be used only once, suggesting that AgNPs need to be freshly prepared every time the detection of the L-cysteine biomolecule is required. Another case was recorded where the quasi-spherical AgNPs managed to interact with trenbolone acetate via UV-Vis spectrophotometry (Juma et al., 2024). AgNPs manage to interact similarly with L-cysteine, with the peak of AgNPs under the spectrum exhibiting an average red shift of about +18 nm. Despite interaction with biomaterials work similar, the interaction with Ag is a bit weaker.

Table 2.4
Compilation of AgNPs in Biosensing Applications

Sensing material	Sensing mechanism	Size and shape	Target biomolecule	Findings	References
Green synthesized AgNPs using banana peel extract as a capping and stabilizing agent	Adsorption	Ag spherical with a size recorded ~20 nm	L-cysteine	The –SH (thiol) group of cysteine can interact with AgNPs via silver-sulfur (Ag–S) bonds, causing the colour of AgNPs (yellow) to fade. A 0.1 nM concentration of cysteine is the lowest concentration that manage produces a signal under UV-Vis spectroscopy.	(Matos et al., 2024)
AgNPs synthesized via laser ablation in liquid (LAL)	Adsorption	quasi-spherical silver shaped with ~20 nm diameter	Trenbolone acetate (anabolic steroid)	UV–Vis spectrophotometry was used to monitor changes in plasmonic absorbance. Upon introducing trenbolone acetate into the AgNPs solution, the LSPR peak exhibits an average red shift of about +18 nm	(Juma et al., 2024)
AgNPs doped with E. coli-specific aptamers embedded	Electrochemical signal transduction	Ag spherical with ~18.7 nm diameter	E. coli Bacteria	The AgNPs–aptamer system serves as an immobilization platform for selective E. coli to capture and produce signal	(Dabhade et al., 2023)

of the surface of screen-printed carbon electrode (SPCE)				transduction. As E. coli concentration increases, the current decreases linearly, indicating bacterial binding affects the electrochemical response. The biosensor could detect E. coli down to a limit of detection (LOD) ≈ 150 CFU/mL (colony-forming units per millilitre)	
Ag nanoprisms embedded with rGO aerogel	Electrochemical signal transduction	Triangular@prism	Doxorubicin (cancer drug)	The glassy carbon electrode was coated with rGO aerogel before being deposited with Ag nanoprism and magnetite via cyclic voltammetry. Differential Pulse Voltammetry is used to detect doxorubicin by having it undergo a redox reaction on the electrode surface to detect a measurable electrochemical signal. LOD recorded was 0.028 µg/mL with a linear dynamic range of 0.075 µg/mL to 5.0 µg/mL.	(Gheybalizadeh et al., 2025)

Silver-nucleated gold-shell bimetallic nanoparticles (Ag@Au NPs) integrated with GO	Optical fibre signal	Ag@Au forms a quasi-spherical with ~20 nm diameter	Human Immunoglobulin G (IgG)	The Ag@Au bimetallic structure was deposited on fibre optics before being coated with GO. The matrix sensor was integrated with IgG-specific biorecognition molecules. The coated fibre manages to generate ~4700 nm/RIU and manages to detect human IgG at least 0.037 µg/mL.	(Q. Xu et al., 2025)

When it comes to using external equipment, the base of the electrode was modified with AgNPs with the purpose of detecting E. coli biomolecules (Dabhade et al., 2023). The purpose of integrating the AgNPs is to enhance the conductivity of the electrode. However, by functionalizing the AgNPs with E. coli-specific DNA aptamers, the biomolecules can bind strongly with AgNPs, causing the electron transfer between the redox probe and the electrode to be hindered. The current reduced from this effect was measured via Differential Pulse Voltammetry (DPV) and it was confirmed that 150 CFU/mL of E. coli biomolecules were enough to detect the interactions.

A similar case was recorded where the electrode was coated with rGO before introducing Ag nanoprism (Gheybalizadeh et al., 2025). The purpose of introducing rGO to the electrode is to exploit its electrical conductivity properties. Moreover, the lattice structure of rGO allows it to support the instability of AgNPs during the integration process. As the GO undergoes a reduction process, the electrode interacts with the solution to allow it to self-assemble on the surface. The rGO is then embedded into the hydrogel matrices, changing itself into aerogel form, before electrodeposited with Ag nanoprism. A similar DPV detection technique was conducted while introducing doxorubicin on the coated electrode, it was confirmed that 0.028 µg/mL of doxorubicin was detected with a linear dynamic range of 0.075 µg/mL to 5.0 µg/mL. These methods show that introducing AgNPs to the external equipment allows a wider range of detection applications.

Among the equipment used, fibre optics embedded with Ag@Au bimetallic structure in detecting human IgG shows promising results. The fibre is coated with GO with the purpose not only as a supporting layer for the bimetallic structure, but also to enhance the SPR biosensor performance of fibre optics. The fibre-coated tricomposite sensing materials manage to produce a strong sensitivity signal with an RI value recorded of 4715 nm/RIU. As the human IgG biomolecule is introduced to the coated fibre, it was confirmed that 0.037 µg/mL of human IgG alone manages to detect with the peak signal red-shifted. In this study, the advantage of using a fibre-optic platform instead of an electrode-based system for embedding AgNPs is that the intrinsic refractive index sensitivity of the sensing layer can be evaluated and quantified before undergoing biomolecular detection. This allows the sensing performance to be optimized and controlled, enabling systematic enhancement of sensitivity before proceeding to the detection of specific biomaterials.

2.5 Reduced Graphene Oxide (rGO)

2.5.1 Introduction to Graphene-Based Materials

Recently, graphene-based materials have been increasingly incorporated into noble-metal nanomaterials due to their unique hexagonal structure and optical properties, thereby enhancing biosensor applications (Dasari et al., 2017). The hexagonal structure of graphene can provide a stable platform for nanoparticles by preventing their agglomeration within the graphitic framework while simultaneously stabilizing them. Thus, studying this method will ensure that a more stable mixed composite sensing material can be produced, and its embedding with an optical fibre will result in a reliable sensor with excellent signal performance.

Graphene compounds that can be converted to GO, rGO, and GQDs have enabled nanomaterial applications by stabilising noble metal nanomaterials. Graphite is composed of a multilayer, with each layer consisting of six carbon atoms that are closely covalently bonded, forming a hexagonal lattice structure, and each layer is bonded via weak van der Waals forces (Dhakate et al., 2011). Despite graphite having strong electrical and thermal conductivity, its structure is not flexible, and it is easily brittle. However, when the multi-layered graphite undergoes exfoliation, the layers break down into single-layered sp^2-bonded carbon atoms called graphene (Dhakate et al., 2011). The exfoliation of graphite makes graphene more flexible, stronger, and lighter. Thus, graphene and its derivatives have been introduced into nanomaterials to enhance their sensor performance.

The previous paper reported that graphene was oxidised via a modified Hummers' method using potassium permanganate as the oxidising agent, allowing the formation of hydroxyl, epoxy, and carboxyl groups between two graphene layers, making it more hydrophilic (Raji et al., 2019). Jabłońska et al. state that graphene is an effective fluorescence quencher that improves the quality of Raman spectra and also enhances the SERS signal via a chemical process (Jabłońska et al., 2018). These additions will allow graphene and its derivatives to be better suited for detecting optical performance when incorporated with nanoparticles.

Interestingly, rGO has been studied recently due to its less hydrophilic properties, which make it suitable for binding to glass or silicon materials (N. Sharma et al., 2020) on fibreglass. Sharma et al. also state that the rGO was synthesized via a

reduction method, using reducing agents such as hydrazine hydrate to reduce the number of oxygen moieties on the graphene surface. The reduction of oxygen moieties will make rGO less hydrophobic and more electrically conductive by removing oxygen from the graphitic structure (Georgitsopoulou et al., 2019).

In conclusion, among the graphene derivatives, rGO was selected in this study due to its larger two-dimensional surface area compared to GO and GQDs. The extended graphitic lattice of rGO provides a larger platform for the immobilisation and distribution of AgNs. This will allow more AgNs particles to be anchored into the graphene lattice structure, preventing the agglomeration of nanoparticles. Furthermore, the improved electrical conductivity and stability of rGO following the reduction process can contribute to enhanced optical performance of the nanocomposite. Therefore, rGO was chosen as the supporting matrix for AgNs in this work to promote nanoparticle stability and maximise the interaction between the plasmonic nanostructures and the fibre-optic sensing platform.

2.5.2 Synthesize of rGO

Multiple reduction methods have been reported to successfully synthesize rGO, including chemical (V. Sharma et al., 2017), thermal (Muzyka et al., 2018), and electrochemical reduction (Zaaba et al., 2017). The GO was commonly reduced chemically using hydrazine hydrate and ascorbic acid as a reducing agent. Hydrazine hydrate is widely used as a reducing agent or an intermediate in the synthesis of various industrial products, including water treatment, chemical treatment processes, and active ingredients. In this method, hydrazine hydrate was used to chemically reduce the oxygen-containing functional groups in GO, making it less hydrophilic and more electrically conductive. Nonetheless, hydrazine hydrate is a powerful acid-base and hazardous, making it unsuitable for large-scale rGO production. Hydrazine hydrate is highly toxic, carcinogenic, and poses significant health and environmental hazards. As a result, using hydrazine hydrate as a reductant is risky, as the toxicity produced during the synthesis of large amounts of rGO can lead to an explosion.

Thus, a new method was introduced in which ascorbic acid, a form of vitamin C, was used as a reducing agent to replace hydrazine hydrate. Not only is ascorbic acid environmentally friendly, which makes it safer and easier to handle, but it is also biocompatible, making it suitable for biosensors, drug delivery systems, and tissue

engineering, where non-toxic materials are essential. Qi et al. state that the toxicity issues arising from using hydrazine hydrate as a reductant are dangerous, prompting them to use ascorbic acid as a new green-reducing agent (Qi et al., 2016). Ascorbic acid, also known as vitamin C, has special properties for donating electrons to other substances, making it a strong green reducing agent (Linnell, 2000). Synthesizing rGO using ascorbic acid is a promising method due to its lower toxicity and safer large-scale production compared to hydrazine hydrate (Tas et al., 2019).

Another green method was also introduced to the world where part of the plant components were used as a reducing agent to replace the hydrazine hydrate. There are certain plants with bioactive compounds, such as moringa, soybeans, grapes, and green tea (Samtiya et al., 2021). The bioactive component can be found in the leaves, seeds, stems, and other parts of the plant. These components have reduction properties that allow the removal of oxygen functional groups in GO, forming an rGO in the process. However, the extraction of these components are quite meticulous as it is hard to exact how much plant components are needed to produce an accurate amount of bioactive components. Moreover, the pH value of plant components plays a pivotal role in determining the quality of bioactive components to ensure the production of high-quality rGO. Hence, it will be challenging to tune this method in order to obtain an optimized rGO. Thus, multiple methods have been used, including synthesising rGO on a small scale to control toxicity, replacing the reducing agent with natural resources, and changing the rGO synthesis methodology, and all these methods have been compiled in Table 2.5.

Table 2.5
Compilation of Past rGO Methods

Samples	Methodology	Benefits	Applications	References
Hydrazine hydrate-treated GO	Graphite prepared via a cold-wall CVD system, producing C-labelled graphite flake. The flake used to create GO via the Modified Hummers method, with potassium permanganate as the oxidising agent. Hydrazine monohydrate is used to reduce GO to rGO.	Capable of synthesising rGO in a large batch. However, it required precautions due to toxic released during the synthesis process. This method increases the grain size and decreases the porosity of FTO.	Generation of aromatic nitrogen doping	(Mbayachi et al., 2021)
rGO via chemical reduction of Ascorbic acid	Ascorbic acid is mixed with the GO solution to reduce the oxygen-containing functional groups. Hydrogen peroxide was added to remove excess ascorbic acid and stop the oxidation process.	Safer synthesis and lower toxicity were observed during the synthesis process compared to using hydrazine hydrate as a reducing agent for mass-producing rGO.	Drug delivery and tissue engineering	(Palomba et al., 2022)
Reduction of GO via Green reducing agent (Plant extraction) using polyphenols.	Parts of plants, such as leaves, roots, seeds, peels, and fruits are collected and thoroughly washed to remove impurities. The plants were then ground into a fine powder, and distilled water was added during boiling and sonication to extract the bioactive compounds. These compounds	Eco-friendly and the resources required are easily accessible. rGO produced using plant extracts is more biocompatible, which is beneficial for applications in biosensors and biomedical devices.	Sensors, catalysts, and biomedical.	(Ismail, 2019)

	will serve as reducing agents to convert GO to rGO.			
Synthesis of rGO via thermal annealing	The GO undergoes high-temperature (330 °C) conditions in an inert or reducing atmosphere (such as argon or hydrogen) to remove oxygen-containing groups.	An alternative or supplementary method to thermal annealing. However, this process requires heating the atmosphere under an inert gas atmosphere.	Energy storage and conversion via supercapacitors, batteries, and fuel cells	(Tas et al., 2019)
Electrochemically reduced GO (ERGO)	GO synthesized via the Hummers method is placed on an electrode in an electrolyte solution. As the voltage applied, the oxygen group began to be removed, forming rGO.	Safer to conduct and no chemical toxic produced during synthesis as electric voltage is used to remove oxygen groups from GO. An excellent alternative to hazardous chemical reduction is using hydrazine hydrate. However, it is limited to large-scale production.	Energy storage and catalysis	(A. Zhou et al., 2022)

Another method also provides a good replacement for hydrazine hydrate: stepwise thermal annealing. Despite requiring the GO to undergo chemical reduction to activate the reduction process, the oxygen composition is removed again through a controlled heating process to remove the oxygen functional group in GO. This process involves multiple heating steps at progressively higher temperatures, allowing selective removal of different types of oxygen groups based on their thermal stability (Tas et al., 2019). Moreover, this method requires the use of ascorbic acid to assist in the reduction of GO before thermal annealing at 70°C, 120°C, and 300°C to further reduce GO and improve electrical conductivity.

Using the ERGO method to obtain rGO also offers an interesting alternative to the reduction method. The GO was synthesized via Hummer's method and was dispersed into the electrolyte before adding the electrode into the electrolyte (A. Zhou et al., 2022). Upon applying the voltage, the oxygen in the GO electrolyte began to be removed via electron transfer. The electron from the electrode transfers into GO and interacts with the oxygen functional group, breaking the bond between carbon and oxygen. This interaction removes the oxygen group, forming a rGO composition with excellent electrical conductivity. However, the drawback of this method is its scalability in rGO production. It is impossible to produce pure rGO in bulk batches, as it depends on the scale of the electrolyte and the amount of electrode used at once. Moreover, production may be more complex and costly depending on the scale of rGO production.

To summarise the method compilation, the synthesis of rGO using ascorbic acid as a replacement for hydrazine hydrate offers a promising approach for integrating with biological components and controlling toxicity during rGO production. Moreover, using plant-based materials may rival ascorbic acid as a natural reductant, yet the method is too complex and time-consuming to produce rGO. Subsequently, thermal annealing and ERGO methods appear more compatible with electrical components than with biological components, as they can interfere with rGO's conductivity in biosensor applications. Hence, applying the reduction method with ascorbic acid as the reducing agent is more suited to this research, as it is required to enhance the stability of AgNs and to adapt them to biological components.

2.5.3 Characterization of rGO

Previous papers have reported that the oxygen functional group in GO managed to reduce with hydrazine hydrae as a reductant to be applied to gas sensing applications, and the result shows the Raman excitation of GO and rGO produced at two laser wavelengths of 532 and 785 nm, and the I_D/I_G band ratio of rGO produced are 1.84 times higher than GO with 1.80 band ratio.

The result also shows that the rGO structure produces more crinkles than GO under the FESEM image, and that the rGO structure becomes highly corrugated as it converts from GO, due to the escape of oxygen-containing groups from the surface. The morphological structure of rGO shows that it has more wrinkle or crumpling features in comparison to GO under SEM imaging, as shown in Figure 2.8, due to the reconstruction of graphene from the removal of the oxygen-functional group (Chuah et al., 2020). This removal caused the GO monolayer to break up into multiple pieces, removing the oxygen groups, before reconstructing and repairing itself into a multilayered rGO. This removal also makes rGO more electrically conductive, as the oxygen groups in GO act as electrical resistors when current passes through the graphene lattice. Moreover, the removal of the oxygen-functional group during the reduction process causes rGO to lose its hydrophilicity, hindering its interaction with water. Due to the removal of the oxygen-functional group from GO and its subsequent fragmentation into multiple pieces, the rGO morphology appears wrinkled or crinkled, as seen under SEM.

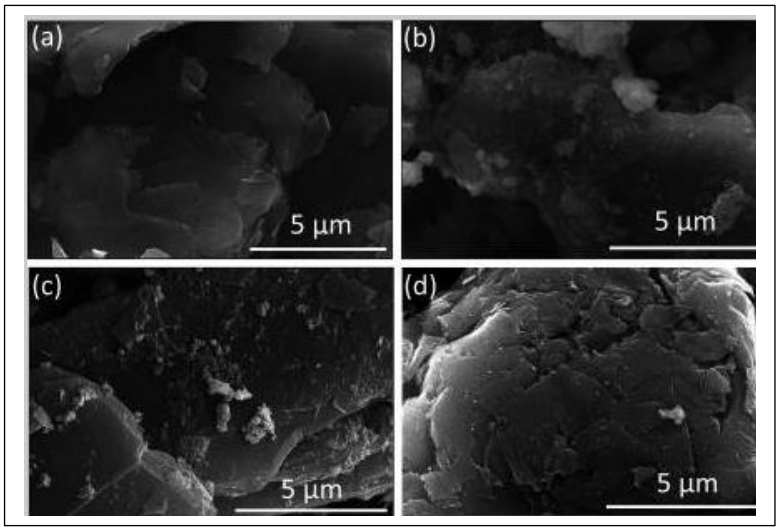

Figure 2.8 Morphological structure of (a) graphite, (b) graphite oxide, (c) GO, and (d) rGO.
Adapted from (Chuah et al., 2020)

Moreover, the removal can also be seen via UV-vis spectrum, where the GO exhibits π-π* absorption band at 230 nm and a shoulder peak of n-π* absorption at 295 nm (S. Yang et al., 2012). Yang et al. state that as the reduction process progressed, the peak of the π-π* transition shifted to 265 nm, indicating that some group on the GO surface was removed and the conjugated structure was restored.

It is also possible to confirm changes in the element composition of GO and rGO by comparing XRD patterns. The GO peak in XRD was previously reported at $2\theta \approx 11.7°$ (001 Plane) with an interlayer spacing (*d-spacing*) of 0.76 nm (Gurunathan et al., 2012). Gurunathan et al. state that, as the reduction process was completed, the original GO 001 in-plane peak will gradually decrease and eventually disappear. At the same time, a new 002 in-plane peak appeared in the range of $2\theta \approx 24°$ to 29°, and the *d-spacing* of rGO was recorded at 0.35 nm. The researchers also stated that the shift in peaks was attributed to the reduction of GO and that the decrease in *d-spacing* indicates the oxygen-functional group are removed but not completely. Moreover, it states that the conjugated graphene network (sp^2 carbon) was also recovered during the reduction process producing an irregular stacking of graphitic structures.

Subsequently, the removal of an oxygen-functional group and the reconstruction of the rGO structure can also be studied using Raman spectroscopy, where two peaks, the D-band and the G-band, are observed (Johra et al., 2014). The D-band corresponds to defects in the graphitic structure, and the G-band corresponds to the level of structural order of sp^2 lattice structures, as evidenced by the vibration of the C-C bond in the in-plane lattice. Using the ratio of the intensities of the D-band and G-band peaks (I_D/I_G), the intensity of the defect and the recovery rate of the sp^2 lattice structures can be characterized. The peaks of D-band and G-band of GO were previously recorded at 1348 cm^{-1} and 1594 cm^{-1} of Raman shift and rGO at 1353 cm^{-1} and 1586 cm^{-1} of Raman shift (Hidayah et al., 2017). The ratio I_D/I_G of GO was recorded at 0.86 and it increased as the reduction process occurred. The increase in the I_D/I_G ratio is due to the recovery of sp^2 carbon and a reduction in the average size of sp^2 domains.

The purpose of FTIR is to determine the structure and functional groups that exist in GO and rGO. By identifying differences in functional groups between GO and rGO, the removal of the oxygen-functional group and its composition can be studied. Previous researchers recorded the spectrum of GO using FTIR spectroscopy, and the result showed a broad peak at 3271 cm^{-1}, corresponding to the O-H stretching of water molecules absorbed onto GO (Hanifah et al., 2015). Another study on the FTIR spectra

of rGO was also conducted and the result managed to produce three peaks, which is the broad and intense peak at ~3400 cm^{-1} arising from OH stretching vibration, a peak at ~1720 cm^{-1} due to C=O stretching vibrations of carboxylic groups, and sharp C-C band within the range of 1600 cm^{-1} (Rodríguez-González et al., 2016). The FTIR spectra of GO and rGO reveal significant changes after reduction, with a decrease in oxygen functionalities and an increase in sp^2-hybridised carbon domains. Therefore, the compiled characterisation from previous studies provides a useful reference for this work, as it enables the identification of key spectral features associated with successful reduction. This, in turn, assists in optimising the rGO synthesis parameters to obtain a material with reduced oxygen content and enhanced sp^2 carbon networks suitable for improved electrical and interfacial performance.

2.6 Hybrid rGO-AgNPs-Based

2.6.1 Synthesis of rGO-AgNPs

The method for incorporating AgNPs into rGO has been reported previously, and the most common method is in situ chemical reduction (Sang et al., 2017). However, there are method that use a layer-by-layer (LbL) or sandwich assembly due to their application (Gao et al., 2016).

The in-situ chemical reduction method involves synthesising AgNPs directly in the GO solution using ascorbic acid as the reducing agent (Sang et al., 2017). Ascorbic acid will reduce silver ions directly onto the rGO sheets, resulting in AgNPs being directly incorporated into the graphene sheets. There is also an LbL method that requires the assembly and mixing ratios, in which NMNPs (AgNPs and AuNPs) and rGO are synthesized separately and assembled layer by layer depending on their purposes. The difference is that the LbL assembly of the composite material is easier to perform, as it can be done by dipping or spraying. The basic procedure for LbL assembly is that the rGO solution is applied to the surface and dried to form the 1st layer. The process was repeated by applying the NMNPs solution to the rGO layer and drying to form the 2nd layer. In some cases, another composition was applied as the 3rd layer, such as graphene or hydrogels. All of these methods are summarized in Table 2.6.

Table 2.6
Records on the Procedure in Synthesizing rGO-NMNPs

rGO-NMNPs	Methods	Benefits	Applications	References
rGO-AgNPs via In-situ method	In-situ method in which silver composition is added to the GO solution. Ascorbic acids were used to simultaneously reduce the silver ion and oxygen composition to produce rGO-AgNPs in a single pot. The dual-composite material was then cladded onto the electrode to enable protein detection.	Exhibits excellent electrochemical activity and high sensitivity for detecting heavy metal ions, including Pb(II), Cd(II), Cu(II), and Hg(II). The modified electrode also demonstrates strong anti-interference capabilities, ensuring accurate detection even in the presence of other substances.	Metal ion detection	(Sang et al., 2017)
rGO-AgNPs using plant extract as reducing agents	The geranium is extracted from the leaf by boiling it with water. In-situ method where silver nitrate is added into the GO solution using geranium extract as a reducing agent.	Eco-friendly synthesize method that produces less toxic during the synthesize process. Achieves a uniform and homogeneous distribution of AgNPs on the GO sheets with a 1:1 weight ratio of GO to Ag.	SERS, catalyst, and biomedical materials.	(Rodríguez-González et al., 2016)
Silver nanoparticles decorated rGO	rGO was reduced using a reducing agent to form a rGO dispersion; silver nitrate was added to the process, and reducing agents were added again to reduce silver ions in the rGO dispersion. This method is similar to the in-situ method yet uses a reduction process twice for rGO and AgNPs in a single pot.	Enhanced the Raman signal of analytes due to LSPR of AgNPs and high surface area of rGO which amplifies the detection of analyte. Capable of detecting multiple analytes such as Rhodamine 6G (R6G), 4-Mercaptobenzoic Acid (4-MBA), and 2,4-Dinitrotoluene (2,4-DNT).	SERS sensors in analyte detection.	(Naqvi et al., 2019)
rGO/AgNPs/rGO Sandwich Structure as a Hole Extraction Layer	AgNPs and rGO were synthesized separately. The LbL sandwich method was applied, with rGO spin-coated as the 1st layer. AgNPs where then spin-coated on the rGO as the 2nd layer.	This method allows a precise tuning of the rGO and AgNPs. The rGO layers provide a conductive pathway, and the AgNPs enhance charge-transport properties. The sandwich structure functions as a hole-extraction layer in polymer solar cells, enhancing the cells' performance.	Polymer Solar Cells	(Tran et al., 2015)

	rGO the spin-coated on the AgNPs as the 3rd layer forming a sandwich method.			
Plasmonic silver sandwich structured photoanode and reflective counter electrode	The photoanode consists of sandwiched SiO_2, AgNPs, and TiO_2. The counter electrode consists of polypyrrole (ppy), rGO, and tin oxide. Add aluminium foil as a reflective layer for the electrode. The photoanode will absorb the sunlight and AgNPs will enhance the absorption. The electrode flows into the power generator through the TiO_2 and the rGO helps stabilize the transfer. The electron returns to the counter electrode to complete the cycle.	The LSPR effect from AgNPs is used to increase the absorption of light by the dye molecules. The TiO_2 and rGO layer efficiently transport the electron to the generator without losing too much electron. Able to harvest the light even more with help of aluminium foil. The modified cells exhibit a twofold increase in PCE (from 0.6% to 1.2%) and a 68.37% rise in short-circuit current density (Jsc), from 2.15 to 3.62 mA cm^{-2}	dye-sensitized solar cell	(I. Ibrahim et al., 2021)

Based on a compilation of all research studies on rGO and AgNPs, the in-situ method is the most common for integrating AgNPs into the graphitic structure in a single pot. The method was even modified to use plant extract as a reducing agent, and the results show promising production of rGO-AgNPs with reduced toxicity and less time-consuming synthesis of the dual composite materials.

The process can be further enhanced by conducting twice the reduction in a single pot, thereby increasing the electrical conductivity of rGO-AgNPs. The method of incorporating nanoparticles into the graphene structure was further investigated using the LbL or sandwich method. This method is also suited to this research, as the layering method allows the study of the effect on each layer. The rGO and AgNPs were synthesized ex situ, separately, and then incorporated together via the layering method. This method can be further tuned with another composite material, depending on its uses and benefits.

Interestingly, the AgNPs method proposed before has yet to be applied to rGO and is a relatively new study. Moreover, the in-situ method is not ideal, as it mostly yields spherical nanoparticles. Additionally, the LbL or sandwich method is more advanced and may be complex to study at this stage. Therefore, conducting the ex-situ method, in which rGO and AgNs are synthesized separately and then incorporated at a controlled volume mixing ratio, would be worth exploring before progressing to more complex methods.

2.6.2 Characteristics of rGO-AgNPs

The morphology of rGO-AgNPs prepared by the in-situ method can be seen in Figure 2.9 (A), where spherical silver nanoparticles are embedded within the graphene structure. Meanwhile, Figure 2.9 (B) shows the white coloured dots that represent the AgNPs in the rGO lattice structure using the LbL sandwich method. Despite different approaches, both still show that the AgNPs were able to integrate into the graphitic lattice structure. Hence, upon conducting the proposed rGO-AgNPs method, the morphological structure should resemble these examples, with white dots visible in the wrinkled structure, indicating successful integration of AgNPs.

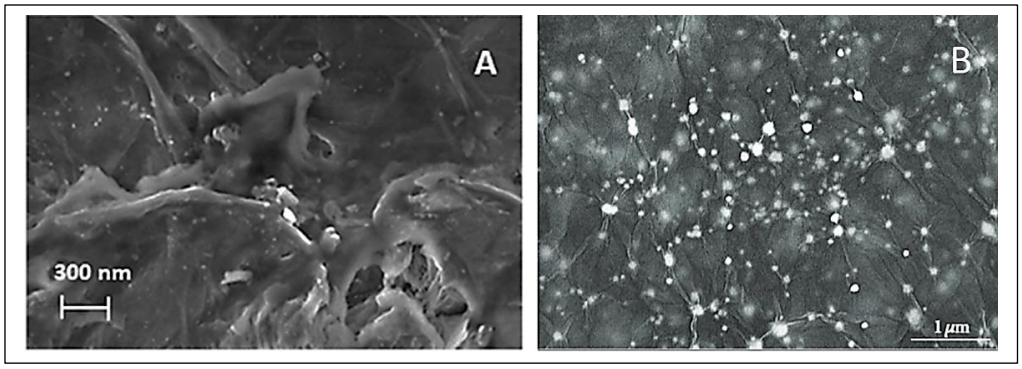

Figure 2.9 SEM Image on the Morphological Structure of rGO-AgNPs Under (A) In-Situ (Kasztelan et al., 2021) and (B) LbL Sandwich Method (Tran et al., 2015).

Additionally, the Raman spectra of the rGO obtained by the in-situ method showed D- and G-band peaks at 1350 cm^{-1} and 1570 cm^{-1}, respectively (Sang et al., 2017). However, the presence of AgNPs in the rGO synthesized by Sang et al. greatly enhances the intensity of Raman detection, producing very strong D- and G-band peaks at 1345 cm^{-1} and 1575 cm^{-1}, respectively. It states that the surge in intensity is due to LSPR effects from AgNPs, which greatly enhance Raman detection. The research results also show an increase in the I_D/I_G ratio from GO (1.0) to rGO (1.2), indicating a successful reduction of GO to rGO upon incorporation of AgNPs.

The crystallinity structure of rGO-AgNPs can be studied by comparing itself with rGO and AgNPs. Previous research reported rGO with a peak at approximately $2\theta \approx 10°$, corresponding to the (001) plane (Tran et al., 2015). Meanwhile, the AgNPs exhibited distinct peaks at 2θ values of approximately 38°, 44°, 64°, and 77°. These peaks correspond to the (111), (200), (220), and (311) crystallographic planes, confirming the crystalline nature of the synthesized AgNPs. Upon conducting the LbL sandwich method on both rGO and AgNPs, the XRD pattern showed a broad peak around $2\theta \approx 25°$, corresponding to the (002) plane of reduced graphene oxide (rGO) and the absence of the GO peak at 10° indicates successful reduction of GO to rGO. Moreover, the AgNPs peak also appeared within the sandwich structure, indicating a successful incorporation of AgNPs between the rGO layers.

When it comes to optical characteristics, UV-vis spectrometer analysis of rGO-AgNPs synthesized by Tran et al. was also recorded, where the intensity of the absorbance peak is stronger compared to AgNPs and rGO itself. The results show that the AgNPs exhibit a SPR peak at approximately 420 nm and a rGO peak at

approximately 270 nm. Both peaks appear at a typical standard peak for both AgNPs and rGO. Upon integrating the AgNPs with GO through layering methods to form an rGO-AgNPs-rGO sandwich structure, the UV-vis spectrum of the sandwich composite shows features corresponding to both rGO and AgNPs. The presence of the SPR peak at 420 nm in the sandwich structure confirmed the incorporation of AgNPs within the rGO layers and the presence of rGO also presented in the peak UV-vis spectrum.

Based on the compiled results for rGO-AgNPs, it is confirmed that incorporating AgNPs into rGO retains the characteristic features of both materials, regardless of the testing method used. Therefore, upon integrating AgNs with rGO, both characteristics and features will appear in a single spectrum.

2.7 Research Gap Analysis on Tri-hybrid Composites of AgNPs-Graphene Based-Hydrogel

2.7.1 Hydrogels

Hydrogels have been extensively explored for drug and gene delivery, regenerative medicine, biodevices, and biosensors. The natural hydrogels, which consist of starch, cellulose, chitosan, gelatine, collagen, and so on, have been applied to drug delivery, tissue scaffolds, and particularly wound dressings, where they can act as an antimicrobial factor lowering the risk of microbial infections (Betancur et al., 2018; Linnell, 2000; Tas et al., 2019). The structure of natural hydrogels was further researched and improved, leading to the development of several hydrogel types, including synthetic, responsive, protein-based, and hybrid hydrogels.

However, depending on the compatibility and applications of hydrogels in integrating them with sensing materials, this procedure will be critical in determining their acceptability. Several research methods for integration graphene-based or AgNPs-based with hydrogel precursors have been reported, commonly using peptide-based (Binaymotlagh et al., 2022), supramolecular (Du et al., 2015), and chitosan-based hydrogels (Hong et al., 2024). Meanwhile, peptide-based hydrogels are hydrogels composed of numerous protein blocks, each made of tiny molecules known as amino acids (Binaymotlagh et al., 2022). These peptide hydrogels exhibit excellent compatibility with AgNPs, enabling the incorporation of silver-based nanocomposites. This synthesis method requires photochemical techniques to reduce the silver content in the hydrogels. The peptide hydrogels are then enzymatically modified using

fluorenylmethyloxycarbonyl phenylalanine (Fmoc-Phe) and diphenylalanine (Phe_2). The tensile strength and stability of the hydrogels will then be improved using honey. This method shows promise for detecting antimicrobial activity, as the AgNPs/hgel and AgNPs/hgel-honey composites exhibited Minimum Inhibitory Concentrations (MICs) of 3.12 mg/L against both S. aureus strains. These results show stronger microbial detection than with AgNPs alone, which require 6.25 mg/L of S. aureus to detect antimicrobial activity. This shows how well the peptides are compatible with the nanoparticles.

Supramolecular hydrogels also show promising compatibility when embedding with GO-AgNPs. This hydrogel is a three-dimensional network structure formed by molecules that self-assemble via non-covalent interactions, such as hydrogen bonds, hydrophobic interactions, or host-guest interactions (Du et al., 2015). This process allows the hydrogel to hold more water while retaining its gel-shaped structure. A report of the interaction between supramolecular hydrogels and AgNPs with GO was published, in which GO and hydrogels were prepared separately.

The AgNPs were synthesized in the hydrogels using plant extract as a reducing agent to reduce silver ions (Ag^{+}) to metallic silver (Ag^{0}). The GO was then dispersed within the hydrogel network to allow it to interact with both the hydrogel matrix and the embedded AgNPs. The inhibition of AgNPs in hydrogels enables sustained, controlled release of silver ions, effectively inhibiting the growth of various pathogens. Meanwhile, GO plays a role in providing structural integrity and durability to the dual composite during integration. The collaboration between the triple composite material allows it to demonstrate significant antimicrobial activity against both Gram-positive and Gram-negative bacteria in biomaterial detection.

Chitosan-based hydrogels are the most widely used method for combining graphene properties with noble metal nanomaterials. Chitosan is a natural polysaccharide derived from chitin, the second-most-abundant biopolymer in nature (after cellulose) (Hong et al., 2024).

Based on the compatibility report, chitosan is the most suitable hydrogel to integrate with AgNs and rGO in this research, as the LbL method applied to bare fibre optics will allow the tri-composite materials to bind during the cladding process. Moreover, the biocompatibility of the hydrogels will enable the use of AgNs and rGO to enhance the performance of fibre biosensors before introducing this system for

protein detection. Additionally, the LbL and sandwich method is straightforward to apply to all the tri-composites together.

2.7.2 Tri-hybrid-Based Graphene/Ag/Hydrogel-Based Fibre Optic Biosensors

Using the LbL method to apply the sensing material to the fibre surface is the most ideal approach. The common method of applying a stack of the tri-composite medium to the surface of fibre optics was via dip-coating. There was a study in which GO and AuNPs were coated onto the surface of fibre optics via dip-coating to serve as a signal amplification element (Chen et al., 2021). The surface of fibre optics was coated with AuNPs via dip-coating to amplify the signal. The GO was then introduced to the duo-composites layer via dip-coating again as a site for antibody immobilisation due to its abundant carboxylic groups. In this study, the anti-immunoglobulin G (IgG) antibodies were covalently attached to the GO layer, enabling the specific detection of IgG molecules. These triple-cladded methods show promise for fibre-optic applications, with the sensor exhibiting a linear response to IgG concentrations ranging from 1.0×10^{10} g/mL to 1.0×10^{6} g/mL. The fibre-coated tri-composite material also managed to achieve a limit of detection (LOD) of 0.038 ng/mL, indicating high sensitivity in detecting IgG. This shows that the dip-coating method can be used in this research to integrate the rGO-AgNs-HH later.

Table 2.7
Research Gap on Utilizing rGO, AgNPs, and HH in Biosensor Applications

Sensing material	Sensing medium	Target biomolecule	Findings	References
Silver Nanostar	Not applicable	Not applicable	Modifying the method to provide wide range of star-shaped growth. Details of optical properties from each shape is yet to be studied. Moreover, it is yet to be applied into fibre biosensor application specifically for for protein detection.	(Garcia-Leis et al., 2013)
Reduced Graphene Oxide	Not applicable	Not applicable	GO exhibited abundant oxygen functional groups while rGO synthesis Tour method showed partial restoration of the graphene sp^2 network	(Habte et al., 2019)
Graphene Oxide	Optical fiibre signal (single-mode)	Not applicable	High-yield GO was synthesized with good oxidation and structural quality. Excellent use as GO precursor for rGO synthesis	(Sahudin et al., 2021)
Reduced Graphene Oxide	Drug delivery platform	Doxorubicin (DOX	Safer synthesis and lower toxicity were observed during the synthesis process using ascorbic acid compared to using hydrazine hydrate as a reducing agent for mass-producing rGO	(Palomba et al., 2022)

rGO-silver nanoparticle (AgNPs)	Catalytic rod	Not Applicatble	Synthesize method of rGO produces less toxic during the synthesize process. Achieves a uniform and homogeneous distribution of AgNPs on the GO sheets with a 1:1 weight ratio of rGO to Ag	(Rodríguez-González et al., 2016)
Silver-nucleated gold-shell bimetallic nanoparticles (Ag@Au NPs) integrated with GO	Optical fibre signal	Human IgG	The Ag@Au bimetallic structure was deposited on fibre optics before being coated with GO. The matrix sensor was integrated with IgG-specific biorecognition molecules. The coated fibre manages to generate ~4700 nm/RIU and manages to detect human IgG at least 0.037 µg/mL.	(Q. Xu et al., 2025)
Fibre optics coated with Au-Ag alloy embedded with a thin layer of $Ge_2Sb_2Te_5$ (GST)	Optical fibre signal (D-shaped)	Cancer biomarker	The reported sensitivity of 8600 nm/RIU, demonstrating significantly enhanced plasmonic coupling due to the Au–Ag alloy and GST layer. The detection accuracy of 0.033 RIU reflects the smallest distinguishable RI variation determined from the resonance spectral characteristics	(Akouibaa et al., 2026)
Fibre optics embedded carbon quantum dots (CQDs)	Optical fibre signal (Multi-mode)	Iron(III) ion (Fe^{3+})	The RI sensitivity of 3440.45 nm/RIU characterizes the intrinsic refractive index response of the fibre SPR platform. Upon Fe^{3+}	(Y. Zhou et al., 2025)

coated with 60 nm AuNPs film			binding to the functionalized CQDs layer, the local refractive index increases, inducing a resonance wavelength shift. The concentration sensitivity of 2.07 nm/lg(M) indicates the logarithmic response of the sensor toward Fe^{3+} concentration, while the calculated LOD of 2.88 × 10^{-13} M demonstrates its ultrahigh detection capability.	
Fibre-embedded GQD coated chitosan-agarose hydrogels (CAH)	Optical fibre signal (Single-mode)	Glucose	Thickness diameter coating recorded at diameter ~2.48 nm with RI sensitivity was measured at 3658 ± 0.23352 RIU^{-1} during glycerol detection	(Noor Akashah, 2022)
Sandwich-like chitosan-based with rGO immobilized AgNPs	Polymer nanocomposite film	Escherichia coli and Staphylococcus aureus.	The material exhibited controlled AgNPs release (~1.9 % over 14 days) and strong antibacterial activity against E. coli and S. aureus. This work focused on antimicrobial food packaging applications and did not evaluate sensing performance such as RI sensitivity and LOD	(Gu et al., 2021)

Moreover, a similar bimetallic Au@Ag was recorded to be embedded with a D-shaped fibre, while a thin layer of Ge2Sb2Te5 (GST) was coated on the embedded fibre (Akouibaa et al., 2026). The purpose of placing GST on top of the Au–Ag alloy is to enhance the electromagnetic field confinement of the surface plasmons. As light travels through an optical fibre, the light at the exposed area will interact with the Au–Ag alloy layer and excite the surface plasmons at the metal–dielectric interface, which will cause a strong resonance feature in the optical spectrum. The GST layer on top of the alloy will enhance the local electromagnetic field where the plasmons exist, making the resonance feature sharper and more sensitive to small changes. This will result a large shift in the resonance wavelength as RI around the surrounding medium changes, which explain the high refractive index sensitivity (~8600 nm/RIU).

There are some cases where the multi-mode fibre optics coated the CQDs as the inner layer coating, followed by a 60 nm AuNP film on the outer layer (Zhou et al., 2025). As light travels through the optical fibre, the evanescent field outside the core will penetrate the CQDs reaching the AuNP film, creating the LSPR effect. It was confirmed that the RI sensitivity of the fibre coated was recorded at 3440.45 nm/RIU. As Fe^{3+} dropped on the sensing layer, it will penetrate the AuNP film and interact with CQDs, causing local RI to increase, resulting in a red-shift of the SPR resonance wavelength. The concentration sensitivity of 2.07 nm/lg(M) was recorded, demonstrating a logarithmic dependence of wavelength shift on Fe^{3+} concentration, typical of surface adsorption processes. The calculated LOD of 2.88×10^{-13} M confirms the ultrahigh detection capability of the sensor at sub-picomolar levels.

When it comes to cladding the hydrogels, a method where the chitosan was cladded on the surface of the fibre optics was recorded, where HH were synthesized by preparing a stock solution of chitosan hydrogel at a concentration of 0.25% (w/v) without crosslinking agents (Akashah et al., 2023). The chitosan solution was then added to an agarose solution (2% w/v) to form an HH. The result shows that as the thickness increases, the signal strength increases. Moreover, the sensor demonstrated significant signal improvement when the hybrid hydrogel was used as the sensitive coating, and the refractive index (RI) sensitivity was measured at 3658 ± 0.23352 RIU^{-1} during glycerol detection.

Hence, the idea of using agarose to enhance the optical properties of chitosan hydrogels for fibre optics is interesting, as agarose can enhance light propagation via the TIR effect and minimise scattering losses, thereby improving the evanescence wave

in fibre optics. Moreover, its special benefits, particularly in detecting changes in the RI, will be beneficial in this research by coating it on the outer layer of the sensing medium via a dip-coating method, allowing the biosensor to detect biological properties later. Thus, adapting this system and detection method into this research will be crucial for assisting the sensor in detecting biomaterials later.

A recent report on integrating chitosan with rGO-AgNs nanocomposite film for packaging materials was published, where the polymer film that consists of chitosan-based, rGO, and AgNPs was immobilized into a single film by sandwiching each other (Gu et al., 2021). The purpose of synthesizing tri-composite material is to kill the specific bacteria (Escherichia coli and Staphylococcus aureus) by releasing silver ions (Ag^{+}) of AgNPs from the polymer film to the food packaging. The polymer film consists of chitosan-based hydrogels with rGO-AgNs embedded into the hydrogel matrix before adding another hydrogel on the surface as a protective layer. The idea of this sequence is to have the film trigger a slow release of Ag^{+} upon contact with a humid environment, and the film successfully releases ~1.9 % of AgNPs in a controlled manner for 14 days. This study expresses the importance of setting a suitable sequencing layer of film, which will be crucial in this study in determining a suitable sequence layer of sensing medium that consists of rGO, AgNs, and HH on the bare fibre optics later.

Based on the studies summarised in Table 2.7, considerable progress has been made in developing fibre-optic biosensors using graphene-based materials, noble metal nanoparticles, and hydrogels either individually or in binary combinations. Nevertheless, several limitations still remain in each method. It can be observed that although numerous fibre optic biosensors have been developed for refractive index and metal ion detection, the application of fibre optics for selective protein detection remains relatively underexplored. Moreover, the combination of AgNPs, rGO, and HH within a single platform has yet to be applied into any of the fibre optic sectors. The incorporation of AgNPs can provide strong plasmonic enhancement, while rGO offers a large surface area and excellent adsorption capability for nanoparticle immobilisation. In addition, the porous and biocompatible nature of hybrid hydrogels can facilitate analyte diffusion and provide an effective matrix for biomolecule immobilisation. The synergistic interaction among these three components therefore has the potential to improve sensitivity, stability, and selectivity of fibre optic biosensors. However, the influence of such a tri-hybrid coating on the sensing performance of fibre optic platforms has not been comprehensively investigated. Therefore, this study aims to

develop and evaluate a tri-hybrid hydrogel-rGO-AgNPs-coated fibre optic sensor for protein detection, thereby addressing the existing gap in fibre optic biosensing applications.

2.8 Summary

In conclusion, to apply fibre optics to protein detection, star-shaped AgNPs were chosen to enhance the sensitivity and performance of fibre-optic sensing. Among the graphene properties, rGO was added to the sensing medium not only to stabilise the composition of AgNs, but also to enhance the hydrophobicity of the sensing medium, which should allow it to bind strongly to the bare surface of the fibre optics. The rGO and AgNPs will be synthesized ex situ, and their compositions will be combined at a controlled mixing ratio to form the first layer of the sensing medium. Chitosan-agarose hydrogels were chosen as the second layer and will be integrated via the LbL method, serving both as a protective barrier for the first layer and as a medium to facilitate bioreceptor integration, thereby fulfilling the requirements for biosensing applications. SMF optics will be used as a sensing tool due to its one-way light propagation, enabling accurate sensing, and the surface will be integrated with a tri-composite sensing material (rGO-AgNs-HH). The LSPR method will be employed for protein detection. This approach is chosen for its compatibility with nanomaterials and its high specificity, achieved through the streptavidin-biotin interaction.

CHAPTER 3
RESEARCH METHODOLOGY

3.1 Introduction

The overview of the research methodology for the entire study is shown in Figure 3.1, which encompasses five phases, each fulfilling all three objectives set forth. The research commenced by synthesizing AgNs and rGO separately via chemical reduction and oxidation-reduction methods, as designated in the first phase (Objective 1). Both AgNPs and rGO were characterized to examine their morphological structures and optical properties. Following characterization, the process transitioned to the second phase (Objective 1), in which rGO and AgNs were combined to form a novel material, rGO-AgNs. The mixing ratios method was employed by combining 1 part of rGO with 5 parts of AgNs, with the process repeated at 1:10, 1:15, and 1:20 ratios. Each rGO-AgNs variant was characterized to analyse its physical, morphological, and optical properties.

Subsequently, the third phase (Objective 2) began, during which rGO-AgNs with different ratios underwent signal analysis to evaluate their performance. During this phase, the effects of dipping time and surface treatment during the fabrication of a fibre-optics sensor platform were investigated to enhance the signal performance of the embedded fibre-optics.

The research then progressed to the fourth phase (Objective 3), where the selected rGO-AgNs were combined with a hybrid hydrogel (HH) to create a new sensing material, termed rGO-AgNs-HH. The dipping sequence was examined to identify the optimal sequence for coating fibre optics using signal analysis and RI sensitivity testing. The chosen sequence was then employed in the fifth phase (Objective 3), focusing on detecting protein interactions through porosity, protein, and specificity testing.

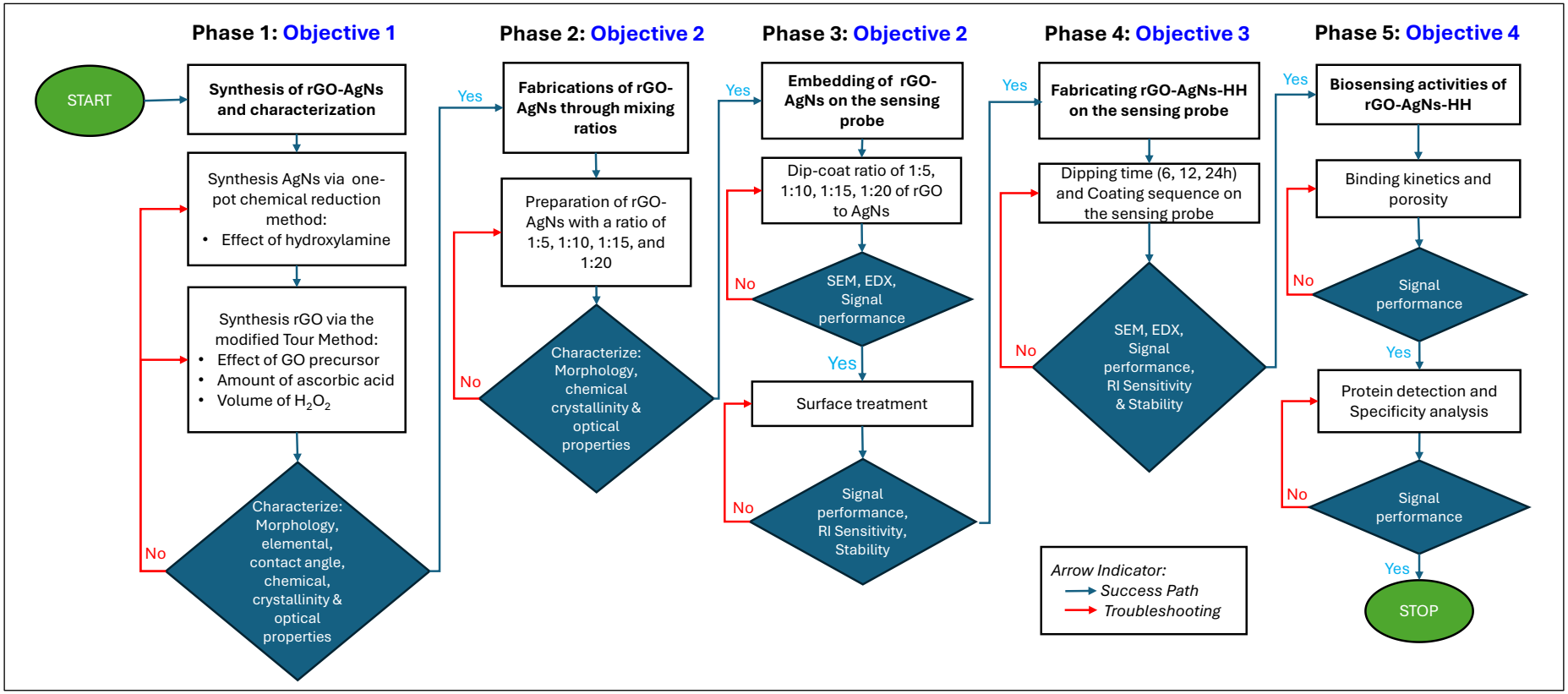

Figure 3.1 Flowchart of the Overall Research Methodology

3.2 Materials and Chemicals

List of materials and chemicals used in this research, as listed in the Table 3.1.

Table 3.1
List of Chemicals and Materials Used in this Research

Process	Material and chemicals	Purity (%)	Product #	Supplier
Cleaning materials	Nitric Acid (HNO_3)	69.0	V800281	Sigma
	Hydrochloric acid (HCl)	37.0	320331	Sigma
Synthesis AgNs	Silver nitrate($AgNO_3$)	≥99.8	209139	Merck
	Sodium hydroxide (NaOH)	99.0	106498	Merck
	Sodium citrate tribasic dehydrate ($Na_3C_6H_5O_7$)	≥99.0	S4641	Sigma
	Hydroxylamine	50 wt.% in H_2O	438227	Sigma
Synthesis GO and rGO	Graphite powder	99.0	282863	Sigma
	Potassium permanganate ($KMnO_4$)	≥99.0	461233	R&M
	Sulphuric acid (H_2SO_4)	98.0	112080	Supelco
	Hydrogen peroxide (H_2O_2)	30.0	822287	Sigma
	Ascorbic acid ($C_6H_8O_6$)	≥99.8	A92902	Merck
	Hydrochloric acid (HCl)	37.0	100317	Supelco
	Ethyl alcohol (C_2H_5OH)	≥99.5	BP28184	Fisher
Synthesis HH	Chitosan (medium molecular weight)	-	448877	Sigma
	Acetic acid (CH_3COOH)	≥99.0	A6283	Sigma
	Agarose (Low Melting Point)	UltraPure™	16520-050	Fisher
	Glutaraldehyde	≥99.8	340855	Sigma
Probe sensor	Single-mode Silica Optical fibre with FC-FC type connectors (1 metre)	-	G652D	YP-Link
	Single-mode Silica Optical fibre	-	A0C00138763	Full Band
RI detection	Glycerol	99.0	AAA162050F	Fisher
Protein detection	Phosphate buffer saline (10x solution, pH 7.4)	-	BP3991	Fisher
	Streptavidin Streptomyces avidinii	-	S4762	Sigma
	Bovine serum albumin	≥98%	A7030	Sigma
	Biotin (lyophilised powder)	≥99	B4501	Sigma

3.3 Phase 1: Synthesis of AgNs and rGO

3.3.1 Synthesis of AgNs

The synthesis of AgNs was conducted via a one-pot chemical reduction method, as illustrated in Figure 3.2. The process starts by adding 0.5 mL of 0.05 M sodium hydroxide and 0.5 mL of 1.8 x 10^{-4} M hydroxylamine to a triangular flask, then stirring at 670 rpm for 1 minute. Then, 9 mL of 8 x 10^{-4} M silver nitrate was added to the mixture, and stirring was continued for 15 minutes at 670 rpm. The mixture solution should turn from colourless to dark green. Hydroxylamine was used as a mild reducing agent to reduce Ag^{+} ions derived from $AgNO_3$ to elemental silver (Ag^{0}), thereby facilitating the formation of silver nanoparticles. Then, 0.1 mL of 0.045 M sodium citrate tribasic dehydrate was added to the mixture, which was stirred for 15 minutes.

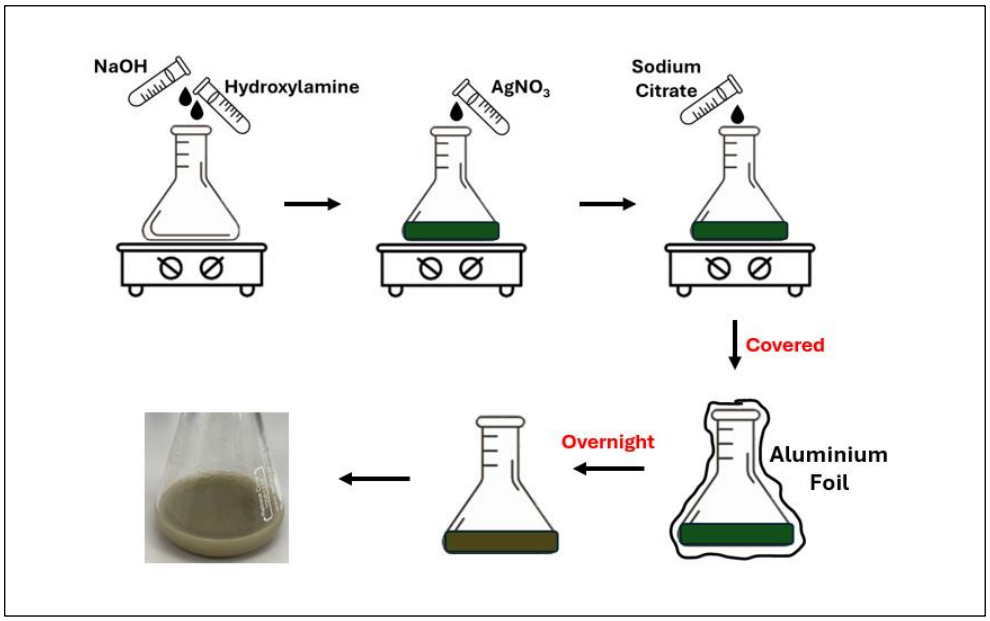

Figure 3.2 Procedure in Synthesizing AgNs

The AgNs solution was then kept in a dark environment by covering the flask with aluminium foil in open spaces and left untouched overnight. The solution should be beige, as shown in Figure 3.2, with a pH range of 7 to 8, indicating a successful AgNPs synthesis. Colours other than beige, which was colourless with black precipitate or a greyish solution, indicate failure to synthesize AgNs. The morphology of AgNs and their optical properties were then studied on TEM, FTIR, EDX, and UV-Visible (UV-Vis) spectroscopy. The procedure was then repeated, varying the hydroxylamine

concentration to assess its effect on nanostar size and diameter, and the concentrations used are listed in Table 3.2. The concentrations of silver nitrate, sodium hydroxide, and sodium citrate were optimized in our earlier work (Roslan et al., 2022), and the optimized parameters were adopted in the present study.

Table 3.2
Parameter Sets on Hydroxylamine Concentrations in Synthesizing AgNs

Sample ID	Sodium Hydroxide (M)	Hydroxylamine (%)	Silver nitrate (M)	Sodium citrate (M)
L	0.05	7.2×10^{-4}	8×10^{-4}	0.045
M		3.6×10^{-4}		
N		1.8×10^{-4}		
O		0.9×10^{-4}		

3.3.2 Synthesis of rGO

In synthesising rGO, two steps were employed. The procedure began by introducing graphite into the modified Hummers' method, initiating the exfoliation process that turned the graphite into graphite oxide. Subsequently, the graphite oxide was oxidised with an oxidant, yielding GO. Finally, the GO underwent oxidation-reduction treatment, in which the oxygen content in GO was partially reduced using an oxidation-reduction agent. Thus, graphite was used as a precursor to synthesize freshly prepared rGO for this research.

3.3.2.1 Synthesis of GO

GO was synthesized via the Modified Hummers' method, with an ice bath prepared beforehand in the hood. 1 g of graphite was mixed with 25 mL of sulphuric acid and stirred for 5 minutes at 600 rpm, during which the sulphuric acid acts as an exfoliation agent, converting the graphite into graphene. Then, the oxidation process began by slowly adding 3 g of potassium permanganate to the mixture over 3 hours, keeping the temperature below 20 °C, before removing the ice bath. 50 mL of Deionised (DI) water was then added dropwise to the solution, and the solution turned from purple to dark brown. Then,100 mL of DI water was added to stop the oxidation process before adding 5 mL of hydrogen peroxide (H_2O_2) to remove excess potassium permanganate.

The solution was then cooled to room temperature and left overnight to separate the supernatant and precipitate. The supernatant was decanted, and the dark green precipitate was washed.

For the washing process, 1.5 mL of GO precipitate was added to a 2 mL test tube, followed by 0.5 mL of 5% hydrochloric acid. The test tube was then vortexed 6 times at 6000 rpm for 15 minutes to remove any metal impurities from the precipitate. The precipitate will change from dark green to black before undergoing 6 washes with DI water. The black GO solution was then dried in a furnace at 60 °C for 12 hours before grinding in a mortar to produce GO powder. The GO powder was then ready for use in the synthesis of rGO.

3.3.2.2 Synthesis of rGO via Tour Method

The GO freshly prepared will undergo a chemical reduction method (Habte et al., 2019), as shown in Figure 3.3, in which the oxygen component will be reduced using ascorbic acid as the reducing agent. The procedure began by diluting 400 mg of GO powder with 50 mL of DI water, and the mixture solution was stirred at 600 rpm for 5 minutes. 4 g of ascorbic acid was added to the mixture, and stirring was continued at a similar speed for 30 minutes at 60 °C. Ascorbic acid will remove oxygen-containing functional groups, turning GO into rGO (Palomba et al., 2022). The mixture solution was then centrifuged at 50000 rpm for 50 minutes to remove the supernatant.

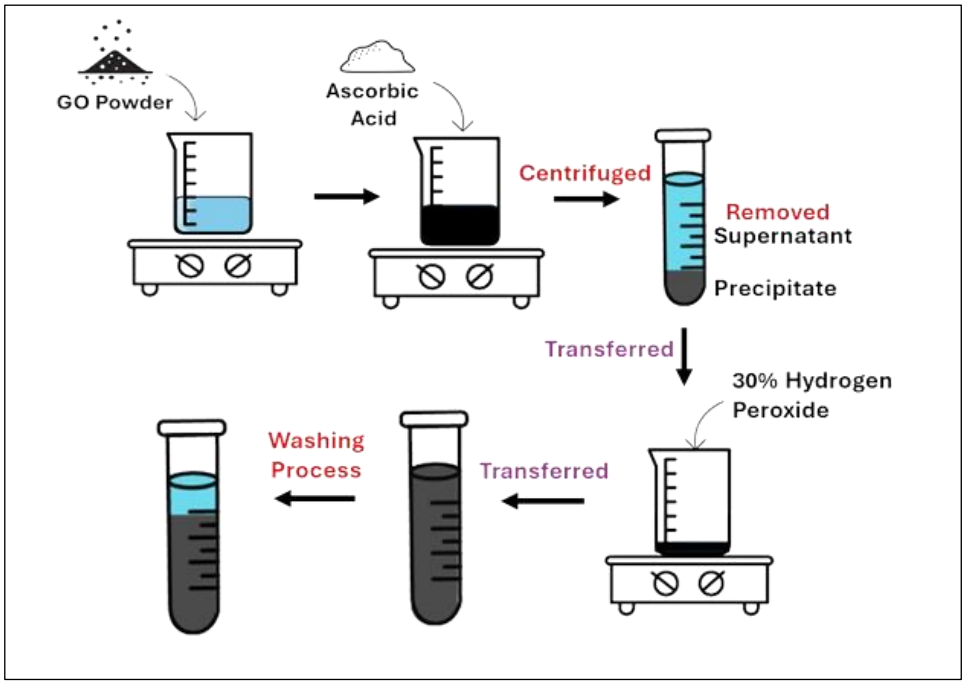

Figure 3.3 Procedure in Synthesizing rGO

The pallets were transferred to the beaker, and 10 mL of 30% H2O2 was added while continuing to stir at 600 rpm and 60 °C for 10 minutes. The H2O2 will further remove any remaining oxygen functional groups from the GO structures. A washing process was then conducted by centrifuging the solution at 50000 rpm, and the supernatant was removed from the centrifuge tube. The ethanol was then filled into the tube with an amount similar to the water that had decanted before. The solution was mixed evenly, and the washing process was repeated twice to remove any residual on the rGO pallet. The washing process was then repeated using distilled water to remove any impurities from the rGO pallets. The washing process using water was repeated 3 times to ensure the rGO was cleaned and ready for further characterisation. Finally, the procedure was repeated by varying the weight of GO and ascorbic acid, and the volume of H_2O_2, as in Table 3.3, to study the effect of each chemical on the synthesis of rGO.

Table 3.3
Parameters Set on Synthesized rGO

Sample ID	GO (mg)	Ascorbic acid (g)	H_2O_2 (mL)
A	500	4	10
B	400		
C	300		

D	200		
E	500	5	10
F		4	
G		3	
H	500	4	12
I			10
J			8

3.4 Phase 2: Fabrications of AgNs Embedded rGO

The AgNs and rGO were physically mixed at a 1:5 ratio (1 part rGO to 5 parts AgNs), and the mixture was vortexed at 3000 rpm for 20 minutes. The mixed solutions were then transferred into the screw-capped bottle and ultrasonicated for 30 minutes at 30 °C to break the rGO into smaller particles. The mixture was then vortexed again to allow the excess AgNs to further mix with the remaining rGO pallets. The rGO-AgNs's physical appearance should be as in Figure 3.4, and the procedure was then repeated with ratios of 1:10, 1:15, and 1:20, as in Table 3.4. Each rGO-AgNs sample with a different ratio was ready for characterisation.

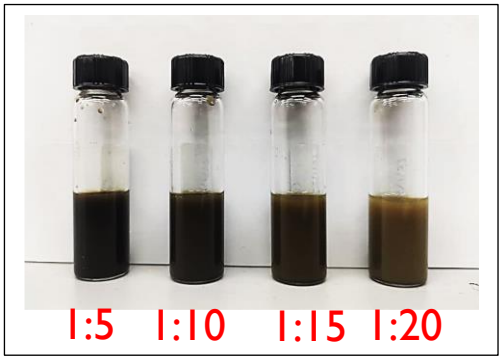

Figure 3.4 Physical Appearance of rGO-AgNs with Ratios of 1:5, 1:10, 1:15, and 1:20

Table 3.4
Parameters on rGO-AgNs with Different Ratios

Sample ID	rGO (mL)	AgNs (mL)
1:5	1.67	8.33
1:10	0.91	9.09
1:15	0.63	9.37

1:20	0.48	9.52

3.4.1 Characterization of AgNs, rGO, and rGO-AgNs on Glass Slide

The optical properties of the samples were characterized using UV-Vis spectroscopy (JASCO V-670 UV-Vis-NIR Spectrophotometer) over the wavelength range 200-1000 nm for AgNs. Nevertheless, UV-Vis analysis was performed on rGO to investigate its optical properties by comparing its peak absorbance intensities with those of GO. Subsequently, the rGO-AgNs composite was subjected to UV-Vis spectroscopy to determine whether rGO genuinely enhances the optical properties of AgNs. All samples were measured in absorption mode using a quartz cuvette with DI water as a reference. The dilution preparation of each sample was conducted at a 99% dilution due to the intense colour of rGO itself. Hence, all samples such as AgNs and rGO-AgNs, will undergo a similar dilution to obtain a reading at a similar state.

The morphological characteristics of the synthesized AgNs were analysed using field emission scanning electron microscopy (FESEM; JEOL JSM-7600F). For analysis, the AgNs suspension was drop-cast onto a clean glass substrate and allowed to dry at room temperature before imaging to confirm the formation of well-defined star-shaped nanostructures. The size distribution of AgNs was analysed using ImageJ (Wayne Rasband, National Institutes of Health, US). Furthermore, SEM analysis (SEM; HITACHI SU3500) was conducted on both GO and rGO with the same sample preparation to investigate their physical morphologies, with rGO expected to exhibit more crinkled features than GO. The internal structure and morphological features of the AgNs were further characterized using transmission electron microscopy (TEM) (Philips CM12), operated at an accelerating voltage of 120 kV. Samples were prepared by drop-casting a diluted AgNs suspension onto a carbon-coated copper grid and drying under ambient conditions prior to imaging.

The hydrophilicity of graphene-based material was measured using a wafer surface analysis system (AST Products, VCA 3000). A droplet of the sample solution was dispensed from a syringe onto a glass slide, forming a sessile droplet. The contact angle between the droplet and the glass surface was then measured. If the recorded contact angle was 90° or less, the bubble is considered hydrophilic; angles ranging from 90° to 150° indicate hydrophobic characteristics (Danish, 2022).

The EDX (HITACHI SU3500) analysis was conducted for each sample of AgNs, rGO, and rGO-AgNs to determine the elemental composition of the samples.

FTIR spectroscopy (Varian 640-IR) was conducted on AgNs, rGO, and rGO-AgNs to characterize their elemental composition and identify any unknown materials within each morphological structure. XRD (Rigaku Ultima IV) analysis, conducted at 40 kV and 40 mA, was performed on AgNs, GO and rGO over the 2θ range of 5° to 80° to characterize the crystal structure of these synthesized materials. The *d-spacing* was calculated by using Bragg's Law as in Equation (3.1), where the d, n, Θ, and λ represent interplanar spacing, reflection order, Bragg angle (half of the peak position), and X-ray

$$d - spacing = \frac{n\lambda}{2sin\theta} \tag{3.1}$$

wavelength. The value of λ produced by the machine is 1.534 nm.

Raman spectroscopy (DXR2xi, Thermo Scientific) analysis was conducted on rGO and rGO-AgNs to evaluate structural disorder and defect density following the reduction process. The intensity ratio of the D band to the G band (I_D/I_G) was analysed to assess changes in defect density and confirm the successful reduction of GO.

3.5 Phase 3: Embedding of rGO-AgNs on the Sensing Probe

3.5.1 Sensing Probe Preparations

Firstly, a 1 m length of fibre optics was cut in half, and the protective layer at each end was removed, as shown in Figure 3.5, leaving only 2 cm of core fibre. The core fibre optics were then cleaned with ethanol to remove any excess cladding particles or dust from their surfaces. The samples were then left in the open air for 10 minutes before being dipped into sensing material solutions.

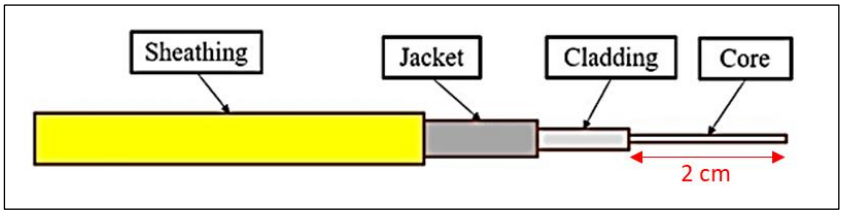

Figure 3.5 Uncladding of Fibre Optics

3.5.2 Embedding the AgNs, rGO, and rGO-AgNs on the Sensing Probe

The bare fibre optics prepared beforehand were dipped into the AgNs solutions, rGO or rGO-AgNs solution (rGO-to-AgNs ratio as in Table 3.4) for 6 hours, then dried in open air at room temperature for 24 hours (Sahudin et al., 2022). The procedure were then repeated by increasing the dipping time into 12 hours and 24 hours to obtain the optimum coating time. The procedure was then repeated using new bare fibre optics that had been prepared for dipping into rGO and rGO-AgNs solutions (rGO-to-AgNs ratio as in Table 3.4), and were ready for further characterisation and signal sensing.

3.5.3 Surface Treatment of rGO-AgNs Embedding the Sensing Probe

Surface treatment was performed on the unclad fibre optic probe prior to the deposition of sensing materials in order to enhance surface activation and improve material adhesion onto the sensing region. Five different surface treatment methods were investigated separately, namely sodium hydroxide (NaOH), silane treatment, ethanol cleaning, chromic acid treatment, and piranha solution treatment. The detailed procedures for each treatment are summarized in Table 3.5.

Table 3.5
Compiled Procedure for Synthesizing Surface Treatment Solutions

Treatments	Methodology
NaOH	0.5g of NaOH was mixed with 1 mL of DI water
Silane	0.5 mL of tris (2-methoxy ethoxy) (vinyl) silane was mixed with 10 mL of ethanol
Ethanol	0.5 mL of ethanol was mixed with 1 mL of ultrapure water
Chromic Acid	0.5 mg of potassium dichromate was mixed with 1 mL of ultrapure
Piranha	7 parts of sulphuric acid was mixed with 3 parts of 30% v/v of hydrogen peroxide

3.6 Phase 4: Embedding the rGO-AgNs-HH on the Sensing Probe

3.6.1 Hybrid Hydrogels

The HH-based sensing materials must be synthesized just before the coating process. Prior to that, chitosan stock was prepared following the previous method (Makhsin et al., 2023), via cross-linking polymerisation, by chemically binding chitosan and agarose using glutaraldehyde as a cross-linker. A 0.25% w/v of chitosan solution was prepared by dissolving 0.05g of chitosan powder with 20 mL of 0.5% v/v of acetic acid. The chitosan solution was stirred at 500 rpm at room temperature for 15 minutes until it turned clear and transparent. The chitosan solution was then filtered through filter paper to remove any undissolved chitosan. Then, a 2% v/v of chitosan stock was prepared by dissolving 0.6 mL of 0.25% w/v chitosan solution with 4.9 mL of distilled water. The chitosan stock was prepared and ready to be mixed with agarose.

A 3% w/v of agarose solution was prepared by dissolving 0.3 g of agarose powder with 10 mL of DI water and the solution was vortexed at 3000 rpm for 10 minutes. The agarose solution was then transferred into the screw cap bottle and the solution was then microwaved without the cap bottle for 10 seconds. The agarose solution should turn transparent over time. The screw cap bottle was then placed on the magnetic stirrer and the solution was stirred and heated at 500 rpm and 90°C for 10 minutes. Next, 5 mL of 2% v/v chitosan stock prepared beforehand was added to 10 mL of 3% w/v agarose solution, and the mixture was vortexed at 3000 rpm for 10 minutes. Then, 12.5 µL of glutaraldehyde was added to the mixed solution, and the stirring and heating were continued at a similar speed and temperature for 15 minutes.

The solution formed a solution-gel structure, and the hydrogels were ready for the fibre-optics samples to be dipped in it for 10 minutes. After 2 hours, the hybrid hydrogels will form a solid gel structure, making them no longer suitable for fibre-optics samples to be dipped into the hydrogels to coat the outer layer of the fibre optics.

3.6.2 Coating the Fibre Optics with rGO-AgNs-HH

The fabrication process began by immersing freshly prepared bare fibre optic probes into the rGO–AgNs suspension. For samples requiring an additional hydrogel layer, the rGO–AgNs-coated fibres were subsequently dipped into freshly prepared HH at room temperature for 10 minutes, followed by air-drying for 20 minutes prior to testing. The same procedure was repeated using new bare fibre probes for the HH–rGO–AgNs sequence and the mixed rGO–AgNs–HH configuration, as summarized in Table 3.6.

Table 3.6
Fibre Optics Dipping Sequence Procedure and Coating Layers

Sample ID	Coating		Descriptions
	1st layer	2nd layer	
rGO-AgNs	rGO-AgNs	-	The bare probe was dipped into rGO-AgNs solutions for 24 hours and was dried in open spaces overnight.
HH	HH	-	The bare probe was dipped into HH for 10 minutes and was dried in open spaces overnight.
rGO-AgNs-HH	rGO-AgNs	HH	The bare fibre was dipped into rGO-AgNs (24 hours) and dried overnight. It was then dipped into HH (10 minutes) and dried overnight.
HH-rGO-AgNs	HH	rGO-AgNs	The bare fibre was dipped into HH (10 minutes) and dried overnight. It was then dipped into rGO-AgNs (24 hours) and dried overnight.
Mixed rGO-AgNs-HH	Mixed		The rGO-AgNs solution and HH were mixed at a 1:1 ratio. The bare probe was then dipped into the mixed rGO-AgNs-HH (10 minutes) and dried overnight.

3.6.3 Characterization of AgNs, rGO, rGO-AgNs, and rGO-AgNs-HH on Sensing Probe

The morphology of the surface of uncladded fibre optic probes was analyzed before and after being embedded with AgNs, rGO, rGO-AgNs, and rGO-AgNs-HH using SEM (HITACHI SU3500). The average core size of the probe was determined from SEM images using ImageJ software. The coating thickness and fibre core diameter were measured at several locations using ImageJ, and the results were reported as mean ± standard deviation to account for measurement variability. Cross-sectional analysis of the embedded fibre optics was performed exclusively on rGO-AgNs-HH to obtain the optimum coating thickness. The end core of the embedded fibre-optics was cleaved using a fibre-optics cleaver (Sumitomo FC-6S) to facilitate this analysis. SEM imaging

was employed to capture the cross-section of the embedded fibre optic, enabling observation and study of the embedded sequence layers in this analysis. EDX analysis was performed to identify the elemental composition of the materials deposited onto the uncladded probe, thus confirming the presence of AgNs, rGO, rGO-AgNs, and rGO-AgNs-HH on the core of the sensor probe.

3.7 Signal Sensing on Embedded Sensor Probe

3.7.1 Signal Performance on The Embedded Sensing Probe

Following the preparation of the fibre-optic sensor configuration (see Figure 1.1 and Appendix 3.2), the end cores on both sides of the embedded fibre were cleaved, leaving only 1 cm of the embedded core. Subsequently, both ends of the embedded core were aligned and fused using a splicer (Sumitomo Type-39 FastCat Core Alignment Fusion Splicer Kit) to restore the fibre-optic cable's continuity, as shown in Figure 3.6. The spliced fibre was then placed on the sensor holder, and the sensor analysis was set up for signal detection. The peak intensity detected by the spectrometer was recorded using Overture software and later compiled together in Excel software to extract the signal sensitivity (RUI^{-1}) and coefficient of determination (R^2).

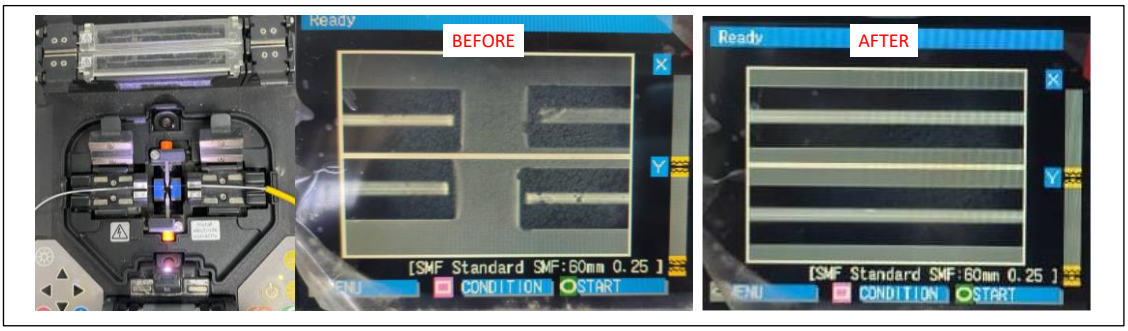

Figure 3.6 Splicing of both fibre optic ends using a fusion splicer prior to signal measurement

The percentage improvement in signal intensity was calculated using Equation (3.2):

$$Signal\ enhancement\ (\%) = \frac{I_{sample} - I_{bare}}{I_{bare}} \times 100\% \qquad (3.2)$$

where I_{sample} represents the measured light intensity from the coated fibre-optic probe, and I_{bare} denotes the light intensity obtained from the uncoated (bare) probe.

3.7.2 RI Detection on The Embedded Sensing Probe

Prior to RI sensing measurements, glycerol solutions of 1%, 3%, 5%, and 10% (v/v) were prepared. The RI of each solution was measured using a refractometer (Fisherbrand) at room temperature. The measured RI values were 1.3334, 1.3339, 1.3367, and 1.3488 for 1%, 3%, 5%, and 10% (v/v) glycerol solutions, respectively. The RI sensitivity using various concentration of glycerol was adopted from (Makhsin et al., 2020). The RI sensitivity of the sensor was calculated from the slope of the light intensity shift versus RI plot and expressed in nm/RIU following the Equation (3.3) as follows:

$$RI\ sensitivity = \frac{\Delta\lambda}{\Delta n} \tag{3.3}$$

The Δλ and Δn in the equation represents the shift in the light intensity peak (a.u.) and change in refractive index (RIU). The RI detection procedure began by dropping DI water onto the microfluidic channel (see Appendix 3.4) coated with AgNs, and the peak intensity was recorded 5 minutes after the drop. The procedure was then repeated by replacing the DI water with 1, 3, 5, and 10% v/v solutions. The peak intensity recorded was compiled in Excel software, and the RI sensitivity (RUI) and coefficient of determination (R^2) were recorded. All RI measurements were performed in triplicate, and the results are reported as mean ± standard deviation. The standard deviation of the three measurements was used to generate error bars and to evaluate the repeatability and uncertainty of the sensor response. Moreover, the Ocean Optics spectrometer used in this study has an instrumental wavelength uncertainty of ±0.5 nm.

3.7.3 Recovery and Reusability Evaluation on The Fibre Sensor

To evaluate the reversibility and recovery performance of the fabricated fibre optic sensors, a washing procedure was introduced between refractive index (RI) measurements. This method is adopted from (Zheng et al., 2021) by having the fibre undergo repetitive tests to confirm its reusability. Prior to exposure to glycerol solutions, the coated fibre was rinsed with DI water to remove any dust particles or loosely attached contaminants on the sensing surface. After washing, DI water was dropped onto the microfluidic channel, and the peak intensity was recorded after 5 minutes. This value was considered the reference peak after washing. Subsequently, 1%

(v/v) glycerol solution was introduced into the microfluidic channel, and the corresponding peak intensity was recorded after 5 minutes. After measurement, the fibre surface was washed again with DI water to remove residual glycerol solution. The peak intensity was recorded once more to determine the extent to which the signal returned to its initial reference value. The recovery error on the washing process after 1% (v/v) glycerol solution was measured following Equation (3.4). The same washing and measurement procedure was repeated sequentially for 3%, 5%, and 10% (v/v) glycerol solutions. For each concentration, the recovery peak intensity after washing was compared with the initial DI water reference peak to evaluate the recovery performance.

$$Recovery\ Error\ \% = \frac{|I_{Ref} - I_{Rec}|}{I_{Ref}} \times 100\% \quad (3.4)$$

where I_{Ref} represents the reference peak intensity before glycerol exposure, and I_{Rec} denotes recovered peak intensity after washing.

3.8 Phase 5: Binding Kinetics and Porosity of Sensor Probe

3.8.1 Coating Sequence Configuration

Upon introducing the HH into the optical fibre coated with rGO-AgNPs, the optimal sequence of the hydrogel and rGO-AgNPs (1:5) layers must be determined to determine which layer will be integrated first. The method for integrating HH with rGO-AgNs onto optical fibres will be determined by studying the sequence of coating layers, as shown in Figure 3.7. The first option is to introduce rGO-AgNs to the bare surface as the first layer with HH on the outer layer of the sensing medium, as in Figure 3.7(a). The purpose of this method is to have HH serve as a protective layer and a binding interface for bioreceptor-protein interactions, while rGO-AgNs serve as the inner sensing layer to enhance the sensitivity and linearity of detection.

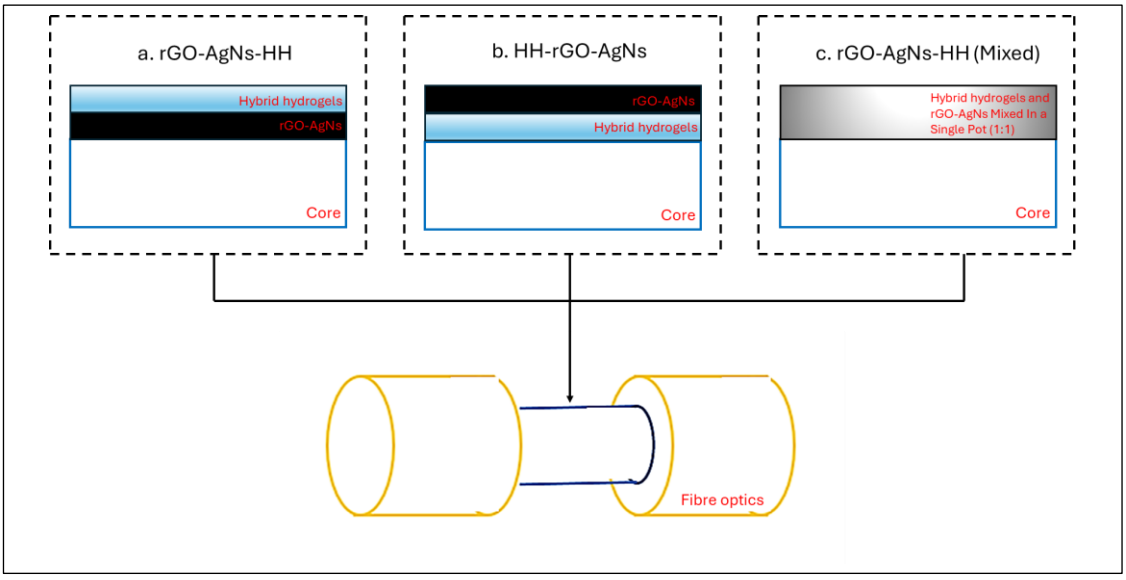

Figure 3.7 Integration of Hybrid Hydrogels and rGO-AgNs on the Surface of Optical Fibre

Meanwhile, by switching the layer position between the sensing medium and HH, as in Figure 3.7(b), the inner-layer HH assists the rGO-AgNs in binding to the fibre surface while allowing the rGO-AgNs to focus solely on detection. Finally, a method for mixing both rGO-AgNs and HH in a single pot at a 1:1 ratio was prepared as shown in Figure 3.7(c) to combine all functionalities, such as protective layering, a binding interface, and enhanced detection sensitivity, into a single medium.

3.8.2 Porosity of Sensor Probe

Binding kinetics is the study of the rate at which molecules or particles interact and bind (McCann et al., 2025). Meanwhile, porosity refers to the presence of voids, or pores, within sensing materials (Chen et al., 2023). The pore characteristics of the hydrogel coating containing rGO–AgNs were evaluated by monitoring changes in peak light intensity upon exposure to solutions with an identical RI value. 1 %v/v of glycerol was first introduced, followed by 0.75 %w/v of bovine serum albumin (BSA) prepared in DI water, both adjusted to the same RI value (n = 1.3346). Since the bulk refractive indices were equivalent, any variation in signal intensity would be attributed to molecular diffusion and interaction within the hydrogel network. If comparable peak intensities were observed for both glycerol (a small molecule) and BSA (a macromolecule), this indicates that the hydrogel possesses sufficiently large, interconnected pores to permit the diffusion of both small and large species,

demonstrating its suitability for biosensing applications (Makhsin et al., 2020). Finally, DI water was flushed through the system to remove residual BSA and prevent protein entrapment within the hydrogel matrix.

3.8.3 Detection of Protein Interaction on the Sensing Probe

The protein detection procedure began by cleaning the surface of the embedded core by dropping 0.01 M phosphate-buffered saline (PBS) onto the fibre, and the PBS remained in the sensor holder for 3 minutes to unbind any biomolecules on the surface of the embedded fibre optics, as shown in Figure 3.8 (A). The PBS solution was then removed from the microfluidic flow cell, and 0.1 mg/mL streptavidin was dropped onto the sensor holder and incubated for 15 minutes.

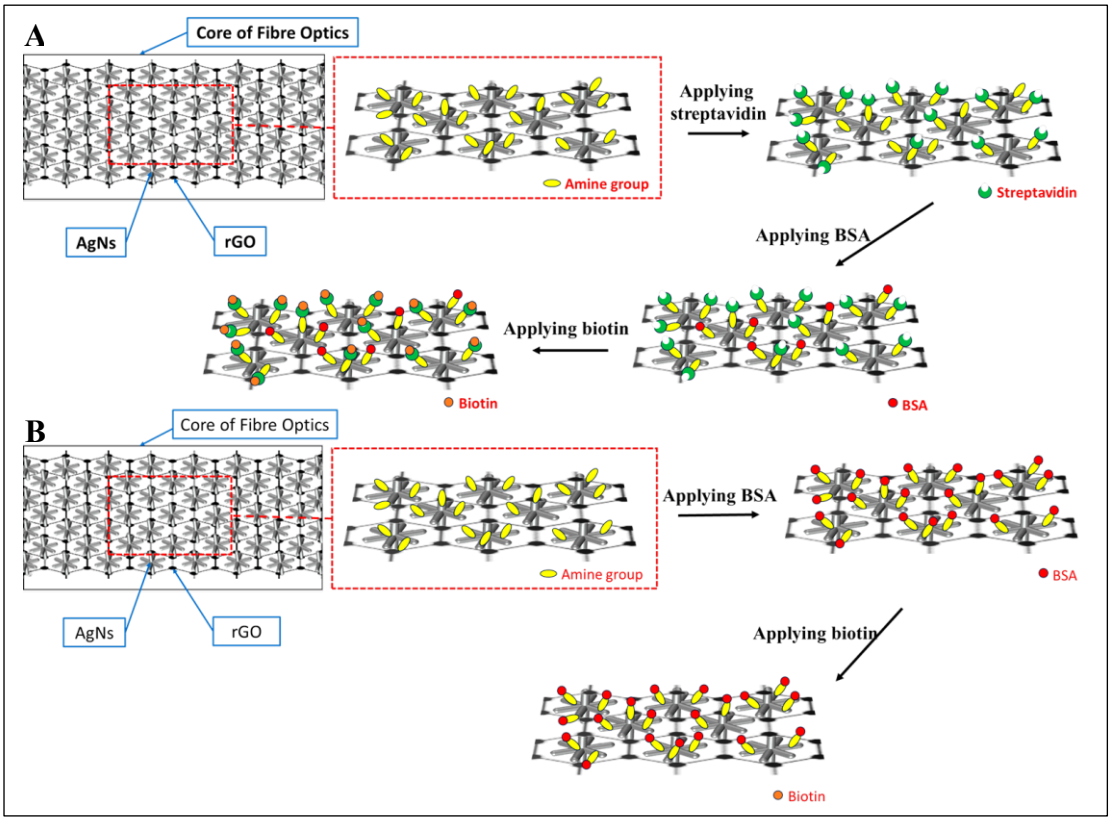

Figure 3.8 Procedure of (A) Protein Detection and (B) Specificity of Protein Detection

Streptavidin was first introduced onto the functionalized fibre-optic surface to serve as the biorecognition interface and allowed to immobilize. The probe was subsequently rinsed with phosphate-buffered saline (PBS) for 3 minutes to remove unbound streptavidin. To block nonspecific binding sites, 10 mg/mL bovine serum

albumin (BSA) was introduced and incubated for 10 minutes, followed by PBS washing to remove excess BSA. Subsequently, 0.1 mg/mL biotin was applied to the sensing region and incubated for 15 minutes to enable specific streptavidin–biotin binding. After each step, PBS was flushed through the flow cell to eliminate unbound molecules.

Spectral responses were monitored in real time using an Ocean Optics spectrometer, and peak intensity and wavelength shifts were recorded. A progressive wavelength shift following biotin introduction confirmed successful streptavidin–biotin interaction at the fibre surface, indicating effective protein detection.

3.8.4 Specificity of Protein Detection

The experiment was repeated as described in Section 3.8.2, but without streptavidin immobilization, as illustrated in Figure 3.8(B). This control experiment was conducted to evaluate whether the embedded fibre-optic sensor could detect biotin in the absence of a biorecognition element. In this configuration, 0.1 mg/mL of biotin was directly immobilized on the sensing surface without prior streptavidin functionalization.

Since no specific binding interface was present, no significant wavelength shift was expected upon exposure to biotin. The absence of a spectral shift would confirm that the sensing response observed in the functionalized system was due to a specific streptavidin–biotin interaction rather than nonspecific adsorption. This approach therefore, validates the specificity of the biosensing platform.

CHAPTER 4
RESULTS AND DISCUSSION

4.1 Overview

This chapter presents the results of the optimisation, synthesis, and characterisation of AgNs, rGO, the rGO–AgNs composite, and the rGO–AgNs–HH, and evaluates their suitability as sensing materials integrated into fibre-optic sensor platforms for protein detection. AgNs were synthesized via a single-step reduction method, where the hydroxylamine concentration was varied to achieve nanostars with the longest spike morphology. rGO was synthesized using the modified Tour method, with systematic investigation of key parameters including the role of GO precursor, ascorbic acid concentration, and H_2O_2 volume.

The synthesized AgNPs samples were characterized using UV–Vis spectroscopy, FTIR, XRD, Zetasizer particle size analysis, and TEM, while the synthesized rGO samples were characterized using FESEM/SEM, EDX, zeta potential analysis, contact angle measurement, UV–Vis, FTIR, XRD, and Raman spectroscopy. The rGO–AgNs nanocomposite was prepared at mixing ratios of 1:5, 1:10, 1:15, and 1:20 (rGO:AgNs) and characterized using SEM, EDX, UV–Vis, FTIR, and Raman spectroscopy to determine the optimal composition prior to fibre-optic integration.

Subsequently, fibre-optic probes were fabricated by encapsulating rGO, AgNs, and rGO–AgNs (at different ratios). Surface treatment of the bare fibre using chromic acid, ethanol, NaOH, piranha solution, and silane was conducted before deposition of the optimized rGO–AgNs sample. Based on optical signal performance, the optimal rGO–AgNs formulation was further incorporated with an agar–chitosan HH. The coating sequence and layer configuration were systematically evaluated. Probe characterization was carried out using SEM, EDX, and refractive index (RI) sensitivity measurements under a fibre-optic sensing configuration to identify the most suitable design for biosensing applications.

Finally, the sensing performance was assessed through streptavidin–biotin biorecognition to evaluate sensitivity, stability, and specificity of the developed fibre-optic biosensor platform.

4.2 Phase 1: Synthesis and Characterization of AgNs and rGO

4.2.1 AgNs

In this study, a single-step chemical reduction method was used to synthesize AgNs involving a few chemicals as described previously in section 3.3.1. By understanding the role of each chemical in the synthesis process, the formation of AgNs can be tuned to produce optimized nanoparticles. The roles of other chemicals involved, including silver nitrate, sodium citrate tribasic, and sodium hydroxide, have been previously optimised in our previous work (Roslan et al., 2022), which found that $8x10^{-4}$ M of silver nitrate, 0.045 M of sodium citrate tribasic dehydrate, and 0.05 M of sodium hydroxide were optimal. While hydroxylamine is recognized as the main reducing agent, its optimal concentration remains undetermined. Hence, this study will be continued by controlling the concentration of hydroxylamine to complete the optimization of tuned AgNs.

Figure 4.1 shows the optical properties of the synthesized AgNs samples after varying the concentrations of hydroxylamine, investigated using UV-vis spectroscopy. The result shows the peak for the AgNs sample O has the highest peak intensity at 392 nm, followed by AgNs samples N, M, and L, with peak intensities recorded at 390 nm, 376 nm, and 372 nm, respectively.

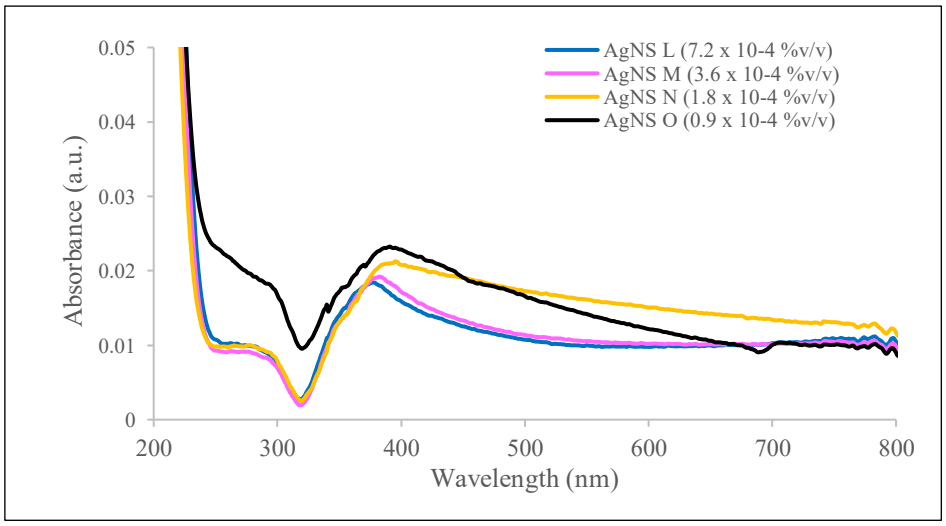

Figure 4.1 UV-Vis on AgNs Samples Synthesized Using Various Concentrations of Hydroxylamine

The peak intensity trend shows a blue shift as the hydroxylamine concentration increases. The wavelength spectrum correlates with the size and shape of nanoparticles (Ameer et al., 2016). These changes indicate that the star-spike of AgNs expanded as more new nucleation was discarded with a limited amount of reducing agent present. Here, hydroxylamine was used as a reducing agent, in which the silver ion (Ag^{+}) was reduced to metallic silver (Ag^{0}) by donating electrons, causing the silver atoms to aggregate and grow on the surface of the seed particle (Mikhailova, 2020), eventually forming a nanostar structure.

In line with the findings of (Garcia-Leis et al., 2017), the lower component observed in the UV-Vis spectra at ~360-380 nm can be attributed to the quadrupolar plasmon resonance of the nanostar's core. Additionally, the component observed at ~415-420 nm may be due to the transversal resonances of the tips or residual quasi-spherical nanoparticles. The dipolar plasmon resonances of nanostars with a diameter of 400 nm are expected to appear in the 600-700 nm range for Ag, as indicated by single-nanostar analysis using an enhanced dark-field technique (Garcia-Leis et al., 2017). However, the absence of clear resonances at these wavelengths for samples L, M, and N can be attributed to two possible reasons. Firstly, there might be a high degree of heterogeneity in the morphology of the resulting nanoparticles. Secondly, significant aggregation of nanoparticles could lead to larger aggregates, which may explain the observed increase in extinction at higher wavelengths in these samples.

AgNs sample N exhibits strong peak intensity and greater morphological uniformity compared to the other samples. The low-wavelength band observed at 363-370 nm corresponds to quadrupolar plasmon resonances, while the second peak observed at 680-750 nm is associated with dipolar plasmon modes. These findings are consistent with previous research (Garcia-Leis et al., 2017) where single nanostars were successfully formed. The branches in star-shaped nanoparticles generate localized electromagnetic field enhancements known as "hot spots", facilitating strong light interactions. Therefore, the size and number of branches in AgNs are crucial in determining the intensity of these interactions. High absorbance within the desired wavelength range, along with a narrow peak width, indicates enhanced optical properties and strong plasmonic resonances. Figure 4.1 illustrates an increase in peak intensity (absorbance) in the UV-Vis spectroscopy for AgNs sample O, indicating a stronger light interaction compared to the other samples.

Morphological analysis on AgNs samples L, M, N, and O was conducted using TEM (see Figure 4.2 a, b, c, and d) and FESEM (see Figure 4.2 e, f, g, and h). TEM analysis was conducted to measure the star-spike length, resulting in values of 198.75 ± 69.03 nm for sample L, 166.58 ± 77.04 nm for sample M, 313.26 ± 66.26 nm for sample N, and 352.62 ± 59.72 nm for sample O. Based on the image in Figure 4.2 (a, b, c, and d), a distinct change in the structure of AgNs can be seen as the concentration of hydroxylamine decreases. This indicates that a reduction in hydroxylamine concentration leads to the formation of star-shaped nanoparticles with longer spikes. The morphological differences are clearly visible in Figure 4.2 (a) and Figure 4.2 (e) for sample L, where fewer star-shaped structures and more irregular shapes, including a mix of round forms and short, coral-like spikes, were observed. This can be attributed to the higher concentrations of the reducing agent, which promote increased nucleation and thus reduce the formation of star-shaped structures.

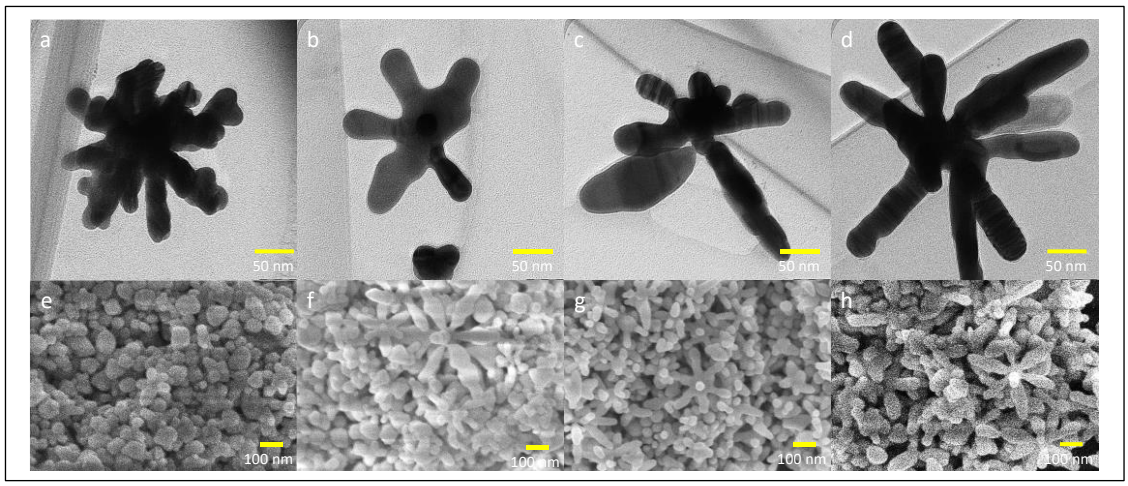

Figure 4.2 TEM Images (a-d) and FESEM Images (e-f) of the Synthesized AgNs Samples with Sample L (a and e), Sample M (b and f), Sample N (c and g), and Sample O (d and h)

In comparison between samples M and N, sample N exhibits a longer spike compared to sample M, indicating that sample N interacts more with light due to the surface area of AgNs. This finding aligns with the result from UV-vis spectrum analysis in Figure 4.1, where the increase in branch length of the spike is attributed to the increase in peak intensity of the UV-Vis spectrum. Moreover, the shape of a star in sample O is more consistent in Figure 4.2(h), with the branch length of the spike recorded being longer than in sample N. The morphological characteristics and

distributions of AgNs can be further examined using FESEM analysis, as shown in Figure 4.2 (e, f, g, and h). This analysis allows for the assessment of overall uniformity and aggregation behavior, which may correlate with the absorption peak observed in the UV-vis spectrum. It can be seen that the AgNs sample O has a higher abundance of star-shaped particles compared to other samples.

Due to its superior morphological uniformity in terms of star shape, AgNs from Sample O, where 0.9×10^{-4} M of hydroxylamine was used to mix together with 0.05 M of NaOH, 8×10^{-4} M of silver nitrate, and 0.045 M of sodium citrate tribasic dehydrate, were selected as the most optimized of tuned AgNs. The consistent, well-defined star shapes in sample O make it an ideal candidate for integration into the graphene families.

4.2.2 rGO

4.2.2.1 Effect of the Amount of GO Precursor

rGO synthesized with changes in the amount of GO were set at 500 mg (rGO sample A), 400 mg (rGO sample B), 300 mg (rGO sample C), and 200 mg (rGO sample D) as the first parameters to determine whether the increase in GO composition will affect the physical changes of the rGO structure and characteristics. The optical properties of the synthesized rGO A, B, C, and D versus their GO precursor were presented in Figure 4.3.

Based on the results obtained, GO exhibits a peak absorption in the UV region at ~234 nm wavelength due to the presence of π-π* transitions in the conjugated carbon-carbon bonds. However, as the oxygen-containing functional group of rGO was reduced, the peak intensity decreased, and the first peak shifted slightly to the right toward ~241 nm. The result also shows that the absorbance intensity of the rGO (rGO Sample A, B, C, and D) decreased as the weight of GO was reduced. With the amount of GO decreasing, the composition of the graphene structure within the rGO decreases, suggesting a smaller amount of the composite interacts with light as the laser spectrometer passes through the samples.

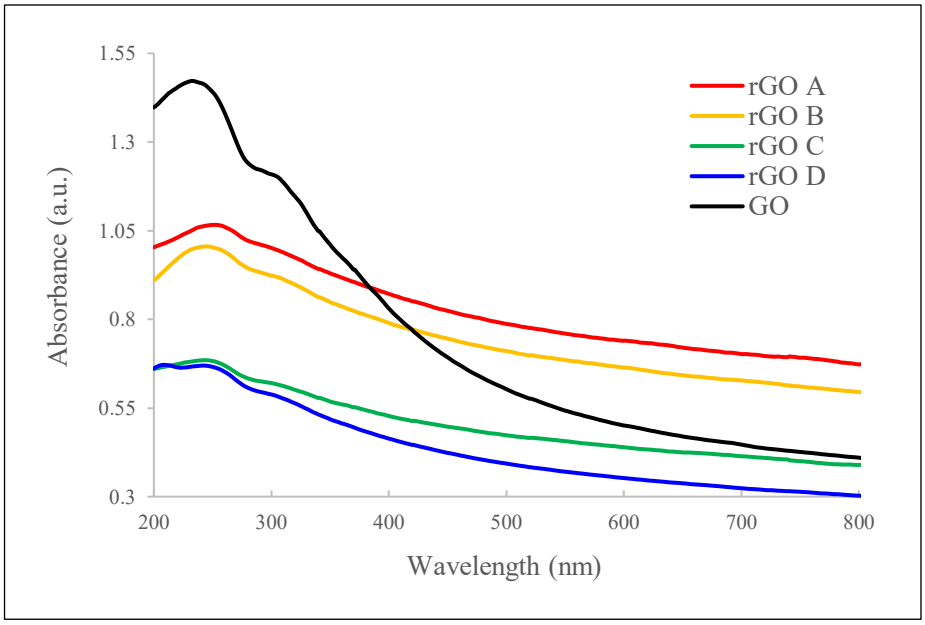

Figure 4.3 UV-vis Spectrum on rGO with Different Amounts of GO

Despite rGO sample A showing higher intensity, rGO sample B produced the sharpest light peak intensity at 241 nm wavelength compared to other samples. Previous researchers attributed the peak observed at 300 nm to π–π* transitions of C=O bonds (Zhang et al., 2022). As the GO reduced, the peak GO weakened, resulting in the π–π* transitions of aromatic C–C bonding at 270 nm (Perumal et al., 2022). These findings confirm a successful reduction of GO, suggesting the absence of restoration of electron conjugation in graphene. Therefore, the obtained results where the second peak of rGO at ~308 nm wavelength weakened also align with previous research, confirming the reduction of GO, but indicating a lack of restoration of graphene conjugations.

SEM analysis was conducted on GO and all rGO samples in Figure 4.4 to study and characterize their morphological structures. The results show that the structures of all rGO samples exhibit more crinkle/wrinkle features than those of the GO sample. Previous researchers state that the wrinkle feature on rGO originates from side effects of oxygen removal in the graphene structure and from graphene-layer stacking during recovery (Liu & Speranza, 2021). From the results obtained in Figure 4.4, rGO samples A, B, C, and D match the statement before indicating a successful reduction of GO. However, among the rGO samples, rGO B (see Figure 4.4c) exhibits more wrinkle features, indicating a clear multi-layer graphene structure that stacks on top of each other, forming a hollow graphene structure.

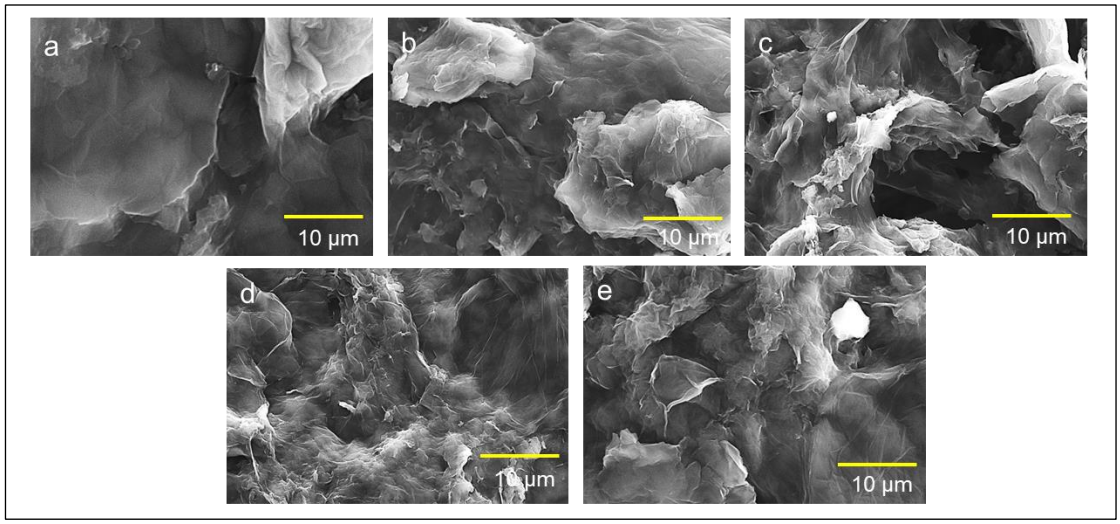

Figure 4.4 SEM Images of (a) GO and (b-e) rGO Samples with (b) Sample A, (c) Sample B, (d) Sample C, and (e) Sample D

Moreover, the rGO A, rGO C, and rGO D images show that the graphene has a smaller amount of graphene layer stacking on top of each other (less crinkle feature) and no hollow was seen on the surface structure, indicating the rGO was not reduced completely. These findings show that as less amount of GO powder is used in the synthesis process, the lower the concentration of GO when mixed with distilled water. Hence, fewer defects of GO were restored, indicating fewer crinkled features observed in SEM imaging. Subsequently, the excessive GO powder might result in the concentration of GO being too strong, causing the reducing agent unable to reduce the GO completely. Hence, this discovery suggests the reason why the peaks of the UV-Vis spectrometer were weakened as the concentration of GO was reduced (see Figure 4.3).

FESEM was also conducted to compare the morphology of graphite, GO, and rGO sample B at higher magnification, as seen in Figure 4.5, thereby enabling understanding of changes across multiple processes. The figure shows that the graphite structure has a rough flake-like form, as in Figure 4.5 (a). However, during the oxidation process, the interlayer space between the graphite layers increases due to the insertion of oxygen functional groups. This expansion will weaken the interlayer forces, allowing the exfoliation process to convert graphite to GO. This process which results in an increase of interlayer spaces and π-π stacking disruption causes the wrinkle effect to appear as in Figure 4.5 (b). As the reduction process began, the interlayer spacing began to increase due to sp^2 carbon breaking up with the removal of the oxygen group and the

strong restoration of the π-conjugated structure. The reduction of the oxygen group causes the graphene layer to break up even more and recover by itself through a stacking layer structure to form a multi-layered rGO as seen in Figure 4.5(c).

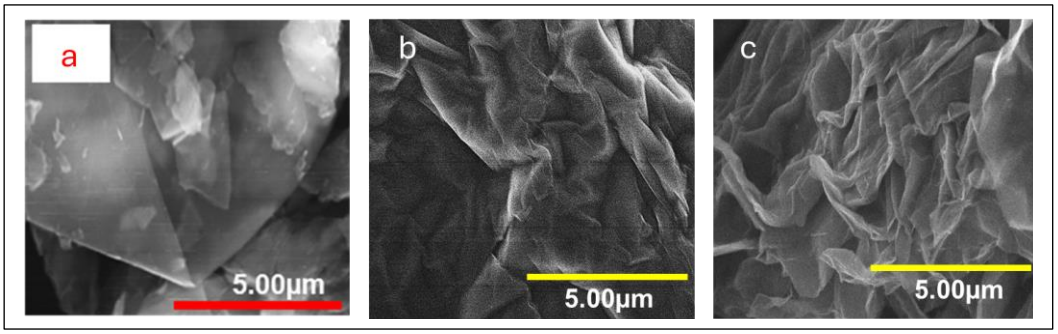

Figure 4.5 Morphological Structure of (a) Graphite (Sahudin et al., 2021), (b) GO, and (c) rGO B under FESEM Imaging

This result is in line with (Adotey et al., 2025), where the rGO exhibits more crinkle features than GO due to the restoration of rGO's π–π conjugated structure. The sp^2 carbon network of graphene was disrupted during GO reduction, leading to structural defects and distortions in the GO sheets. These defects were then restored by combining the π–π conjugated structure, forming a crinkled structure that frequently appears on the rGO surface. Hence, the obtained result for rGO sample B met the characteristics described earlier, indicating that GO was successfully removed.

The element composition of GO and all rGO samples was determined by EDX to quantify the carbon and oxygen content in each sample. Their carbon-to-oxygen (C/O) ratios will quantify how much oxygen composition was reduced and the composition's content. Based on the results obtained in Table 4.1, the C/O ratio of GO was recorded at 0.5267, indicating a high content of oxygen functional groups inside the graphene structure of GO. rGO sample A shows the highest value of C/O ratio with a record of 1.0747, followed by rGO sample B, C, and D with a ratio value recorded at 1.0305, 0.9802, and 09455.

Table 4.1
EDX Analysis Results on GO and rGO Samples A, B, C, and D

Atomic weight percentage (at.%)	GO	rGO A	rGO B	rGO C	rGO D
Carbon, C	34.5	51.8	50.7	49.5	48.6
Oxygen, O	65.5	48.2	49.2	50.5	51.4
C to O Ratio (C/O)	0.53	1.07	1.03	0.98	0.94

All rGO samples show an increase in C/O ratios, indicating a successful reduction of oxygen functional groups in the graphene structure of rGO. The increase in the C/O ratio from GO to rGO has been reported by previous researchers, who attribute it to the reduction of oxygen functional groups in the graphene structure (Liu & Speranza, 2021). A previous study by Chasanah et al. reported an increase in the C/O ratio from 1.63 (GO) to 2.77 (rGO), indicating a reduction in oxygen functional groups in the graphene lattice (Chasanah et al., 2022). The increase in value signifies a high removal of the oxygen group and strong restoration intensity of sp^2-bonded carbon.

The crystallinity of GO and rGO was studied using XRD to gain an insight into their graphitic structural properties. Figure 4.6 shows the GO manages to produce a high peak intensity at the 001 planes ($2\theta=10°$), following the JCPDS code 01-0646. These peaks indicate that the GO contains high oxygen-containing functional groups. For rGO formation, as the oxygen functional group of GO was reduced, the peak in the plane (001) should have been removed due to the reduction of the oxygen functional group and the appearance of a new peak in the plane (002) at a diffraction angle (2Θ) of 26.6° (Sieradzka et al., 2021).

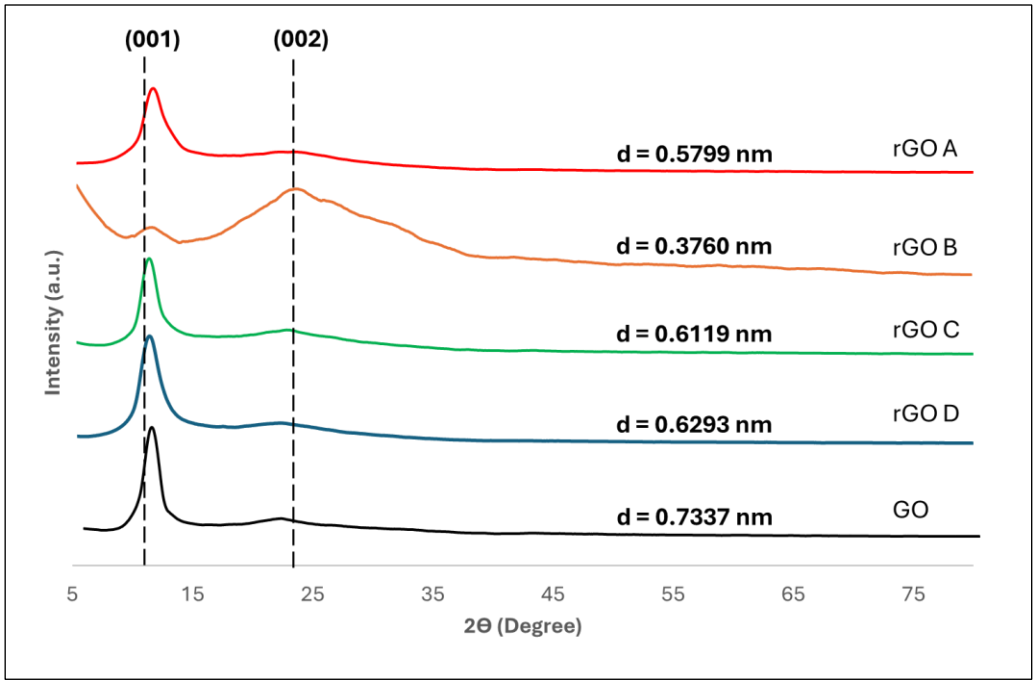

Figure 4.6 XRD Results on GO and rGO Samples A, B, C, and D

The peak in plane (002) represents the successful reduction of GO and the restoration of a graphitic-like structure, showing a decrease in the interlayer spacing from the GO state back towards that of graphite (Ganguly et al., 2011). The effect of removal also caused the graphene sheets to re-stack due to van der Waals forces, resulting in the formation of a thicker layer (Dhakate et al., 2011). Hence, the XRD peak pattern of rGO sample B shows great similarity to the pattern described by previous researchers' findings compared to rGO samples A, C, and D. The samples of rGO A, C, and D show that the peak in plane (001) (2θ =12°) shifted slightly to the right indicating the rGO is not fully reduced and this might explain the morphologies obtained from SEM analysis.

Bragg's Law equation was also calculated based on the peak GO to obtain the interlayer spacing (*d*) to understand the structural condition of GO. The *d-spacing* represents the average distance between the layers of graphene within the GO. The *d-spacing* of GO was measured at 0.7337 nm, consistent with previous studies reporting a value of approximately 0.782 nm (Kumar et al., 2018). This spacing is attributed to the presence of oxygen-containing functional groups such as hydroxyl, epoxy, and carboxyl groups. Subsequently, the d-spacing of the rGO result obtained was recorded with a value of 0.5799 nm for rGO sample A, 0.3760 nm for rGO sample B, 0.6119 nm for rGO sample C, and 0.6293 nm for rGO sample D. Among these, rGO sample B

exhibited the closest *d-spacing* value and structural features consistent with the typical characteristics of rGO, indicating a more effective reduction process.

Zeta potential was studied and measured on the GO and rGO samples A, B, C, and D by applying the electrostatic potential at the slipping plane of a particle in a colloid system. Based on the result obtained in Figure 4.7, the zeta potential of GO was recorded at with a value of –26.7 mV, which met the requirement of the GO, where the zeta potential value should be in the range from –20 mV to –40 mV (Sezer et al., 2019). Meanwhile, the zeta potential value of rGO sample A was recorded with the value of –31.3 mV, followed by rGO sample B with a value of –35.3 mV, rGO sample C with a value of –-34.5 mV, and rGO sample D with a value of –30.6 mV. The recorded value of rGO samples A, B, C, and D falls within the expected requirement, where the range should be between –30 mV to – 60 mV as reported by (Yu et al., 2017). Furthermore, previous researchers also managed to produce a similar pattern where the value of enhanced rGO, which is −47.0 mV increases from GO with a value of –35.9 mV, indicating an enhancement in the colloidal stability of rGO (Cao et al., 2016). These statements are also in agreement with Kepekçi et al., where the Zeta potential values that are more negative than –30 mV are considered to form a stable suspension due to interparticle electrostatic repulsion (Kepekçi et al., 2021).

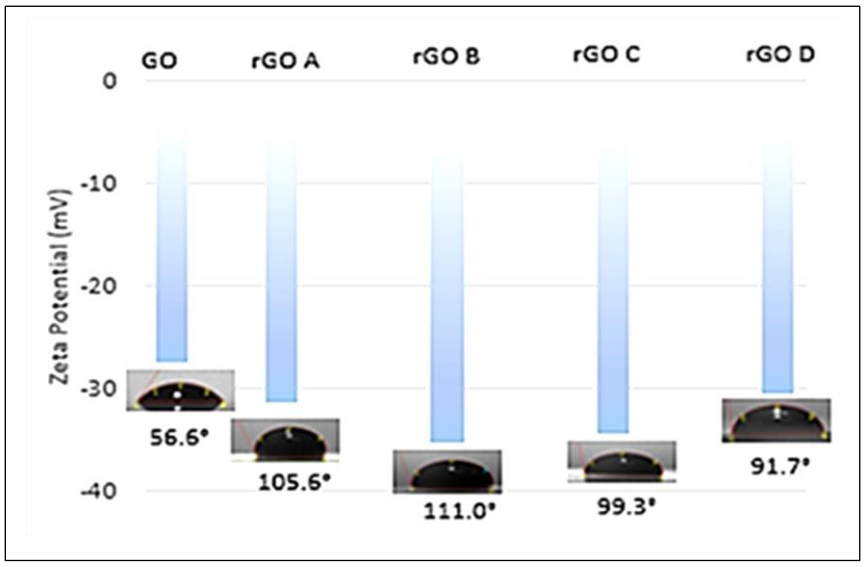

Figure 4.7 Zeta Potential and Contact Angle of GO and rGO A, rGO B, rGO C, and rGO D

The relation between the Zeta potential value and the hydrophobicity of rGO can be proved by the findings from (Kumar et al., 2018) where the increase in hydrophobicity is due to the increase in aggregation tendency of rGO rather than decreased surface charge negativity. Therefore, contact angle analysis was conducted to further confirm the hydrophilicity of GO and rGO. Figure 4.7 (inset) shows the result obtained by dropping a droplet of the sample on the glass plate, indicating that the angle of the GO bubble was recorded at 56.6°. Meanwhile, the sample rGO sample A was recorded with a side angle of 105.6°, followed by rGO sample B at 111.0°, rGO sample C at 99.3°, and rGO sample D at 91.7°. According to contact angle analysis, the sample surface is considered hydrophilic when the contact angle is less than 90°, indicating good wettability (Law, 2014). However, the sample surface is hydrophobic when the angle is recorded higher than 90° (Law, 2014). The results show that all rGO samples exhibit angles greater than 90°, indicating hydrophobic characteristics. Among them, rGO B shows the highest Zeta potential, as confirmed by contact angle analysis.

A physical observation of the rGO samples was conducted after 24 hours, and the results are shown in Figure 4.8. The purpose of leaving the sample in normal temperature conditions for 24 hours is to observe the changes in rGO within the solution. The results show that the graphene within the rGO samples A, B, and C was naturally separated from the solution due to the hydrophobicity of the graphene. Moreover, the amount of graphene separated reflected the amount of graphite used during the synthesis process (see the red arrows).

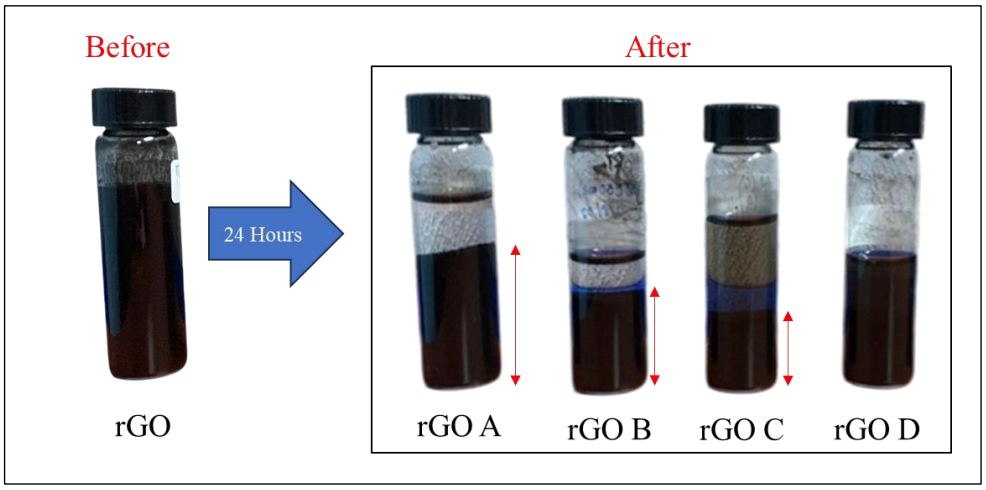

Figure 4.8 Physical Observation of the rGO Samples A, B, C, and D After 24 Hours

However, the graphene within the rGO sample C is not fully separated, as indicated by the supernatant's unclear, transparent colour. Subsequently, the rGO sample D, where 200 mg of graphite was used in the synthesis process, shows that the graphene within the solution didn't naturally fall after 24 hours, indicating the GO is not fully reduced However, the graphene within the rGO sample C is not fully separated, as indicated by the supernatant's unclear, transparent colour. Subsequently, the rGO sample D, where 200 mg of graphite was used in the synthesis process, shows that the graphene within the solution didn't naturally fall after 24 hours, indicating the GO is not fully reduced (Some et al., 2013). These findings align with the result obtained from contact angle analysis, where the angles recorded for rGO samples C and D which is less than 100°, suggesting that the samples are weak in hydrophobicity. Meanwhile, as the contact angle increases above 100°, the samples become more hydrophobic, allowing the graphene to naturally separate from the water, leaving only a clear, transparent supernatant.

The GO and rGO samples A, B, C, and D will then undergo FTIR analysis to understand material composition within the structural form of graphene, as seen in **Error! Reference source not found.**. From the result obtained, the GO composition consists of a broad peak of C=C at ~1635 cm^{-1}, C=O at ~1829 cm^{-1}, and O-H at ~3326 cm^{-1}. Theoretically, upon the reduction process, the appearance of the peak C=O and O-H from GO should be weakened due to the removal of the oxygen functional group (Liu & Speranza, 2021). Moreover, with the reduction of C=O, the appearance of C=C results from the recovery of sp^2 hybridisation that was broken during the removal of oxygen-functional groups. The appearance of C=C indicates that the rGO is fully stabilized after the recovery process. These findings align with the result obtained from contact angle analysis, where the angles recorded for rGO samples C and D which is less than 100°, suggesting that the samples are weak in hydrophobicity. Meanwhile, as the contact angle increases above 100°, the samples become more hydrophobic, allowing the graphene to naturally separate from the water, leaving only a clear, transparent supernatant.

The GO and rGO samples A, B, C, and D will then undergo FTIR analysis to understand material composition within the structural form of graphene, as seen in Figure 4.9. From the result obtained, the GO composition consists of a broad peak of C=C at ~1635 cm^{-1}, C=O at ~1829 cm^{-1}, and O-H at ~3326 cm^{-1}. Theoretically, upon the reduction process, the appearance of the peak C=O and O-H from GO should be

weakened due to the removal of the oxygen functional group (Liu & Speranza, 2021). Moreover, with the reduction of C=O, the appearance of C=C results from the recovery of sp^2 hybridisation that was broken during the removal of oxygen-functional groups. The appearance of C=C indicates that the rGO is fully stabilized after the recovery process.

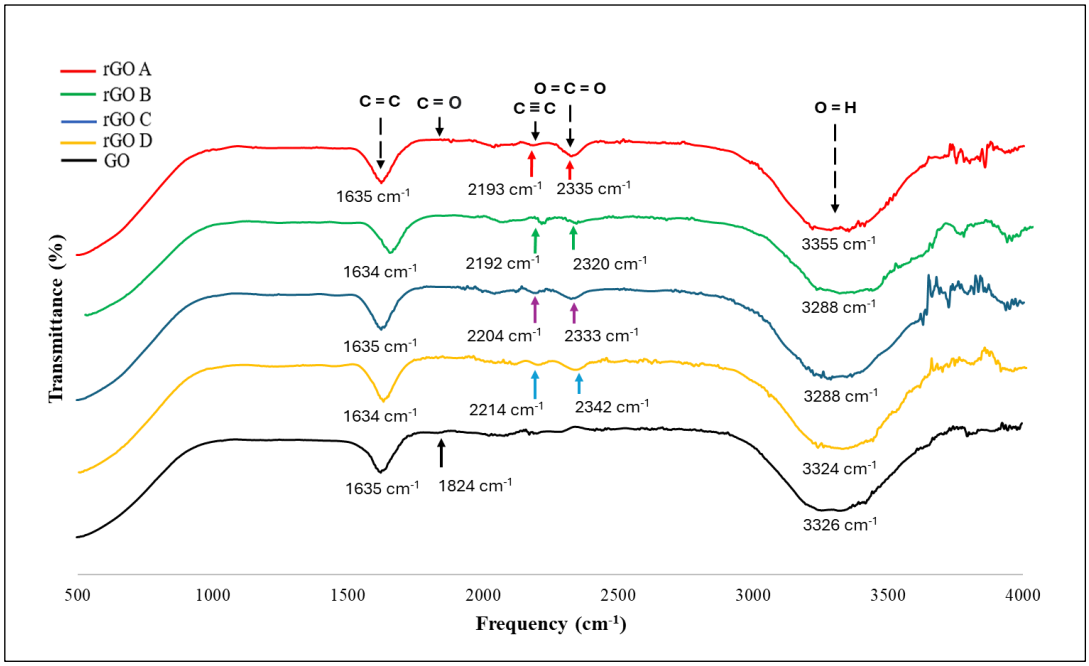

Figure 4.9 FTIR Analysis on GO and rGO Samples A, B, C, and D

However, the GO spectrum obtained shows a broad C=C composition, suggesting the GO is already in a stable sp^2-hybridized carbon honeycomb structure and the weak C=O composition suggests fewer carboxyl groups were formed after the oxidation process was completed. The O-H in the GO spectrum represents hydroxyl groups that were attached to the basal plane as well as possible contributions from adsorbed water molecules. As the reduction process progressed, the rGO spectrum shows that the C=O band at ~1824 cm^{-1} is completely removed, indicating the removal of oxygen groups. Moreover, the appearances of new compositions such as C≡C at ~2204 cm^{-1} and O=C=O (carbon dioxide) at ~2333 cm^{-1} are the result of the recovery of the sp^2 lattice structure, where the carbon bonding strengthens even more through the π-π stacking formations. The broad peak of O-H at ~3324 cm^{-1} in the rGO spectrum is due to the water residual within the samples.

Raman spectra were conducted on the GO and rGO samples A, B, C, and D to analyse the structural defects and restoration after the reduction process, which can be

seen in the Figure 4.10. As the GO undergoes the oxygen reduction process, the oxygen component that is attached to the carbon lattice structure is removed, leaving a vacant or empty space on the graphene sheets called a defect (Melchioni et al., 2023). These defects correspond to the D-band in the Raman spectrum, which can be found at a 1343.97 cm^{-1} shift in Figure 4.10. The addition of a defect in the lattice structure will cause the disruption within the sp^2 carbon structure. However, due to the special characteristic of rGO, the defect in the carbon sp^2 lattice structure causes the carbon to reform, leading to the restoration of the π-conjugated structure (Guo et al., 2024). These recoveries correspond to the G-band in the Raman spectrum, which can be seen at the 1596.60 cm^{-1} shift.

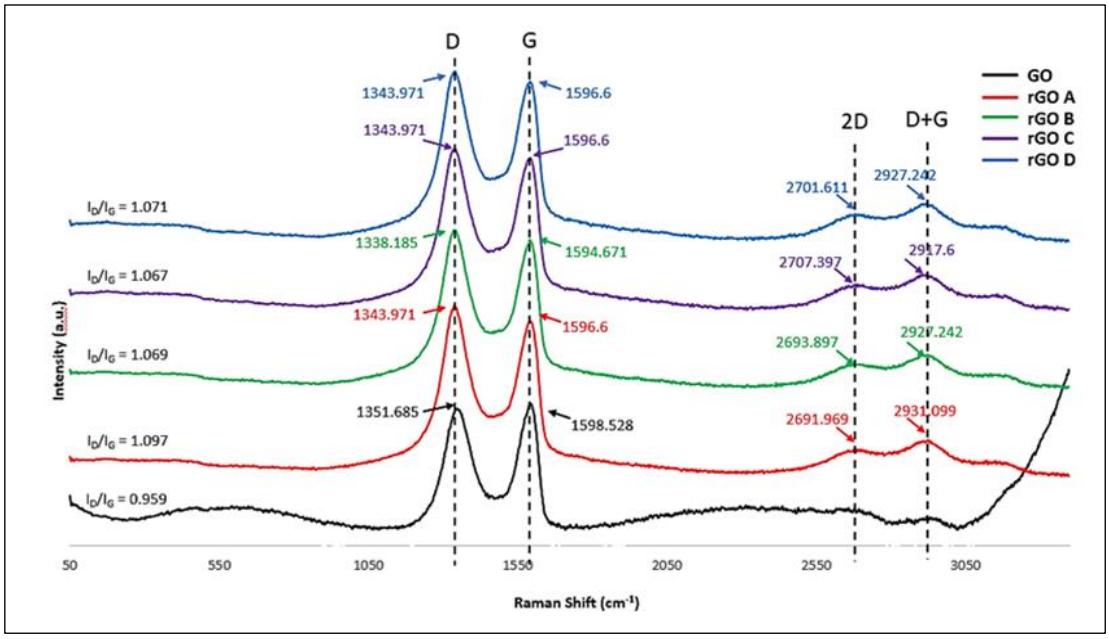

Figure 4.10 Raman Spectra of GO and rGO A, rGO B, rGO C, and rGO

The intensity ratio of the D-band and G-band, or in short for I_D/I_G, can be calculated to determine the structural defect of rGO as the reduction process occurs. Based on the result in Figure 4.10, the value of I_D/I_G of GO was recorded at 0.959, followed by rGO sample A with a value of 1.097, rGO sample B with a value of 1.069, rGO sample C with a value of 1.067, and rGO sample D with a value recorded at 1.071. An increase in the I_D/I_G value indicates a higher density of defects in the structural properties, while a lower value indicates a more structured surface of the graphene structure (R. Sharma et al., 2017). Furthermore, the value of I_D/I_G of GO and rGO was previously recorded at 0.9 and 1.0 (Bansal et al., 2022). These statements match the

pattern of the obtained result, indicating a successful reduction of GO. Amongst the results obtained, rGO sample A was recorded with the highest value of I_D/I_G compared to other rGO samples, suggesting a higher removal of oxygen-functional groups during the reduction process and higher sp^2 recovery of carbon bonding and π-conjugated structure within the graphene structure.

Subsequently, the appearance of the 2D-band peak in the Raman spectrum was recorded in the range from 2691.9 cm^{-1} to 2707.3 cm^{-1}. Hidayah et al. state that the peak that appeared at 2679.3 cm^{-1} in the Raman spectrum indicates the layer of graphene is in a monolayer formation, while the peak that appears at 2716.77 cm^{-1} indicates it is a multilayered rGO (Hidayah et al., 2017). Hence, the result of rGO obtained in Figure 4.10 indicates that they are in a multilayered form, which aligns with the appearance of crinkled features that were found under the SEM imaging. Hidayah et al. also state that the recovery of the graphitic lattice structure after the reduction process was conducted in a stacking manner, forming a multilayered rGO (Hidayah et al., 2017). Meanwhile, the D+G-band peak that appeared in 2927 cm^{-1} indicates the phonon reaction between the D-band and the G-band, which is basically a second-order of Raman modes (Puech et al., 2019).

In a summary, an increase in the amount of GO weight during the synthesis process will produce more graphene in the rGO structure, which has been confirmed in the physical observation analysis after the samples were left for 24 hours. Moreover, as the graphene content in rGO increases, light absorption intensity increases because more graphene interacts with light, as confirmed by UV-vis spectral analysis. Based on all of the analysis conducted, 400 mg of graphite is the most appropriate quantity required to obtain a rGO with a full reduction process. Thus, 400 mg of GO will be used as a baseline to further study the effect of ascorbic acid's weight in the synthesis process.

4.2.2.2 Effect of Ascorbic Acid Concentration

Ascorbic acid was introduced in this method as an oxygen reduction agent to reduce the GO into rGO. This study is conducted to analyse the effect on the optical, chemical, and structural properties of rGO by setting 6 g of ascorbic acid for rGO sample E.1, 5g for rGO sample E, 4 g for rGO sample F, and 3g for rGO sample G. Figure 4.11shows the absorption peak intensity of all rGO samples using a UV-vis spectroscopy, where rGO sample E manages to record the highest peak at ~241 nm with

a secondary broad peak appearing at ~305 nm. Based on the result obtained, the UV spectrum of rGO sample E shows the strongest intensity and sensitivity of light absorbance compared to the other rGO samples.

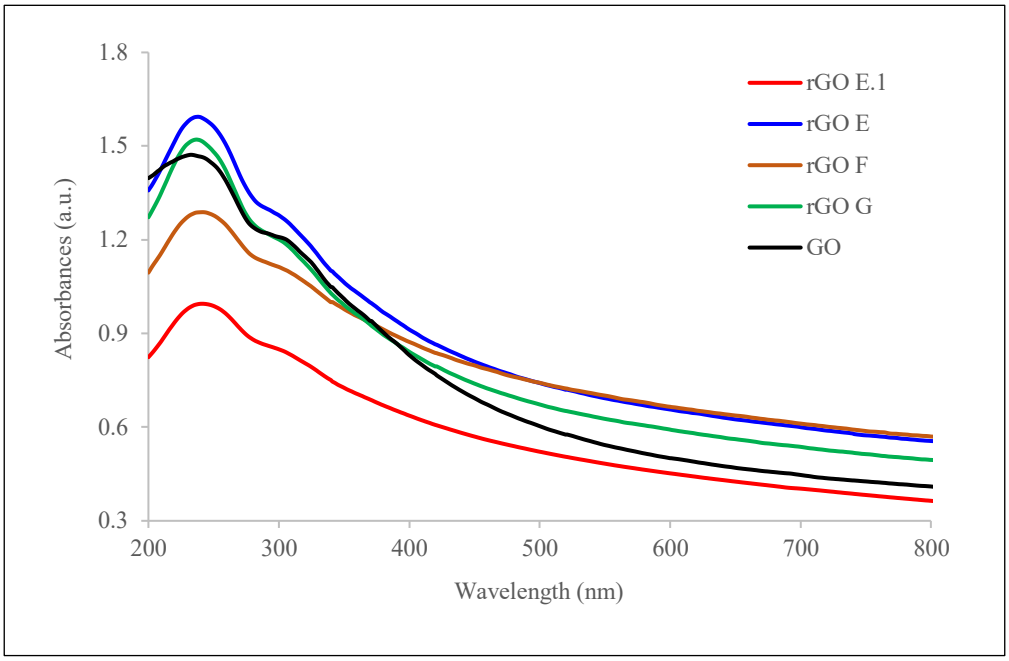

Figure 4.11 UV Spectrum of the Synthesized rGO Sample E.1, E, F, and G

Theoretically, as the weight of ascorbic acid used in the reduction process increases, more oxygen-functional groups will be removed (Palomba et al., 2022). Thus, a higher degree of π-conjugated structures will be recovered. This enhanced reduction efficiency will lead to a higher concentration of sp^2 carbon bonds in the rGO material, resulting in increased light absorption in the UV-vis spectrum. Even so, the result shown by the rGO sample E.1 indicates the weakest absorbance peak despite having a greater amount of ascorbic acid used. During the synthesis method of rGO sample E.1, the amount of ascorbic acid used shows that there is a small faint of white powder not fully mixed, indicating an excess of ascorbic acid not fully mixed during the synthesis process due to the saturation of the solution. This incomplete process might deter the graphene structure due to the excess ascorbic acid, increasing the impurities of rGO in which affects the structural and performance of rGO. However, a simple analysis was conducted, such as Zeta potential and contact angle analysis, to highlight the issue regarding the completion of the synthesis method for rGO sample E.1.

Result on the Zeta potential in Figure 4.12 shows that rGO sample E produces the highest potential with a value recorded at -36.1 mV, followed by rGO samples F, G,

and E.1 with a value of –35.3 mV, –33.2 mV, and –28.1 mV. This indicates that the rGO sample E possesses better colloidal stability and stronger electrostatic repulsion between particles, which may contribute to improved charge distribution across the graphene plane compared to the other samples. Additionally, the contact angle analysis on rGO droplet on the plate shows that rGO sample E records the highest angle, followed by rGO samples F, G, and E.1 with a value of angle recorded at 111.0°, 106.1°, 96.9°, and 67.0°. The results show that the rGO sample E exhibits higher hydrophobicity than the other samples. Both analyses show a similar trend, indicating that a higher amount of reducing agent introduced into the process can yield a more stable, more hydrophobic rGO. However, the result from the rGO sample E.1 in the Zeta potential analysis indicates that it is closer to the GO value. Moreover, the angle of the droplet recorded by the rGO sample E.1 shows that they are in a hydrophilic state, which is very uncommon for the characteristic of rGO to appear.

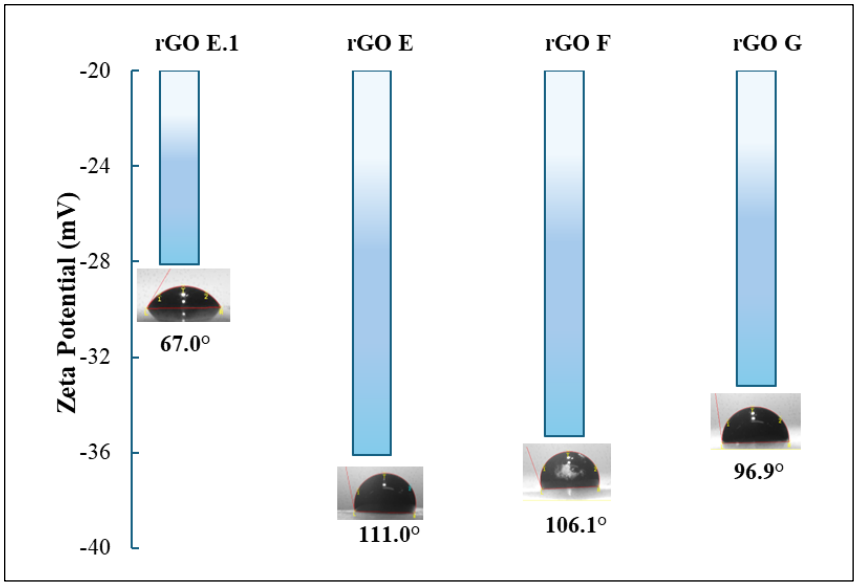

Figure 4.12 Zeta Potential and Contact Angle Analysis on rGO Sample E.1, E, F, and G

Physical observation was also conducted on rGO samples E.1, E, F, and G, as shown in Figure 4.13, after leaving them in open spaces for 24 hours. The result shows that the graphene sheets within the rGO sample E.1 were not separated, suggesting the reduction process was incomplete. The incomplete reduction of GO is due to excess ascorbic acid that was not homogeneously mixed during synthesis, leading to GO retaining its oxygen-functional groups and its hydrophilic nature. These findings align

with the results of contact angle analysis, in which the angle between the bubble droplet and the surface is less than 90°.

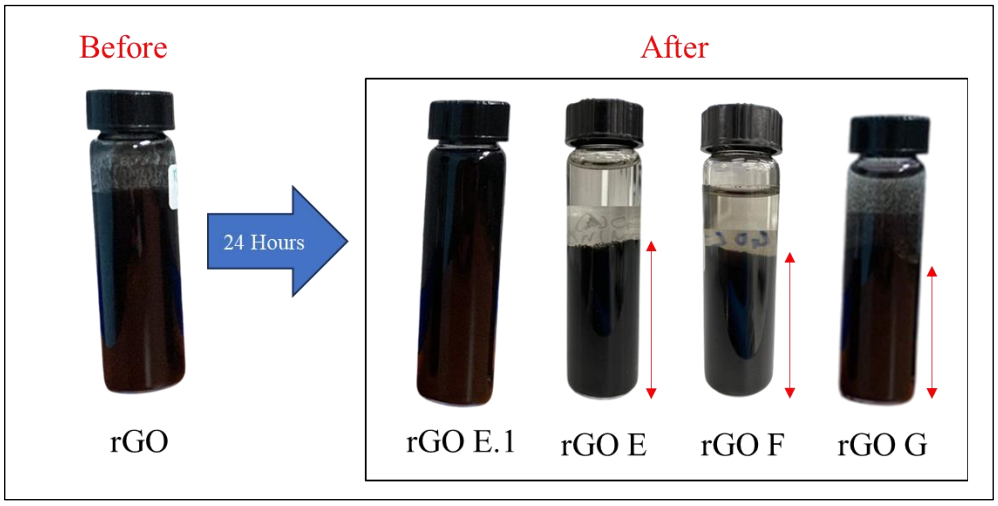

Figure 4.13 Physical Observation on rGO Samples E.1, E, F, and G After 24 Hours

Meanwhile, the graphene in the rGO sample E naturally separated from the water, leaving a clear, transparent supernatant, indicating successful reduction of GO. Additionally, the graphene in the rGO sample F naturally separates from the solution. However, the supernatant is slightly murky rather than completely clear, indicating that a very small amount of graphene remains in the water solution. As the amount of ascorbic acid used in the synthesis method decreased, the effectiveness of the reducing agent also diminished. The graphene in the rGO sample G is not fully separated, and the supernatant is grey, indicating that the rGO is partially reduced. Hence, this result shows that the rGO sample E shows better stability, conductivity, and hydrophobicity in colloidal particles. Also, due to the incomplete reduction of GO in the rGO sample E.1, further analysis and characterization of E.1 shall not be continued, as it shows poor light absorbance, weak surface charging and stability, and poor hydrophobicity, as proven by these data.

The morphological structure of the rGO samples E, F, and G was studied under SEM imaging, as seen in Figure 4.14. The result shows that the rGO sample E has more crinkled features (multi-layered stacked graphene) than the other samples, indicating good recovery of π-conjugation and a higher degree of recovery of sp^2 carbon structure. This discovery supports the results obtained in UV-vis spectrometer analysis. Moreover, the defect in the image of the rGO samples F and G shows that, despite a

lower amount of ascorbic acid used, their defects indicate that the hydroxyl group was removed and that the structure and π-conjugated structure were recovered properly.

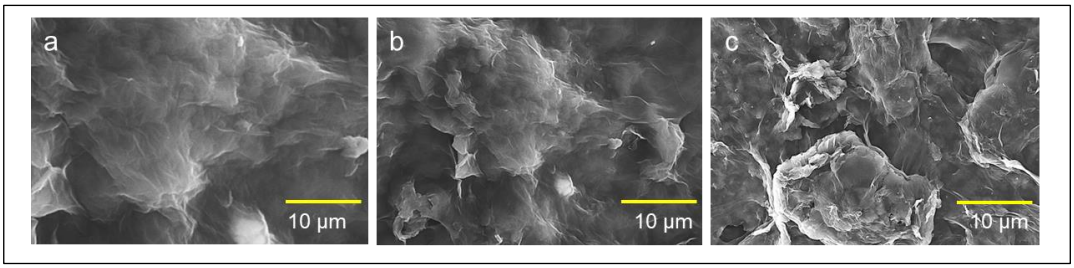

Figure 4.14 SEM Images of rGO Samples (a) Sample E, (b) Sample F, and (c) Sample G

EDX analysis was then conducted on rGO samples E, F, and G, and the atomic weight values were recorded in Table 4.2. The results obtained show that the C/O ratio of rGO sample E indicates that it has more oxygen-functional groups removed during the synthesis process than rGO samples F and G, with ratios of 0.85 and 0.82, respectively. The removal of the hydroxyl group explains the crinkled morphology observed in rGO E.

Table 4.2
EDX Analysis on GO, rGO E, rGO F, and rGO G

Atomic weight percentage (at. %)	GO	rGO E	rGO F	rGO G
Carbon, C	34.5	51.8	46.0	45.1
Oxygen, O	65.5	48.2	54.0	54.9
C to O Ratio (C/O)	0.53	1.08	0.85	0.82

Crystallinity of the structure in the rGO samples E, F, and G was detected via XRD analysis, and the results are shown in Figure 4.15. rGO sample E shows the peak intensity in plane (001) at a diffraction angle (2Θ) of 11.0 °, which is reduced significantly after being reduced, indicating a high intensity of oxygen-functional group being removed. Moreover, the strong peak in plane (002) at 2Θ = 24.6 ° indicates a high recovery of the sp^2-hybridised carbon structure. Subsequently, the *d-spacing* of the rGO sample E was calculated to be 0.3854 nm, corresponding to an average thickness of the graphene layers, indicating a successful reduction of GO. A similar pattern was observed in planes (001) and (002) for rGO sample F, with a *d-spacing* of 0.3760 nm recorded. However, the peak intensity in the plane (002) for rGO F is stronger compared

to rGO sample E, indicating a stronger recovery of sp^2 and π-conjugated structure occurred. Meanwhile, the rGO sample G shows that the peak intensity in the plane (001) was slightly red-shifted, and a weak peak was observed in the plane (002), indicating a very small amount of hydroxyl groups were reduced, forming a more concentrated oxygen-functionalized rGO. The *d-spacing* for the rGO sample G was calculated to be 0.8150 nm, indicating that the sample retains the GO structure, with only a very small amount of hydroxyl groups removed. Hence, this pattern indicates that as more oxygen-functional groups are removed from the graphene lattice, the peak on the (001) plane will be further reduced. At the same time, the peak in plane (002) increases as well, indicating the intensity of recovery of the sp^2 and π-conjugated graphene structure.

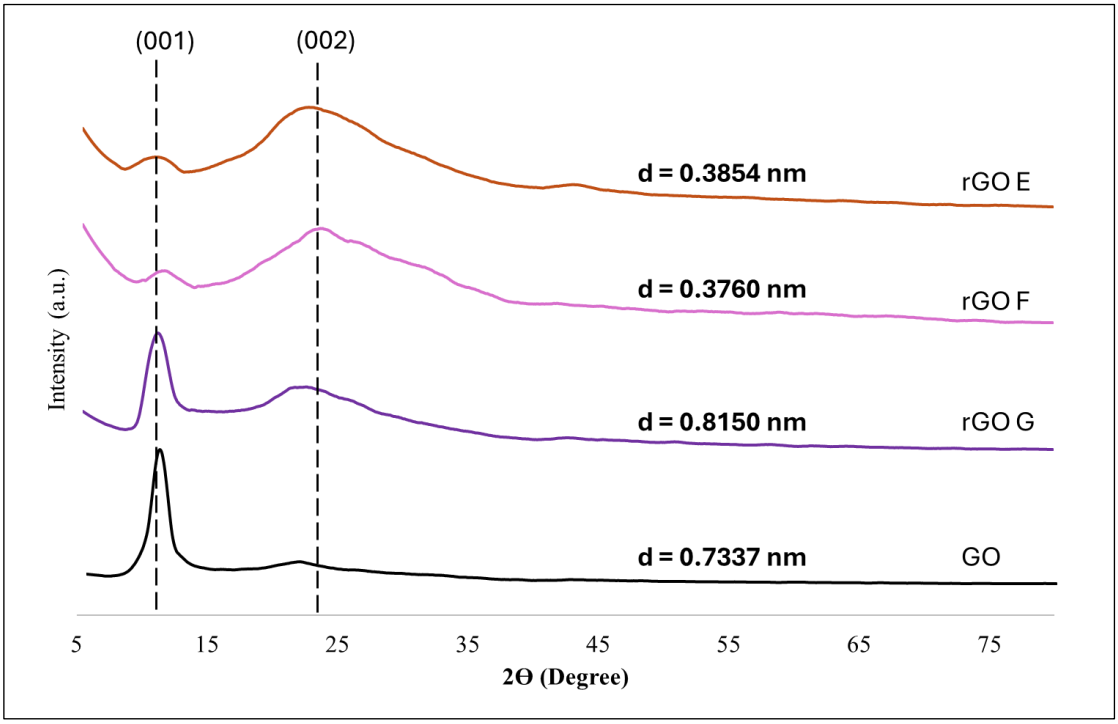

Figure 4.15 XRD Spectrum on rGO Samples E, F, and G

FTIR analysis was conducted on the rGO samples E, F, and G to study the chemical compositions within the rGO, and the result was recorded as shown in Figure 4.16. The results on the spectrum of all samples of rGO show the removal of C=O and the appearance of a new composition, which is C≡C and O=C=O, indicating that the oxygen-functional group was removed and the new composition is the result of sp^2 recovery in π-conjugated structures. However, in this case, the FTIR spectrum of the rGO samples revealed weak, sharp bands at ~1045 and ~1084 cm^{-1}, indicating C–O

stretching vibrations of alkoxy or epoxy groups. These peaks were absent in the GO spectrum, suggesting that while the reduction process removed a significant portion of oxygen functionalities, certain C–O bonds were retained or became clearer in the rGO structure. Hence, the clear detection of C-O within the rGO structure indicates that the rGO samples E, F, and G were reduced from oxygen-functional groups but not completely.

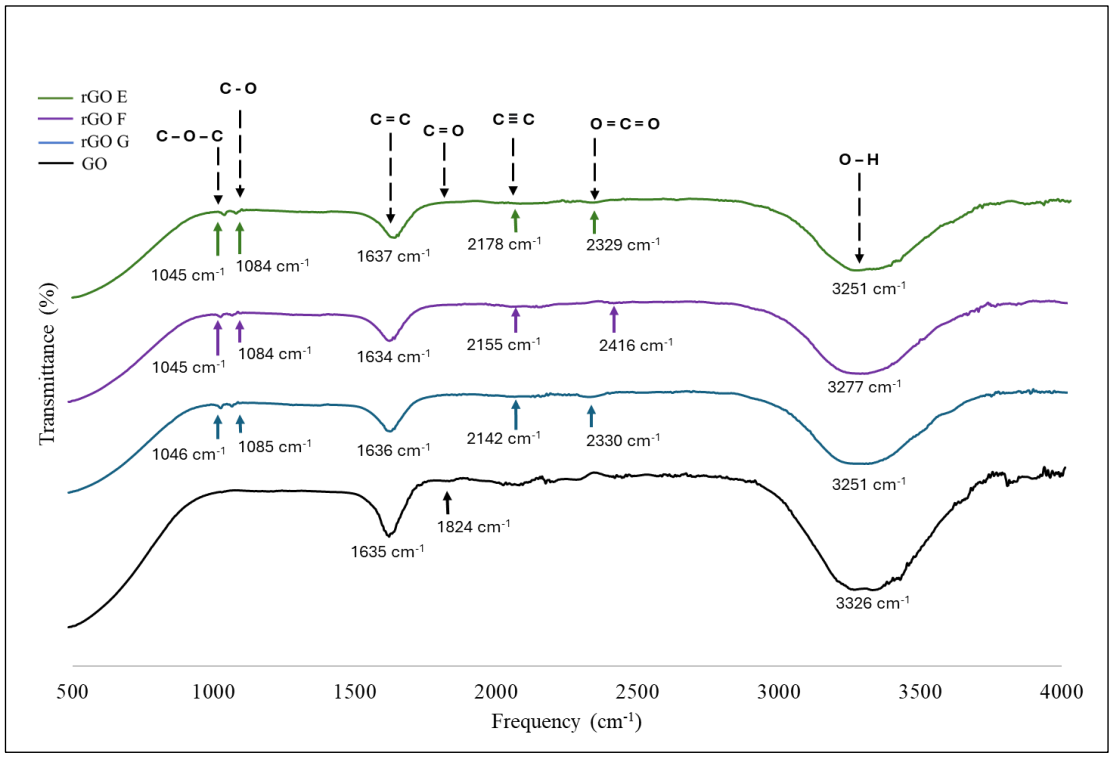

Figure 4.16 Result of FTIR Analysis on GO and rGO Samples E, F, and G

Raman spectra analysis was then conducted on rGO samples E, F, and G, as in Figure 4.17. The results show that the peaks of the D-band, G-band, 2D band, and D+G band are present in the rGO spectrum. The value of the I_D/I_G ratio was also measured; for rGO sample E, it was 1.102, followed by 1.063 and 1.043 for rGO samples F and G, which align with the previous result (Bansal et al., 2022). Moreover, the 2D appearance indicates that all rGO samples are in a multi-layered graphene structure. Among the samples, sample E shows a higher defect value due to more oxygen-functional groups being removed and stronger recovery of the π-conjugated structure. These findings align with previous analysis results from UV-Vis, Zeta, SEM, EDX, and XRD, which show that using 5 g of ascorbic acid is the most ideal for producing a stable, well-structured

rGO. Hence, 5 g of ascorbic acid used in the synthesis method has been proven to produce a better rGO compared to rGO samples F and G.

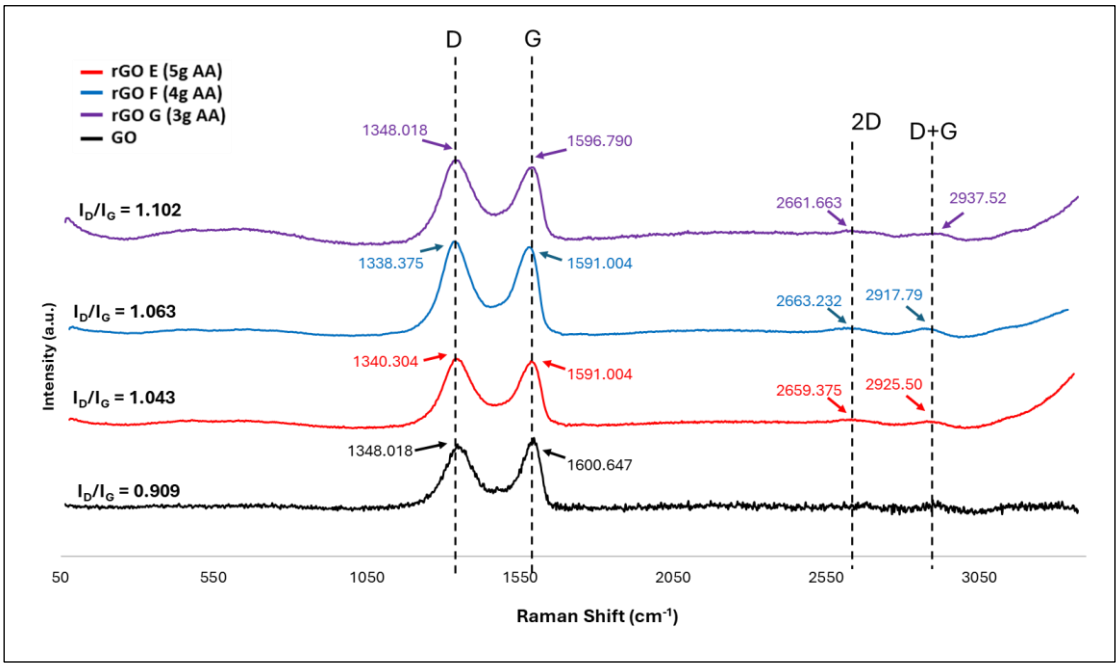

Figure 4.17 Raman Spectrum on rGO Samples E, F, and G

In conclusion, the results indicate that as more ascorbic acid is used as a reducing agent during synthesis, more oxygen-containing functional groups are reduced, yielding a stable suspension of rGO. However, there is a limit to how much the GO can be reduced. The results (UV-vis spectra, Zeta potential, contact angle, and physical observation) obtained on the rGO sample E.1, where 6 g of ascorbic acid was used, show that the reduction of GO was not completed due to the excess of ascorbic acid that was not fully mixed during the early process, leading to the re-oxidation of the rGO. By compiling all the characterization results, it can be concluded that 5 g of ascorbic acid is optimal for reducing 400 mg of GO, yielding a stable rGO with a higher degree of reduction and a higher defect density. The sample also demonstrated excellent hydrophobicity, improved optical properties, and good colloidal stability. Thus, 400 mg of GO and 5 g of ascorbic acid will serve as a new baseline for the subsequent parameters in studying the effect of hydrogen peroxide as a washing agent.

4.2.2.3 Effect of Hydrogen Peroxide Volume

The purpose of introducing hydrogen peroxide into this synthesis method is to remove the excess reducing agent (ascorbic acid) by oxidising it, so that the oxygen-functional group in the rGO is not completely removed. At the same time, it will be used to remove impurities, prevent unwanted reactions within the lattice structure, and ensure the purity of rGO production (Vimalanathan et al., 2022). Hence, the volume of hydrogen peroxide used will play a crucial role in ensuring the purity of rGO. In this work, new parameters were set: 8 mL of hydrogen peroxide for rGO sample H, 10 mL for rGO sample I, and 12 mL for rGO sample J with 400 mg of GO and 5 g of ascorbic acid used along the process.

UV-vis spectra analysis was conducted on rGO samples, H, I, and J, to study their optical properties, and the peak intensity was recorded in Figure 4.18. The result shows that rGO sample I displays a strong interaction with the light, followed by rGO samples J and H. The peak of the rGO sample I was recorded at 241 nm, corresponding to the π-π transition of aromatic carbon bonding, followed by the appearance of the second peak recorded at 306 nm, which can be attributed to the n-π* transition of residual C=O groups (Vimalanathan et al., 2022). The increase in intensity of the peak at 241 nm compared to GO indicates partial restoration of the conjugated π-system, confirming the successful reduction process.

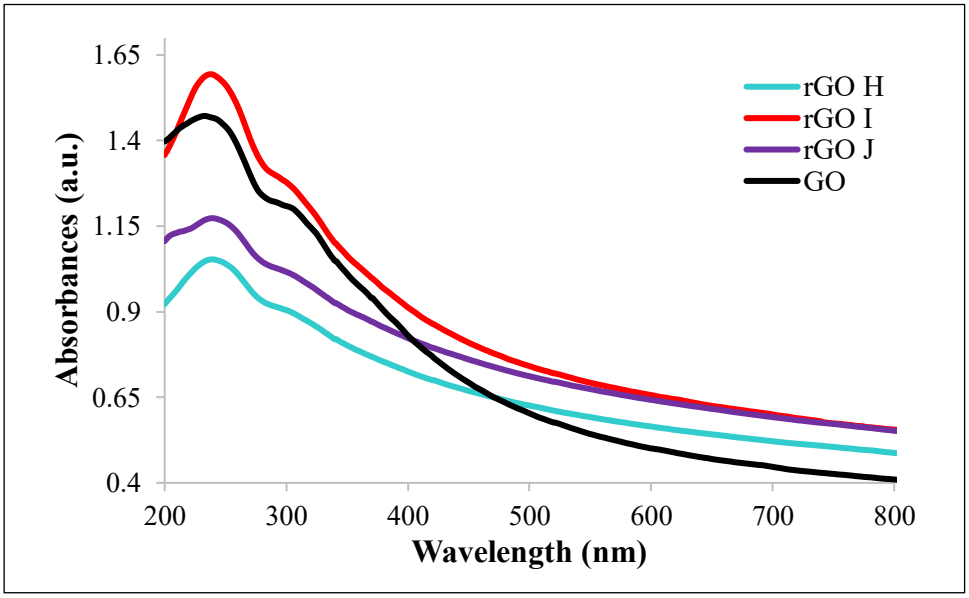

Figure 4.18 Absorbance Performance of GO, rGO H, rGO I, and rGO J

It should be expected that, as the volume of the cleansing agent used increases during the synthesis process, a higher purity of rGO should be able to be produced (Zikalala et al., 2024). The rGO sample J, where 12 mL of hydrogen peroxide was used, shows a weaker intensity of the peak spectrum recorded compared to the rGO sample I. These findings might relate to the excess hydrogen peroxide affecting the physical structure of graphene. Characterization of the composition of graphene and its defects after the reduction process will confirm this possibility. The weak peak intensity observed for the rGO sample H is likely due to insufficient hydrogen peroxide used during the post-reduction process. Inadequate oxidation of the residual ascorbic acid can lead to incomplete removal of by-products, thereby hindering the overall reduction efficiency and resulting in weaker peak intensity in the UV-vis spectrum.

Zeta potential analysis was conducted on rGO samples H, I, and J, and the result was recorded in Figure 4.19. The results show that the rGO sample I recorded the highest potential at -36.1 mV, followed by -30.3 mV for rGO sample J and -24.5 mV for rGO sample H. These findings show that rGO sample I is more stable and electrically conductive compared to other rGO samples, indicating a high number of oxygen-functional groups were removed within the lattice structure. A droplet of the rGO samples was placed on a glass slide to assess their hydrophobicity, as shown in Figure 4.19 (inset).

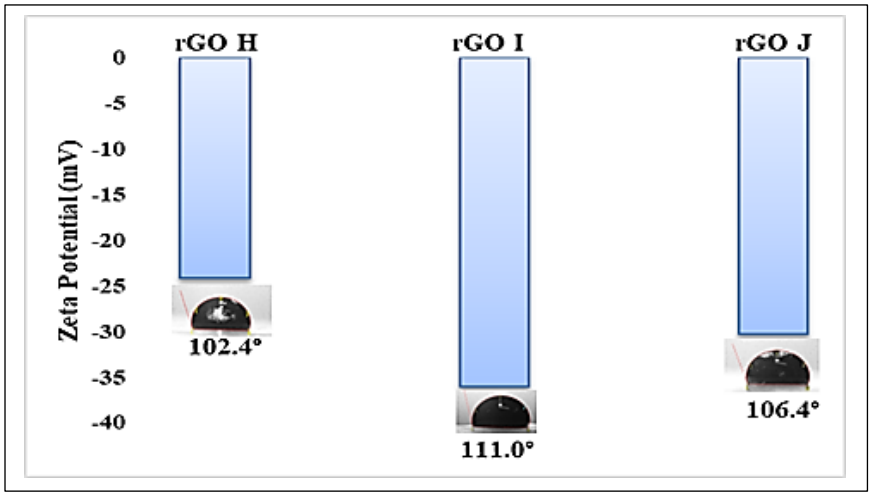

Figure 4.19 Zeta Potential and Contact Angle Analysis on rGO H, rGO I, and rGO J

The results show that rGO sample I recorded an angle of 111.0°, followed by rGO sample J at 106.4°, and rGO sample H at 102.4°. The rGO sample yielded the highest angle, indicating the highest degree of hydrophobicity among the rGO samples.

These findings demonstrate that rGO sample I possesses a stable colloidal structure, as evidenced by its highest zeta potential, and an enhanced hydrophobicity, as shown by the contact angle measurement. In contrast, rGO sample J exhibited lower hydrophobicity and reduced colloidal stability, which may be attributed to the excess hydrogen peroxide used during synthesis, leading to modifications of the morphology structure. Meanwhile, the relatively poor performance of the rGO sample H can be attributed to the limited volume of hydrogen peroxide, which prevented the complete oxidation of residual ascorbic acid, leaving impurities within the rGO structure.

Physical observation on the rGO samples was analyzed after 24 hours in an open area, and the physical sample was recorded, as in Figure 4.20. The observation after 24 hours shows that the amount of graphene naturally separated from the water residual is equal, indicating a consistent amount of GO used during the synthesis method. Among the samples recorded, the supernatant from rGO sample I is clearer than that of the other samples, suggesting that the rGO was highly hydrophobic and that no visible impurities remained in the suspension. Meanwhile, the supernatant of rGO sample H exhibited a slightly greyish coloration, which can be attributed to residual impurities that were not fully removed due to insufficient oxidation of ascorbic acid. As for rGO sample J, the supernatant displayed a similar coloration to sample H, which may be caused by the excess amount of hydrogen peroxide used during synthesis, leading to a slight alteration in the suspension colour.



Figure 4.20 Physical Observation on rGO Sample H, I, and J After 24 Hours

Figure 4.21 shows the SEM imaging of synthesized rGO samples H, I, and J to analyze the morphological structure of the samples. The image shows that the rGO

sample I produced has a more uniform crinkled feature than other rGO samples, indicating successful reduction of hydroxyl groups and good recovery of sp^2 carbon structure through layered stacking.

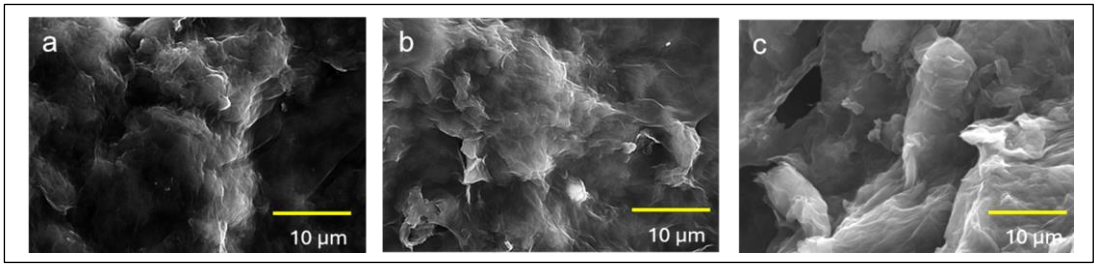

Figure 4.21 SEM Images of rGO Samples (a) rGO H, (b) rGO I, and (c) rGO J

The successful reduction of the rGO sample I can be supported by the EDX analysis in Table 4.3, where the C/O ratio was recorded with the value of 1.08, indicating more oxygen-functional groups being removed. Hence, a crinkled feature on the rGO surface structure was formed after recovering the sp^2 carbon structure by removing hydroxyl defects. Despite the limited volume of hydrogen peroxide used, the rGO sample H also shows good removal of the hydroxyl group, with a crinkle feature forming on the surface structure. The C/O ratio of the rGO sample H was recorded at 0.91, indicating the intensity of the oxygen-functional group is still higher compared to rGO sample I. The irregular morphology can be observed in the rGO sample J, where the structure resembles the salt structure, as reported by (Namvari et al., 2017), rather than the common crinkled feature. This irregular formation might be due to limited hydrogen peroxide causing rGO to undergo a recovery process via agglomeration rather than layered stacking. This irregularity might also explain why the peak of the UV-vis spectrum weakened. The C/O ratio was recorded at 0.96, indicating the oxygen-functional group is also higher than the rGO sample I. The excess of hydrogen peroxide not only alters the structural properties of rGO but also increases the content of oxygen groups.

Table 4.3
EDX Analysis Result on rGO H, rGO I, and rGO J

Atomic weight percentage (at. %)	GO	rGO H	rGO I	rGO J
Carbon, C	34.5	47.7	51.8	48.9
Oxygen, O	65.5	52.3	48.2	51.1
C to O Ratio (C/O)	0.53	0.91	1.08	0.96

XRD analysis was conducted on rGO samples H, I, and J, and the peak spectra for each sample are shown in Figure 4.22. The results show that the peak on the (001) plane of all samples weakened after the reduction process, indicating successful reduction of the hydroxyl group. Moreover, the presence of a peak in a plane (002) indicates successful recovery of the sp^2 carbon lattice structure of the rGO. Successful removal of the oxygen-functional group in the lattice structure causes the spacing between the layers of the lattice structure to be reduced.

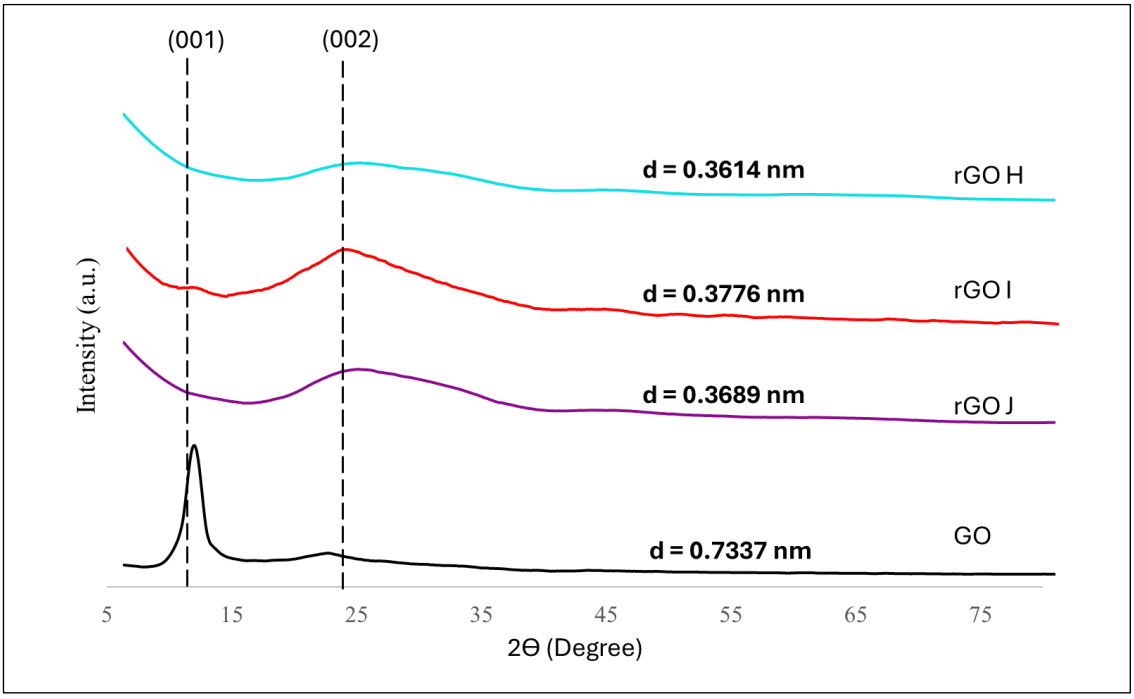

Figure 4.22 Plane Peak Appearance on GO, rGO H, rGO I, and rGO J under XRD Analysis

rGO sample H managed to record a *d-spacing* of 0.3614 nm between the graphene layers, followed by rGO sample I with 0.3776 nm between the graphene layers, and rGO sample H with an average diameter length of 0.3689 nm. The result indicates that rGO samples H, I, and J are successfully reduced. However, based on the

plane (002) appearance, the rGO sample I produced showed the sharpest peak, indicating a strong sp^2 recovery of the carbon structure. Meanwhile, rGO samples J and H produce a broad peak in plane (002), indicating weak recovery of the sp^2 lattice structure, affecting the surface structure of graphene. These occurrences support the previous findings under SEM imaging, where the irregularity of the structure shown by rGO J didn't meet the common structure produced by rGO, which is layered stacking. Moreover, the broad peak of the plane (002) of the rGO H indicates that the recovery of the sp^2 carbon structure is weak due to the lack of volume of hydrogen peroxide in washing the impurities. The impurities that remain within the lattice structure will disrupt the ordered stacking of graphene layers, and this supports the findings of zeta potential, where a weak surface charge is recorded due to impurity disturbances within the graphitic plane of rGO.

The FTIR spectrum results for the rGO samples H, I, and J were collected to analyze their composition within the structure, and their results are compiled in Figure 4.23. The results show that rGO samples H, I, and J successfully reduce the C=O composition, indicating a reduction of oxygen-functional groups within the lattice structure. rGO sample H, where 8 mL of hydrogen peroxide was used during the synthesis process, managed to record a peak at 2047 cm^{-1} and 2218 cm^{-1}, which represent C≡C composition, indicating a recovery of sp^2 lattice structure through π-π stacking conjugation. However, the appearance of a new peak at 2591 cm^{-1} corresponds to S-H stretching vibrations. This composition is very uncommon to appear within the reduced graphene lattice structure (Chuah et al., 2020). In other words, the only possibility for the appearances on the S-H composition can be traced to either contamination within the GO precursor or residual impurities after the reduction process. Between the two possibilities, the latter aligns with the findings, as the appearance of S-H composition within the GO spectrum was not detected. The peak observed at 2340 cm^{-1}, which appears upward instead of downward, is likely due to interference during the detection process. This interference may be attributed to impurities within the sample that affected the signal response during FTIR measurement. Subsequently, the presence of an epoxy group in the rGO sample H was not detected.

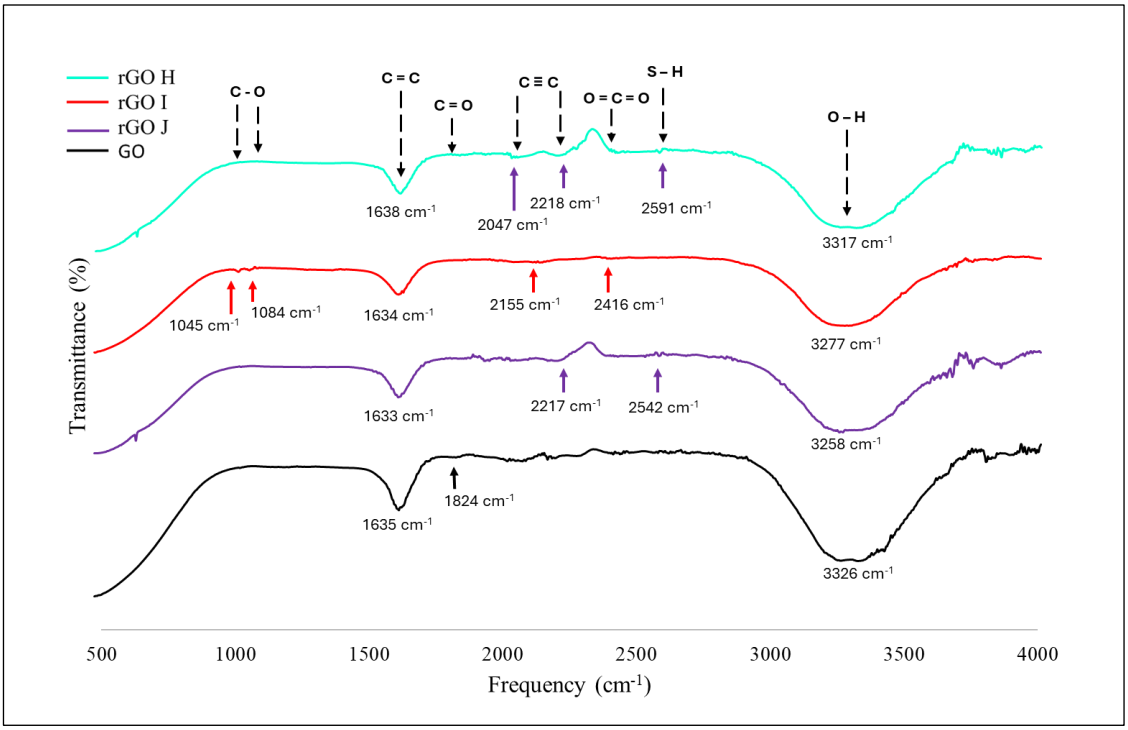

Figure 4.23 FTIR Spectrum on GO and rGO Samples H, I, and J

For the rGO sample I, the presence of C≡C and O=C=O compositions were detected at 2155 cm^{-1} and 2416 cm^{-1}, respectively. The appearance of these peaks suggests the partial restoration of the sp^2-hybridized carbon network after the reduction process, attributed to the reformation of conjugated π–π stacking between graphene layers. The peak appearance at 1045 cm^{-1} and 1084 cm^{-1} represents the C-O composition, suggesting the epoxy group exists within the rGO structure. The presence of epoxy groups indicates that a small amount of oxygen-functional groups was formed within the graphene structure, producing a partial reduction of GO. These findings suggest the GO was reduced but not completely. As for rGO sample J, the C≡C composition at 2217 cm^{-1} was detected, indicating the recovery of the lattice structure occurred after the reduction process. However, the appearance of S-H composition at 2542 cm^{-1} was detected, indicating the residual impurities within the rGO were present. It is possible that the change in physical structure, as seen in the SEM imaging, can lead to an increase in impurities within the rGO. Among the samples recorded, the rGO sample I shows a closer characteristic of chemical composition to the rGO spectrum.

The peaks of the Raman spectrum for rGO samples H, I, and J were presented in Figure 4.24. The result shows that the highest value of I_D/I_G ratio was recorded at 1.102 for rGO sample I, followed by rGO sample J with a ratio of 1.086, and rGO

sample H with a ratio of 1.057. The peak intensities of the D-band and G-band for all samples recorded are higher than GO, indicating a high defect density and good sp^2 carbon recovery.

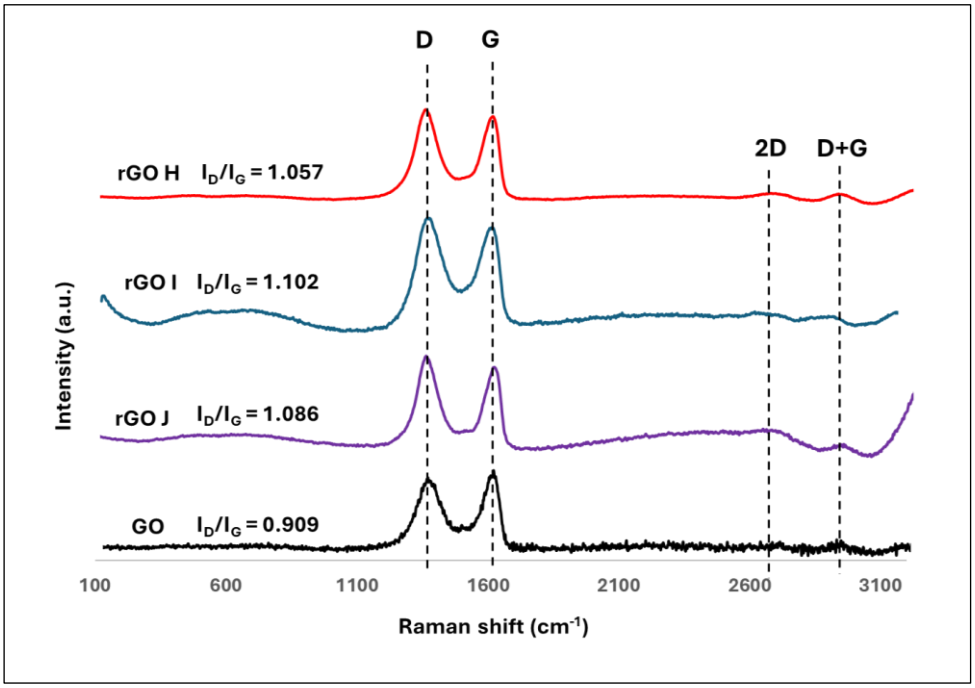

Figure 4.24 Raman Spectra Analysis Result on GO, rGO H, rGO I, and rGO J

However, the decrease in value of the I_D/I_G ratio for rGO sample H can be attributed to the lack of volume of the cleansing agent, causing the intensity of the D-band to weaken compared to rGO sample I. These findings suggest that the number of oxygen-functional groups being removed in rGO sample H is less than rGO I. Moreover, the weak broad peak of the 2D-band of the rGO samples H and I indicate that the graphitic lattice structure is in a multi-layered structure, as confirmed under SEM imaging. The value I_D/I_G ratio recorded on rGO sample J is weaker compared to rGO sample I, indicating a lower degree of reduction occurred and fewer oxygen-functional groups were removed. Moreover, the decrease in the peak of the D+G Band of rGO sample J is due to agglomeration rather than stacking into multilayer structures, which explains the salt-like structure observed under SEM imaging.

Based on the characterization results obtained, rGO sample I was identified as the best-performing sample among all those tested. Hence, TEM imaging was carried out on this sample to compare its morphology with the graphite and GO images reported by (Sahudin et al., 2022) in Figure 4.25. This comparison serves as a purpose to study

and understand the differences in the morphological structure of an updated GO synthesized by Rafal et al. and its reduction, which is currently being researched. An image of graphite shows a cluster of nanometre-sized platelets, indicating the original graphitic structure. A black, thick, and big flake of graphite was recorded under TEM imaging. As the graphite undergoes exfoliation and oxidation, a crinkled feature is observed on the surface of GO. The darker area indicates the stacking of multiple GO layer sheets, and the transparent area represents the area with a single or a few layers of GO. These findings indicate that the darker the area, the more layers are being stacked.

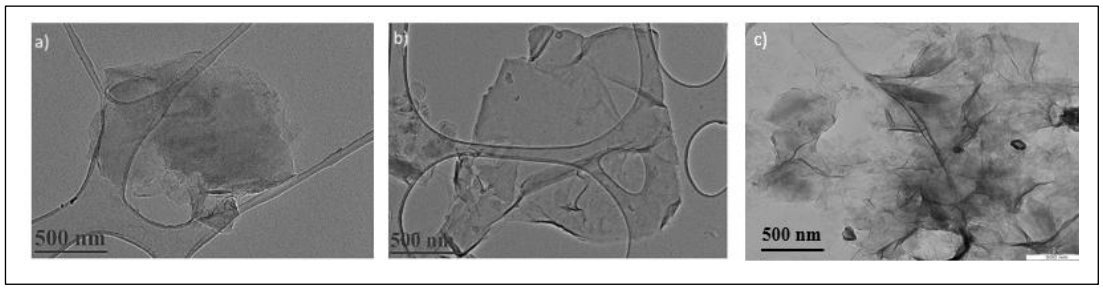

Figure 4.25 TEM Imaging on (a) Graphite, (b) GO, and (c) Synthesized rGO I. TEM images of graphite and GO were previously reported by (Sahudin et al., 2022)

As the reduction process progressed, the intensity of the crinkling features increased, with the dark area on the surface increasing exponentially, indicating that more rGO layers in rGO sample I are stacked than in GO. These findings align with previous studies (Huang et al., 2018), in which the intensity of the wrinkle feature on GO is weaker than on rGO under TEM imaging. Moreover, these findings align with the Raman spectrum, in which the 2D peak was observed during the analysis, indicating that the morphology of rGO sample I is multi-layered.

Summarising all the data, the rGO sample I, in which 10 mL of hydrogen peroxide was used to neutralise 5 g of ascorbic acid after reducing 400 mg of GO, shows the optimum volume needed to produce a stable rGO with strong optical properties, excellent stability and functionality. rGO H and J, which use 8 and 12 mL of hydrogen peroxide, show a murky colourless supernatant, indicating the impurities are still available within the sample. Yet, all graphene samples appear in a hydrophobic state, as confirmed via physical observation and contact angle. Even so, the rGO J shows the morphological structure that is similar to the salt-like structure, as a consequence of

increasing the volume of hydrogen peroxide that was introduced during the synthesis process. The change in structural properties also weakens the optical properties and the electrical conductivity of the samples. Moreover, lessening the volume introduced (8 mL) not only will reduce the intensity of the crinkled feature, but also weaken the optical properties and electrical conductivity compared to other samples. Hence, rGO I was chosen to be integrated with AgNs to form a new sensing material.

4.3 Phase 2: rGO-AgNs

A similar mixing method used by GO-AgNs will be adapted to the method in embedding the AgNs into rGO to produce rGO-AgNs. In this process, a similar mixing ratio is set so that the amount of rGO remains constant while the proportion of AgNs increases. A similar objective was conducted as well, where it is used to determine whether a higher AgNs content, mixed with a fixed amount of rGO, will result in greater physical and optical characteristics. Hence, a new parameter will be set where 1 part of rGO will be mixed physically with 5 parts of AgNs to produce a composite material called rGO-AgNs with a ratio of 1:5 and the parts of AgNs will be increased by 10, 15, and 20. This composite material will be tested with a UV-Vis spectrometer, SEM, EDX, FTIR, and Raman analysis.

4.3.1 Optical Properties of rGO-AgNs

The optical properties of rGO-AgNs with different ratios were studied via a UV-vis spectrometer, and the peak absorbance intensity produced by each ratio can be seen in Figure 4.26. The peak of rGO was recorded at 246 nm, indicating a successful reduction of GO. Meanwhile, the rGO-AgNs at ratios of 1:5, 1:10, 1:15, and 1:20 exhibit peaks at 234 nm, 215 nm, 210 nm, and 209 nm, respectively. By including the rGO into AgNs, the increase in light absorption and scattering intensity can be explained through plasmon coupling. Similar to GO-AgNs, plasmon coupling occurs when AgNs particles are very close to each other, with support through interaction with the rGO plane. Their individual surface plasmons can interact, leading to a redshift in the LSPR peak and a broadening of the absorption spectrum (Rohizat et al., 2021). Moreover, the rGO plane allows AgNs to interact with light even more, resulting in a higher peak intensity in the UV spectrum than that of AgNs alone.

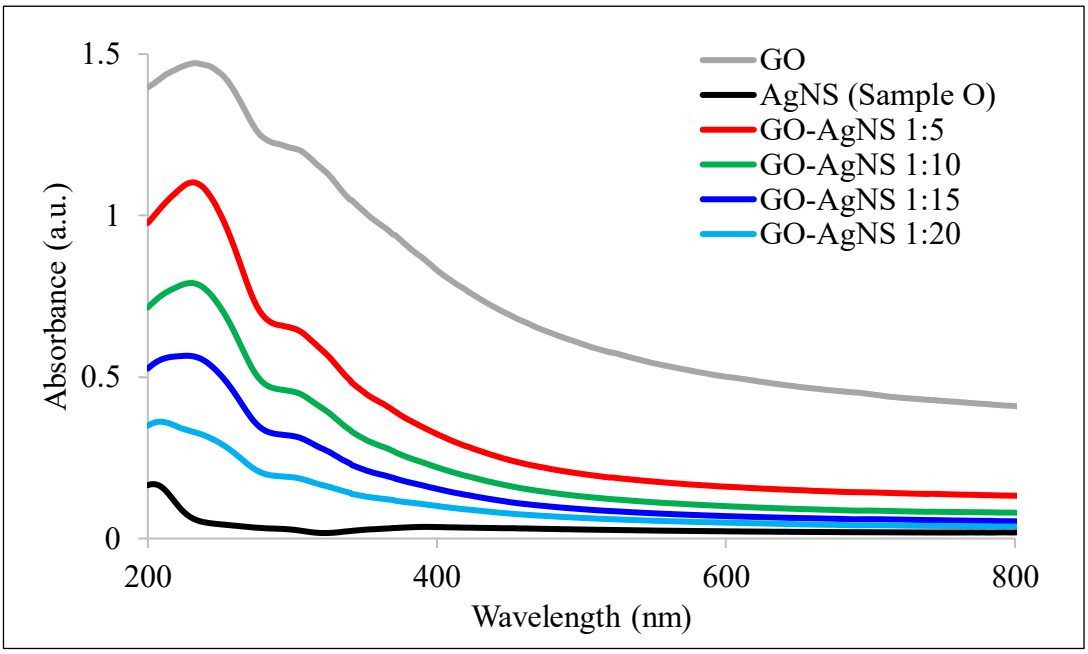

Figure 4.26 Absorbance Peak Intensity Produced by rGO-AgNs with Different Ratios Using a UV-vis Spectrometer

Based on the result obtained in Figure 4.26, rGO-AgNs with a ratio of 1:5 manage to produce the highest light absorbance intensity, followed by rGO with a ratio of 1:10, 1:15, and 1:20. It is expected that as more volume of AgNs was integrated into the rGO, the stronger the light absorbance intensity it produced. However, the peak intensity indicates that the more AgNs are used to integrate with 1 part of rGO, the weaker the peak intensity. This pattern indicates that excess AgNs that do not interact with the rGO plane will gradually deteriorate, and it will gradually affect the optical properties of the rGO-AgNs itself (Gurunathan et al., 2012). Even so, rGO with a ratio of 1:5, 1:10, 1:15, and 1:20 is still able to produce peak intensity stronger than AgNs alone.

4.3.2 Surface Morphology of rGO-AgNs with Different Ratios

The morphological structure of rGO-AgNs with different ratios under SEM imaging was recorded at 5000 magnification (refer to Figure 4.27(a)) and 10000 magnification (refer to Figure 4.27(b)). The white dots on the surface of the rGO lattice structure represent AgNs. As the amount of AgNs introduced into the rGO plane increases, the presence of white dots on the graphene structure increases. With more

volume of AgNs introduced into a part of rGO, more excess AgNs begin floating outside the rGO plane. Subsequently, the excess AgNs seem to agglomerate instead of floating around in a single particle, as seen in Figure 4.27(b). The agglomeration of excess AgNs will affect the LSPR reading greatly (Loiseau et al., 2019), which explains why the peak of the UV spectrum obtained from rGO-AgNs weakens as the volume of AgNs introduced into the rGO layer increases.

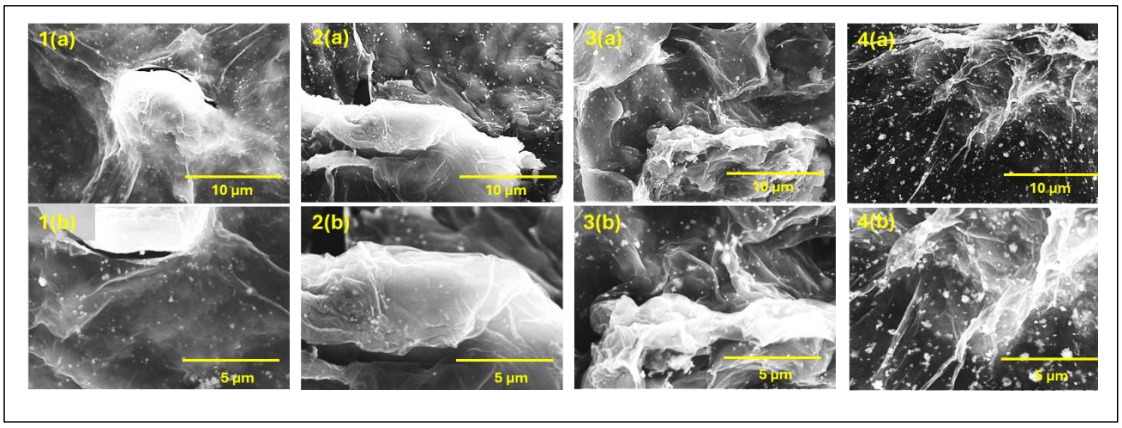

Figure 4.27 SEM Images of rGO-AgNs with a Mixing Ratio of (1) 1:5, (2) 1:10, (3) 1:15, and (d) 1:20 at 5000 (a) and 10000 (b) Magnification under SEM Imaging

EDX analysis was then conducted on the rGO-AgNs with different ratios to confirm the elemental composition of both materials. Based on Table 4.4, as the amount of AgNs introduced into the rGO increases, the Ag composition in a single area increases, aligning with the number of white dots observed in the surface structure under SEM imaging. Moreover, the amount of oxygen-functional group within rGO was increased upon integration of AgNs (refer to rGO-AgNs 1:5 in Table 4.4), suggesting the increase in the functional group originates from AgNs. Subsequently, the intensity of the functional group decreased as more AgNs were introduced. The decrease is likely due to the limited availability of active binding sites on the defected rGO structure, which restricts further attachment of oxygen-functional groups from the AgNs. The excess of AgNs may cause nanoparticles to deteriorate and aggregate, thereby diminishing the overall optical performance of rGO, which explains the reduction in the UV-vis peak intensity as more AgNs are introduced. Thus, based on the collected data, rGO-AgNs (1:5) are considered a suitable ratio to be prepared to produce rGO-AgNs with better optical properties.

Table 4.4
EDX Results of GO, rGO, AgNs, and rGO-AgNs at Various Mixing Ratios

Atomic weight percentage (at. %)	GO	rGO	AgNs O	rGO-AgNs 1:5	rGO-AgNs 1:10	rGO-AgNs 1:15	rGO-AgNs 1:20
Carbon, C	34.5	51.8	0	44.0	42.6	41.0	47.3
Oxygen, O	65.5	48.2	91.2	54.1	53.6	51.7	47.9
Silver, Ag	0	0	8.8	1.9	3.7	7.3	10.8

4.3.3 Chemical and Structural Analysis of rGO–AgNs Nanocomposite

The FTIR spectrum of the rGO–AgNs (1:5) nanocomposite in Figure 4.28 (purple line) displays a broad peak at 3260 cm^{-1}, corresponding to the O-H stretching, indicating the sample contains a hydroxyl group and is in an aqueous state. The C=C stretching at 1635 cm^{-1} and O=C=O stretching at 2429 cm^{-1} in rGO-AgNs (1:5) correspond to the rGO carbon-related spectrum. Moreover, the C-H overtone bending at 1865 cm^{-1} and 1957 cm^{-1}, a C≡C alkyne stretching at 2072 cm^{-1}, and C≡N nitrile stretching at 2221 cm^{-1}, corresponding to the capping and reducing agent used in the AgNs. By integrating AgNs into the rGO, the rGO-AgNs (1:5) spectrum shows both the origin spectrum of rGO and AgNs itself, indicating a successful formation of rGO-AgNs hybrid materials, where the Ag nanoparticles remain associated with the functional groups on the rGO surface.

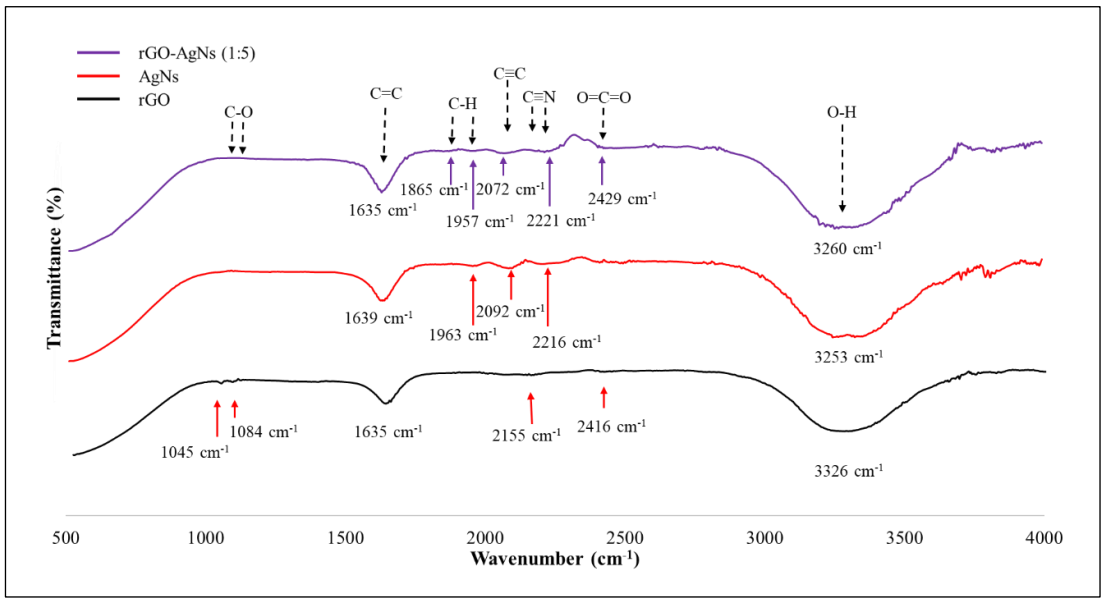

Figure 4.28 FTIR Spectrum on rGO, AgNs, and rGO-AgNs (1:5)

Raman spectra were then obtained for GO, rGO, GO-AgNs (1:5), and rGO-AgNs (1:5), and the spectra were compiled in Figure 4.29 to study the effect of AgNs on the graphene surface. The I_D/I_G of GO was recorded at a value of 0.909. As the AgNs are introduced into GO, the value I_D/I_G of GO-AgNs increases with the value recorded at 0.963, despite the peak intensity of D-band and G-band being weakened. A similar occurrence also happened to the value of the I_D/I_G of rGO as the AgNPs were introduced, where the I_D/I_G value of rGO-AgNs recorded at 1.167 is higher than rGO alone with the value recorded by rGO at 1.102. Similar studies were reported where the increase in the value of the I_D/I_G from rGO (I_D/I_G = 1.00) to AgNPs/RGO (I_D/I_G = 1.20) is due to the attachment of the AgNPs to the surface of the graphene structure (Orellana et al., 2025). This attachment introduces a new defect on the graphene surface, increasing the D-band peak intensity in the Raman spectrum. This explanation aligns with the result in Figure 4.29, where the D-band peak of rGO-AgNs is higher than that of rGO. Moreover, in biosensing applications, Sonawane et al. demonstrated that an increase in the I_D/I_G ratio of graphene properties enhances its interaction with plasmonic fields, indicating stronger coupling with SPR effects (Sonawane et al., 2019). Hence, in comparison between rGO-AgNs (1:5) and GO-AgNs (1:5), a higher value of I_D/I_G ratio, which is rGO-AgNs (1:5), suggests being more suited to be applied in biosensing applications.

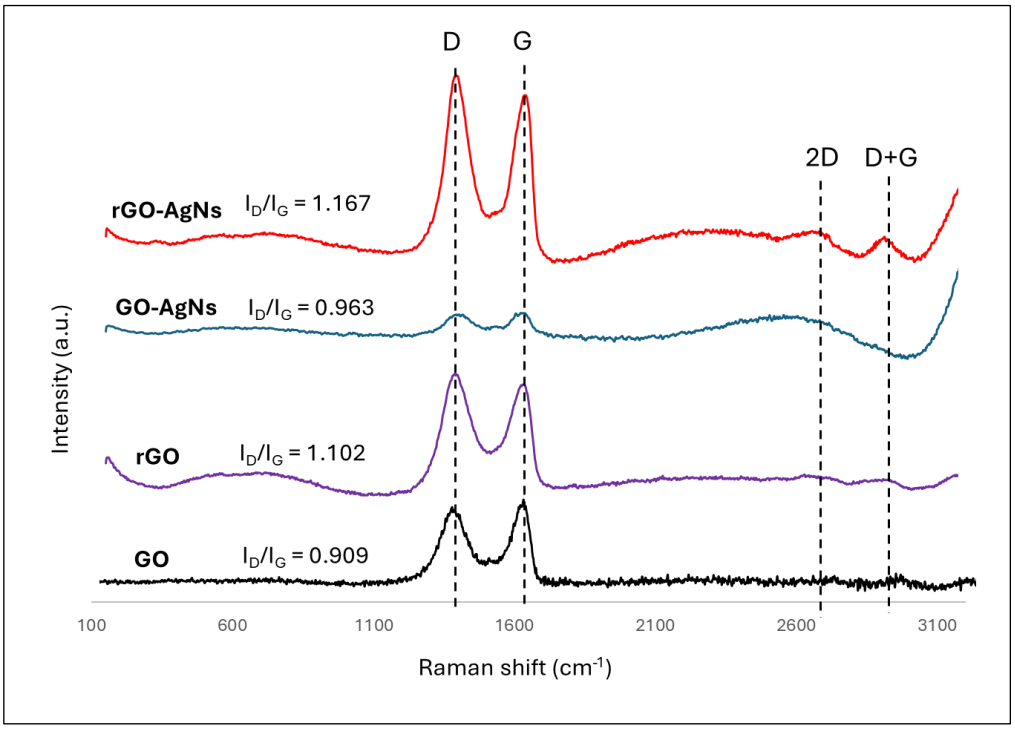

Figure 4.29 Raman Spectrum of GO, rGO, GO-AgNs (1:5), and rGO-AgNs (1:5)

4.4 Phase 3: Characterization of Optical Fibre Coated with Sensing Materials (AgNs, rGO, and rGO-AgNs)

4.4.1 SEM and EDX Analysis

Figure 4.30 shows SEM images of the surface structure of fibre-optic coatings with rGO at different ratios. These images enabled the measurement of the average thickness of the coated fibre optics after 24 hours of dip-coating. The image shows that the fibre-optic coated with rGO alone exhibits a 122.6 ± 0.5 µm diameter. Meanwhile, the thickness of rGO-AgNs (1:5) manages to record a 123.0 ± 0.8 µm diameter length, followed by rGO-AgNs (1:10) with a diameter of 123.3 ± 0.9 µm, 123.7 ± 0.5 µm diameter length for rGO-AgNs (1:15), and 124.9 ± 1.7 µm diameter length for rGO-AgNs (1:20). As the volume of AgNs increases, the thickness of the cladded fibre increases, indicating more AgNs were cladded on the surface.

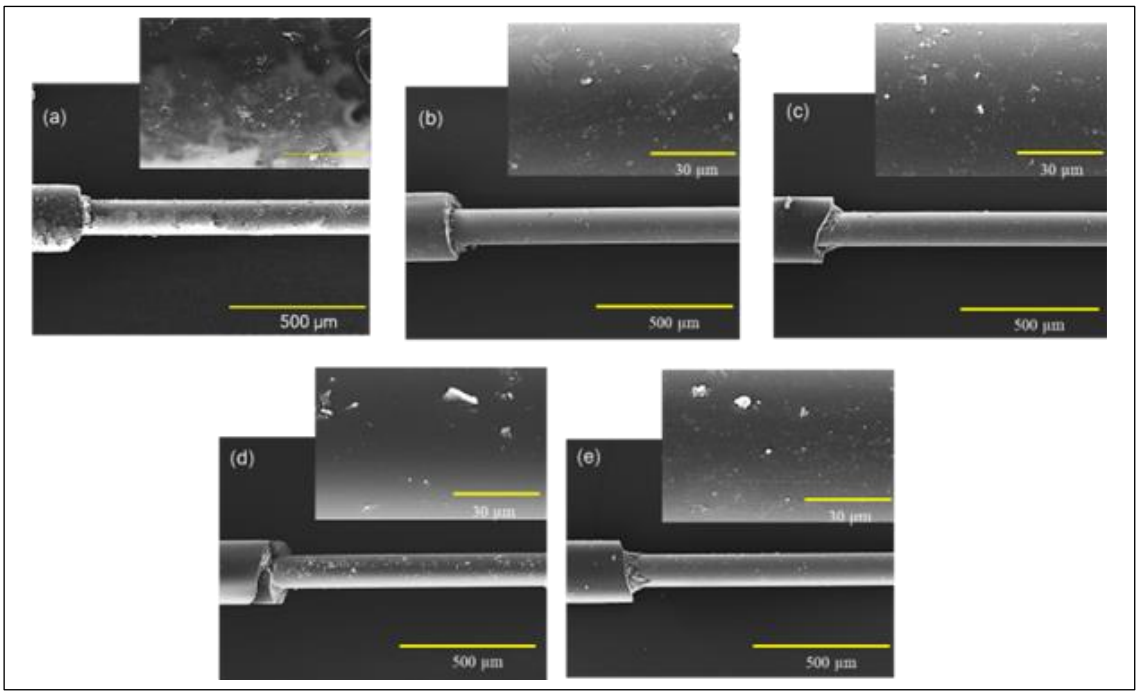

Figure 4.30 SEM Images of the Sensing Platform Coated with (a) AgNs, (b) rGO, and rGO-AgNs with a Ratio of (c) 1:5, (d) 1:10, (e) 1:15, and (f) 1:20

Based on the EDX diagnosis in Table 4.5, the C element reading on all ratios of rGO-AgNs manages to record a reading higher than rGO alone due to the special characteristic of AgNs in enhancing the surface coverage of rGO, allowing better signal and reading detection during the diagnosis process. With AgNs, rGO-AgNs (1:10)

manage to record the highest C element value, followed by rGO-AgNs (1:20), rGO-AgNs (1:15), and rGO-AgNs (1:5).

Table 4.5
EDX Analysis and Thickness Measurement of Uncoated and Coated Fibre Optics Probes with AgNS, rGO, and rGO-AgNS at Various Mixing Ratios

Element (*at.*%)	**Carbon, C**	**Oxygen, O**	**Silver, Ag**	**Silica, Si**	**Thickness (µm)** (From SEM image)
AgNS	7.0	58.9	0.1	36.0	122.0 ± 1.0
rGO	0.9	46.7	0	52.4	122.6 ± 0.5
rGO-AgNS 1:5	5.3	45.7	0.2	48.9	123.0 ± 0.8
rGO-AgNS 1:10	9.6	45.0	0.1	45.3	123.3 ± 0.9
rGO-AgNS 1:15	5.4	44.0	0.1	49.6	123.7 ± 0.5
rGO-AgNS 1:20	6.5	44.7	0.2	48.6	124.9 ± 1.7
Uncoated optical fibre	59.69	36.76	0	3.5	121.1 ± 0.2

rGO-AgNs (1:5) manage to record 5.3% of atomic percentage for the C element and 0.2% for the Ag element. As the volume of AgNs increases by 5 parts, the percentage of the C element increases to 9.6%, indicating that more rGO composition was deposited on the surface of the optical fibre. However, the decrease in the percentage of the Ag element is due to a watery environment in the colloidal solution, leading to fewer AgNs incorporating onto the surface fibre. As the AgNs content increases, the percentage of C element in rGO-AgNs (1:15) decreases abruptly, while the percentage of Ag element remains constant, which can be explained by the increase in excess water volume within the colloidal solutions. The increase in the volume of excess water dilutes the C element in rGO, reducing its concentration in the mixture. However, as the volume of AgNs reaches 20 parts, the C and Ag elements increase, indicating that the increase in AgNs enhances the reading of the C element slightly. The agglomerated AgNs can be observed on the surface of the coated fibre, appearing as white, pebble-shaped structures as shown in Figure 4.30(e). As the AgNs part increases, the appearance of agglomerated AgNs on the coated fibre increases as well. The cross-sectional area of fibre-optic coatings coated with rGO-AgNs at different ratios will be scanned under SEM to analyse differences in thickness.

Figure 4.31(a) shows the image of the cross-sectional area of the bare fibre optics with a diameter recorded at 120.77 ± 0.3 µm. The appearance of a granular structure on the bare fibre optics represents a sputtered platinum coating. The thickness of rGO-AgNs (1:5) manages to record a diameter length of 120.86 ± 1.69 µm, followed by rGO-AgNs (1:10) with a diameter of 121.34 ± 1.07 µm, 121.39 ± 0.81 µm for rGO-AgNs (1:15), and 121.95 ± 0.94 µm for rGO-AgNs (1:20). As the volume of AgNs incorporated onto the fibre surface increases, the overall diameter of the coated fibre becomes thicker. At the same time, the optical strength of fibre optics decreases. To summarize, although rGO–AgNPs (1:20) produce a thicker coating on the fibre optics, rGO–AgNPs (1:5) are more suitable for the next objective due to their stronger optical performance compared to rGO–AgNPs (1:20). Therefore, fibres coated with rGO–AgNs (1:5) will be used in the subsequent stage, where they will undergo surface enhancement before integrating them with hydrogels.

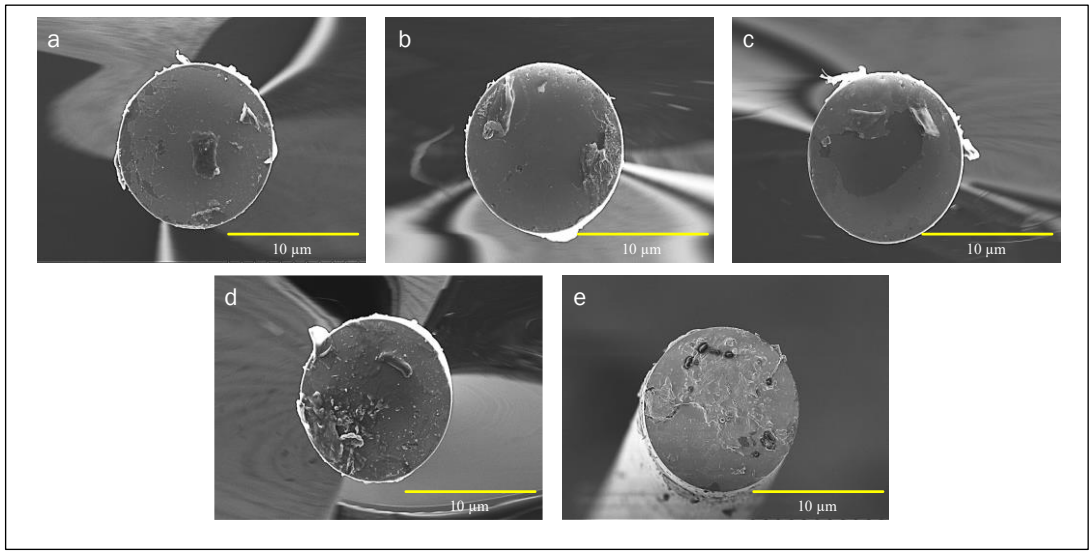

Figure 4.31 Surface of Cross-Sectional Structure of the (a) Uncoated/Bare Fibre Optics (a) and Fibre Optics Coated with rGO-AgNs with a Ratio of (b) 1:5, (c) 1:10, (d) 1:15, and (e) 1:20

4.4.2 Signal Sensor on Fibre Optics Coated with The Sensing Materials

Signal detection from fibre-optic-coated rGO-AgNs with different ratios will be recorded to study the effect of the sensing medium on the fibre optic. Before proceeding with the study of signal performance, the coating duration for rGO–AgNs with different ratios on the optical fibre needs to be optimised to ensure sufficient coating while maintaining strong light transmission through the fibre. Therefore, the coating time of

the core fibre optics will be studied, with coating times set at 6, 12, and 24 hours to determine the optimal duration that yields the highest peak intensity.

The signal strength of the fibre-coated was recorded and compiled in Figure 4.32, and the highest peak intensity for each spectrum is recorded in Table 4.6. Based on the peak intensity produced by the fibre-coated AgNs for 6 hours, the fibre-coated AgNs exhibit 2774 a.u. of light intensity, while the rGO-coated AgNs exhibit 1363 a.u. of light intensity. Moreover, the result also shows that the fibre optic coated rGO-AgNs (1:5) manage to exhibit the highest intensity with a record of 5613 a.u., followed by rGO-AgNs (1:10) exhibiting at 5104 a.u., rGO-AgNs (1:15) producing a 4151 a.u. of light intensity, and a 3149 a.u. of light intensity exhibited by rGO-AgNs (1:20).

Table 4.6
Signal of Light Intensity Reading Detected when the Sensing Platform of Fibre Optic Probe Coated with AgNs, rGO, and rGO-AgNs at Various Mixing Ratios

Sensing Material	6 hours (a.u.)	12 hours (a.u.)	24 hours (a.u.)
AgNs	2774.68	2745.95	3148.47
rGO	1363.63	2573.37	3536.48
rGO-AgNs 1:5	5613.26	6042.47	7287.79
rGO-AgNs 1:10	5104.00	5150.08	6582.42
rGO-AgNs 1:15	4151.63	4177.63	5349.11
rGO-AgNs 1:20	3149.74	3235.95	4797.32

Upon coating the fibre with the sensing medium for 12 hours, the signal performance improved, with the rGO-AgNs exhibiting a stronger intensity than the peak intensity produced by a fibre coated for 6 hours. Fibre-coated AgNs manage to exhibit an intensity of 2745 a.u. alone, while fibre-coated rGO exhibits a light intensity of 2573 a.u. The consistent peak intensity observed for fibre-coated AgNs (12 hours) shows that 6 hours is sufficient to coat the bare fibre, as there is no improvement in signal intensity with extended coating time. In contrast, fibre-coated rGO (12 hours) shows significant improvement over fibre-coated rGO (6 hours), indicating that the extended coating time allows rGO to further overlay the bare fibre, yielding better signal performance. As for the rGO-AgNs 12-hour fibre coating, a ratio of 1:5 sensing medium manages to exhibit the strongest signal, with light intensity recorded at 6070 a.u. followed by a ratio of 1:10, 1:5, and 1:20 with a signal strength recorded at 5150 a.u., 4177 a.u., and 3235 a.u.

As for the 24 hours of dipping time, the signal performance was slightly enhanced with fibre-coated AgNs, and rGO alone achieved signal strengths of 3148 a.u. and 3536 a.u. The signal performance of fibre-coated rGO-AgNs with different ratios manages to surpass the signal strength of fibre-coated AgNs and rGO alone. Among the fibre-coated rGO-AgNs, a sensing medium with a ratio of 1:5 manages to exhibit the strongest signal with the light intensity of 7287 a.u., followed by 1:10, 1:15, and 1:20 with signal strengths recorded at 6582 a.u., 5349 a.u., and 4797 a.u. Despite increasing the AgNs ratio, the declining signal intensity can be attributed to the coating thickness. With the thickness coating reduced, the LSPR effect will diminish due to less light interacting with the rGO-AgNs.

After compiling the collected data, all signal spectra show a similar trend: coating the bare fibre with rGO-AgNs at a 1:5 ratio yields the strongest signal, regardless of coating time. Moreover, the results show that a 24-hour coating time is suitable for coating bare fibres to achieve stronger signal strength. With a stronger signal, the fibre's sensitivity to light will be enhanced, allowing it to detect changes in light wavelength and intensity upon interacting with protein during the application test later. Thus, 24 hours of coating rGO-AgNs (1:5) on the bare fibre will be set as the baseline for the final objectives in studying the protein interactions.

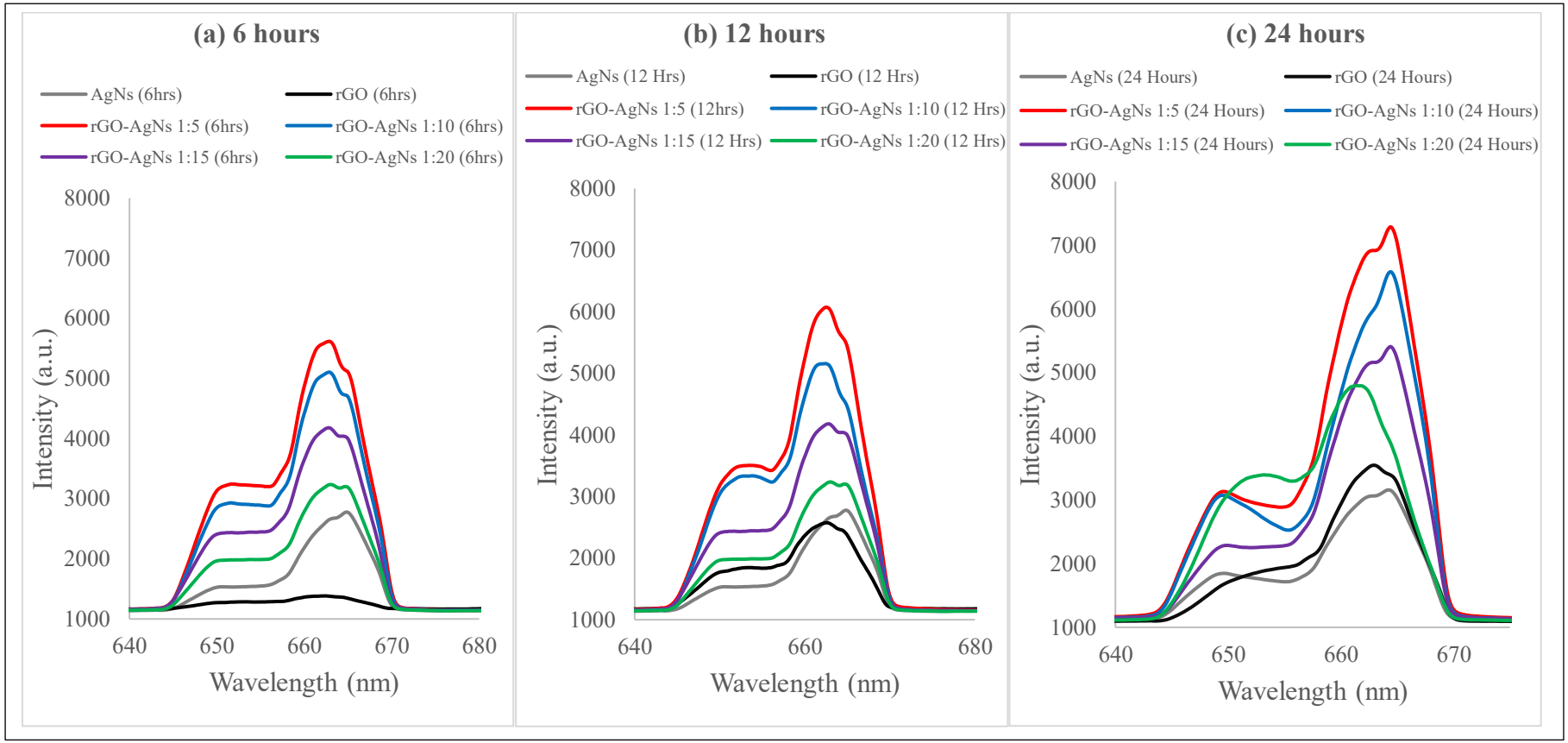

Figure 4.32 Signal Strength on the Fibre Optics Coated rGO-AgNs with Different Ratios for (a) 6 Hours, (b) 12 Hours, and (c) 24 Hours

4.4.3 Effect of Surface Enhancer on Sensing Medium

Multiple methods have previously been reported in which the bare fibre-optic surface was pre-treated with surface enhancers such as chromic acid, ethanol, NaOH, piranha solution, and silane. The purpose of the surface enhancer is to allow the sensing medium to bind strongly with the surface of the fibre, especially on rGO, where it has a hydrophobic characteristic. The hydrophobicity of rGO can hinder its ability to adhere to the bare fibre surface, making it difficult to coat the fibre consistently. Thus, introducing the surface enhancer to rGO-AgNs (1:5) should allow it to be fully coated on the bare fibre-optic surface. The surface enhancement method will be adapted from previous researchers (Akashah et al., 2023), in which the fibre is treated to enhance the binding of GQDs to its surface.

The light-intensity responses of treated and untreated fibre-optic probes embedded with rGO–AgNs (1:5) are presented in Figure 4.34. The NaOH-treated fibre exhibited the highest peak intensity (8061.16 a.u.), followed by chromic acid (4560.58 a.u.), ethanol (4170.21 a.u.), silane (3629.00 a.u.), and piranha solution treatment (3055.84 a.u.). In comparison, the untreated probe recorded a peak intensity of 3016.58 a.u. These results demonstrate that surface modification enhances the adhesion of rGO–AgNs onto the fibre surface, thereby improving optical signal response relative to the untreated probe.

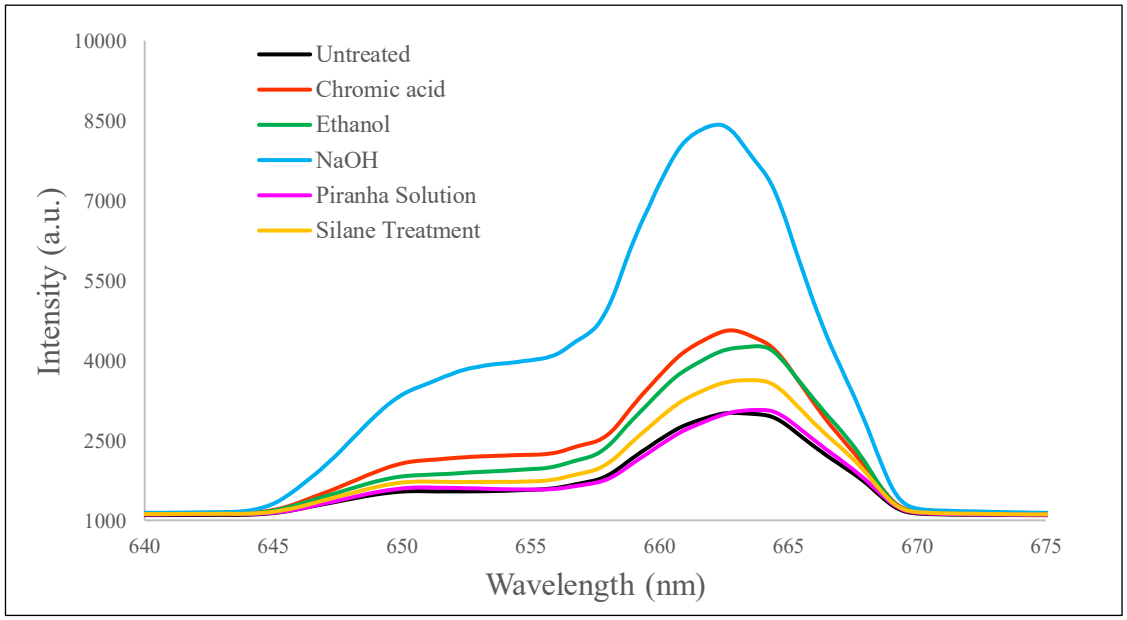

Figure 4.33 Light Intensity on Treated Fibre Optics Coated with rGO-AgNs (1:5)

4.4.3.1 RI Detection

RI detection was then conducted for each treatment using DI water (RI value = 1.3330) and varying glycerol concentrations. The glycerol concentration was set at 1% with an RI of 1.3334, followed by 3% with 1.3339, 5% with 1.3367, and 10% with 1.3488. The purpose of conducting this test is to study whether the RI of the surrounding medium directly correlates with the binding of biomolecules to the sensor surface. This is crucial in biosensing applications, where the binding event on the coated surface alters the evanescent field, which interacts with the plasmonic resonance of the AgNs, leading to measurable changes in the optical properties. These signals were then plotted against the RI value to form a linear line ($\gamma = m\chi + C$), where the slope (m) represents the sensor's sensitivity to RI changes. The coefficient of determination (R^2) was then calculated to assess how well the linear model fits the data; the closer it is to 1, the stronger the correlation between RI changes and the optical signal response.

Based on the linear graph produced in Figure 4.34, the untreated is more responsive to RI changes with a sensitivity value of 18304 intensity/RIU, followed by the chromic acid treated with 17275 intensity/RIU, ethanol treatment with a sensitivity of 15909 intensity/RIU, silane treatment with 14540 intensity/RIU, piranha solution treatment with 9683 intensity/RIU, and NaOH treatment with 4371 intensity/RIU. Yang Cao et al. stated that the slope obtained from the linear regression of the detection signal represents the sensitivity of the detection system (Cao et al., 2018). A larger absolute slope value indicates higher detectability and a stronger response to changes. Conversely, a smaller slope suggests a weaker signal response, indicating lower sensitivity and reduced reliability in detecting changes. Hence, the untreated demonstrates the greatest suitability for enhancing sensitivity compared to other treatments.

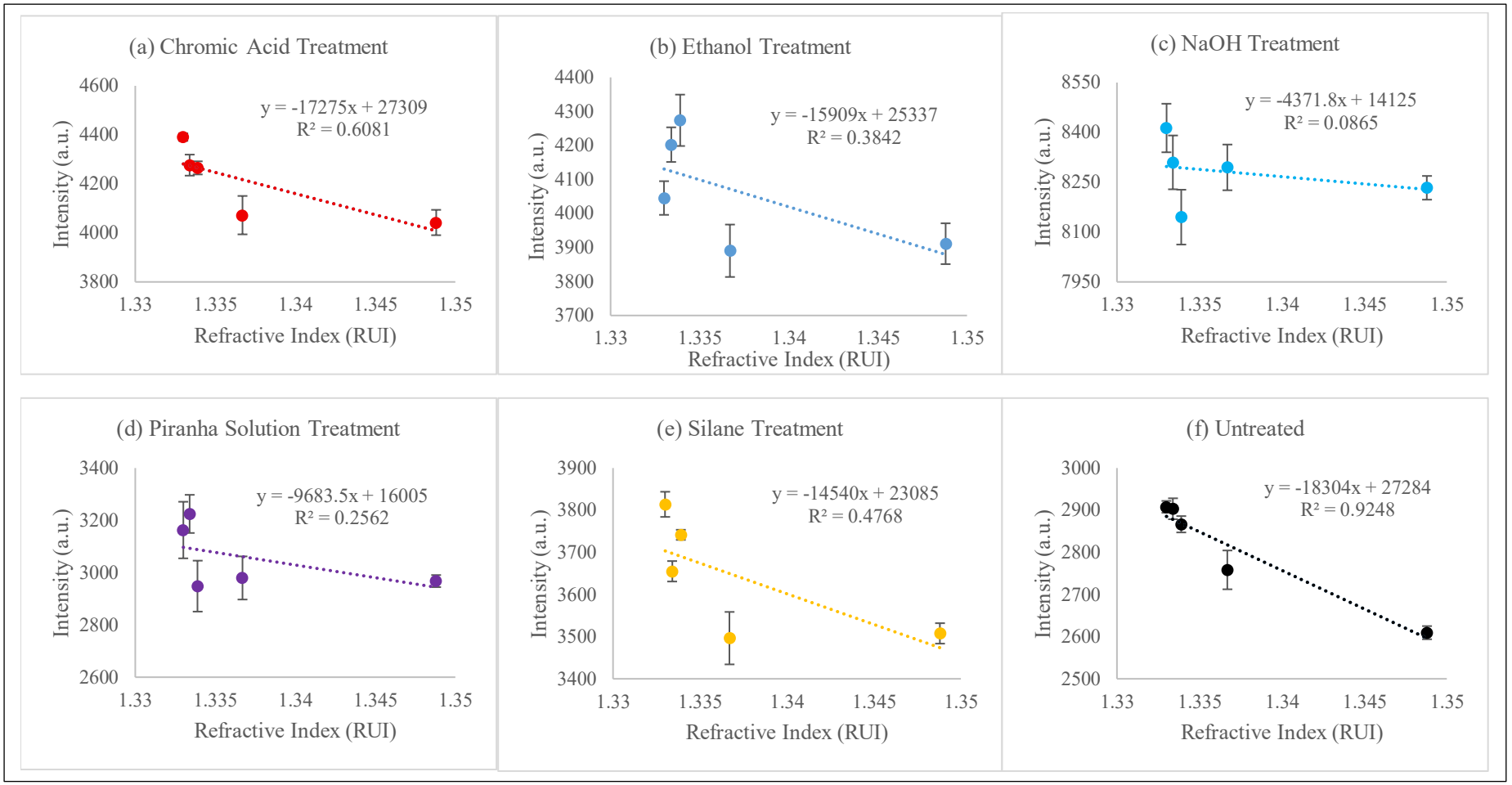

Figure 4.34 RI Detection on Treated Fibre Optics Coated with rGO-AgNs (1:5) with (a) Chromic Acid, (b) Ethanol, (c) NaOH, (d) Piranha Solution, (e) Silane, and (f) Untreated Probe

The linearity of the sensor response was evaluated using the coefficient of determination (R^2). The untreated fibre exhibited the highest linearity (R^2 = 0.9248), followed by chromic acid treatment (0.6081), silane (0.4768), ethanol (0.3842), piranha solution (0.2562), and NaOH treatment (0.0865). Linearity assessment is essential to simplify calibration and ensure accurate interpretation of sensor data, as a higher R^2 value indicates a stronger correlation between the measured output and refractive index variation. Previous researchers state that a linearity of 0.9 or higher ($R^2 \geq 0.9$) is generally considered acceptable to good for many fiber optic biosensor applications, particularly in complex biological or early-stage research (De Acha et al., 2021). Based on these results, the untreated fibre demonstrated the most reliable linear response.

Similarly, while silane, ethanol, piranha, and NaOH treatments produced higher optical intensities during signal performance evaluation, their low R^2 values indicate limited responsiveness and poor linearity, which reduces their suitability for accurate and reliable RI detection in biosensing applications.

To further validate the performance of the proposed sensor, the obtained RI sensitivity was compared with previously reported fibre-optic biosensors. Fibre-optics coated with GQDs-hybrid hydrogels reported a sensitivity of 36,658 ± 0.2335 RIU^{-1}, demonstrating a highly responsive plasmonic interaction under RI variation (Akashah et al., 2023). In another study, fibre-optics embedded with an Ag-Au alloy with support from GST managed to exhibit a sensitivity of 8600 nm/RIU in cancer biomarker detection (Akouibaa et al., 2026). Although the sensitivity values reported in the literature vary depending on the sensing mechanism, coating materials, and detection method, these studies provide a benchmark for evaluating the performance of the current work. In comparison, the untreated fibre in this study demonstrates a comparatively high intensity-based sensitivity response, indicating strong interaction between the evanescent field and the surrounding medium, which supports its suitability for RI sensing applications.

4.4.3.2 Stability of Coating Materials to the Treated Probe

Based on the linear graph produced in Figure 4.34, the untreated is more responsive to RI changes with a sensitivity value of 18304 intensity/RIU, followed by the chromic acid treated with 17275 intensity/RIU, ethanol treatment with a sensitivity of 15909 intensity/RIU, silane treatment with 14540 intensity/RIU, piranha solution

treatment with 9683 intensity/RIU, and NaOH treatment with 4371 intensity/RIU. Cao et al. stated that the slope obtained from the linear regression of the detection signal represents the sensitivity of the detection system (Cao et al., 2018). A larger absolute slope value indicates higher detectability and a stronger response to changes. Conversely, a smaller slope suggests a weaker signal response, indicating lower sensitivity and reduced reliability in detecting changes. Hence, the untreated sample demonstrates the highest suitability for enhancing sensitivity.

The full cycle of the RI detection test on both treated and untreated fibre-optic-coated rGO-AgNs is shown in Figure 4.35, and the results are collected. From the results, the patterns of chromic acid treatment, silane treatment, and untreated fibre are similar, with the peak strength gradually decreasing after multiple uses. Table 4.7 shows the results of calculating the change in peak height to determine how much the signal peak was reduced after the washing process. Despite the untreated fibre showing a consistent decrease in peak as it undergoes multiple washing processes, chromic acid treatment retains its signal strength after the third cycle. As for the silane-treated fibre, the signal after the first cycle of the washing processes increases, suggesting that the sensing medium's surface is free of impurities. The signal strength began to decrease after the second cycle began.

Table 4.7
Recovery Error (%) on Treated and Untreated Fibre Optics Coated rGO-AgNs

Cycle	Untreated	Chromic Acid	Ethanol	NaOH	Piranha Solution	Silane
Water 1	3.7	3.9	43	0.5	0.2	4.9
Water 2	6.4	4.2	1.0	2.6	4.5	1.8
Water 3	7.5	7.0	0.2	4.4	28.1	2.7
Water 4	12.7	6.5	2.0	5.3	1.9	2.9
Water 5	15.6	7.3	5.2	2.1	3.0	3.0

This reduction in signal performance after washing the process multiple times is due to the sensing medium's surface gradually losing its effect as it interacts with water, which dilutes the surface after each use, as in agreement with (Yang & Dai, 2011). Ethanol treatment shows an increase in signal strength after the second cycle of the washing process, yet the signal intensity recorded upon interaction with different RIs decreases as the RI value increases. Despite enhancing the signal strength after the

second washing process, the signal strength recorded across different RI values is attributed to the weak sensitivity and linearity, as previously studied in the RI detection test.

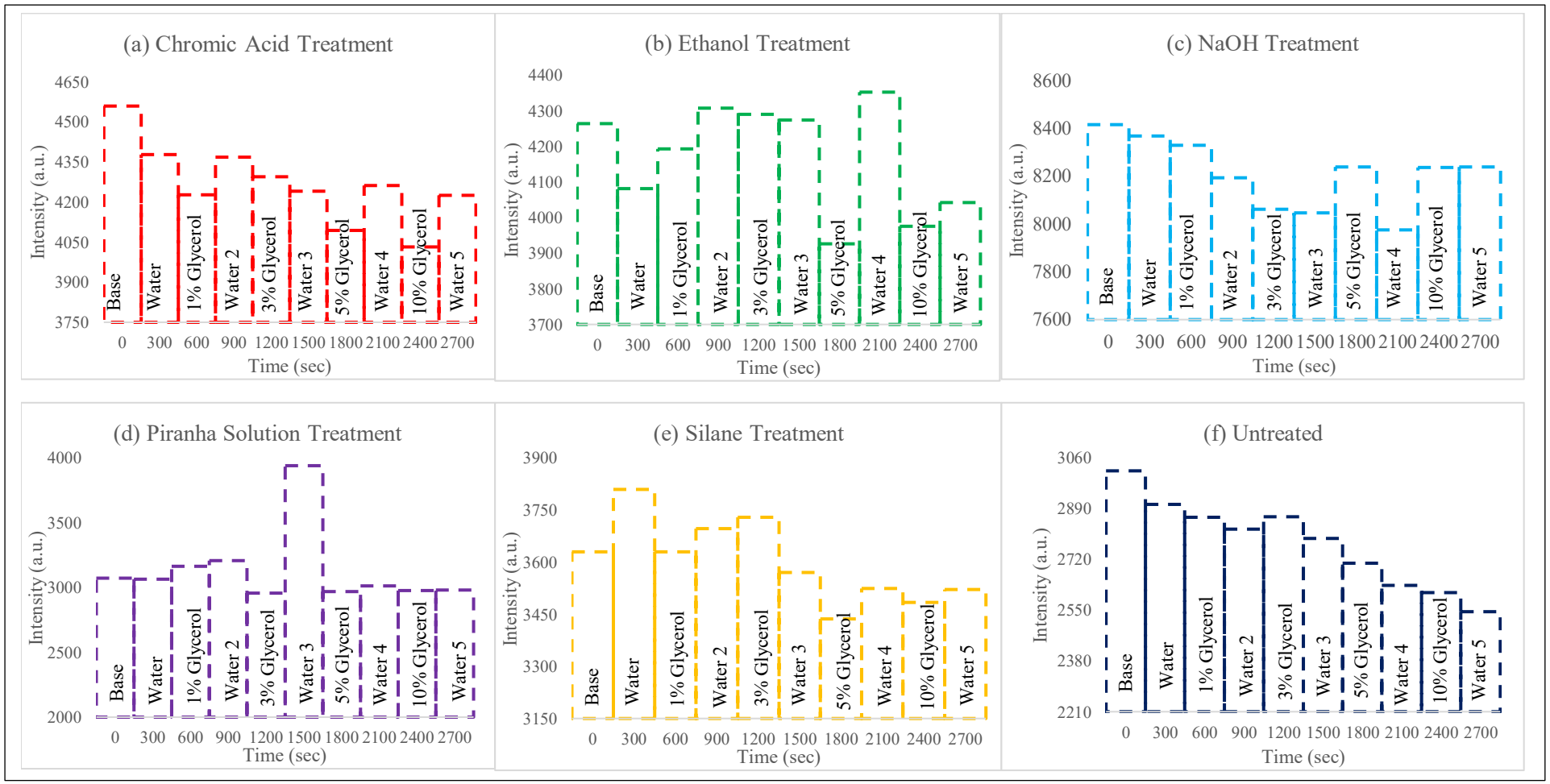

Figure 4.35 Full RI Detection Cycles of rGO–AgNs (1:5)-Coated Fibre-Optic Probes Under Different Surface Treatments: (a) Chromic Acid, (b) Ethanol, (c) NaOH, (d) Piranha Solution, (e) Silane, and (f) Untreated Fibre

Based on As for NaOH treatment, the pattern from the first cycle of the washing process to the fourth cycle follows a standard pattern, with signal performance decreasing over time due to dilution of the sensing medium. However, in the fifth cycle, the signal strength increased, possibly because part of the sensing medium's surface was removed from the effects of dilution and subsequent scraping. The piranha solution treatment showed weak changes during the RI detection test and the washing process, suggesting that the treatment's side effect not only assists in the binding of rGO-AgNs but also affects the structural properties of the sensing medium. The corrosiveness of the treatment may cause material damage to the sensing medium, altering its structural morphology and further affecting the optical performance of the fibre. The recovery error for each treatment was calculated and compiled in Table 4.8 to examine how much signal strength deviates from the baseline peak during the washing process.

Table 4.8
Recovery Error on Untreated and Treated Fibre Coated rGO-AgNs (1:5)

Sensing medium	Baseline peak intensity (a.u.)						Standard deviation (a.u.)	Percentage Error (%)
	Base	Water 1	Water 2	Water 3	Water 4	Water 5		
Untreated	3016.58	2903.89	2821.21	2789.58	2633.63	2545.63	2738.79 ± 147.7	9.21
Chromic Acid	4560.58	4378.26	4368.63	4241.16	4262.42	4226.53	4295.40 ± 71.9	5.81
Ethanol	4264.89	4081.89	4307.84	4275.05	4353.16	4042.53	4212.09 ± 124.5	2.56
NaOH	8417.00	8369.79	8193.79	8047.95	7977.16	8240.47	8165.83 ± 152.2	2.98
Piranha Solution	3070.74	3063.63	3208.05	3936.26	3013.37	2977.95	3239.85 ± 380.3	7.56
Silane	3629.11	3809.53	3696.11	3570.26	3523.53	3521.95	3624.28 ± 112.9	2.86

Table 4.8, the untreated fibre exhibited the highest recovery error of 9.21%, indicating larger signal variation during repeated washing cycles. In contrast, fibres treated with ethanol, NaOH, and silane demonstrated lower percentage errors of 2.56%, 2.98%, and 2.86%, respectively, suggesting improved signal stability and more consistent recovery behaviour. Meanwhile, the chromic acid-treated fibre showed

moderate stability with an error of 5.81%, while the fibre treated with piranha solution recorded an error of 7.56%, indicating relatively higher signal fluctuation. These results suggest that certain surface treatments can improve the repeatability of the fibre sensor by enhancing surface cleanliness and coating adhesion.

Although the uncoated fibre exhibited a slightly higher recovery error compared to some surface-treated fibres, it demonstrated the highest RI sensitivity and linearity during the sensing experiments. In optical sensing applications, sensitivity is considered a more critical parameter than repeatability alone because it determines the capability of the sensor to detect small changes in the surrounding refractive index (Wang et al., 2025). While surface treatments such as chromic acid improved signal stability and baseline intensity, they also reduced the magnitude of signal change when exposed to different sensing media. The uncoated fibre, however, showed a larger variation in peak response with increasing glycerol concentration, indicating stronger interaction between the sensing layer and the surrounding environment. Hence, despite its relatively higher recovery variation, the uncoated fibre was selected for subsequent sensing experiments due to its superior sensitivity and overall sensing performance. Therefore, considering both RI sensitivity and recovery behaviour, the untreated fibre-coated rGO–AgNs (1:5) was selected as the most suitable platform for further integration of an HH for protein detection.

4.5 Phase 4: Embedding rGO-AgNs-HH on the Sensing Probe

4.5.1 Signal Detection

The main purpose of introducing HH into the sensing medium is to allow the activity of protein detection to be detected on the surface of the fibre coated rGO-AgNs (1:5). Anna et. al. state that the hydrogel offers a highly aqueous and biocompatible environment that supports higher loading of recognition elements and preserves the stability and activity of biomolecules, which is essential for reliable biosensing (Herrmann et al., 2021). Thus, introducing HH into the detection system will provide a stable, hydrated interface for protein immobilization on the surface of the coated fibre. Moreover, the presence of HH will support protein activity and enhance interaction with the sensing surface, thereby improving the sensitivity and reliability of protein detection (Herrmann et al., 2021).

A simple optical strength test was conducted on each sequence variation, and the result in Figure 4.36 shows the rGO-AgNs-HH interact strongly with light, followed by HH-rGO-AgNs and rGO-AgNs-HH (mixed). The peak intensity from the variation sequence in Figure 4.36 shows that rGO-AgNs-HH interacts strongly with light at 9179 a.u. followed by HH-rGO-AgNs with 7582 a.u. of light intensity and rGO-AgNs-HH (mixed) with 7261 a.u. of light intensity.

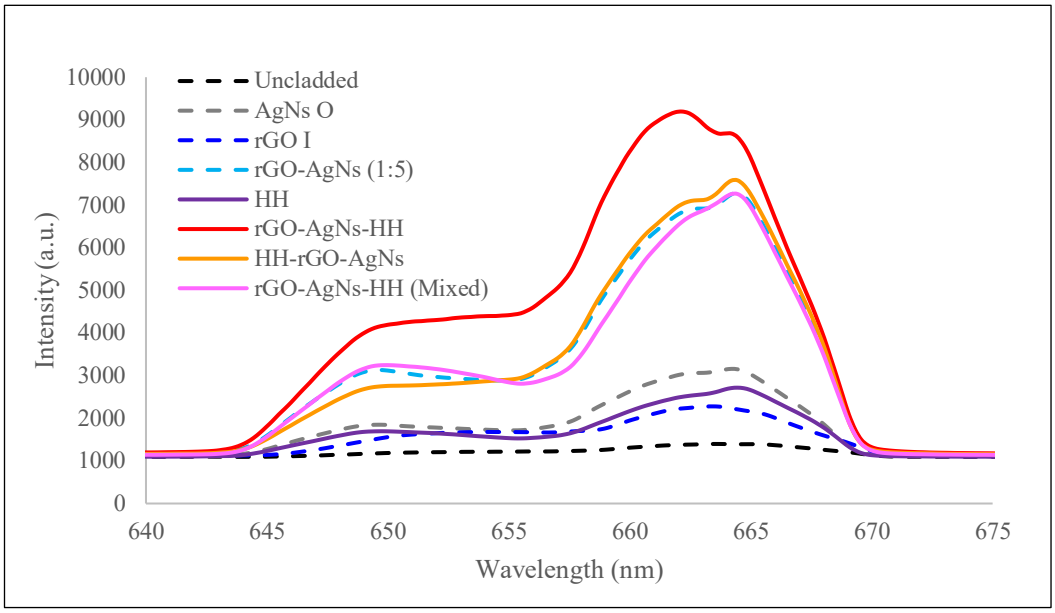

Figure 4.36 Peak Intensity of Different Variations of rGO-AgNs-HH

The results from rGO-AgNs-HH align with the theory: the rGO-AgNs in the first layer strongly interact with the light passing through, and the HH of the second layer acts as a protective layer, reflecting light back toward the fibre and allowing more light to be detected (Zhang et al., 2018). It is possible because HH has a slightly different RI than the surrounding medium, trapping the evanescent field within the sensing region rather than allowing it to leak out, thereby increasing TIR efficiency. Moreover, using HH as the first layer might weaken the penetration of the evanescent wave, as it is trapped there, leading to a lack of light interacting with the second layer of rGO-AgNs.

Even so, optical fibre coated with HH-rGO-AgNs still manages to record the intensity of light surpassing the intensity recorded by fibre-coated rGO-AgNs (1:5). Hence, with the integration of rGO-AgNs into the HH structure, the evanescence wave that was trapped inside should be able to interact with AgNs to enhance the strength of the field waves through the LSPR effect.

However, the peak light intensity recorded indicates that the field wave strength enhancement is weak, indicating no improvement compared to the peak produced by fibre-coated HH-rGO-AgNs. This situation might be due to the water content in HH diluting the concentration of rGO-AgNs, thereby affecting the LSPR performance of AgNs. Dilution weakens the LSPR effect, thereby preventing a significant enhancement of the trapped evanescent wave. Despite this, the recorded light intensity is on par with the peak intensity recorded for fibre-coated rGO-AgNs (1:5). In conclusion, the rGO-AgNs-HH configuration shows promising potential for further evaluation in protein detection tests.

4.5.2 SEM and EDX

The surface of the fibre-coated rGO-AgNs-HH was then subjected to SEM imaging to study the surface structure of the sensing medium. Figure 4.37(a) shows the surface morphological structure of the sensing medium with rGO-AgNs as the first layer and a transparent hydrogel on the second layer. The thickness of the coated fibre recorded is 124.160 ± 0.6 μm, which is thicker than that of the fibre coated with rGO-AgNs (1:5) alone. A closer look reveals a clear flaky surface structure in Figure 4.37(b), indicating the presence of rGO-AgNs from the first layer, with a smooth background originating from HH as the second layer. The transparency of HH allows the rGO-AgNs to be clearly visible on the surface compared to those without HH. The cross-sectional image of the coated fibre was captured as shown in Figure 4.37(c), with a diameter length of 124.162 ± 4.7 μm. It can be seen clearly at the cleaved surface in Figure 4.37(d), where the irregular structure suggests it originates from the damaged hydrogel and contains rGO-AgNs within the matrix.

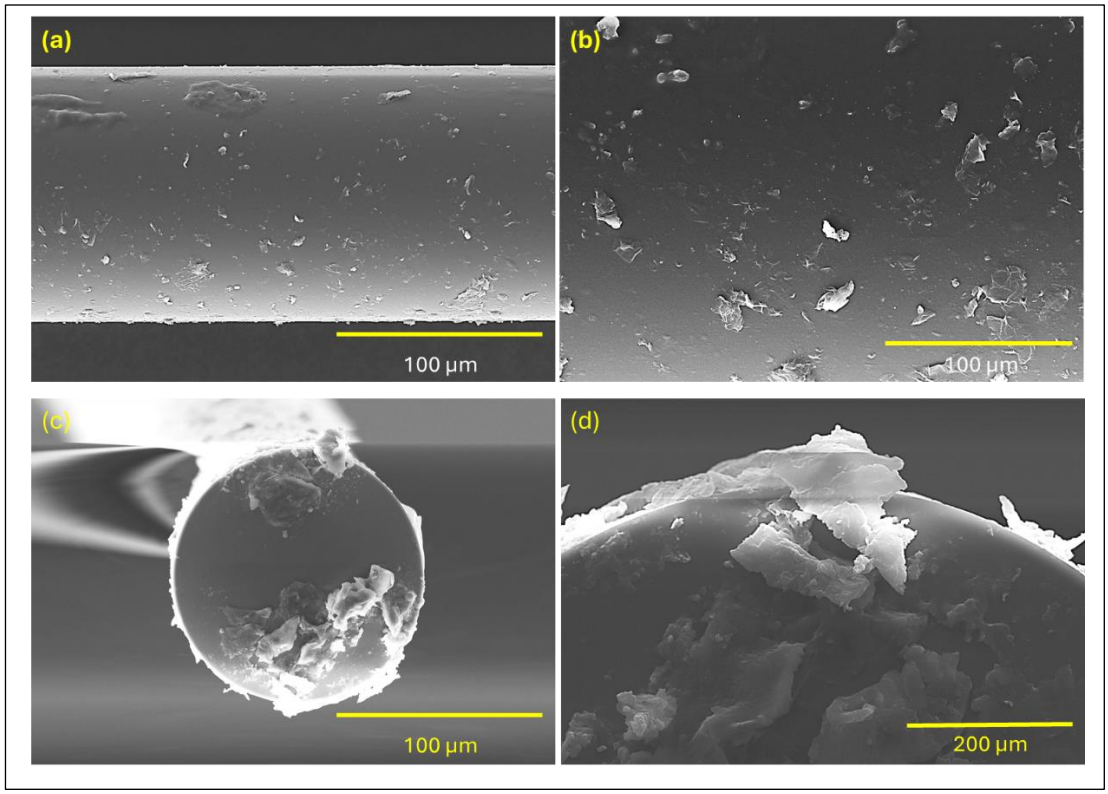

Figure 4.37 SEM Images of rGO–AgNs–HH-Coated Fibre-Optic Probes Showing Side-View Morphology (a, b) and Cross-Sectional Structure (c, d) at Low (a, c) and High Magnifications (b, d)

EDX analysis was conducted to study the composition of the structure on the cleaved surface. However, elemental analysis will be performed using both spot and area scanning on the cleaved surface, as shown in Figure 4.38, due to high silica and oxygen composition readings masking the detection of carbon and silver. The results from area and spot scanning were compiled in

Table 4.9. The area-scanning results show that the oxygen element records the highest reading at 40.4%, followed by carbon (35.1%), silica (24.5%), and silver (0%). In comparison with fibre optics coated with rGO-AgNs (1:5), with element reading recorded for oxygen (45.7%), carbon (5.3%), silica (48.9%), and silver (0.2%). The explosive increase in the C element is attributed to the presence of HH in the outer layer. Chitosan is a natural polysaccharide derived from chitin and agarose is also another form of polysaccharide. Both are primarily composed of carbon, hydrogen, and oxygen (Teixeira-Costa & Andrade, 2021) which explains the sudden increase in the C element. Moreover, the undetected Ag element is due to the AgNs hidden within the rGO in the first layer. However, upon spot scanning of the cleaved surface, a small amount of AgNs

was detected in each spot, suggesting that cleaving the sensing medium breaks its matrix, leaving only large granules on the fibre surface. This occurrence explains the increase in the cross-sectional diameter of the coated fibre relative to its surface diameter.

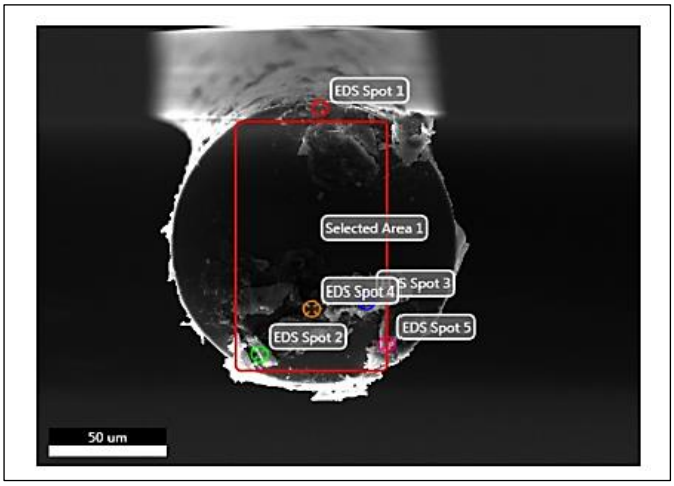

Figure 4.38 EDX Spot and Area Analysis of the Cross-Sectional Area on the Surface of Cleaved Fibre Optics Coated rGO-AgNs-HH

Table 4.9
Element Composition on the Surface of the Cleaved Fibre Optics Coated rGO-AgNs-HH

Element (*at.*%)	**Area**	**Spot 1**	**Spot 2**	**Spot 3**	**Spot 4**	**Spot 5**
Carbon, C	35.1	24.0	71.0	65.4	63.7	62.8
Oxygen, O	40.4	37.0	24.0	34.0	35.7	63.3
Silver, Ag	0.0	0.1	0.1	0.1	0.2	0.1
Silica, Si	24.5	38.9	4.9	0.4	0.4	0.8

4.6 Phase 4: Signal Sensing (RI Sensitivity and Stability) on Fibre-Coated rGO-AgNs-HH

4.6.1 RI sensitivity

Sensitivity test where different concentrations of glycerol will interact with the sensing medium to study the relationship between the rGO-AgNs-HH and the changes in RI value. The linearity line, formed by plotting peak intensity against changes in RI, was recorded, as shown in Figure 4.39. From the linearity line, the sensitivity of fibre-

coated rGO-AgNs-HH manages to record 63132 intensity/RUI, which is stronger compared to fibre-coated rGO-AgNs (1:5) with intensity recorded at 18304 intensity/RUI. Moreover, the linearity of fibre-coated rGO-AgNs-HH manages to record a value of 0.8012, which is slightly less than fibre optic-coated rGO-AgNs (R^2 = 0.9248). Despite the enhancement of the sensitivity with the changes of the RI medium, the coefficient of determination for the fibre-coated rGO-AgNs-HH is still within an acceptable range.

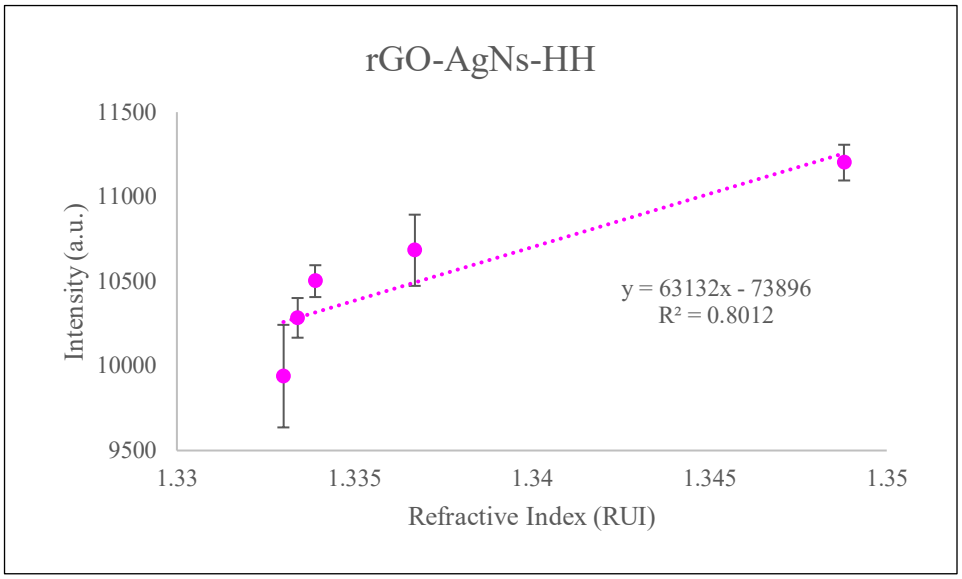

Figure 4.39 RI Sensitivity and Linearity Performance of Fibre-Coated rGO-AgNs-HH

4.6.2 Stability - Recovery Error on Fibre-Coated rGO-AgNs-HH After Washing Processes

During the RI detection test, the washing process on the sensing medium was performed each time it interacted with a glycerol of a different RI value. Figure 4.40 shows the flow of RI detection and its washing process over time, and the results indicate that the signal performance after washing remained consistent from the first to the fourth cycle. Despite the increase in signal strength during the fifth cycle, the recovery error indicates that the peak drift occurs at similar error rates compared to other cycles, as shown in Table 4.10. The improved consistency in recovery error is likely attributed to the incorporation of the HH as the second coating layer. The HH functions as a protective matrix, shielding the underlying rGO–AgNs layer from dilution and mechanical disturbances during repeated measurement cycles. This

protective effect enhances structural stability and preserves the integrity of the sensing interface.

As a result, RI measurements during glycerol exposure remain more stable and reproducible. The introduction of HH significantly improved recovery performance, with recovery error reduced from 9.21% for the untreated rGO–AgNs-coated probe (see section 4.5.3.2) to 2.92% after the addition of the HH protective layer. This demonstrates that the dual-layer configuration enhances durability, repeatability, and overall sensing reliability.

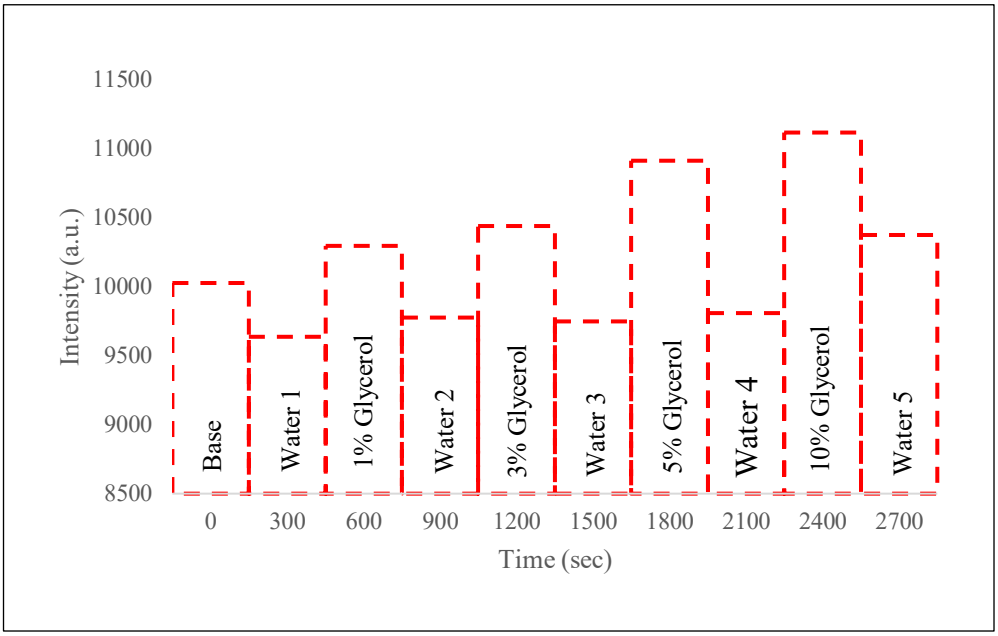

Figure 4.40 Full Test Cycle of the RI Detection Test on Fibre Optics Coated rGO-AgNs-HH

Table 4.10
Recovery Error on Fibre Optics Coated rGO-AgNs-HH

Sensing Medium	Baseline peak intensity (a.u.)						Percentage Error (%)
	Base	Water 1	Water 2	Water 3	Water 4	Water 5	
rGO-AgNs-HH	10026.21	9636.53	9773.05	9747.21	9805.16	10371.53	2.92

4.7 Phase 5: Binding Kinetics and Porosity of Sensor Probe

4.7.1 Porosity of Sensor Probe

The signal response of the fibre sensor in the presence of 1% glycerol and 0.75% BSA was recorded in Figure 4.41. The test began by collecting the RI value of 1% glycerol and 0.75% BSA, with both RI values recorded at 1.3346. The use of two different media with similar RI values in this test allows the evaluation of the immobilization capability of the sensing medium while minimizing the influence of refractive index variation. In this case, glycerol and BSA possess significantly different molecular sizes, with BSA having a much larger molecular structure compared to glycerol despite having similar RI values (Husband et al., 2001), making it a suitable material for testing the porosity of the sensing system. When introducing 1% glycerol to the sensor system, a slight increase in signal intensity was observed at 663 nm with signal enhanced from 9942 a.u. to 10147 a.u., indicating that the glycerol molecules were able to diffuse and interact with the sensing surface. However, when introducing the 0.75% BSA on the microfluidic channel, the signal began to amplify to 11008 a.u., suggesting that the BSA molecules were successfully immobilized closer to the fibre core region, producing a stronger interaction with the evanescent field. A previous study was conducted where molybdenum disulfide and gold plate were used to coat the plastic fibre optics in detecting BSA (Kaushik et al., 2019). The BSA concentration was set with a range from 10 μg/mL to 50 μg/mL to show the interaction between biosensor and BSA (protein), and the result shows that the peak signal continues to red-shift in resonance wavelength as the BSA concentration introduced increases. Kaushik et al. also state that the red-shift resonance is due to the protein successfully immobilized within the sensing medium, changing the local RI (Kaushik et al., 2019).

Hence, these findings suggest that the rGO-AgNs-HH matrix manages to provide sufficient porosity for biomolecule diffusion, which allows effective interaction between the target protein and the plasmonic sensing interface.

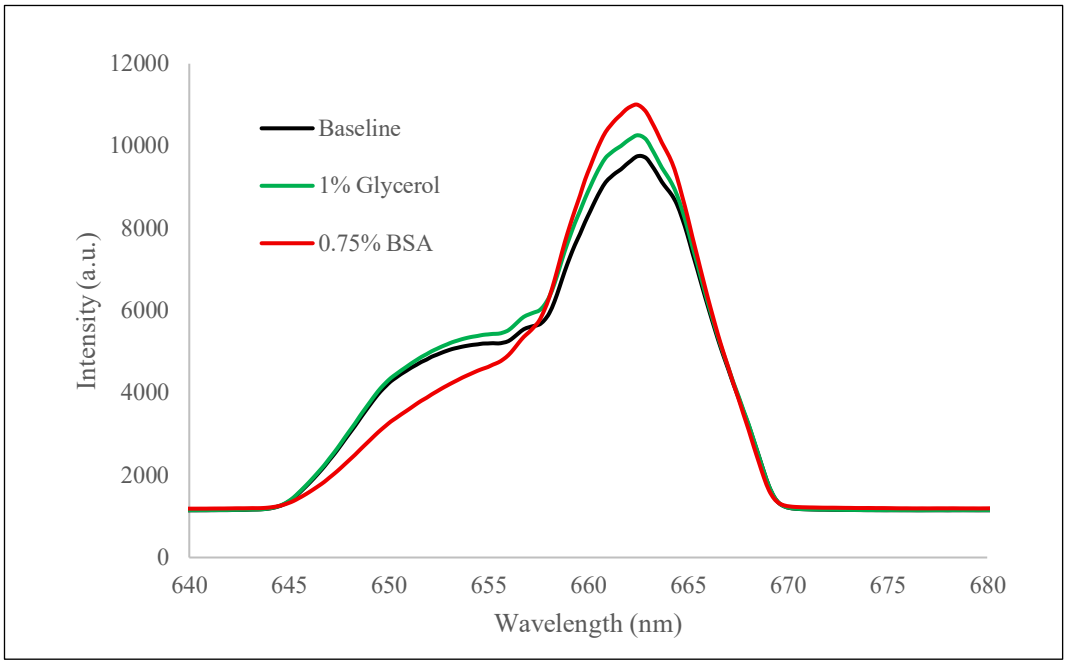

Figure 4.41 Porosity Test on Fibre Optics Coated rGO-AgNs-HH

4.7.2 Detection of Protein (Streptavidin-Biotin) Interactions on The Sensing Probe

To determine if the sensing medium can interact with the proteins, streptavidin and biotin were introduced into this test. Streptavidin is a protein isolated from the bacterium Streptomyces avidinii, and biotin is a water-soluble vitamin (B7 or H) that is essential for many biological processes (Balzer & Whitehurst, 2023). Streptavidin has a remarkable affinity for biotin due to special pockets on its surface that bind biotin strongly. Upon contact, hydrogen bonds and van der Waals interactions on the pocket surface hold biotin tightly and stably, due to the excellent fit between biotin and the pocket. This highly specific interaction will allow the sensor-coated streptavidin to selectively capture biotin, making it a reliable approach for protein detection. Upon binding, changes in the local optical environment of the sensing layer will result in a measurable shift in peak intensity, indicating successful detection of protein interaction. Haziq et. al. managed to record a shift in the signal performance produced by fibre-coated HH-GQDs upon introducing the streptavidin and biotin, indicating that the protein interactions' activity was detected on the surface of the coated fibre (Noor Akashah, 2022). These findings will be used as a reference to confirm successful detection of the protein's activity.

A protein detection test was then conducted, where the peaks of the baseline and PBS were recorded at 662.41 nm in Figure 4.42. Streptavidin was then dropped onto the surface of the sensing medium, and the peak was successfully recorded at 662.92 nm. A slight red shift in the peak indicates that the protein binds to available sites within the hydrogel structure, as shown by the arrow in the inset Figure 4.42 (a). A PBS was then dropped and the peak intensity at 662.92 nm weakened as seen in Figure 4.42 to remove the unbound streptavidin.

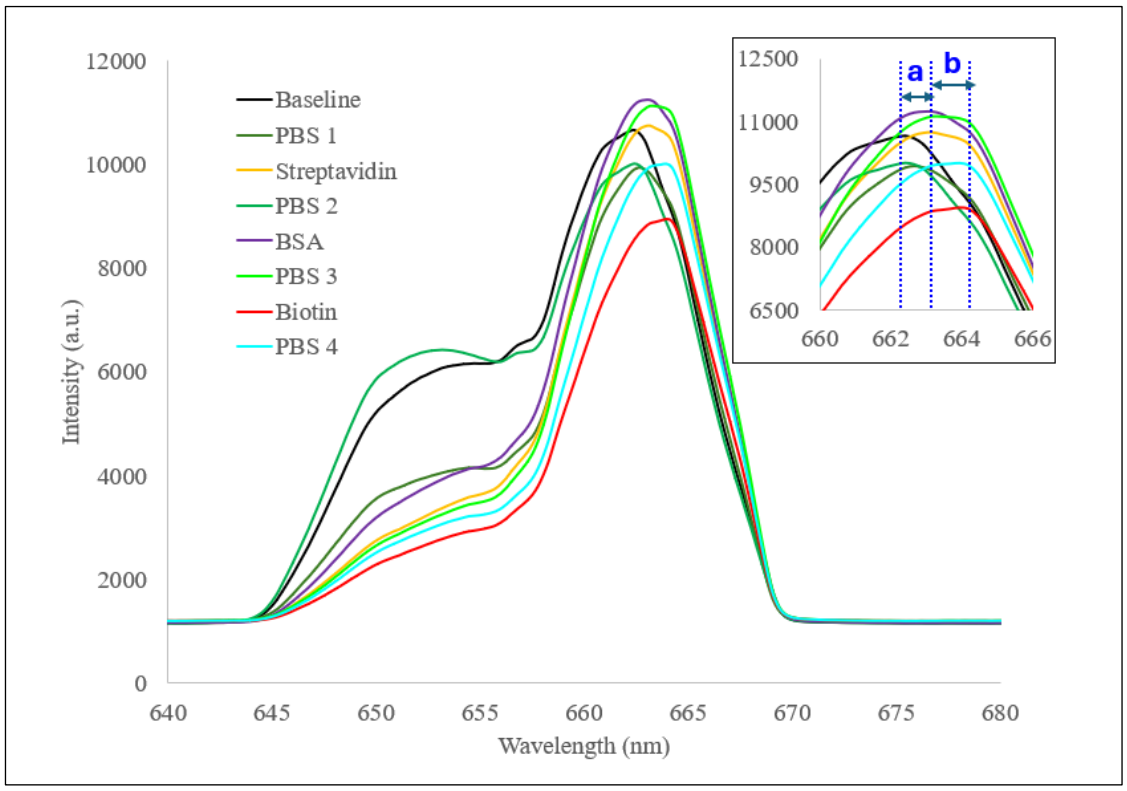

Figure 4.42 Protein Detection of Fibre-Coated rGO-AgNs-HH

The blocking agent of BSA was then introduced on the surface of the sensing medium, and the result shows that the peak was recorded at 663.17 nm. A small shift suggests that most of the streptavidin had already occupied the available binding pockets, and only a small number of unoccupied sites were accessible to the blocking agent. The PBS was then introduced again to wash away the unbound BSA so that it does not interfere with the binding of biotin, causing the signal intensity to weaken. Biotin was then released to allow it to interact with streptavidin, and the result showed that the peak intensity was recorded at 664.2 nm when biotin was released. This significant change indicates that a large quantity of biotin successfully bound to the

immobilized streptavidin (see arrow in inset Figure 4.49, b), thereby confirming the sensing medium's ability to detect and target specific biomolecular binding events. Upon complete detection of the protein interaction, the PBS was applied to the channel, with the signal peak not shifting and only showing an increase in intensity. This result confirms that the biotin successfully binds with streptavidin permanently after being washed with PBS and the increase in signal intensity indicates the interaction with PBS RI.

4.7.3 Specificity of Detection

Before undergoing a protein detection test, a simple specificity test will be conducted, where the streptavidin will be removed from the process. The procedure began by recording the baseline peak as seen in Figure 4.43 before dropping the PBS on the surface of the fibre-coated rGO-AgNs-HH as a washing process. BSA was then dropped on the biosensor as the blocking agent to prevent unnecessary binding within the HH layer. Previous researchers reported that BSA interacts with the hydroxyl and amino groups of chitosan mainly through hydrogen bonding, reducing the availability of these sites for non-specific adsorption (Balzer & Whitehurst, 2023). This blocking effect prevents other molecules from binding non-specifically to the hydrogel, which allows the intended specific interaction to occur. Biotin was then dropped on the surface of the sensing medium, interacting with any remaining unoccupied sites. With no bioreceptors to hold onto, the result in Figure 4.43 (inset) shows that there is no shift in peak when the biotin was introduced, suggesting no interactions occurred on the selective binding sites. Subsequently, the washing process with PBS also indicates that no biomolecules were immobilized during the interaction with BSA and biotin, indicating the increase in signal intensity signifies the interaction between rGO-AgNs-HH with a medium of different RI values.

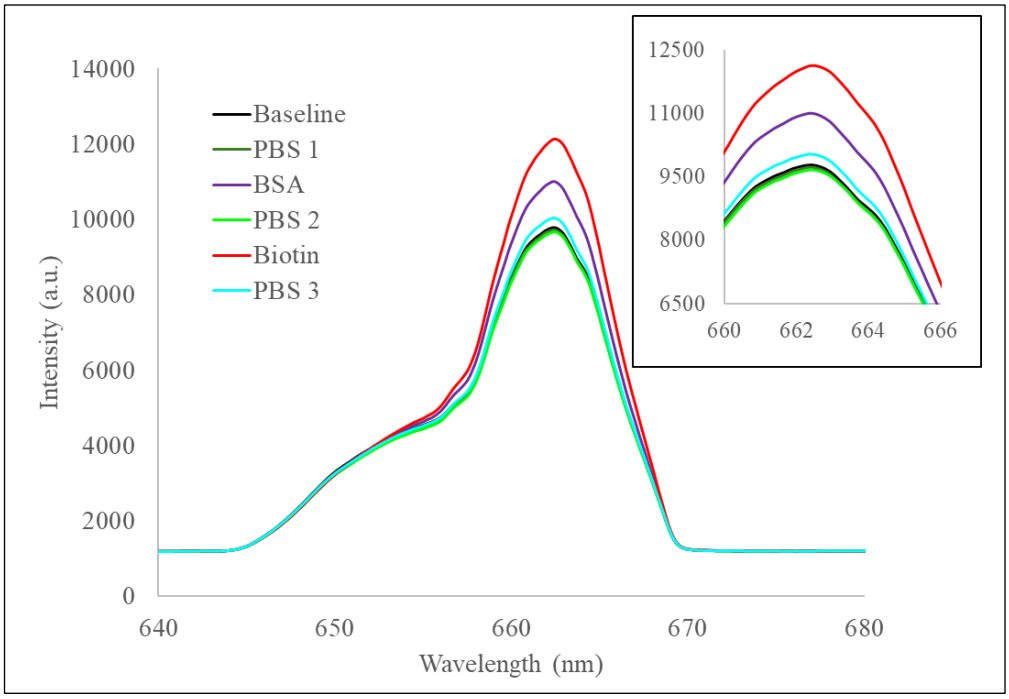

Figure 4.43 Specificity Test on Fibre Optics Coated rGO-AgNs-HH

4.8 Mechanism for Protein Detection in the rGO-AgNs-HH Based Fibre Optic Biosensor

The mechanism for protein detection in the rGO–AgNs–HH based fibre optic biosensor is illustrated in Figure 4.44. The sensing process begins when broadband light propagates through the uncladded region of the optical fibre, generating an evanescent wave at the fibre surface (Song et al., 2021). Evanescent waves are the direct result of TIR occurring at the boundary between the inner core and the outer cladding (or surrounding medium) of a fibre optic cable. These waves allow the fibre optics coated with sensing medium to detect the biomaterials through changes in local RI.

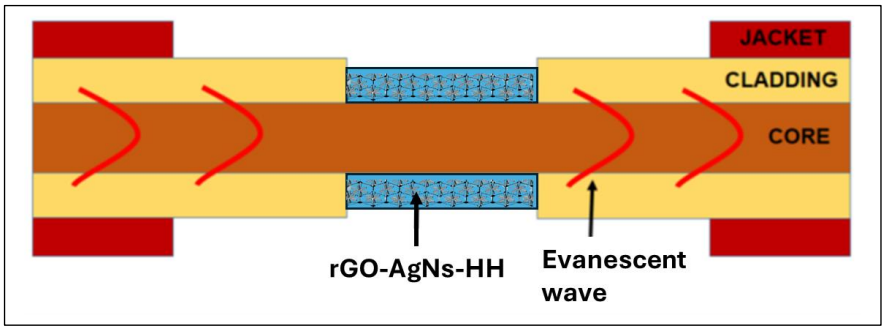

Figure 4.44 Schematic Diagram of Fibre Optics Coated rGO-AgNs-HH in Biosensing Mechanism

To introduce fibre optics into biosensing applications, the signal performance and sensitivity detection need to be improved to allow the detection of biomaterials (Li et al., 2022). In this study, the AgNs will play the roles of enhancing the signal performance and sensitivity detection of the fibre optics due to their LSPR effect (Garcia-Leis et al., 2017). However, with stability issues of AgNs, rGO is introduced to the sensing system, allowing the graphene layer to provide a supporting platform by preventing the agglomeration of nanoparticles (Mondal et al., 2021). Moreover, the rGO layer can improve electron transfer and enhance the adsorption of biomolecules of the duo-composite material (rGO-AgNs) due to its high surface area and functional groups, making it more suited to be embedded on the bare fibre optics.

With the signal properly enhanced, the HH, which is composed of chitosan and agarose, forms a porous matrix on top of the rGO–AgNs sensing layer. The purpose of introducing HH into the sensing medium is to provide a suitable water-based platform that allows the biomolecule to be diffused and immobilized inside the sensing medium. As the target protein penetrates the porous hydrogel structure, it will interact with the sensing surface located within the evanescent field region (Kaushik et al., 2019). The evanescent wave generated at the fibre surface is highly sensitive to changes in the surrounding RI; therefore, the adsorption of protein molecules within the sensing layer will alter the local optical environment. This interaction leads to measurable changes in the transmitted optical signal, which can be observed in the form of a resonance wavelength shift or variation in signal intensity, enabling the detection of the target protein (Akashah et al., 2023). In this case, introducing the streptavidin-biotin interaction on the coating sensor material will be crucial in confirming it via RI detection and porosity test.

CHAPTER 5
CONCLUSION AND RECOMMENDATIONS

5.1 Conclusions

This study focuses on optimizing the AgNs method for fibre optic biosensing applications by integrating it together with graphene-based materials and hybrid hydrogels for protein detection. The first objective of this research was to optimise the synthesis parameters of AgNs and rGO. Based on the result obtained, it can be confirmed that sample O, where 0.9 × 10-4 M of hydroxylamine was used to synthesize together with 0.05 M of NaOH, 8 × 10-^{4} M of silver nitrate, and 0.045 M of sodium citrate tribasic dehydrate, was proven to produce highly optical AgNs.

The second objective was confirmed through several characterizations conducted. This includes a UV-Vis spectrometer measurement, in which the intensity under light is stronger than that of other samples. The shape of AgNs was confirmed via TEM, with a spike length of 352.62 ± 59.72 nm recorded. Subsequently, the SEM analysis also confirms that a hydroxylamine concentration of 0.9 × 10^{-4} M yields consistent star shapes with longer branches. Meanwhile, the rGO sample I was chosen to address the stability issue of the AgNs sample O. It can be confirmed that the rGO synthesis method was optimised using 400 mg of GO, 5g of ascorbic acid, and 10 mL of hydrogen peroxide, producing a highly optical graphene-based sample. This can be confirmed by UV-Vis spectroscopy, which shows higher light intensity than that of other rGO samples. At the same time, the crinkled graphitic structure was confirmed under the SEM imaging. rGO also showed the highest hydrophobicity at 111.0°, with a zeta potential of –36.1 mV. The structural composition was also confirmed under EDX and FTIR analysis. The defect structure was confirmed via Raman spectra, with an I_D/I_G ratio of 1.102, indicating a high defect density and good sp^2 carbon recovery.

The third objective was to develop an integrated structure of AgNs loaded rGO embedded HH as sensing materials for a fibre optic sensing configuration. When it comes to incorporating the AgNs into the graphene-based materials, rGO-AgNs with a ratio of 1:5 was chosen due to better optical properties and stability, which was confirmed during the UV-Vis analysis and EDX. SEM imaging also confirmed that the AgNs were successfully embedded within the rGO graphitic structure, with a white spot

visible on the graphene lattice layer. The structural characteristics of rGO were also confirmed via FTIR, indicating the successful reduction of GO. The I_D/I_G value of rGO-AgNs recorded at 1.167, which is higher than that of rGO alone, with a record of 1.102. Embedding the rGO-AgNs on the bare fibre was also successfully cladded with a record of 123.0 ± 0.8 μm diameter length, and the coating was confirmed to have 5.3 at% of atomic percentage for the C, 45.7 at% of oxygen, and 0.2 at% of element composition for the Ag element. The cross-sectional area of the bare fibre optics coated rGO-AgNs was recorded with a diameter length of 120.86 ± 1.69 μm, slightly higher than bare fibre alone, with a diameter length recorded at 120.77 ± 0.3 μm.

The fourth objective of this work was to analyze and compare the sensing characteristics of rGO-AgNs-HH nanocomposites in terms of signal sensitivity and suitability for fibre optic biosensor applications. Signal strength produced by rGO-AgNs (1:5) manages to enhance the fibre-coated with rGO by 106.06% and 131.47 % against the AgNs coating. Despite the signal produced by GO-AgNs alone managing to enhance the signal performance by 218% compared to the signal generated by GO and 174% compared to the AgNs signal, rGO–AgNs with a 1:5 mixing ratio were selected as the sensing medium due to its balanced signal enhancement, improved stability, and greater suitability for subsequent fibre-optic biosensing and protein detection. Fibre-coated rGO-AgNs (1:5) with a support of surface enhancement was conducted, and it can be concluded that the untreated fibre was suited to proceed with the RI detection test. untreated fibre-coated rGO-AgNs (1:5) manage to record the highest sensitivity of 17130 intensity/RIU with the highest linearity record at 0.8286 compared to other treatments.

Before introducing it to the biomaterial, it can be confirmed that the sequence of rGO-AgNs-HH via the LbL method was successfully configured with a signal strength recorded at 9194.89 a.u. of signal performance, an improvement by. Untreated fibre-coated rGO-AgNs-HH manages to improve the signal performance by 192.04% compared to fibre-coated AgNs alone, 160% against fibre-coated with rGO, and 26.16% against rGO-AgNs coating. The coating of tri-composite material also manages to enhance the sensitivity of the fibre-coated, with a record at 63132 intensity/RUI. Despite an enhancement in signal sensitivity, the linearity of the fibre is still within the acceptable range of 0.8012. By introducing the biotin alone to the fibre sensor system, no change in shift was detected, indicating no interaction occurred. Upon introducing streptavidin, the signal finally shifted from 662.92 nm to 663.17 nm, indicating that the

streptavidin was successfully incorporated into the sensing medium. The peak began to shift again as biotin entered the system, with a wavelength change from 663.17 nm to 664.2 nm, indicating successful detection of protein interactions.

5.2 Recommendations

In future work, the sensing platform developed in this study may be extended by replacing rGO with graphene quantum dots (GQDs). Due to their size-dependent optical properties, strong photoluminescence, and high surface-to-volume ratio, GQDs may offer enhanced sensitivity and new transduction pathways compared to rGO-based systems. Subsequently, integrating AgNs with GQDs and hybrid hydrogels could open alternative sensing routes beyond protein detection, including metal detection, gas sensing, or environmental monitoring applications.

In addition, future studies may also focus on functionalizing the hybrid hydrogel layer with specific bioreceptors such as antibodies, aptamers, or enzymes to improve the selectivity of the sensing platform. The incorporation of such recognition elements within the porous HH matrix could enable highly selective detection of specific biomolecules, including disease biomarkers or pathogens. This approach would transform the current RI-based sensing mechanism into a more targeted biosensing platform, expanding its potential applications in biomedical diagnostics, food safety monitoring, and clinical analysis.

Further enhancements could involve optimizing the fiber optic configuration itself, such as employing tapered fibers, long-period gratings, or multi-core fibers, to amplify light–matter interactions and improve signal-to-noise ratios. The stability and reproducibility of the sensor could also be studied by varying the environmental conditions, including temperature, pH, and ionic strength, to ensure reliable operation in real-world settings.

Moreover, future work could focus on integrating a built-in microfluidic channel within the tri-hybrid coating through 3D printing technology. The incorporation of a microfluidic system would enable automated sample delivery and controlled fluid handling, thereby reducing sample preparation time and minimizing operator-dependent errors. Such a design would allow healthcare personnel, such as nurses or medical technicians, to perform diagnostic tests directly at the point of care with minimal preparation steps. Consequently, the sensing platform could be developed into

a portable, user-friendly, and disposable biosensor suitable for hospital and clinical applications, particularly for rapid disease screening and bedside assessment tests.

Finally, combining the sensor with portable readout systems could enable treatment applications, remote monitoring, and real-time data acquisition. Machine learning algorithms could also be integrated for advanced signal processing and pattern recognition, allowing multiplexed detection of multiple analytes from a single sensing platform. Such directions would significantly broaden the practical utility and commercial potential of the hybrid hydrogel–nanomaterial-based fiber optic sensor.

REFERENCES

Adányi, N., Majer-Baranyi, K., & Székács, A. (2017). Evanescent field effect–based nanobiosensors for agro-environmental and food safety. *Nanobiosensors*, 429–474. https://doi.org/10.1016/B978-0-12-804301-1.00011-4

Adotey, E., Kurbanova, A., Ospanova, A., Ardakkyzy, A., Toktarbay, Z., Kydyrbay, N., Zhazitov, M., Nuraje, N., & Toktarbaiuly, O. (2025). Development of Superhydrophobic Reduced Graphene Oxide (rGO) for Potential Applications in Advanced Materials. *Nanomaterials 2025, Vol. 15, Page 363*, *15*(5), 363. https://doi.org/10.3390/nano15050363

Agrell, E., Karlsson, M., Chraplyvy, A. R., Richardson, D. J., Krummrich, P. M., Winzer, P., Roberts, K., Fischer, J. K., Savory, S. J., Eggleton, B. J., Secondini, M., Kschischang, F. R., Lord, A., Prat, J., Tomkos, I., Bowers, J. E., Srinivasan, S., Brandt-Pearce, M., & Gisin, N. (2016). Roadmap of optical communications. *Journal of Optics*, *18*(6), 063002. https://doi.org/10.1088/2040-8978/18/6/063002

Akashah, M. H. N., Makhsin, S. R., Rani, R. A., Saad, N. H., Razak, K. A., Gardner, P., & Scully, P. J. (2023). Signal Improvement on Fibre Optic Evanescent Wave Sensor Based Polymeric Sensitive Coating of Chitosan-Agarose Hydrogel. *Lecture Notes in Mechanical Engineering*, 109–115. https://doi.org/10.1007/978-981-19-9509-5_15/COVER

Akgönüllü, S., Kılıç, S., Esen, C., & Denizli, A. (2023). Molecularly Imprinted Polymer-Based Sensors for Protein Detection. *Polymers*, *15*(3), 629. https://doi.org/10.3390/POLYM15030629

Akouibaa, A., Masrour, R., Akouibaa, A., Heryanto, H., Benhamou, M., Rezzouk, A., Veeravelan, K., & Kailash. (2026). Study on the Enhancement of a Square-Core D-Shaped Optical Fiber Sensor Based on Surface Plasmon Resonance Functionalized With AgφAu1−φ Alloy and Amorphous Ge2Sb2Te5 Nanolayer. *Advanced Theory and Simulations*, *9*(1), e01851. https://doi.org/10.1002/adts.202501851

Alam, S. N., Sharma, N., & Kumar, L. (2017). Synthesis of Graphene Oxide (GO) by Modified Hummers Method and Its Thermal Reduction to Obtain Reduced Graphene Oxide (rGO)*. *Graphene*, *06*(01), 1–18. https://doi.org/10.4236/graphene.2017.61001

Ameer, F. S., Varahagiri, S., Benza, D. W., Willett, D. R., Wen, Y., Wang, F., Chumanov, G., & Anker, J. N. (2016). Tuning Localized Surface Plasmon Resonance Wavelengths of Silver Nanoparticles by Mechanical Deformation. *The Journal of Physical Chemistry. C, Nanomaterials and Interfaces*, *120*(37), 20886. https://doi.org/10.1021/acs.jpcc.6b02169

Apriyanto, H., Ravet, G., Bernal, O. D., Cattoen, M., Seat, H. C., Chavagnac, V., Surre, F., & Sharp, J. H. (2018). Comprehensive Modeling of Multimode Fiber Sensors for Refractive Index Measurement and Experimental Validation. *Scientific Reports 2018 8:1*, *8*(1), 1–13. https://doi.org/10.1038/s41598-018-24153-0

Arumugam, M. (2001). Optical fiber communication - An overview. *Pramana - Journal of Physics*, *57*(5–6), 849–869. https://doi.org/10.1007/S12043-001-0003-2/METRICS

Aziz, A., Lim, H. N., Girei, S. H., Yaacob, M. H., Mahdi, M. A., Huang, N. M., & Pandikumar, A. (2015). Silver/graphene nanocomposite-modified optical fiber sensor platform for ethanol detection in water medium. *Sensors and Actuators B: Chemical*, *206*, 119–125. https://doi.org/10.1016/j.snb.2014.09.035

Balzer, A. H. A., & Whitehurst, C. B. (2023). An Analysis of the Biotin–(Strept)avidin System in Immunoassays: Interference and Mitigation Strategies. *Current Issues in Molecular Biology*, *45*(11), 8733. https://doi.org/10.3390/cimb45110549

Bansal, K., Singh, J., & Dhaliwal, A. S. (2022). Synthesis and characterization of Graphene Oxide and its reduction with different reducing agents. *IOP Conference Series: Materials Science and Engineering*, *1225*(1), 012050. https://doi.org/10.1088/1757-899x/1225/1/012050

Bartlett, R. J., Philip-Chandy, R., Eldridge, P., Merchant, D. F., Morgan, R., & Scully, P. J. (2000). Plastic optical fibre sensors and devices. *Http://Dx.Doi.Org/10.1177/014233120002200507*, *22*(5), 431–457. https://doi.org/10.1177/014233120002200507

Bellacicco, M., Vellucci, V., Scardi, M., Barbieux, M., Marullo, S., & D'ortenzio, F. (2019). Quantifying the Impact of Linear Regression Model in Deriving Bio-Optical Relationships: The Implications on Ocean Carbon Estimations. *Sensors 2019, Vol. 19, Page 3032*, *19*(13), 3032. https://doi.org/10.3390/S19133032

Betancur, A. F., Ornelas-Soto, N., Garay-Tapia, A. M., Pérez, F. R., Salazar, Á., &

García, A. G. (2018). A general strategy for direct synthesis of reduced graphene oxide by chemical exfoliation of graphite. *Materials Chemistry and Physics*, *218*, 51–61. https://doi.org/10.1016/J.MATCHEMPHYS.2018.07.019

Binaymotlagh, R., Chronopoulou, L., Haghighi, F. H., Fratoddi, I., & Palocci, C. (2022). Peptide-Based Hydrogels: New Materials for Biosensing and Biomedical Applications. *Materials*, *15*(17), 5871. https://doi.org/10.3390/MA15175871

Binaymotlagh, R., Del Giudice, A., Mignardi, S., Amato, F., Marrani, A. G., Sivori, F., Cavallo, I., Di Domenico, E. G., Palocci, C., & Chronopoulou, L. (2022). Green In Situ Synthesis of Silver Nanoparticles-Peptide Hydrogel Composites: Investigation of Their Antibacterial Activities. *Gels 2022, Vol. 8, Page 700*, *8*(11), 700. https://doi.org/10.3390/GELS8110700

Bourdine, A. V., Demidov, V. V., Ter-Nersesyants, E. V., Pchelkin, G. A., Shurupov, D. N., Khokhlov, A. V., Kashin, A. I., Bureev, S. V., Sachuk, K. P., Zaitseva, E. S., Dukelskii, K. V., & Tiwari, M. (2023). Silica microstructured optical fiber with centralized inclusion of seven GeO2-doped capillaries and induced twisting. Part I: fabrication of pilot samples. *Https://Doi.Org/10.1117/12.3012147*, *12743*, 204–213. https://doi.org/10.1117/12.3012147

Cao, L., Li, Z., Su, K., & Cheng, B. (2016). Hydrophilic Graphene Preparation from Gallic Acid Modified Graphene Oxide in Magnesium Self-Propagating High Temperature Synthesis Process. *Scientific Reports*, *6*. https://doi.org/10.1038/SREP35184

Cao, Y., Xie, Y., & Gebraeel, N. (2018). Multi-sensor slope change detection. *Annals of Operations Research*, *263*(1–2), 163–189. https://doi.org/10.1007/S10479-016-2185-5/TABLES/2

Cao, Y., Yu, X., Cao, Y., Huang, Z., Xu, J., Zhao, J., & Li, G. (2025). Electrochemistry-empowered nano-labeling for versatile aptamer-based biosensing of tumor-associated proteins. *Chemical Engineering Journal*, *504*, 158630. https://doi.org/10.1016/J.CEJ.2024.158630

Capek, I. (2017). *Noble Metal Nanoparticles*. 125–210. https://doi.org/10.1007/978-4-431-56556-7_2

Castañeda-Aude, J. E., Morones-Ramírez, J. R., De Haro-Del Río, D. A., León-Buitimea, A., Barriga-Castro, E. D., & Escárcega-González, C. E. (2023). Ultra-Small Silver Nanoparticles: A Sustainable Green Synthesis Approach for Antibacterial Activity. *Antibiotics*, *12*(3), 574.

https://doi.org/10.3390/ANTIBIOTICS12030574

Chasanah, U., Trisunaryanti, W., Oktaviano, H. S., Triyono, Santoso, I., & Fatmawati, D. A. (2022). Study of green reductant effects of highly reduced graphene oxide production and their characteristics. *Communications in Science and Technology*, *7*(2), 103–111. https://doi.org/10.21924/CST.7.2.2022.906

Chen, C. H., Chiang, C. Y., Wu, C. W., Wang, C. T., & Chau, L. K. (2021). Integrated Graphene Oxide with Noble Metal Nanoparticles to Develop High-Sensitivity Fiber Optic Particle Plasmon Resonance (FOPPR) Biosensor for Biomolecules Determination. *Nanomaterials (Basel, Switzerland)*, *11*(3), 1–15. https://doi.org/10.3390/NANO11030635

Chen, J., Liu, B., & Zhang, H. (2011). Review of fiber Bragg grating sensor technology. *Frontiers of Optoelectronics*, *4*(2), 204–212. https://doi.org/10.1007/S12200-011-0130-4

Chen, W., Gan, L., & Huang, J. (2023). Design, Manufacturing and Functions of Pore-Structured Materials: From Biomimetics to Artificial. *Biomimetics*, *8*(2), 140. https://doi.org/10.3390/biomimetics8020140

Chuah, R., Gopinath, S. C. B., Anbu, P., Salimi, M. N., Yaakub, A. R. W., & Lakshmipriya, T. (2020). Synthesis and characterization of reduced graphene oxide using the aqueous extract of Eclipta prostrata. *3 Biotech*, *10*(8), 364. https://doi.org/10.1007/s13205-020-02365-4

Culshaw, B. (2000). Fiber optics in sensing and measurement. *IEEE Journal on Selected Topics in Quantum Electronics*, *6*(6), 1014–1021. https://doi.org/10.1109/2944.902150

D'Souza, S. F. (2001). Immobilization and stabilization of biomaterials for biosensor applications. *Applied Biochemistry and Biotechnology - Part A Enzyme Engineering and Biotechnology*, *96*(1–3), 225–238. https://doi.org/10.1385/ABAB:96:1-3:225/METRICS

Dabhade, A. H., Verma, R. P., Paramasivan, B., Kumawat, A., & Saha, B. (2023). Development of silver nanoparticles and aptamer conjugated biosensor for rapid detection of E. coli in a water sample. *3 Biotech 2023 13:7*, *13*(7), 244-. https://doi.org/10.1007/s13205-023-03663-3

Danish, M. (2022). Contact Angle Studies of Hydrophobic and Hydrophilic Surfaces. *Handbook of Magnetic Hybrid Nanoalloys and Their Nanocomposites*, 761–782. https://doi.org/10.1007/978-3-030-90948-2_24

Dasari, B. L., Nouri, J. M., Brabazon, D., & Naher, S. (2017). Graphene and derivatives – Synthesis techniques, properties and their energy applications. *Energy*, *140*, 766–778. https://doi.org/10.1016/J.ENERGY.2017.08.048

De Acha, N., Socorro-Leránoz, A. B., Elosúa, C., & Matías, I. R. (2021). Trends in the Design of Intensity-Based Optical Fiber Biosensors (2010–2020). *Biosensors*, *11*(6), 197. https://doi.org/10.3390/BIOS11060197

Devaraj, P., Kumari, P., Aarti, C., & Renganathan, A. (2013). Synthesis and Characterization of Silver Nanoparticles Using Cannonball Leaves and Their Cytotoxic Activity against MCF-7 Cell Line. *Journal of Nanotechnology*, *2013*(1), 598328. https://doi.org/10.1155/2013/598328

Dhakate, S. R., Chauhan, N., Sharma, S., Tawale, J., Singh, S., Sahare, P. D., & Mathur, R. B. (2011). An approach to produce single and double layer graphene from re-exfoliation of expanded graphite. *Carbon*, *49*(6), 1946–1954. https://doi.org/10.1016/J.CARBON.2010.12.068

Dike, J. N., & Ogbe, D. A. (2013). Optimizing the efficiency of Fiber-Optics Technology in Telecommunications systems. *2nd International Conference on Emerging and Sustainable Technologies for Power and ICT in a Developing Society, IEEE NIGERCON 2013 - Proceedings*, 135–142. https://doi.org/10.1109/NIGERCON.2013.6715647

Doria, G., Conde, J., Veigas, B., Giestas, L., Almeida, C., Assunção, M., Rosa, J., & Baptista, P. V. (2012). Noble Metal Nanoparticles for Biosensing Applications. *Sensors 2012, Vol. 12, Pages 1657-1687*, *12*(2), 1657–1687. https://doi.org/10.3390/S120201657

Du, X., Zhou, J., Shi, J., & Xu, B. (2015). Supramolecular Hydrogelators and Hydrogels: From Soft Matter to Molecular Biomaterials. *Chemical Reviews*, *115*(24), 13165–13307. https://doi.org/10.1021/ACS.CHEMREV.5B00299/ASSET/IMAGES/MEDIUM/CR-2015-002993_0041.GIF

Ealias, A. M., & Saravanakumar, M. P. (2017). A review on the classification, characterisation, synthesis of nanoparticles and their application. *IOP Conference Series: Materials Science and Engineering*, *263*(3), 032019. https://doi.org/10.1088/1757-899X/263/3/032019

Fabian, M., Lewis, E., Newe, T., & Lochmann, S. (2009). Fibre-optic evanescent-wave field fluid concentration sensor. *2009 6th International Multi-Conference*

on Systems, Signals and Devices, SSD 2009. https://doi.org/10.1109/SSD.2009.4956701

Gangopadhyay, T. K. (2019). Historical Facts toward Introduction of Fiber-Optics and Photonics. *Photonics and Fiber Optics*, 1–37. https://doi.org/10.1201/9780429026584-1

Ganguly, A., Sharma, S., Papakonstantinou, P., & Hamilton, J. (2011). Probing the Thermal Deoxygenation of Graphene Oxide Using High-Resolution In Situ X-ray-Based Spectroscopies. *Journal of Physical Chemistry C*, *115*(34), 17009–17019. https://doi.org/10.1021/jp203741y

Gao, S. S., Shang, S. B., Liu, X. Y., Li, Z., Sheng, Y. Q., Zhang, C., Yang, C., Qiu, H. W., Huo, Y. Y., & Jiang, S. Z. (2016). An optical fiber SERS sensor based on GO/AgNPs/rGO sandwich structure hybrid films. *RSC Advances*, *6*(85), 81750–81756. https://doi.org/10.1039/c6ra16869h

Garcia-Leis, A., Garcia-Ramos, J. V., & Sanchez-Cortes, S. (2013). Silver nanostars with high SERS performance. *Journal of Physical Chemistry C*, *117*(15), 7791–7795. https://doi.org/10.1021/jp401737y

Garcia-Leis, A., Rivera-Arreba, I., & Sanchez-Cortes, S. (2017). Morphological tuning of plasmonic silver nanostars by controlling the nanoparticle growth mechanism: Application in the SERS detection of the amyloid marker Congo Red. *Colloids and Surfaces A: Physicochemical and Engineering Aspects*, *535*, 49–60. https://doi.org/10.1016/J.COLSURFA.2017.09.013

Georgitsopoulou, S., Petrai, O., & Georgakilas, V. (2019). Highly conductive functionalized reduced graphene oxide. *Surfaces and Interfaces*, *16*, 152–156. https://doi.org/10.1016/J.SURFIN.2019.05.010

Gheybalizadeh, H., Goli, M., Hasanzadeh, M., Vaez-Gharamaleki, Y., Jouyban, A., & Soleymani, J. (2025). Magnetic reduced graphene oxide aerogel decorated silver nanoparticles towards efficient recognition of doxorubicin in patients' blood plasma. *Scientific Reports 2025 15:1*, *15*(1), 37701-. https://doi.org/10.1038/s41598-025-21459-8

Gu, B., Jiang, Q., Luo, B., Liu, C., Ren, J., Wang, X., & Wang, X. (2021). A sandwich-like chitosan-based antibacterial nanocomposite film with reduced graphene oxide immobilized silver nanoparticles. *Carbohydrate Polymers*, *260*, 117835. https://doi.org/10.1016/J.CARBPOL.2021.117835

Guo, M., Yuan, H., Ni, K., Ye, C., Pan, F., Xiong, J., & Zhu, Y. (2024). Structural

Repair of Reduced Graphene Oxide Promoted by Single-Layer Graphene. *Advanced Science*, *12*(7), 2410088. https://doi.org/10.1002/advs.202410088

Gurunathan, S., Han, J. W., Abdal Dayem, A., Eppakayala, V., & Kim, J. H. (2012). Oxidative stress-mediated antibacterial activity of graphene oxide and reduced graphene oxide in Pseudomonas aeruginosa. *International Journal of Nanomedicine*, *7*, 5901–5914. https://doi.org/10.2147/IJN.S37397

Habte, A. T., Ayele, D. W., & Hu, M. (2019). Synthesis and Characterization of Reduced Graphene Oxide (rGO) Started from Graphene Oxide (GO) Using the Tour Method with Different Parameters. *Advances in Materials Science and Engineering*, *2019*. https://doi.org/10.1155/2019/5058163

Hanifah, M. F. R., Jaafar, J., Aziz, M., Ismail, A. F., Rahman, M. A., & Othman, M. H. D. (2015). Synthesis of graphene oxide nanosheets via modified Hummers' method and its physicochemical properties. *Jurnal Teknologi*, *74*(1), 195–198. https://doi.org/10.11113/JT.V74.3555

Harms, G. S., Cognet, L., Lommerse, P. H. M., Blab, G. A., & Schmidt, T. (2001). Autofluorescent Proteins in Single-Molecule Research: Applications to Live Cell Imaging Microscopy. *Biophysical Journal*, *80*(5), 2396–2408. https://doi.org/10.1016/S0006-3495(01)76209-1

Hart, A. E., Akers, D. B., Gorosh, S., & Kitchens, C. L. (2013). Reverse micelle synthesis of silver nanoparticles in gas expanded liquids. *The Journal of Supercritical Fluids*, *79*, 236–243. https://doi.org/10.1016/J.SUPFLU.2013.02.014

Herrmann, A., Haag, R., & Schedler, U. (2021). Hydrogels and Their Role in Biosensing Applications. *Advanced Healthcare Materials*, *10*(11), 2100062. https://doi.org/10.1002/ADHM.202100062;WGROUP:STRING:PUBLICATION

Hidayah, N. M. S., Liu, W. W., Lai, C. W., Noriman, N. Z., Khe, C. S., Hashim, U., & Lee, H. C. (2017). Comparison on graphite, graphene oxide and reduced graphene oxide: Synthesis and characterization. *AIP Conference Proceedings*, *1892*. https://doi.org/10.1063/1.5005764

Hong, F., Qiu, P., Wang, Y., Ren, P., Liu, J., Zhao, J., & Gou, D. (2024). Chitosan-based hydrogels: From preparation to applications, a review. *Food Chemistry: X*, *21*, 101095. https://doi.org/10.1016/J.FOCHX.2023.101095

Hong, G., Antaris, A. L., & Dai, H. (2017). Near-infrared fluorophores for biomedical imaging. *Nature Biomedical Engineering 2017 1:1*, *1*(1), 1–22.

https://doi.org/10.1038/s41551-016-0010

Hosny, S., Gaber, G. A., Ragab, M. S., Ragheb, M. A., Anter, M., & Mohamed, L. Z. (2025). A Comprehensive Review of Silver Nanoparticles (AgNPs): Synthesis Strategies, Toxicity Concerns, Biomedical Applications, AI-Driven Advancements, Challenges, and Future Perspectives. *Arabian Journal for Science and Engineering 2025*, 1–48. https://doi.org/10.1007/s13369-025-10612-0

Huang, H. H., De Silva, K. K. H., Kumara, G. R. A., & Yoshimura, M. (2018). Structural Evolution of Hydrothermally Derived Reduced Graphene Oxide. *Scientific Reports 2018 8:1*, *8*(1), 1–9. https://doi.org/10.1038/s41598-018-25194-1

Husband, F. A., Garrood, M. J., Mackie, A. R., Burnett, G. R., & Wilde, P. J. (2001). Adsorbed Protein Secondary and Tertiary Structures by Circular Dichroism and Infrared Spectroscopy with Refractive Index Matched Emulsions. *Journal of Agricultural and Food Chemistry*, *49*(2), 859–866. https://doi.org/10.1021/jf000688z

Ibrahim, I., Lim, H. N., Wan, N. W. K., Huang, N. M., Lim, S. P., Busayaporn, W., & Nakajima, H. (2021). Plasmonic silver sandwich structured photoanode and reflective counter electrode enhancing power conversion efficiency of dye-sensitized solar cell. *Solar Energy*, *215*, 403–409. https://doi.org/10.1016/J.SOLENER.2020.12.055

Ibrahim, N., Jamaluddin, N. D., Tan, L. L., & Yusof, N. Y. M. (2021). A Review on the Development of Gold and Silver Nanoparticles-Based Biosensor as a Detection Strategy of Emerging and Pathogenic RNA Virus. *Sensors 2021, Vol. 21, Page 5114*, *21*(15), 5114. https://doi.org/10.3390/s21155114

Ismail, Z. (2019). Green reduction of graphene oxide by plant extracts: A short review. *Ceramics International*, *45*(18), 23857–23868. https://doi.org/10.1016/J.CERAMINT.2019.08.114

Jabłońska, A., Jaworska, A., Kasztelan, M., Berbeć, S., & Pałys, B. (2018). Graphene and Graphene Oxide Applications for SERS Sensing and Imaging. *Current Medicinal Chemistry*, *26*(38), 6878–6895. https://doi.org/10.2174/0929867325666181004152247

Jachetta, J. (2007). *Fiber-Optic Transmission Systems National Association of Broadcasters ENGINEERING HANDBOOK 10 th Edition*.

http://www.linkedin.com/in/jimjachetta

Jain, A., & Cheng, K. (2016). The Principles and Applications of Avidin-Based Nanoparticles in Drug Delivery and Diagnosis. *Journal of Controlled Release : Official Journal of the Controlled Release Society*, *245*, 27. https://doi.org/10.1016/J.JCONREL.2016.11.016

Johra, F. T., Lee, J. W., & Jung, W. G. (2014). Facile and safe graphene preparation on solution based platform. *Journal of Industrial and Engineering Chemistry*, *20*(5), 2883–2887. https://doi.org/10.1016/J.JIEC.2013.11.022

Juma, M. W., Birech, Z., Mwenze, N. M., Ondieki, A. M., Maaza, M., & Mokhotjwa, S. D. (2024). Localized surface plasmon resonance sensing of Trenbolone acetate dopant using silver nanoparticles. *Scientific Reports 2024 14:1*, *14*(1), 5721-. https://doi.org/10.1038/s41598-024-56456-w

Kaushik, S., Tiwari, U. K., Deep, A., & Sinha, R. K. (2019). Two-dimensional transition metal dichalcogenides assisted biofunctionalized optical fiber SPR biosensor for efficient and rapid detection of bovine serum albumin. *Scientific Reports 2019 9:1*, *9*(1), 6987-. https://doi.org/10.1038/s41598-019-43531-w

Kepekçi, R. A., Yener İlçe, B., & Demir Kanmazalp, S. (2021). Plant-derived biomaterials for wound healing. *Studies in Natural Products Chemistry*, *70*, 227–264. https://doi.org/10.1016/B978-0-12-819489-8.00001-6

Korposh, S., James, S. W., Lee, S. W., & Tatam, R. P. (2019). Tapered Optical Fibre Sensors: Current Trends and Future Perspectives. *Sensors (Basel, Switzerland)*, *19*(10). https://doi.org/10.3390/S19102294

Kriaa, K., Fadhillah, F., Alghamdi, A. M., Ali, F. A. A., & Aljlil, S. (2025). Spin-spray assisted layer-by-layer assembly of polyelectrolyte multilayer nanofiltration membranes with competitive organic fouling resistance. *Desalination and Water Treatment*, *323*, 101306. https://doi.org/10.1016/J.DWT.2025.101306

Kumar, S., Garg, A., & Chowdhuri, A. (2018). Comparison of water purification properties of Graphene Oxide (GO) membranes with tuned interlayer spacings. *Materials Research Express*, *6*(1), 015604. https://doi.org/10.1088/2053-1591/aae416

Lee, B. H., Kim, Y. H., Park, K. S., Eom, J. B., Kim, M. J., Rho, B. S., & Choi, H. Y. (2012). Interferometric fiber optic sensors. *Sensors*, *12*(3), 2467–2486. https://doi.org/10.3390/S120302467

Lee, J. R., Dhital, D., & Yoon, D. J. (2011). Investigation of cladding and coating stripping methods for specialty optical fibers. *Optics and Lasers in Engineering*, *49*(3), 324–330. https://doi.org/10.1016/J.OPTLASENG.2010.10.008

Li, B., Zhang, R., Bi, R., & Olivo, M. (2022). Applications of Optical Fiber in Label-Free Biosensors and Bioimaging: A Review. *Biosensors*, *13*(1), 64. https://doi.org/10.3390/bios13010064

Li, X., Jiang, L., Zhan, Q., Qian, J., & He, S. (2009). Localized surface plasmon resonance (LSPR) of polyelectrolyte-functionalized gold-nanoparticles for bio-sensing. *Colloids and Surfaces A: Physicochemical and Engineering Aspects*, *332*(2–3), 172–179. https://doi.org/10.1016/J.COLSURFA.2008.09.009

Linnell, J. C. (2000). VITAMINS | Water-Soluble: Thin-Layer (Planar) Chromatography. *Encyclopedia of Separation Science*, 4454–4460. https://doi.org/10.1016/B0-12-226770-2/03021-0

Liu, S., Tao, H., Zeng, L., Liu, Q., Xu, Z., Liu, Q., & Luo, J. L. (2017). Shape-Dependent Electrocatalytic Reduction of CO2 to CO on Triangular Silver Nanoplates. *Journal of the American Chemical Society*, *139*(6), 2160–2163. https://doi.org/10.1021/JACS.6B12103

Liu, W., & Speranza, G. (2021). Tuning the Oxygen Content of Reduced Graphene Oxide and Effects on Its Properties. *ACS Omega*, *6*(9), 6195–6205. https://doi.org/10.1021/ACSOMEGA.0C05578/SUPPL_FILE/AO0C05578_SI_001.PDF

Loiseau, A., Asila, V., Boitel-Aullen, G., Lam, M., Salmain, M., & Boujday, S. (2019). Silver-based plasmonic nanoparticles for and their use in biosensing. In *Biosensors* (Vol. 9, Issue 2). MDPI. https://doi.org/10.3390/bios9020078

Londero, C. M., Delgado-Pinar, M., Cuadrado-Laborde, C., & Andres, M. V. (2023). Resonant Couplings in U-Shaped Fibers for Biosensing. *Journal of Lightwave Technology*, *41*(13), 4230–4237. https://doi.org/10.1109/JLT.2023.3261706

Lou, B., Liu, Y., Shi, M., Chen, J., Li, K., Tan, Y., Chen, L., Wu, Y., Wang, T., Liu, X., Jiang, T., Peng, D., & Liu, Z. (2022). Aptamer-based biosensors for virus protein detection. *TrAC Trends in Analytical Chemistry*, *157*, 116738. https://doi.org/10.1016/J.TRAC.2022.116738

Makhsin, S. R., Goddard, N. J., Gupta, R., Gardner, P., & Scully, P. J. (2020). Optimization Synthesis and Biosensing Performance of an Acrylate-Based Hydrogel as an Optical Waveguiding Sensing Film. *Analytical Chemistry*,

92(22), 14907–14914. https://doi.org/10.1021/acs.analchem.0c00586

Makhsin, S. R., Zakaria, M. H., Noor Akashah, M. H., Abdul Rani, R., Scully, P. J., & Gardner, P. (2023). Enhancing fibre optic sensor signals via gold nanoparticle-decorated agarose hydrogels. *Optical Materials*, *143*, 114247. https://doi.org/10.1016/J.OPTMAT.2023.114247

Matos, M. R., Rezende, E. F. G., Antão, P. P. C., Xavier, L. M. S., Fernandes, F. C., & Castro, T. J. (2024). Green synthesis of silver nanoparticles and their application for colorimetric detection of L-cysteine: a spectroscopic investigation. *Inorganic Chemistry Communications*, *167*, 112767. https://doi.org/10.1016/j.inoche.2024.112767

Mbayachi, V. B., Ndayiragije, E., Sammani, T., Taj, S., Mbuta, E. R., & khan, A. ullah. (2021). Graphene synthesis, characterization and its applications: A review. *Results in Chemistry*, *3*, 100163. https://doi.org/10.1016/J.RECHEM.2021.100163

McCann, B., Tipper, B., Shahbeigi, S., Soleimani, M., Jabbari, M., & Nasr Esfahani, M. (2025). A Review on Perception of Binding Kinetics in Affinity Biosensors: Challenges and Opportunities. *ACS Omega*, *10*(5), 4197–4216. https://doi.org/10.1021/acsomega.4c10040

Melchioni, N., Bellucci, L., Tredicucci, A., & Bianco, F. (2023). Operability timescale of defect-engineered graphene. *Surfaces and Interfaces*, *37*(31), 102662. https://doi.org/10.1016/j.surfin.2023.102662

Mikhailova, E. O. (2020). Silver Nanoparticles: Mechanism of Action and Probable Bio-Application. *Journal of Functional Biomaterials*, *11*(4), 84. https://doi.org/10.3390/jfb11040084

Millis, B. A. (2012). Evanescent-wave field imaging: An introduction to total internal reflection fluorescence microscopy. *Methods in Molecular Biology*, *823*, 295–309. https://doi.org/10.1007/978-1-60327-216-2_19

Mondal, A., Prabhakaran, A., Gupta, S., & Subramanian, V. R. (2021). Boosting Photocatalytic Activity Using Reduced Graphene Oxide (RGO)/Semiconductor Nanocomposites: Issues and Future Scope. *ACS Omega*, *6*(13), 8734–8743. https://doi.org/10.1021/acsomega.0c06045

Morris, A. S., & Langari, R. (2021). Sensor technologies. *Measurement and Instrumentation*, 381–411. https://doi.org/10.1016/B978-0-12-817141-7.00013-X

Mostufa, S., Rezaei, B., Ciannella, S., Yari, P., Gómez-Pastora, J., He, R., & Wu, K.

(2024). Advancements and Perspectives in Optical Biosensors. *ACS Omega*, *9*(23), 24181. https://doi.org/10.1021/acsomega.4c01872

Mujahid, M. H., Upadhyay, T. K., Khan, F., Pandey, P., Park, M. N., Sharangi, A. B., Saeed, M., Upadhye, V. J., & Kim, B. (2022). Metallic and metal oxide-derived nanohybrid as a tool for biomedical applications. *Biomedicine & Pharmacotherapy*, *155*, 113791. https://doi.org/10.1016/J.BIOPHA.2022.113791

Multimode Fiber and Multimode Fiber Optic Cable Tutorial – Fosco Connect. (n.d.). Retrieved April 17, 2024, from https://www.fiberoptics4sale.com/blogs/archive-posts/95152198-multimode-fiber-and-multimode-fiber-optic-cable-tutorial

Muzyka, R., Drewniak, S., Pustelny, T., Chrubasik, M., & Gryglewicz, G. (2018). Characterization of Graphite Oxide and Reduced Graphene Oxide Obtained from Different Graphite Precursors and Oxidized by Different Methods Using Raman Spectroscopy. *Materials 2018, Vol. 11, Page 1050*, *11*(7), 1050. https://doi.org/10.3390/MA11071050

Nahid, E., Kaysir, M. R., Islam, M. J., Hossain, S. S., & Rahman, M. S. (2025). Comparative Study of the Temperature-Sensitive Materials for D-Shaped Optical Fiber-Based Temperature Sensor. *Plasmonics*, 1–12. https://doi.org/10.1007/S11468-025-02926-4/TABLES/2

Namvari, M., Biswas, C. S., Galluzzi, M., Wang, Q., Du, B., & Stadler, F. J. (2017). Reduced graphene oxide composites with water soluble copolymers having tailored lower critical solution temperatures and unique tube-like structure. *Scientific Reports 2017 7:1*, *7*(1), 44508-. https://doi.org/10.1038/srep44508

Naqvi, T. K., Srivastava, A. K., Kulkarni, M. M., Siddiqui, A. M., & Dwivedi, P. K. (2019). Silver nanoparticles decorated reduced graphene oxide (rGO) SERS sensor for multiple analytes. *Applied Surface Science*, *478*, 887–895. https://doi.org/10.1016/J.APSUSC.2019.02.026

Nellambakam, Y., Haritha, K., & Shiv Chaitanya, K. V. S. (2023). Evanescent wave in multiple slit diffraction and n-array antennas in metamaterial using Cesàro convergence. *Scientific Reports*, *13*(1). https://doi.org/10.1038/S41598-023-36894-8

Noor Akashah, M. H. (2022). *Synthesis of 3D hydrogel graphene quantum dots nanocomposites modified fibre optic for biosensors application / Muhammad Haziq Noor Akashah*.

Oliva, A., Llabrés, M., & Fariña, J. B. (2009). Estimation of uncertainty in size-

exclusion chromatography with a double detection system (light-scattering and refractive index). *Talanta*, *78*(3), 781–789. https://doi.org/10.1016/J.TALANTA.2008.12.039

Orellana, B., Vivas, L., Manquian, C., Brito, T. P., & Singh, D. P. (2025). Ecosynthesis and Optimization of Nano rGO/Ag-Based Electrode Materials for Superior Supercapacitor Coin Cell Devices. *International Journal of Molecular Sciences*, *26*(19), 9578. https://doi.org/10.3390/ijms26199578

Pahurkar, V. G., Tamgadge, Y. S., Gambhire, A. B., & Muley, G. G. (2015). Evanescent wave absorption based polyaniline cladding modified fiber optic intrinsic biosensor for glucose sensing application. *Measurement*, *61*, 9–15. https://doi.org/10.1016/J.MEASUREMENT.2014.10.029

Palomba, M., Carotenuto, G., & Longo, A. (2022). A Brief Review: The Use of L-Ascorbic Acid as a Green Reducing Agent of Graphene Oxide. *Materials*, *15*(18). https://doi.org/10.3390/MA15186456

Pathak, A. K., Bhardwaj, V., Gangwar, R. K., & Singh, V. K. (2016). SPR based fiber sensor to measure refractive index of glycerol and acetone. *Proceedings of the 2015 International Conference on Microwave and Photonics, ICMAP 2015*. https://doi.org/10.1109/ICMAP.2015.7408711

Paulie, S., Perlmann, P., & Perlmann, H. (2023). Enzyme Linked Immunosorbent Assay. *Cell Biology: A Laboratory Handbook*, 533–538. https://doi.org/10.1016/B978-012164730-8/50065-4

Pawlik, V., Zhou, S., Zhou, S., Qin, D., & Xia, Y. (2023). Silver Nanocubes: From Serendipity to Mechanistic Understanding, Rational Synthesis, and Niche Applications. *Chemistry of Materials*, *35*(9), 3427–3449. https://doi.org/10.1021/ACS.CHEMMATER.3C00472

Pendão, C., & Silva, I. (2022). Optical Fiber Sensors and Sensing Networks: Overview of the Main Principles and Applications. *Sensors 2022, Vol. 22, Page 7554*, *22*(19), 7554. https://doi.org/10.3390/s22197554

Perumal, D., Albert, E. L., Saad, N., Hin, T. Y. Y., Zawawi, R. M., Teh, H. F., & Che Abdullah, C. A. (2022). Fabrication and Characterization of Clinacanthus nutans Mediated Reduced Graphene Oxide Using a Green Approach. *Crystals 2022, Vol. 12, Page 1539*, *12*(11), 1539. https://doi.org/10.3390/cryst12111539

Pesapane, A., Lucotti, A., & Zerbi, G. (2010). Fiber-optic SERS sensor with optimized geometry: testing and optimization. *Journal of Raman Spectroscopy*,

41(3), 256–267. https://doi.org/10.1002/JRS.2451

Puech, P., Kandara, M., Paredes, G., Moulin, L., Weiss-Hortala, E., Kundu, A., Ratel-Ramond, N., Plewa, J.-M., Pellenq, R., & Monthioux, M. (2019). Analyzing the Raman Spectra of Graphenic Carbon Materials from Kerogens to Nanotubes: What Type of Information Can Be Extracted from Defect Bands? *C 2019, Vol. 5, Page 69*, *5*(4), 69. https://doi.org/10.3390/c5040069

Qi, Y., Xia, T., Li, Y., Duan, L., & Chen, W. (2016). Colloidal stability of reduced graphene oxide materials prepared using different reducing agents. *Environmental Science: Nano*, *3*(5), 1062–1071. https://doi.org/10.1039/C6EN00174B

Raji, M., Zari, N., el kacem Qaiss, A., & Bouhfid, R. (2019). Chemical Preparation and Functionalization Techniques of Graphene and Graphene Oxide. *Functionalized Graphene Nanocomposites and Their Derivatives: Synthesis, Processing and Applications*, 1–20. https://doi.org/10.1016/B978-0-12-814548-7.00001-5

Ramzan, M., Abusalah, M. A. H. A., Ahmed, N., Yean, C. Y., & Zeshan, B. (2024). Green Synthesis and Characterization of Silver Nanoparticles Using Zingiber officinale Extracts to Investigate Their Antibacterial Potential. *International Journal of Nanomedicine*, *19*, 13319. https://doi.org/10.2147/IJN.S475656

Rekha, C. R., Nayar, V. U., & Gopchandran, K. G. (2018). Synthesis of highly stable silver nanorods and their application as SERS substrates. *Journal of Science: Advanced Materials and Devices*, *3*(2), 196–205. https://doi.org/10.1016/J.JSAMD.2018.03.003

Rickelt, L. F., Ottosen, L. D. M., & Kühl, M. (2015). Etching of multimode optical glass fibers: A new method for shaping the measuring tip and immobilization of indicator dyes in recessed fiber-optic microprobes. *Sensors and Actuators B: Chemical*, *211*, 462–468. https://doi.org/10.1016/J.SNB.2015.01.091

Rithesh Raj, D., & Sudarsanakumar, C. (2017). Surface plasmon resonance based fiber optic sensor for the detection of cysteine using diosmin capped silver nanoparticles. *Sensors and Actuators A: Physical*, *253*, 41–48. https://doi.org/10.1016/J.SNA.2016.11.019

Rivero, P. J., Goicoechea, J., & Arregui, F. J. (2019). Layer-by-Layer Nano-assembly: A Powerful Tool for Optical Fiber Sensing Applications. *Sensors 2019, Vol. 19, Page 683*, *19*(3), 683. https://doi.org/10.3390/s19030683

Rodríguez-González, C., Velázquez-Villalba, P., Salas, P., & Castaño, V. M. (2016). Green synthesis of nanosilver-decorated graphene oxide sheets. *IET Nanobiotechnology*, *10*(5), 301. https://doi.org/10.1049/IET-NBT.2015.0043

Rohizat, N. S., Ripain, A. H. A., Lim, C. S., Tan, C. L., & Zakaria, R. (2021). Plasmon-enhanced reduced graphene oxide photodetector with monometallic of Au and Ag nanoparticles at VIS–NIR region. *Scientific Reports*, *11*(1), 19688. https://doi.org/10.1038/s41598-021-99189-w

Roslan, A. H., Makhsin, S. R., Abdul Rani, R., & Siddique, B. (2024). *Amplifying fibre optic sensor signals with graphene oxide-silver nanostars / Azib Haiman Roslan ... [et al.]*.

Roslan, A. H. Bin, Makhsin, S. R. B., Rani, R. A., Razak, K. A., & Zourob, M. (2022). One-Step Synthesis of Nanostar Shaped Silver Nanoparticles and its Optical Stability. *IEEE International Conference on Semiconductor Electronics, Proceedings, ICSE*, *2022-August*, 129–132. https://doi.org/10.1109/ICSE56004.2022.9863200

Roslan, N. H. I., Makhsin, S. R., Abdul Rani, R., & Siddique, B. (2025). Effect of Gold Nanoparticle Size Conjugated with Graphene Quantum Dots on the Signal of a Fibre Optic Sensor. *Malaysian Journal of Chemistry*, *27*(5), 190–199.

Sadani, K., Nag, P., & Mukherji, S. (2019). LSPR based optical fiber sensor with chitosan capped gold nanoparticles on BSA for trace detection of Hg (II) in water, soil and food samples. *Biosensors and Bioelectronics*, *134*, 90–96. https://doi.org/10.1016/j.bios.2019.03.046

Sager, M. (1992). Chemical speciation and environmental mobility of heavy metals in sediments and soils. *Techniques and Instrumentation in Analytical Chemistry*, *12*(C), 133–175. https://doi.org/10.1016/S0167-9244(08)70106-9

Sahota, J. K., Gupta, N., & Dhawan, D. (2020). Fiber Bragg grating sensors for monitoring of physical parameters: a comprehensive review. *Optical Engineering*, *59*(06), 1. https://doi.org/10.1117/1.OE.59.6.060901

Sahudin, M. R. (2022). *Synthesis of gold nanoparticles embedded graphene oxide for fibre optic gas sensor applications / Mohd Rafal Sahudin*.

Sahudin, M. R., Makhsin, S. R., Ayub, M. A., Saad, N. H., Rani, R. A., & Zourob, M. (2021). Effect of Sodium Nitrate on the Formation of Graphene Oxide via Modified Hummers Method for Sensors Application. *Proceedings - 2021 IEEE Regional Symposium on Micro and Nanoelectronics, RSM 2021*, 54–57.

https://doi.org/10.1109/RSM52397.2021.9511574

Sakamoto, S., Putalun, W., Vimolmangkang, S., Phoolcharoen, W., Shoyama, Y., Tanaka, H., & Morimoto, S. (2017). Enzyme-linked immunosorbent assay for the quantitative/qualitative analysis of plant secondary metabolites. *Journal of Natural Medicines*, *72*(1), 32. https://doi.org/10.1007/S11418-017-1144-Z

Samavati, Z., Samavati, A., Ismail, A. F., Othman, M. H. D., & Rahman, M. A. (2019). Comprehensive investigation of evanescent wave optical fiber refractive index sensor coated with ZnO nanoparticles. *Optical Fiber Technology*, *52*. https://doi.org/10.1016/J.YOFTE.2019.101976

Samtiya, M., Aluko, R. E., Dhewa, T., & Moreno-Rojas, J. M. (2021). Potential Health Benefits of Plant Food-Derived Bioactive Components: An Overview. *Foods*, *10*(4), 839. https://doi.org/10.3390/FOODS10040839

Sang, S., Li, D., Zhang, H., Sun, Y., Jian, A., Zhang, Q., & Zhang, W. (2017). Facile synthesis of AgNPs on reduced graphene oxide for highly sensitive simultaneous detection of heavy metal ions. *RSC Advances*, *7*(35), 21618–21624. https://doi.org/10.1039/C7RA02267K

Sau, T. K., Rogach, A. L., Jäckel, F., Klar, T. A., & Feldmann, J. (2010). Properties and Applications of Colloidal Nonspherical Noble Metal Nanoparticles. *Advanced Materials*, *22*(16), 1805–1825. https://doi.org/10.1002/ADMA.200902557

Sengar, R., & Dubey, S. (2026). *Introduction and History of Hydrogels*. 1–26. https://doi.org/10.1007/978-981-95-1598-1_1

Sezer, N., Atieh, M. A., & Koç, M. (2019). A comprehensive review on synthesis, stability, thermophysical properties, and characterization of nanofluids. *Powder Technology*, *344*, 404–431. https://doi.org/10.1016/j.powtec.2018.12.016

Sharma, N., Vyas, R., Sharma, V., Rahman, H., Sharma, S. K., & Sachdev, K. (2020). A comparative study on gas-sensing behavior of reduced graphene oxide (rGO) synthesized by chemical and environment-friendly green method. *Applied Nanoscience (Switzerland)*, *10*(2), 517–528. https://doi.org/10.1007/S13204-019-01138-7/METRICS

Sharma, R., Chadha, N., & Saini, P. (2017). Determination of defect density, crystallite size and number of graphene layers in graphene analogues using X-ray diffraction and Raman spectroscopy. *Indian Journal of Pure & Applied Physics*.

Sharma, V., Jain, Y., Kumari, M., Gupta, R., Sharma, S. K., & Sachdev, K. (2017).

Synthesis and Characterization of Graphene Oxide (GO) and Reduced Graphene Oxide (rGO) for Gas Sensing Application. *Macromolecular Symposia*, *376*(1), 1700006. https://doi.org/10.1002/MASY.201700006

Sieradzka, M., Ślusarczyk, C., Biniaś, W., & Fryczkowski, R. (2021). The Role of the Oxidation and Reduction Parameters on the Properties of the Reduced Graphene Oxide. *Coatings 2021, Vol. 11, Page 166*, *11*(2), 166. https://doi.org/10.3390/coatings11020166

Singh, A. K., Mittal, S., Das, M., Saharia, A., & Tiwari, M. (2023). Optical biosensors: a decade in review. *Alexandria Engineering Journal*, *67*, 673–691. https://doi.org/10.1016/J.AEJ.2022.12.040

Some, S., Kim, Y., Yoon, Y., Yoo, H., Lee, S., Park, Y., & Lee, H. (2013). High-Quality Reduced Graphene Oxide by a Dual-Function Chemical Reduction and Healing Process. *Scientific Reports*, *3*, 1929. https://doi.org/10.1038/srep01929

Sonawane, A., Mujawar, M. A., & Bhansali, S. (2019). Atmospheric Plasma Treatment Enhances the Biosensing Properties of Graphene Oxide-Silver Nanoparticle Composite. *Journal of The Electrochemical Society*, *166*(9), B3084–B3090. https://doi.org/10.1149/2.0161909JES/XML

Song, Y., Ling, L., Westerhoff, P., & Shang, C. (2021). Evanescent waves modulate energy efficiency of photocatalysis within TiO2 coated optical fibers illuminated using LEDs. *Nature Communications 2021 12:1*, *12*(1), 4101-. https://doi.org/10.1038/s41467-021-24370-8

Stoneman, M. R., & Raicu, V. (2023). Fluorescence-Based Detection of Proteins and Their Interactions in Live Cells. *Journal of Physical Chemistry B*, *127*(21), 4708–4721. https://doi.org/10.1021/ACS.JPCB.3C01419/ASSET/IMAGES/LARGE/JP3C01419_0004.JPEG

Sudas, D. P., Jitov, V. A., & Kuznetsov, P. I. (2023). Various Types of Light Guides for Use in Lossy Mode Resonance-Based Sensors. *Sensors 2023, Vol. 23, Page 6049*, *23*(13), 6049. https://doi.org/10.3390/S23136049

Tan, A., Ahmad, Z., Vukusic, P., & Cabral, J. T. (2023). Multifaceted Structurally Coloured Materials: Diffraction and Total Internal Reflection (TIR) from Nanoscale Surface Wrinkling. *Molecules*, *28*(4), 1710. https://doi.org/10.3390/molecules28041710

Tas, M., Altin, Y., & Celik Bedeloglu, A. (2019). Reduction of graphene oxide thin

films using a stepwise thermal annealing assisted by l-ascorbic acid. *Diamond and Related Materials*, *92*, 242–247. https://doi.org/10.1016/J.DIAMOND.2019.01.009

Teixeira-Costa, B. E., & Andrade, C. T. (2021). Chitosan as a Valuable Biomolecule from Seafood Industry Waste in the Design of Green Food Packaging. *Biomolecules*, *11*(11), 1599. https://doi.org/10.3390/biom11111599

Thinh, D. B., Dat, N. M., Tuyen, N. N. K., Tai, L. T., Hai, N. D., Tinh, N. T., Huong, L. M., Do Dat, T., Huong, Q. T. T., Nam, N. T. H., Oanh, D. T. Y., Phong, M. T., & Hieu, N. H. (2022). A review of silver-dopped graphene oxide nanocomposite: Synthesis and multifunctional applications. *Vietnam Journal of Chemistry*, *60*(5), 553–570. https://doi.org/10.1002/VJCH.202200034

Tran, Q. T., Thu, H. T., Tran, V. S., Cuong, T. V., & Hong, C.-H. (2015). Solution-Processed rGO/AgNPs/rGO Sandwich Structure as a Hole Extraction Layer for Polymer Solar Cells. *Journal of Materials*, *2015*, 1–5. https://doi.org/10.1155/2015/652645

Unser, S., Bruzas, I., He, J., & Sagle, L. (2015). Localized Surface Plasmon Resonance Biosensing: Current Challenges and Approaches. *Sensors (Basel, Switzerland)*, *15*(7), 15684. https://doi.org/10.3390/S150715684

Villar, I. Del. (2020). Propagation of Light Through Optical Fibre. *Optical Fibre Sensors: Fundamentals for Development of Optimized Devices*, 17–48. https://doi.org/10.1002/9781119534730.ch2

Vimalanathan, K., Scott, J., Pan, X., Luo, X., Rahpeima, S., Sun, Q., Zou, J., Bansal, N., Prabawati, E., Zhang, W., Darwish, N., Andersson, M. R., Li, Q., & Raston, C. L. (2022). Continuous flow fabrication of green graphene oxide in aqueous hydrogen peroxide. *Nanoscale Advances*, *4*(15), 3121. https://doi.org/10.1039/d2na00310d

Wang, W. C., Zhou, B., Xu, S. H., Yang, Z. M., & Zhang, Q. Y. (2019). Recent advances in soft optical glass fiber and fiber lasers. *Progress in Materials Science*, *101*, 90–171. https://doi.org/10.1016/J.PMATSCI.2018.11.003

Wang, X., & Li, Y. (2007). Monodisperse nanocrystals: general synthesis, assembly, and their applications. *Chemical Communications*, *28*, 2901–2910. https://doi.org/10.1039/B700183E

Wang, Y., Chen, B., Wu, G., Xue, C., & Gao, L. (2025). Fiber-Optic Pressure Sensors: Recent Advances in Sensing Mechanisms, Fabrication Technologies,

and Multidisciplinary Applications. *Sensors (Basel, Switzerland)*, *25*(20), 6336. https://doi.org/10.3390/s25206336

Warier, S. (n.d.). *ABCs of Fiber Optic Communication : a Practical Handbook*. 205. Retrieved April 17, 2024, from https://www.researchgate.net/publication/350789710_ABCs_of_Fiber_Optic_Communication_A_Practical_Handbook

Wu, S. ;, Xu, C. ;, Zhao, Y. ;, Shi, W. ;, Li, H. ;, Cai, J. ;, Ding, F. ;, Qu, P., Wu, S., Xu, C., Zhao, Y., Shi, W., Li, H., Cai, J., Ding, F., & Qu, P. (2023). Recent Advances in Chitosan-Based Hydrogels for Flexible Wearable Sensors. *Chemosensors 2023, Vol. 11, Page 39*, *11*(1), 39. https://doi.org/10.3390/chemosensors11010039

Wu, S., Wu, S., Zhang, X., Feng, T., & Wu, L. (2023). Chitosan-Based Hydrogels for Bioelectronic Sensing: Recent Advances and Applications in Biomedicine and Food Safety. *Biosensors*, *13*(1), 93. https://doi.org/10.3390/bios13010093

Xi, F., & Wu, J. (2004). Macroporous chitosan layer coated on non-porous silica gel as a support for metal chelate affinity chromatographic adsorbent. *Journal of Chromatography A*, *1057*(1–2), 41–47. https://doi.org/10.1016/J.CHROMA.2004.09.059

Xu, C., & Wang, X. (2012). Graphene oxide-mediated synthesis of stable metal nanoparticle colloids. *Colloids and Surfaces A: Physicochemical and Engineering Aspects*, *404*, 78–82. https://doi.org/10.1016/j.colsurfa.2012.04.017

Xu, Q., Yin, H., Cui, M., Huang, R., & Su, R. (2025). An Enhanced Bimetallic Optical Fiber SPR Biosensor Using Graphene Oxide for the Label-Free and Sensitive Detection of Human IgG. *Sensors 2025, Vol. 25, Page 1630*, *25*(5), 1630. https://doi.org/10.3390/s25051630

Yang, M., & Dai, J. (2011). Review on optical fiber sensors with sensitive thin films. *Photonic Sensors 2011 2:1*, *2*(1), 14–28. https://doi.org/10.1007/s13320-011-0047-y

Yang, S., Yue, W., Huang, D., Chen, C., Lin, H., & Yang, X. (2012). A facile green strategy for rapid reduction of graphene oxide by metallic zinc. *RSC Advances*, *2*(23), 8827–8832. https://doi.org/10.1039/C2RA20746J

Yasmin, S., Shamsuddin Ahmed, M., & Jeon, S. (2017). A noble silver nanoflower on nitrogen doped carbon nanotube for enhanced oxygen reduction reaction. *International Journal of Hydrogen Energy*, *42*(2), 1075–1084.

https://doi.org/10.1016/J.IJHYDENE.2016.09.145

Yu, X., Wu, Q., Zhang, H., Zeng, G., Li, W., Qian, Y., Li, Y., Yang, G., & Chen, M. (2017). Investigation on Synthesis, Stability, and Thermal Conductivity Properties of Water-Based SnO2/Reduced Graphene Oxide Nanofluids. *Materials*, *11*(1), 38. https://doi.org/10.3390/ma11010038

Zaaba, N. I., Foo, K. L., Hashim, U., Tan, S. J., Liu, W. W., & Voon, C. H. (2017). Synthesis of Graphene Oxide using Modified Hummers Method: Solvent Influence. *Procedia Engineering*, *184*, 469–477. https://doi.org/10.1016/J.PROENG.2017.04.118

Zare, Y. (2016). Study of nanoparticles aggregation/agglomeration in polymer particulate nanocomposites by mechanical properties. *Composites Part A: Applied Science and Manufacturing*, *84*, 158–164. https://doi.org/10.1016/J.COMPOSITESA.2016.01.020

Zhang, . D, Lau, M., Lu, S., Barcikowski, S., Gökce, B., Neto, ; C, Guinea, F., Peres, N. M., Novoselov, K. S., Geim, A. K., Sun, ; Z, Yuan, Q., Ding, F., Tao, X., Yan, F., & Zheng, Z. (2018). Enhanced nonlinear optical properties of reduced graphene oxide decorated with silver nanoparticles. *Optical Materials Express, Vol. 8, Issue 3, Pp. 698-703*, *8*(3), 698–703. https://doi.org/10.1364/ome.8.000698

Zhang, Y., Li, H., Wu, Q. Y., & Gu, L. (2022). Non-covalent functionalization of graphene sheets by pyrene-endcapped tetraphenylethene: Enhanced aggregation-induced emission effect and application in explosive detection. *Frontiers in Chemistry*, *10*, 970033. https://doi.org/10.3389/fchem.2022.970033

Zhao, H., Ren, S., Wei, Z., & Lou, X. (2022). Evanescent Wave Optical-Fiber Aptasensor for Rapid Detection of Zearalenone in Corn with Unprecedented Sensitivity. *Biosensors*, *12*(7), 438. https://doi.org/10.3390/BIOS12070438/S1

Zheng, Y., Yu, J., Zhu, Z. W., Zeng, B., & Yang, C. (2021). Design, sensing principle and testing of a novel fiber optic displacement sensor based on linear macro-bending loss. *Optik*, *242*, 167194. https://doi.org/10.1016/j.ijleo.2021.167194

Zhou, A., Bai, J., Hong, W., & Bai, H. (2022). Electrochemically reduced graphene oxide: Preparation, composites, and applications. *Carbon*, *191*, 301–332. https://doi.org/10.1016/J.CARBON.2022.01.056

Zhou, Y., Huang, X., Xia, B., Chen, X., Jing, X., Wang, N., & Li, J. (2025). An ultrasensitive optical fiber SPR sensor enhanced by functionalized carbon

quantum dots for Fe3+ measurement. *Journal of Alloys and Compounds*, *1030*, 180784. https://doi.org/10.1016/j.jallcom.2025.180784

Zibaii, M. I., Latifi, H., Saeedian, Z., & Chenari, Z. (2014). Nonadiabatic tapered optical fiber sensor for measurement of antimicrobial activity of silver nanoparticles against Escherichia coli. *Journal of Photochemistry and Photobiology B: Biology*, *135*, 55–64. https://doi.org/10.1016/J.JPHOTOBIOL.2014.03.017

Zikalala, N. E., Azizi, S., Thema, F. T., Cloete, K. J., Zinatizadeh, A. A., Mokrani, T., Mketo, N., & Maaza, M. M. (2024). Modification of graphene-based nanomaterials with gamma irradiation as an eco-friendly approach for diverse applications: A review. *FlatChem*, *45*, 100662. https://doi.org/10.1016/J.FLATC.2024.100662

APPENDICES

APPENDIX 1

1.1 Visual Appearances of AgNs During the Seed and Growth Stages

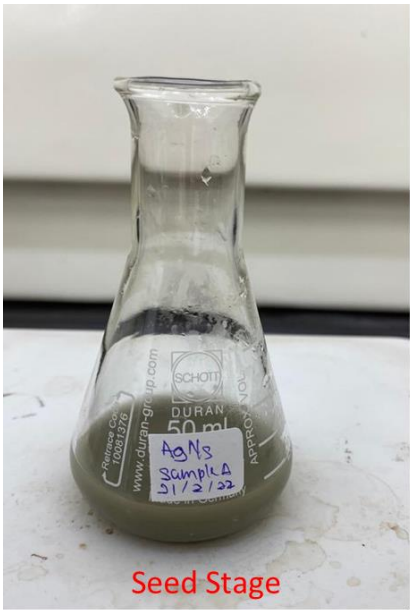

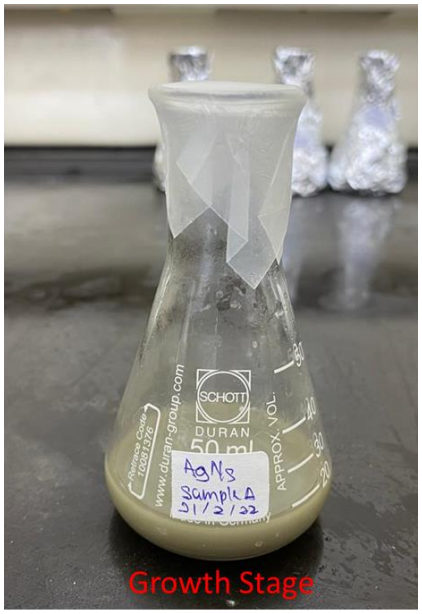

1.2 Ice Bath Preparation During Synthesis of GO

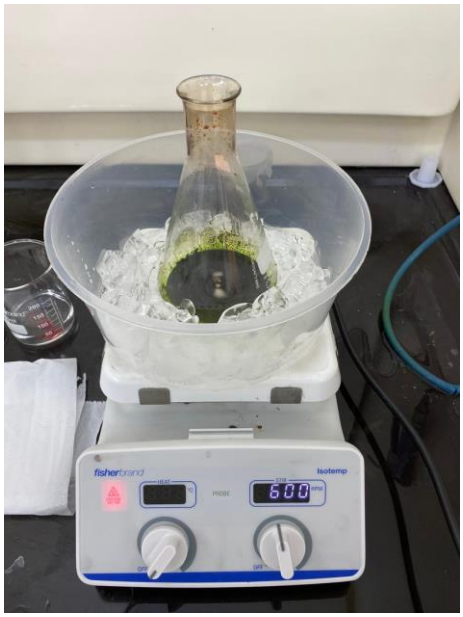

1.3 Leaving the Synthesized GO Overnight Before the Washing Process

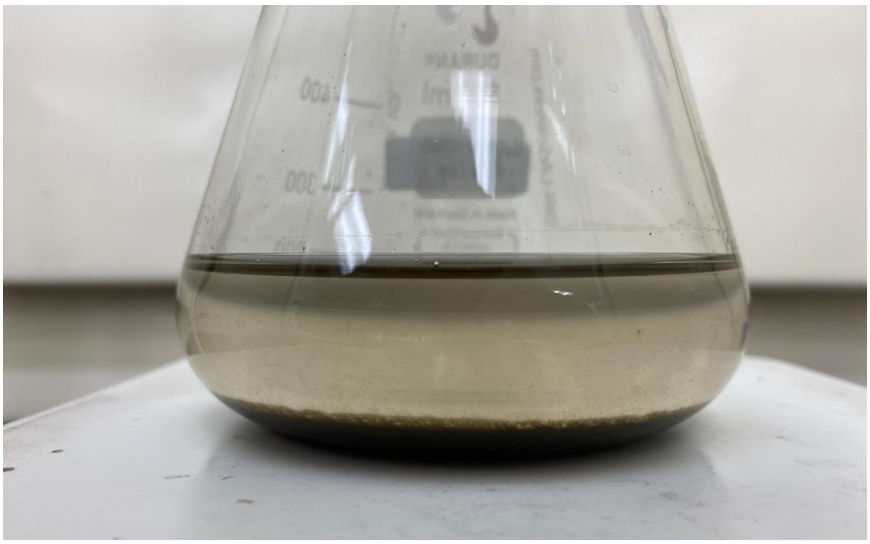

1.4 Result in Mixing the AgNs with GO at Different Volume Ratios

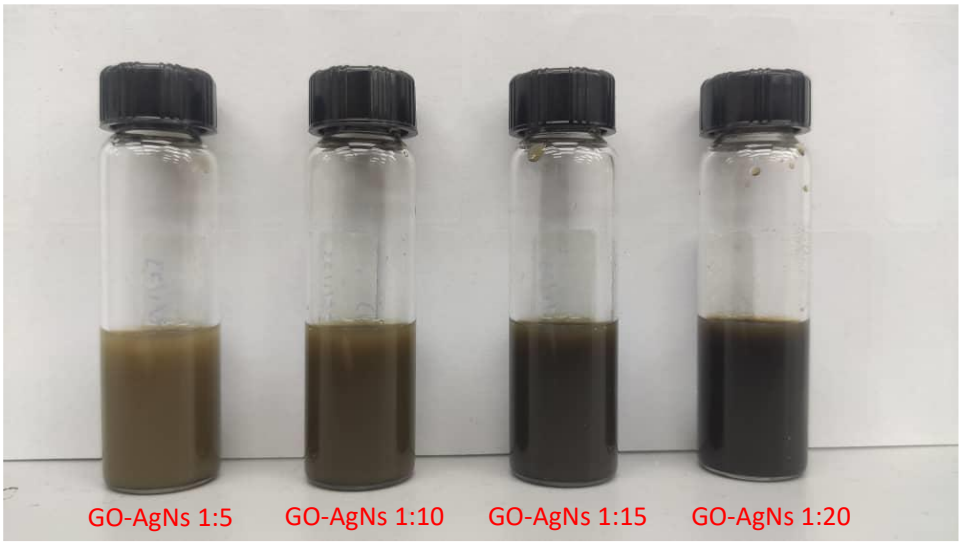

1.5 Result in Mixing the AgNs with rGO with Different Volume Ratios

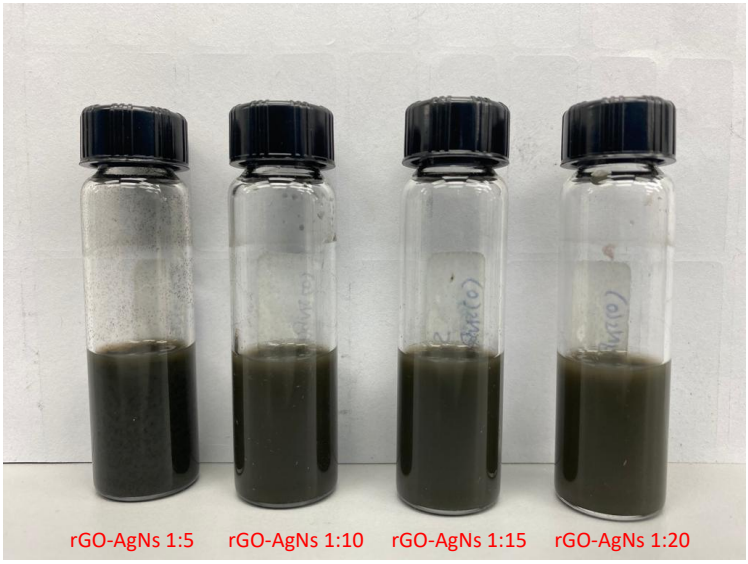

1.6 Physical Observation of Chitosan-Agarose Hybrid Hydrogels



APPENDIX 2

2.1 UV-VIS Spectrometer Analysis on the Sensing Medium



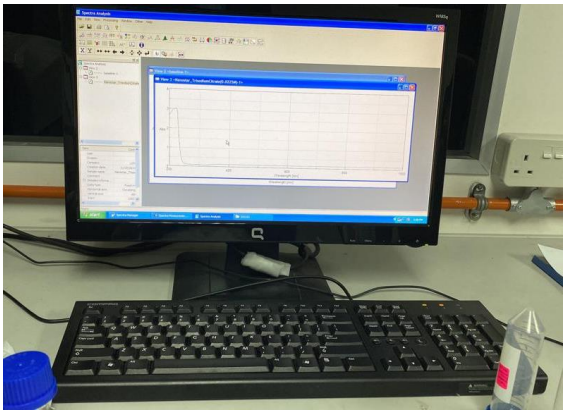

JASCO, V-670 UV-VIS-NIR Spectrophotometer

2.2 Contact Angle Testing on Graphene-Based Materials

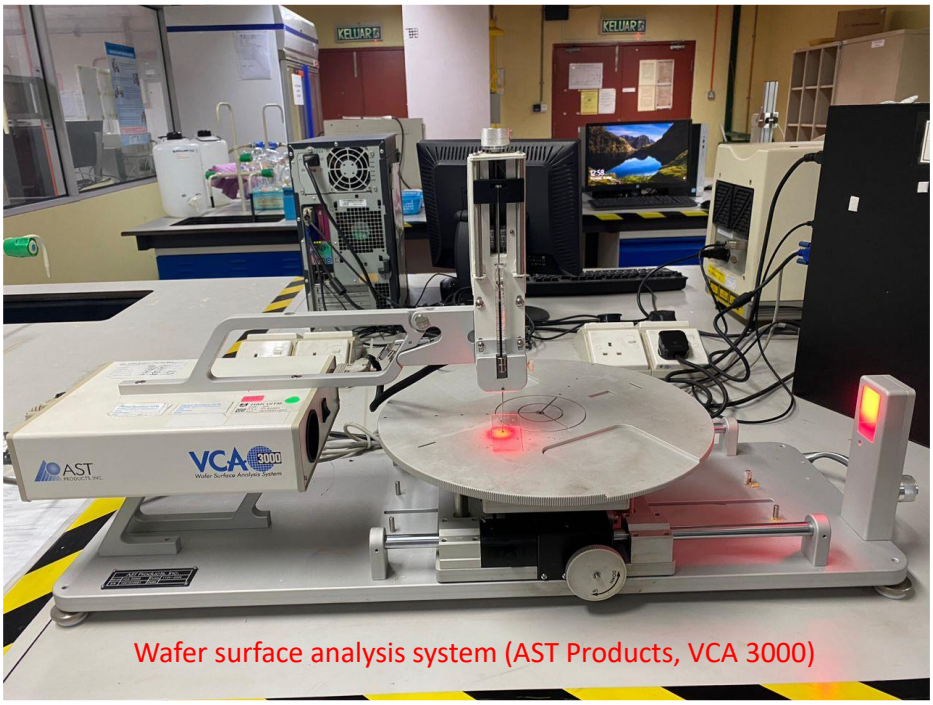

Wafer surface analysis system (AST Products, VCA 3000)

2.3 Zeta Sizer and Potential Analysis Equipment



Zetasizer (Malvern Instruments, Zetasizer Nano series)

2.4 SEM Equipment Used in Analyzing the Sensing Medium's Morphological Structure

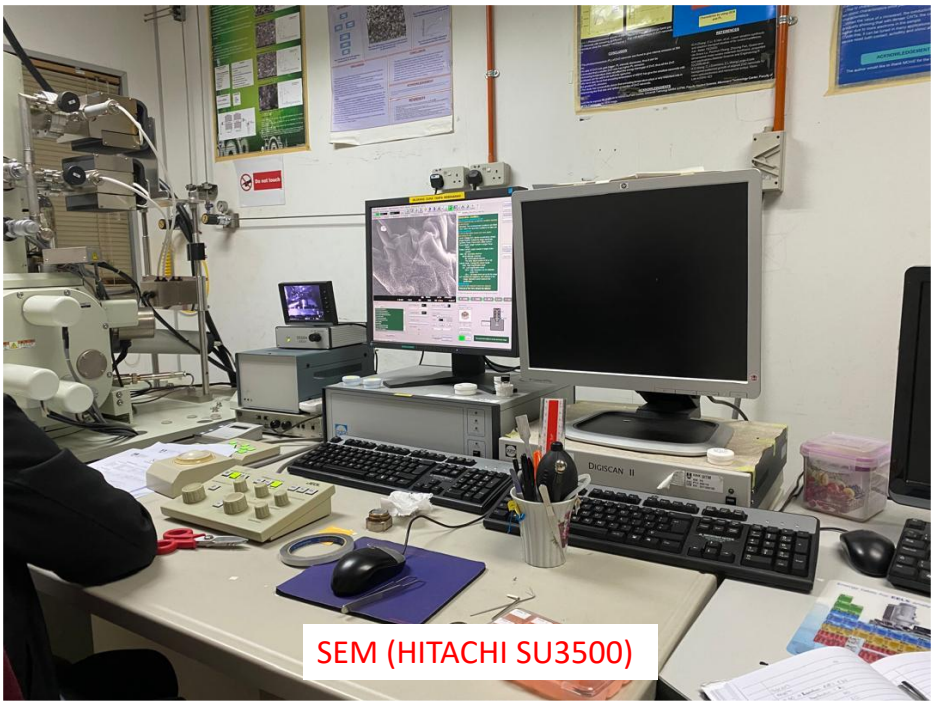

SEM (HITACHI SU3500)

2.5 FTIR Spectroscopy Equipment



FTIR spectroscopy (Varian 640-IR)

2.7 Raman Spectrometer Equipment

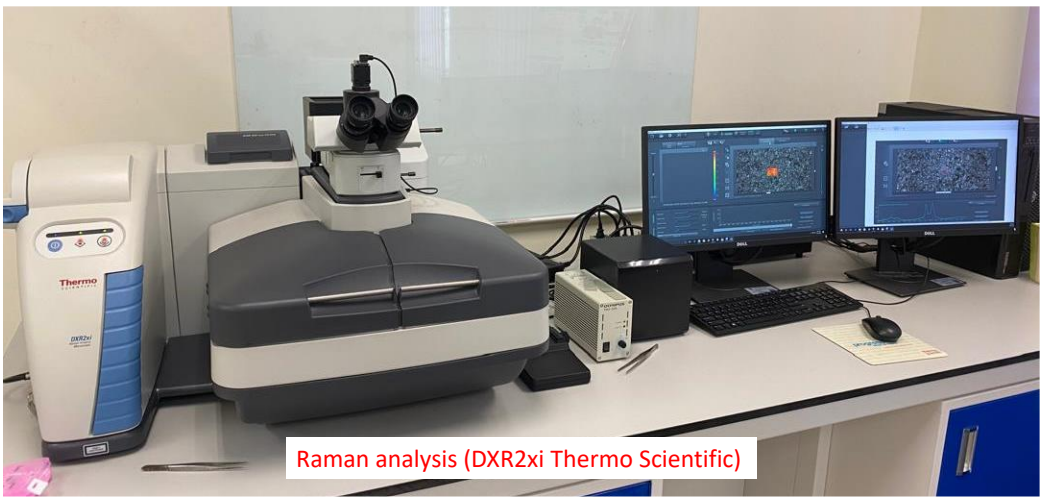

Raman analysis (DXR2xi Thermo Scientific)

APPENDIX 3

3.1 Process of Coating the Bare Fibre with the GO Solution

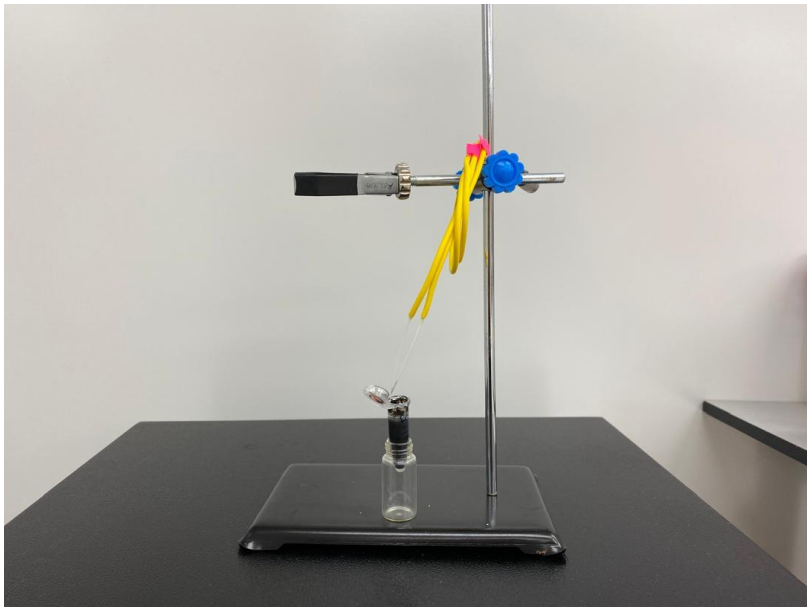

3.2 Process of Coating the Fibre Sensor with Hydrogels

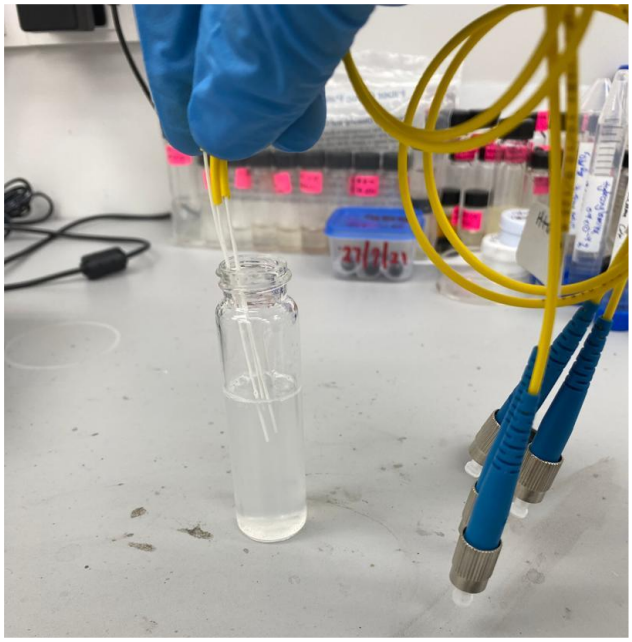

3.3 Set Up the Fibre Optics for Signal Performance

laser light source (wavelength 785 nm, SDL-785-LM-500M72)	Laser power supply (1064 nm, SDL-1064-500M72)	Optical fibre fusion splicer (Sumitomo Type-39, USA)	Ocean Optics spectrometer (HR400CG-UV-NIR)

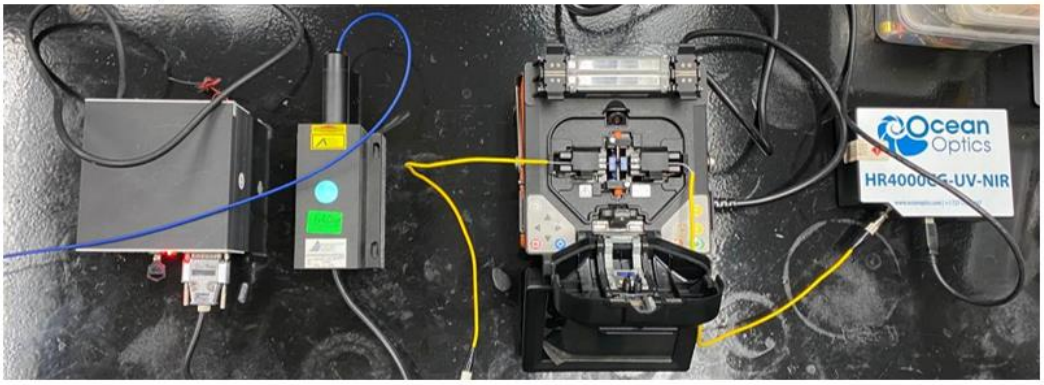

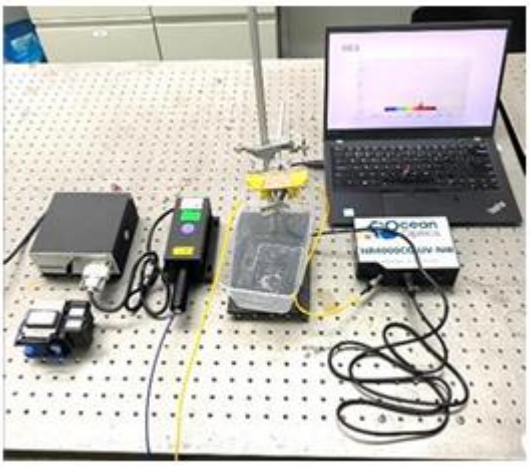

3.4 Placing the Spliced Fibre on the Microfluidic Channel to Study the RI and Protein Detection



AUTHOR'S PROFILE



Azib Haiman Roslan obtained a Bachelor of Mechanical Engineering in year 2022 from Faculty of Mechanical Engineering, Universiti Teknologi MARA (UiTM) Shah Alam. His final-year project (FYP) thesis involves several methods for synthesising AgNPs and introduces them to GO for optical sensor applications. Currently, he is working on introducing rGO, a graphene-based material, into the sensor system for biosensing applications.

LIST OF PUBLICATIONS

Roslan, A. H. Bin, Makhsin, S. R. B., Rani, R. A., Razak, K. A., & Zourob, M. (2022). One-Step Synthesis of Nanostar Shaped Silver Nanoparticles and its Optical Stability. *IEEE International Conference on Semiconductor Electronics, Proceedings, ICSE*, 2022-August, 129–132. https://doi.org/10.1109/ICSE56004.2022.9863200

Roslan, A. H., Makhsin, S. R., Abdul Rani, R., & Siddique, B. (2024). Amplifying fibre optic sensor signals with graphene oxide-silver nanostars / Azib Haiman Roslan ... [et al.]. Journal of Mechanical Engineering (JMechE), 21(3), 297–317. https://ir.uitm.edu.my/id/eprint/101341/

LIST OF CONFERENCES

Roslan, A. H., Makhsin, S. R., Rani, R. A., & Siddique, B. (2025). Insights into the influence of chemical variables on reduced graphene oxide formation in the modified Tour method. *6th Malaysia-Japan International Conference on Nanoscience, Nanotechnology, and Nanoengineering 2025* (MJIC 2025), 21-23 February 2025.

Roslan, A. H. Bin, Makhsin, S. R. B., Rani, R. A., Razak, K. A., & Zourob, M. (2022). One-Step Synthesis of Nanostar Shaped Silver Nanoparticles and its Optical Stability. *IEEE International Conference on Semiconductor Electronics, Proceedings, ICSE*, 2022-August, 129–132. https://doi.org/10.1109/ICSE56004.2022.9863200.

Johari, F. H., Makhsin, S. R., & Roslan, A. H. (2025, December 18). Synthesis of graphene quantum dots from rice husk for water treatment applications. *Symposium of Mechanical, Manufacturing, Mechatronics and Aerospace Engineering 2025.* Shah Alam, 18 December 2025.

LIST OF GRANT INVOLVES

Geran Inisiatif Penyeliaan (GIP), Universiti Teknologi MARA (UiTM). (2022–2023). Feasibility study on reduced graphene oxide loaded silver nanostars (rGO-AgNs) embedded hydrogel conjugated biomolecules for fibre optic biosensors [Research grant, RM18,000]. Completed